# A Down-to-Earth Examination of Hydrological Natural Disasters and Risk Using Earth Observations

A

Dissertation

Presented to

the faculty of the School of Engineering and Applied Science

University of Virginia

in partial fulfillment

of the requirements for the degree

Doctor of Philosophy

By

Gigi Pavur

May 2024

# APPROVAL SHEET

This Dissertation is submitted in partial fulfillment of the requirements
for the degree of
Doctor of Philosophy

Author: Gigi Pavur

This Dissertation has been read and approved by the examining committee:

Advisor: Venkataraman Lakshmi
Committee Member: Jonathan L. Goodall
Committee Member: James H. Lambert
Committee Member: James A. Smith
Committee Member: Benjamin D. Trump

Accepted for the School of Engineering and Applied Science:

Jennifer L. West, School of Engineering and Applied Science

May 2024

# Abstract

Hydrological natural disasters, such as floods, droughts, and hurricanes, historically result in significant social, economic, and environmental loss. With predictions that climate change will likely increase the intensity and frequency of hydrological hazards, there is a need to improve understanding of hydrological extremes and their associated risk to society. The objectives of this dissertation are to advance the applications of space-based Earth Observations for monitoring components of the terrestrial water cycle and to assess risk of hydrological disasters with attention to societal priorities. The following five interdisciplinary studies are investigated in this dissertation. First, a foundational comparison of optical versus radar Earth Observations is demonstrated for delineation of inland waterbodies, a vital storage component of the hydrological cycle. Second, recent hydrometeorological extremes are spatially and temporally examined in the Lake Victoria Basin, a data-sparse region particularly vulnerable to climate extremes. Third, risk of hurricane scenarios is quantified and mapped as the disruption of system order using social vulnerability indices and hydrology data from disparate sources. Fourth, resilience of vulnerable populations to multidecadal climate change is modeled for examination of environmental justice priorities in a region of the southeastern USA. Fifth, basins that face current and/or future water scarcity risk are identified and mapped in Iraq and transboundary regions. Methodologies and findings of this dissertation serve as an important step in supporting global efforts aimed to increase decision maker accessibility to timely and accurate Earth Observations in support of hydrological disaster risk reduction, particularly for the most vulnerable communities.

*To my mom and dad*

# Acknowledgements

Thank you to the moon and back to all those who have supported me in this work. First, thank you to my PhD advisor, Dr. Venkataraman Lakshmi. Thank you for always encouraging me to reach for the stars and to just go for it – whether on the basketball court or beyond. It has been an honor to be your doctoral student.

Thank you to Dr. James H. Lambert for your phenomenal Risk Analysis course which changed the way I think about the world. I am so grateful to have worked alongside your research group.

Thank you to my dissertation committee members: Dr. Jonathan L. Goodall, Dr. James A. Smith, Dr. Benjamin D. Trump, Dr. James H. Lambert, and Dr. Venkataraman Lakshmi. Your generous time, feedback, and questions were greatly appreciated every step of the way.

Thank you to Lawrence Friedl and Kathy Carroll for setting me on a trajectory of curiosity and wonder for Earth Observations at just the right moment in my life.

Thank you to all the inspiring researchers who encouraged me to pursue a PhD in the first place, especially Dr. Keith Gaddis, Dr. David Green, Dr. Ted Russell, Dr. Kenton Ross, and Dr. Dalia Kirschbaum.

Thank you to my mentors, colleagues, and friends at the National Aeronautics and Space Administration (NASA), the National Geospatial-Intelligence Agency (NGA), the United Nations Office for Outer Space Affairs (UNOOSA), the Georgia Institute of Technology, and the University of Virginia. I would especially like to thank Dr. Kevin Dobbs, Dr. Rachel Bernstein, Dr. David Blauvelt, Dr. Macarena Ortiz, Dr. Argyo Kavvada, Dr. Helena Chapman, Dr. Michael Chang, Dr. Andrew Newman, Dr. Zachary Handlos, Dr. Rebecca Foote, Nahom Solomon, Kelley Tobler, Veronica Cesco, Macaulay Eddy, Daniel Nikbakht, Andy Peebles, Markus Woltran, Auset Taylor, Sydney Neugebauer, Alex Ronan, Sean Bauld, Audrey Buehler, Madison Townsend, Kate Todd, and Valerie Fanelle.

Thank you to the outstanding and bright graduate students at the University of Virginia for being my classmates and friends. I would like to especially thank Jessica Besnier, Aya Yehia, Maral Zhiyanpour, Haley Green, Lauren Bramblett, Beatrice Li, Sophia Bakar, Aashutosh Aryal, Son Do, Benjamin Goffin, Robin Kim, Mohammad Saeedi, Duc Tran, Daniella Quintero Garcia, Avery Walters, Ziyue Zhu, Prakrut Kansara, Hyung Kim, Runze Zhang, Hung Le, Chelsea Dandridge, Megan Marcellin, Davis Loose, Rebecca Rebar, DeAndre Johnson, Ronnie Hill, Collyn Clark, Rayshaun Wheeler, Megan Gunn, and Negin Moghadasi.

Thank you to the Klempay family for graciously sharing encouragement and Wi-Fi (especially at Big Moose Lake).

Thank you to my family: my mom and dad, James and Casey, Elisabeth, and Sam. Thank you for never letting me forget that I am loved.

Lastly, thank you to my fiancé, Oscar Klempay, who is undoubtedly the happiest person on the entire planet now that this dissertation is complete! Thank you for your unconditional patience and confidence in me. It turns out that you were right – I could do it!

# Table of Contents

**Abstract** .......... 4

**Acknowledgements** .......... 6

**Table of Contents** .......... 8

**List of Figures** .......... 11

**List of Tables** .......... 18

**Chapter 1:** Introduction .......... 21

1.1 Motivation .......... 21
1.2 Purpose and Scope .......... 22
1.3 Organization .......... 28

**Chapter 2**: Spatial Comparison of Inland Water Observations from CYGNSS, MODIS, Landsat, and Commercial Satellite Imagery .......... 29

2.1 Abstract .......... 29
2.2 Introduction .......... 30
2.3 Data and Methods .......... 34
2.4 Results and Discussion .......... 39
2.5 Future Research and Limitations .......... 49
2.6 Conclusions .......... 50
2.7 Acknowledgements .......... 51

**Chapter 3:** Observing the Recent Floods and Drought in the Lake Victoria Basin Using Earth Observations and Hydrological Anomalies ........ 52

3.1 Abstract ........ 52
3.2 Introduction ........ 53
3.3 Study Area ........ 58
3.4 Data ........ 61
3.5 Methodology ........ 68
3.6 Results and Discussion ........ 70
3.7 Conclusions ........ 85
3.8 Acknowledgements ........ 87

**Chapter 4:** Risk Comparison of Hurricane Scenarios as Disruptions of Hydrologic Basin Order with Criteria of Social Vulnerability ........ 88

4.1 Abstract ........ 88
4.2 Introduction ........ 89
4.3 Geographic Area of the Demonstration ........ 95
4.4 Sources of Data for the Demonstration ........ 96
4.5 Methods ........ 100
4.6 Sample of Results ........ 105
4.7 Discussion ........ 119
4.8 Conclusions ........ 120
4.9 Acknowledgements ........ 123

**Chapter 5:** Modeling Resilience of System Order for Investments in Environmental Justice and Social Vulnerability ........ 124

5.1 Abstract ........ 124
5.2 Introduction ........ 125
5.3 Data ........ 127
5.4 Methodology ........ 128
5.5 Sample of Results of Demonstration ........ 132
5.6 Discussion and Conclusions ........ 135
5.7 Acknowledgements ........ 136

**Chapter 6:** Uncertainty and Sensitivity of Development Goals to Water Scarcity of Iraq and Transboundary Regions ........ 137
6.1 Abstract ........ 137
6.2 Introduction ........ 138
6.3 Sources of Data for the Demonstration ........ 142
6.4 Methods ........ 147
6.5 Results and Discussion ........ 151
6.6 Conclusions ........ 157
6.7 Acknowledgements ........ 160
**Chapter 7:** Conclusions ........ 161
7.1 Overview ........ 161
7.2 Research Summary ........ 161
7.3 Summary of Key Contributions ........ 162
7.4 Future Work in Natural Disasters Hydrology and Risk ........ 164
7.5 Final Remarks ........ 165
**Appendices** ........ 166
**References** ........ 196

# List of Figures

***Fig. 2.1:*** *CYGNSS observations and bivariate water mask products for the contiguous United States between latitudes of approximately 24-37°N for 2019.* ***(A)*** *Spatial plot of CYGNSS 1-km 50th percentile surface reflectivity signal-to-noise-ratio (SNR) data.* ***(B)*** *CYGNSS bivariate water mask at 1-km spatial resolution derived from basin-specific binary thresholding of SNR values.* ***(C)*** *MODIS bivariate water mask at 1-km spatial resolution derived from the Land Water Mask (MCD12Q1) for 2019.* ***(D)*** *Landsat bivariate water mask at 1-km spatial resolution derived from the Landsat Global Surface Water product (commonly referred to as the Pekel water mask) for 2019.* ______ *41*

***Fig. 2.2:*** *Comparison Water Mask derived from CYGNSS, Landsat, and MODIS for the contiguous United States between latitudes of approximately 24-37°N for 2019.* ***(A)*** *1-km Comparison Water Mask across the study area for 2019 derived from the CYGNSS, Landsat, and MODIS bivariate water masks.* ***(B)*** *The 1-km Comparison Water Mask subdivided into USGS Hydrological Unit Code-02 Watersheds. The watersheds are referred to as the South Atlantic Gulf basin (B03), the Tennessee basin (B06), the Lower Mississippi basin (B08), the Arkansas-White River basin (B11), the Texas-Gulf basin (B12), the Rio Grande basin (B13), the Lower Colorado (B15), and the California basin (B18).* ______ *42*

***Fig. 2.3:*** *CYGNSS, Landsat, and MODIS bivariate water mask confusion matrix statistics visualized as heat maps for* ***(A)*** *Recall (R),* ***(B)*** *Precision (P),* ***(C)*** *Specificity (SP),* ***(D)*** *Miss Rate*

*(M),* ***(E)*** *False Detection Rate (FDR),* ***(F)*** *Accuracy, and* ***(G)*** *F1-score (F1). For each, the total study area (AOI) or sub-basin of interest (USGS HUC-02) is indicated. The assumed reference water mask is indicated as either Landsat or MODIS. The predicted water mask is indicated as either CYGNSS, MODIS, Landsat, a combination of MODIS and CYGNSS, or a combination of Landsat and CYGNSS.* ________ *46*

***Fig. 2.4:*** *Comparison water mask overlayed onto high-resolution commercial satellite imagery from Planet Labs, Inc. and DigitalGlobe for select locations:* ***(A)*** *Salton Sea, CA,* ***(B)*** *Lake Maurepas and Pontchartrain, LA,* ***(C)*** *Lake Hartwell, GA/SC,* ***(D)*** *Tennessee River, TN,* ***(E)*** *Lake Kissimmee, FL,* ***(F)*** *Sam Rayburn Reservoir, TX.* ***(G)*** *Reference locations for the commercial images are provided on the comparison water mask. Hand drawn water masks are displayed in light blue for visual purposes. For additional information on the high-resolution imagery, including date of acquisition and image identification number(s), see Appendix 2.11.* ________ *48*

***Fig. 3.1: (A)*** *Map of watershed delineations for the Nile and Lake Victoria watersheds. Lake Victoria is the source of the White Nile River and thus plays a critical role in the hydrology of downstream countries within the Nile watershed. Country boundaries are provided to give context to the watershed at the continental scale (ESRI, 2021; World Bank, 2019; WWF, 2019).* ***(B)*** *Digital elevation model (DEM) for the Lake Victoria Basin, derived from the Shuttle Radar Topography Mission (SRTM). Delineation of the basin includes portions of Uganda, Kenya, Tanzania, Rwanda, and Burundi. Major lakes are displayed in light blue. The highest topography is found in the northwestern portion of the basin in Kenya and along the southwestern rim in Burundi and Rwanda. The lowest topography is found along the perimeter of Lake Victoria (ESRI, 2021; USGS, 2018; World Bank, 2019; WWF, 2019).*________*60*

***Fig. 3.2:*** *Land cover classifications for the Lake Victoria Basin in 2019 derived from MODIS/Terra + Aqua Yearly L3 Global 500 m SIN GRID (MCD12Q1 V006). The classifications are based on the Annual International Geosphere-Biosphere Program (IGBP) classification scheme.* ________ *61*

***Fig. 3.3:*** *Time series of average monthly anomalies for hydrological variables (precipitation, evapotranspiration, runoff, root zone soil moisture, total water storage anomaly (TWSA), and lake height) in the Lake Victoria Basin. The local maxima positive anomaly during the 2019 – 2020 flood period is indicated by a blue vertical line (representing the wet month). The local minima negative anomaly during the 2021 – 2022 drought period is indicated by a red vertical line (representing the dry month). Geospatial anomaly plots of the indicated wet and dry months for each hydrological variable are shown:* ***(A)*** *Time series of average monthly precipitation anomalies from Jan. 2002 – Jun. 2022 derived from GPM IMERG.* ***(B)*** *Time series of average monthly evapotranspiration anomalies from Jun. 2002 – Jun. 2022 derived from MODIS abord the Terra mission.* ***(C)*** *Time series of average monthly runoff anomalies from Jun. 2002 – Jun. 2022 derived from GLDAS.* ***(D)*** *Time series of average monthly root zone soil moisture (0 – 2 m depth) anomalies from Jun. 2002 – Jun. 2022 derived from GLDAS.* ***(E)*** *Time series of total water storage anomaly (TWSA) from Jun. 2002 – May 2022 derived from GRACE.* ***(F)*** *Time series of average monthly lake height anomalies relative to mean sea level (MSL) derived from Jason-1, Jason-2, and Jason-3.* *70*

***Fig. 3.4:*** *Average monthly geospatial anomalies of hydrological parameters during the anomalously high (wet) and low (dry) months between Sept. 2019 – Jan. 2022. These months are the local maxima and minima in the basin-averaged monthly time series of hydrological anomalies shown in Figure 3 as the vertical blue and red lines to indicate wet and dry anomalies. For visual purposes, the scalebar was manually selected to represent variability within the basin by displaying outliers as the maximum/minimum colors.* ***(A1)*** *Monthly precipitation anomalies in Oct. 2019 (wet month).* ***(A2)*** *Monthly precipitation anomalies in Nov. 2021 (dry month).* ***(B1)*** *Monthly evapotranspiration anomalies in Mar. 2020 (wet month).* ***(B2)*** *Monthly evapotranspiration anomalies in Jan. 2022 (dry month).* ***(C1)*** *Monthly runoff anomalies in Mar. 2020 (wet month).* ***(C2)*** *Monthly runoff anomalies in Nov. 2021 (dry month).* ***(D1)*** *Monthly root zone soil moisture anomalies in Mar. 2020 (wet month).* ***(D2)*** *Monthly root zone soil moisture anomalies in Dec. 2021 (dry month).* ***(E1)*** *Monthly total water storage anomaly (TWSA) in May 2020 (wet month).* ***(E2)*** *Monthly total water storage anomaly (TWSA) in Dec. 2021 (dry month)* *75*

***Fig. 3.5:*** *Spatial plots of monthly soil moisture (0–5 cm depth) observations derived from SMAP. March 2020 and November 2021 were respectively selected as the wet and dry months, based on the time series of monthly root zone soil moisture anomalies (Fig. 4 C1 and C2). The spatial plots are shown at both 9-km and 1-km resolutions. (A1) 9-km monthly soil observations in Mar. 2020 (wet month); (A2) 9-km monthly soil moisture observations in Nov. 2021 (dry month); (B1) 1-km monthly soil moisture observations in Mar. 2020 (wet month); (B2) 1-km monthly soil moisture observations in Nov. 2021 (dry month).* ______ *79*

***Fig. 3.6:*** *Results of validation of in-situ near-surface soil moisture observations from the International Soil Moisture Network with the 1-km and 9-km Soil Moisture Active Passive (SMAP) observations at 6:00AM overpasses.* ______ *80*

***Fig. 3.7:*** *Time series of in-situ near-surface soil moisture observations from four TAHMO stations compared with 1-km and 9-km SMAP soil moisture observations from 2015 to 2021.* _ *81*

***Fig. 3.8:*** *Variability of monthly climatological values of precipitation, lake height, and total water storage anomaly (TWSA) which were calculated from the duration of the study period from June 2002 – January 2022 using equation 2. This graph shows the seasonality of precipitation, lake height, and TWSA within the basin. It is important to note that lake height is managed by hydropower dams at Lake Victoria's outlet near Jinja, Uganda.* ______ *83*

***Fig. 3.9:*** *Time series of monthly total water storage anomaly (TWSA, shown as purple bars), observed basin-averaged monthly precipitation (shown as solid blue line), and climatological monthly precipitation (black dashed line) from Jan. 2019 – Jan. 2022. If the monthly precipitation is greater than the climatological precipitation, the basin experienced a positive anomaly meaning it was wetter than the climatological average. Likewise, if the monthly precipitation is less than the climatological precipitation, the basin experienced a negative anomaly meaning it was drier than the climatological average. Note, TWSA data was not yet published for Nov. 2021-Jan. 2022 when this analysis was conducted.* ______ *84*

**Fig. 4.1:** *Area of demonstration within the southeastern United States.* **(A)** *Digital elevation model (DEM) and HydroBASINS Level 08 sub-basins.* **(B)** *Hurricane Ian track and wind swath estimates from NOAA National Weather Service and HydroBASINS Level 08 sub-basins.* ____ *96*

**Fig. 4.2:** *Spatial maps of the observed social vulnerability and hydrology variables resampled per sub-basin for* **(A)** *Social Vulnerability Index,* **(B)** *cumulative precipitation,* **(C)** *maximum hourly precipitation,* **(D)** *five-day antecedent soil moisture, and* **(E)** *maximum hourly wind speed.* ____ *101*

**Fig. 4.3:** *Histograms of the observed social vulnerability and hydrology variables resampled per sub-basin in the area of demonstration for* **(A)** *Social Vulnerability Index (SVI),* **(B)** *total precipitation,* **(C)** *hourly maximum precipitation,* **(D)** *hourly maximum wind speed, and* **(E)** *five-day antecedent soil moisture.* ____ *105*

**Fig. 4.4:** *Maps of the ordered percentiles within the area of demonstration at the sub-basin level for the following social vulnerability and hydrology variables:* **(A)** *Social Vulnerability Index (SVI),* **(B)** *cumulative precipitation,* **(C)** *maximum hourly precipitation,* **(D)** *five-day antecedent 1-km soil moisture, and* **(E)** *maximum hourly wind speed.* ____ *107*

**Fig. 4.5:** *Average order of the top 10% of basins from Scenario $S_{20}$ across all scenarios ($S_1$ – $S_{20}$). The overall ordering stabilizes as more hydrology and social vulnerability variables contribute to a given scenario.* ____ *110*

**Fig. 4.6:** *Normalized score of disruptiveness for scenarios ($S_2$ – $S_{20}$) to determine the most and least disruptive scenarios compared to the baseline SVI order ($S_1$).* ____ *111*

**Fig. 4.7:** *Spatial plot of the basin ordering for the following scenarios:* **(A)** *$S_9$ – SVI and Hurricane Ian 5-day antecedent soil moisture,* **(B)** *$S_{16}$ – SVI, Hurricane Ian maximum cumulative precipitation, maximum hourly precipitation, and maximum hourly wind speed, and* **(C)** *$S_{19}$ –*

*SVI, Hurricane Ian maximum hourly precipitation, maximum hourly wind speed, and 5-day antecedent soil moisture.* 113

***Fig. 4.8:*** *Spatial plot of the basin risk for the following scenarios:* ***(A)*** $S_9$ *– SVI and Hurricane Ian 5-day antecedent soil moisture,* ***(B)*** $S_{16}$ *– SVI, Hurricane Ian maximum cumulative precipitation, maximum hourly precipitation, and maximum hourly wind speed, and* ***(C)*** $S_{19}$ *– SVI, Hurricane Ian maximum hourly precipitation, maximum hourly wind speed, and 5-day antecedent soil moisture. Basins which increased in order are depicted in red. Basins which decreased in order are depicted in green.* 116

***Fig. 4.9:*** *Reference maps for the following:* ***(A)*** *Top 20 basins (2%) with highest prioritization in the disrupted order for scenario* $S16$. *A table summary of these basins can be found in Table 4.* ***(B)*** *Top 10 basins (1%) with greatest increase in priority across any scenario compared to the baseline order* $S1$. *A table summary of these basins can be found in Table 5A.* ***(C)*** *Top 10 basins (1%) with greatest decrease in priority across any scenario compared to the baseline order* $S1$. *A table summary of these basins can be found in Table 5B.* 119

***Fig. 5.1:*** *The basin order for scenario s.00: Social Vulnerability Index. This is described as the baseline order in the demonstration.* 132

***Fig. 5.2:*** *Summary of normalized score of disruption for each of the scenarios, s.01 – s.16, in the demonstration.* 133

***Fig. 5.3:*** *The maps describe the disruptions to system order across water basins for the following scenarios:* ***(A)*** *the most disruptive scenario, s.11, and* ***(B)*** *the least disruptive scenario, s.13.* 134

***Fig. 5.4:*** *The maps describe the disruption to system order across basins for the following scenarios:* ***(A)*** *the most disruptive scenario, s.11, and* ***(B)*** *the least disruptive scenario, s.13.* 135

***Fig. 6.1: (A)*** *Digital elevation model (DEM) derived from NASA Shuttle Radar Topography Mission (SRTM) for the geographic area of demonstration with basin delineations shown for the Haditha, Mosul, Dokan, and Euphrates-Tigris River basins.* ***(B)*** *Sub-basin delineations for the geographic area of demonstration, as defined by the Level 05 HydroBASINS dataset.* ***(C)*** *Land use/land cover map of Iraq and surrounding countries derived from Sentinel-2 data.* ______ *142*

***Fig. 6.2:*** *Basin ordered spatial plots for single variable scenarios* ($S1 - S9$) *and multiple variable scenarios* ($S10 - S15$). *Basins in black are low order values (near or equal to 1) representing high priority/high concern. Basins in white are high order values (near or equal to the maximum number of basins) representing low priority/little concern.* ________________ *152*

***Fig. 6.3:*** *Spatial maps of basin-level risk for scenarios of three or more factors (i.e.,* $S10 - S15$). *Basins in red indicate increased risk (i.e., a positive change in basin order). Basins in green indicate decreased risk (i.e., a negative change in basin order).* ________________________ *155*

***Fig. 6.4: (A)*** *Sum of least square difference in order for scenarios* $S2 - S15$ *and* ***(B)*** *normalized score of disruption in order for scenarios* $S2 - S15$. *Both metrics are used to determine the most and least disruptive scenarios compared to the baseline order* ($S1$). _____________________ *157*

# List of Tables

**Table 3.1:** *Population forecasts for Burundi, Kenya, Rwanda, Tanzania, and Uganda for mid-2020 to mid-2050 (Kaneda et al., 2020).* 54

**Table 3.2:** *Summary of hydrological data used in this study.* 63

**Table 3.3:** *Summary of wet/dry months and positive/negative anomaly values for hydrological variables during the recent flood and drought events. These were determined from the time series of monthly basin-averaged anomalies constructed from 20 years of Earth observations or model data (see Fig. 3).* 72

**Table 4.1:** *Summary of hydrology and social vulnerability data used in this study, including the variable, sensor/model, native spatial resolution, resampled resolution, resampling method, temporal resolution, study period, and sources.* 97

**Table 4.2:** *A swing-weight technique is used to update factor weights for each of the twenty (20) scenarios of the contributing hydrology and social vulnerability variables. These include Social Vulnerability Index (SVI), cumulative precipitation (P1), maximum hourly precipitation (P2), maximum hourly wind speed (W), and five-day antecedent soil moisture (SM).* 102

***Table 4.3:*** *Summary of the number of basins within 10% increments of disruption across scenarios $S_2 – S_{20}$ compared to the baseline order ($S_1$).* ______ *112*

***Table 4.4:*** *Summary of top-20 basins (2% of the study area) which prioritized highest in the disrupted order (D) for scenario $S_{16}$. The HydroBASINS Level-08 basin name, state, basin type (coastal or inland), and baseline order ($S_1$) are provided. A reference map of the basin locations is available in Fig. 9A.* ______ *115*

***Table 4.5:*** *Summary of top 10 basins (1%) with* ***(A)*** *largest increase and* ***(B)*** *largest decrease in priority across scenarios compared to the baseline order ($S_1$). The rank of largest increase/decrease in priority, HydroBASINS Level-08 basin name, increase/decrease in prioritization percentage, baseline order ($S_1$), scenario of minimum order, and minimum order are provided for each basin. Reference maps for Table 5A and 5B are respectively shown in Fig. 9B and 9C.* ______ *118*

***Table 4.6:*** *Summary of qualitative results of this study including descriptions and figures/tables to references within the manuscript.* ______ *121*

***Table 5.1:*** *Sample of importance criteria and sorting methods in modeling disruption of system order.* ______ *128*

***Table 5.2:*** *Sample of scenarios and criteria in modeling of disruption of system order.* ______ *130*

***Table 6.1:*** *Summary of open data used in this study including variable, sensor/model, native spatial resolution, resampled resolution, resampling method, temporal resolution, study period, and sources.* ______ *143*

***Table 6.2:*** *Scenario descriptions and swing weights for each of the fifteen scenarios using social, hydrological, and other environmental factors. These include youth population density (YPD), population growth rate (PGR), percentage of urbanized basin area in 2022 (URB), percentage of agricultural basin area in 2022 (AGR), distance from earthquake epicenters to basin centroids (D), annual average precipitation (P), annual average air surface temperature (T), annual average root zone soil moisture (RZSM), and annual average normalized difference vegetation index (NDVI).* ____ *149*

***Table 6.3:*** *Qualitative summary of results from this study including descriptions of figures/tables to reference within the manuscript and appendix.* ____ *159*

# **Chapter 1:** Introduction

## 1.1 Motivation

Floods, droughts, and tropical cyclones are naturally occurring hydrological phenomena. However, communities across the globe are continually disrupted by the complex and interconnected challenges of society, economy, and environment due to hydrological extremes. There is an urgent need to effectively decrease the loss of life and property to hydrological disasters, particularly for the most vulnerable communities.

The United Nations Office for Disaster Risk Reduction (UNDRR) defines a *disaster* as, "a serious disruption of the functioning of a community or a society at any scale due to hazardous events interacting with conditions of exposure, vulnerability, and capacity, leading to one or more of the following: human, material, economic, and environmental losses and impacts." Thus, the intersection of hydrological extremes and populations (whether resilient or vulnerable) is vital to the understanding of disaster prediction, response, and management.

Climate change is predicted to likely exacerbate the challenges of hydrological disasters by increasing the frequency and intensity of hydrological extremes (Lavell et al., 2012; UNDRR, 2015). Given this, the United Nations Sendai Framework for Disaster Risk Reduction has identified the need for improved understanding of both climate-related disasters and the risk associated with these extreme events (UNDRR, 2015). These are vital steps to support sustainable development of resilient communities (UNDRR, 2015).

Evidence-based decision making is a highly effective tool for supporting sustainable resources management and promoting risk-informed societies (Kavvada et al., 2022). However, many locations of the world still suffer from insufficient in-situ hydrological observations which limits the ability for evidence-based sustainable water management. Satellite-based Earth Observations, from public and commercial entities, can be used to fill data gaps in data-sparse regions by providing high-resolution hydrological data collected at regular temporal scales across the globe. These data can be used to inform and improve hydrological disaster preparation, monitoring, forecasts, models, and risk analysis.

This dissertation aims to support global efforts of disaster risk reduction by demonstrating applications of Earth Observations research to improve understanding of the spatial and temporal variability of hydrological extremes, as well as the risk associated with hydrological disasters. We define and quantify *risk* as the disruption of system order (Bonato et al., 2022; Eddy et al., 2022; Hamilton et al., 2013; Hassler et al., 2019; Sambo et al., 2023; You et al., 2014). Five chapters in this dissertation discuss timely challenges of hydrological extremes and risk for study areas within the United States (Chapters 2, 4, and 5), Eastern Africa (Chapter 3), and the Middle East (Chapter 6).

## 1.2 Purpose and Scope

This section describes the purpose and scope of the dissertation as research questions and brief literature reviews of each chapter. Section 1.2.1 describes the two chapters focused on hydrological monitoring (corresponding with Chapter 2 and Chapter 3). Section 1.2.2 describes the three chapters focused on hydrological risk analysis (corresponding with Chapter 4, Chapter 5, and Chapter 6).

### 1.2.1 Hydrological Monitoring

**Research Question #1: Chapter 2**

*To what extent do inland waterbody masks derived from optical versus radar sensors agree or disagree on the extent and location of inland water, which are important storage components of the hydrological cycle?*

Inland waterbodies (defined as lakes, rivers, streams, reservoirs, and wetlands for purposes of this chapter) play a critical role in terrestrial water storage and hydrological processes (Bronmark & Hansson, 2002; Bullock & Acreman, 2003). Accurate and timely inland waterbody extent and location data are foundational information to support a variety of hydrological applications and water resources management. Space-based Earth Observations are a reasonable method for remotely generating inland water masks (Asadzadeh Jarihani et al., 2013; Palmer et al., 2015; Soman & Indu, 2022). This has been demonstrated by two widely accepted global inland water mask products: 1) the Landsat (Pekel) water mask (Pekel et al., 2016), and 2) the Moderate Resolution Imaging Spectroradiometer (MODIS) (Sulla-Menashe et al., 2019). However, these water masks are constrained by their dependence on optical sensors which are impeded by cloud cover and limited temporal revisit intervals. This is concerning because the maximum inland waterbody extent likely occurs during rainy/cloudy conditions. Recently, NASA's Cyclone Global Navigation Satellite System (CYGNSS) mission has emerged as a new opportunity to delineate inland water using a constellation of eight microsatellites with passive bistatic radars to receive reflected L-band signals from the Global Positioning System (GPS) constellation (Al-Khaldi et al., 2021; Chew & Small, 2020; Gerlein-Safdi & Ruf, 2019; Ghasemigoudarzi et al., 2022; Morris et al., 2019; C. Ruf et al., 2021; C.S. Ruf et al., 2018; Wang et al., 2022). However, there is currently no standard method for generating a CYGNSS-based inland water mask. In this chapter, we contribute a foundational comparison of a 1-km CYGNSS water mask to Landsat and MODIS water masks, by employing a mosaic of surface reflectivity signal-to-noise ratio (SNR) thresholds at the sub-basin level.

### Research Question #2: Chapter 3

*In data-sparse regions of the world lacking in-situ observations, how can we map components of the hydrological cycle?*

Africa's largest lake, Lake Victoria, provides valuable ecosystem services to five Eastern African countries within its basin: Burundi, Kenya, Rwanda, Tanzania, and Uganda. As a source of the White Nile River and a sub-basin of the greater Nile watershed, the Lake Victoria Basin plays a critical role in supplying freshwater locally to an estimated 35 million people and indirectly to 340 million people in downstream countries (Ramilien et al., 2014; Mugu et al., 2020; Awanage, 2020; Awange, 2006; Awange, 2005). Over the previous decades, hydrometeorological extremes such as floods and droughts have proven to be continual and recurrent in the Lake Victoria Basin (Nyeko-Ogiramoi et al., 2013). Furthermore, previous research has identified the Lake Victoria Basin as a significant hotspot for population-climate burdens (Lopez-Carr et al., 2014). As with many regions in Africa, the Lake Victoria Basin lacks sufficient in-situ hydrological observations for accurate and continual hydrological monitoring to support sustainable water resources management (Alsdorf et al., 2016; Paris et al., 2022). In this chapter, satellite remote sensing is leveraged to obtain spatial and temporal estimates of components of the hydrological cycle, including identification and quantification of the recent extreme flood and drought events in the Lake Victoria Basin.

### 1.2.2 Hydrological Risk Analysis

**Research Question #3: Chapter 4**

*How does risk spatially vary across sub-basins given exposure to hydrological extremes during major hurricanes and in combination with existing social vulnerability factors?*

Compared to other disasters in the United States, hurricanes generate the greatest damages and highest number of fatalities per year, averaging approximately $30.9 billion in damages and 157 fatalities per year since 1980 (NOAA, 2023; Smith, 2023). The Southeastern United States is a hotspot for disproportionately high losses due to climate-sensitive hazards because of its elevated exposure and high concentration of socially vulnerable populations (Cutter et al., 2003; Emrich & Cutter, 2011). Social vulnerability of an individual or community refers to their “capacity to anticipate, confront, repair, or recover from the effects of a disaster” (Flanagan et al., 2018). Previous studies have shown that communities of high social vulnerability face significant short and long-term challenges following disasters which adversely affect their ability to recover (Bakkensen et al., 2017; Flanagan et al., 2011, 2018; Fothergill & Peek, 2004; Highfield et al., 2014; Karimiziarani & Moradkhani, 2023; Meyer et al., 2018; Yarveysi et al., 2023). Disparities of social vulnerability have even been found within neighboring blocks, meaning communities with varying social vulnerability will likely suffer different impacts if exposed to the same tropical cyclone conditions (Bakkensen et al., 2017; Yarveysi et al., 2023). Often during major hurricanes, it is not possible to collect sufficient in-situ observations due to instrument failure and dangerous collection conditions. Thus, Earth Observations using satellite sensors serve as a valuable tool to obtain hydrology data with sufficient spatial and temporal resolution to characterize extreme events. In this chapter, satellite-derived hydrological observations are compared with social vulnerability data in a risk register of basins which can serve as a tool for improving understanding of basin-level risk as change in baseline order.

### Research Question #4: Chapter 5

*What is the resilience of system order considering long-term hydrological conditions and social vulnerability?*

Resilience of vulnerable populations to environmental extremes is a concern for policymaking across environmental justice, economic development, technology innovation, etc. The multidisciplinary perspective of *environmental justice* can improve understanding of the extent that environmental conditions disproportionately impact vulnerable populations, such as the socially vulnerable (Mohai et al., 2009). As climate change is predicted to increase the frequency and intensity of hydrological and environmental extremes, criteria of environmental conditions are expected to further exacerbate environmental justice concern in the future (Brinkley & Wagner, 2024; Mohai et al., 2009). To support priorities aimed to address environmental justice, there is a need to improve understanding of system risk when multidisciplinary criteria of society and the environment are jointly considered. In this chapter, a demonstration is provided for a region of the Southeastern United States, which previous studies have identified as a hotspot for concerns of vulnerable populations with high exposure to extreme environmental conditions (Cutter et al., 2003; Emrich & Cutter, 2011; Flanagan et al., 2011, 2018). Criteria of social vulnerability examined include socioeconomic status, household composition and disability, minority status and language, and housing type and transportation (Flanagan et al., 2011, 2018). In this chapter, we demonstrate methods of modeling resilience of system order given priorities of environmental justice by considering criteria of long-term hydrological and environmental conditions in combination with criteria of social vulnerability.

**Research Question #5**: **Chapter 6**

*How do interdisciplinary factors of water scarcity (i.e., social, hydrological, and environmental) contribute to basin-level risk of population and water scarcity in Iraq and transboundary basins?*

The arid and semi-arid basins of Iraq and transboundary regions are highly vulnerable to both climate change and upstream water management of riparian countries of the Euphrates and Tigris Rivers (US NIE, 2022; Al-Ansari et al., 2014; Ethaib et al., 2022). In the Middle East, factors compounding the severity of drought on society include, but are not limited to, development of upstream countries, population growth, food insecurity, economic insecurity, decreased power availability, insufficient health and sanitation systems, slow-onset disaster events (i.e., prolonged drought), and rapid-onset disaster events (i.e., floods and earthquakes) (Chumky et al., 2022; Jaime et al., 2022; McAuliffe & Triandayfllidou, 2022; Peters, 2021; UNICEF, 2021). Despite the need for cooperative water management in the region, international disagreements prevent the ubiquitous sharing of in-situ hydrology data to support sustainable development (Albarakat & Lakshmi, 2019; Amini et al., 2023). Thus, Earth Observations through satellite remote sensing and publicly available global model outputs presents a valuable opportunity to improve the spatial and temporal understanding of hydrological conditions in the region. In this chapter, scenarios of water scarcity in Iraq and transboundary regions are modeled and quantified as the disruption of system order using criteria of remotely sensed hydrological observations and population data.

## 1.3 Organization

The remainder of this dissertation is organized as follows. Chapter 2 describes a spatial comparison of inland water observations from CYGNSS, MODIS, Landsat, and commercial satellite imagery. Chapter 3 describes observing the recent floods and droughts in the Lake Victoria Basin using Earth Observations and hydrological anomalies. Chapter 4 describes a risk comparison of hurricane scenarios as disruptions of hydrological basin order with criteria of social vulnerability. Chapter 5 describes modeling resilience of system order for investments in environmental justice and social vulnerability. Chapter 6 describes uncertainty and sensitivity of development goals to water scarcity of Iraq and transboundary regions. Chapter 7 provides a summary of contributions, concluding remarks, and future work.

# **Chapter 2**: Spatial Comparison of Inland Water Observations from CYGNSS, MODIS, Landsat, and Commercial Satellite Imagery[1]

## 2.1 Abstract

Accurate and timely inland waterbody extent and location data are foundational information to support a variety of hydrological applications and water resources management. Recently, the Cyclone Global Navigation Satellite System (CYGNSS) has emerged as a promising tool for delineating inland water due to distinct surface reflectivity characteristics over dry versus wet land which are observable by CYGNSS's eight microsatellites with passive bistatic radars that acquire reflected L-band signals from the Global Positioning System (GPS) (i.e., signals of opportunity). This study conducts a baseline 1-km comparison of water masks for the contiguous United States between latitudes of 24°N-37°N for 2019 using three Earth observation systems: CYGNSS (i.e., our baseline water mask data), the Moderate Resolution Imaging

---

[1] The work presented in this chapter resulted in the following journal article:

Pavur, G. K., Kim, H., Fang, B., Lakshmi, V. Spatial comparison of inland water observations from CYGNSS, MODIS, Landsat, and commercial satellite imagery. *Geosci. Lett.* 11, 12 (2024). https://doi.org/10.1186/s40562-024-00321-1

Spectroradiometer (MODIS) (i.e., land water mask data), and the Landsat Global Surface Water product (i.e., Pekel data). Spatial performance of the 1-km comparison water mask was assessed using confusion matrix statistics and optical high-resolution commercial satellite imagery. When a mosaic of binary thresholds for 8 sub-basins for CYGNSS data were employed, confusion matrix statistics were improved such as up to a 34% increase in F1-score. Further, a performance metric of ratio of inland water to catchment area showed that inland water area estimates from CYGNSS, MODIS, and Landsat were within 2.3% of each other regardless of the sub-basin observed. Overall, this study provides valuable insight into the spatial similarities and discrepancies of inland water masks derived from optical (visible) versus radar (Global Navigation Satellite System Reflectometry, GNSS-R) based satellite Earth observations.

## 2.2 Introduction

Inland waterbodies (defined as lakes, rivers, streams, reservoirs, and wetlands for purposes of this study) play a critical role in terrestrial water storage and hydrological processes (Brönmark & Hansson, 2002; Bullock & Acreman, 2003). The extent and location of inland waterbodies are key inputs for hydrological models that inform water resources management for a variety of agricultural, industrial, climate applications, and algorithm development for soil moisture retrievals (Papa et al., 2010; Vörösmarty et al., 2022). *Water masks* convey this information by classifying inland areas as either water or non-water (land, vegetation, impervious surface, etc.). While water masks may be derived from fieldwork, drone observations, or aerial surveillance, these methods tend to be labor-intensive, time consuming, and difficult to replicate at frequent timescales for continuous monitoring.

Space-based Earth observations have emerged as a reasonable method for remotely generating inland water masks (Asadzadeh Jarihani et al., 2013; Palmer et al., 2015; Soman & Indu, 2022). This has been demonstrated by two widely accepted global inland water mask products: 1) the Landsat (Pekel) water mask which aggregated 3 million optical Landsat images to categorize water occurrence from 1984-2020 at 30 m spatial resolution (Pekel et al., 2016) and 2) the Moderate Resolution Imaging Spectroradiometer (MODIS) instrument onboard the NASA Terra and Aqua satellites through land cover classifications from 2001-02021 at 250 m spatial resolution (Sulla-Menashe et al., 2019). However, these water masks are constrained by their dependence on optical sensors which are impeded by cloud cover and limited temporal revisit intervals, such as one day for MODIS and over 10 days for Landsat, contingent on latitude. For example, King et al. (2013) estimates MODIS-observed cloud fraction over land to be ~55% (King et al., 2013). This is concerning because the maximum inland waterbody extent likely occurs during rainy/cloudy conditions. Furthermore, these water masks are only available at annual timescales because a year's worth of data are required to obtain sufficient cloud-free observations at a global scale (Pekel et al., 2016; Sulla-Menashe et al., 2019).

Recently, the Cyclone Global Navigation Satellite System (CYGNSS) has proven to be a useful Earth observation system for delineating inland waterbodies. This constellation of microsatellites, developed by the University of Michigan and the Southwest Research Institute, was launched by the National Aeronautics and Space Administration (NASA) for the primary research objective of monitoring tropical cyclone intensification via constellations of eight microsatellites using passive bistatic radars to observe signals of opportunity from reflected Global Positioning System (GPS) L-band signals (Ruf et al., 2018; see Appendix 2.4 for a summary table of CYGNSS).

Several approaches have been proposed for detecting inland waterbodies using CYGNSS via Global Navigation Satellite System Reflectometry (GNSS-R) using properties of coherent surface reflectivity which is greater over inland water than over land (Al-Khaldi et al., 2021; Gerlein-Safdi & Ruf, 2019; C. Ruf et al., 2021). These methods include binary thresholding prediction (Al-Khaldi et al., 2021; Morris et al., 2019; Wan et al., 2019), forward modeling (Chew et al., 2018), random walker algorithms (Gerlein-Safdi & Ruf, 2019; Wang et al., 2022), and machine learning (Ghasemigoudarzi et al., 2022).

Three relevant studies which compared a CYGNSS-derived water mask to either Landsat or MODIS products are described as follows. First, Gerlein-Safdi and Ruf (2019) used a random walker algorithm to delineate inland water based on the standard deviation of CYGNSS surface reflectivity data (Gerlein-Safdi & Ruf, 2019). It performed well when compared with MODIS-derived water masks and handdrawn water masks for select regions (Gerlein-Safdi & Ruf, 2019). A need was identified to develop and validate a reliable long-term CYGNSS-based water mask, such as the annual map demonstrated in this study, to serve as a basemap which CYGNSS data could then be used to identify anomalous variations in inland waterbody extent at sub-annual temporal scales (Gerlein-Safdi & Ruf, 2019). Second, Al-Khaldi et al. (2021) used a method of binary signal-to-noise ratio (SNR) thresholding to delineate inland waterbodies within the maximum CYGNSS spatial coverage (Al-Khaldi et al., 2021). A comparison was conducted with the Landsat (Pekel) water mask and regional uncertainties were identified from relying on a single SNR threshold at a global scale, such as missing waterbodies which were obstructed by vegetation (Al-Khaldi et al., 2021). Third, Wang et al. (2022) used a similar method as Gerlein-Safdi and Ruf (2019) by using a random walker algorithm to delineate inland water based on the power ratio of

CYGNSS data (Wang et al., 2022). The accuracy of the method was high when compared with Landsat-derived water masks for the Congo Basin and Amazon Basin.

Currently, there is no standard method (i.e., a procedure which is widely used and accepted) for generating a CYGNSS-based inland water mask as shown through previous studies by the variety of methods such as binary thresholding prediction, forward modeling, random walker algorithms, and machine learning. The novelty of this study is to provide a foundational comparison of CYGNSS-based water masks to Landsat and MODIS water masks to improve understanding of the spatial agreement and disagreement of these products, specifically by employing a mosaic of surface reflectivity SNR thresholds at the sub-basin level. This is a necessary step toward achieving a standardized CYGNSS water mask.

This study aims to improve understanding of the spatial extent by which three water masks independently derived from Landsat, MODIS, and CYGNSS agree or disagree on the extent and location of inland water. Specifically, the main research goals of this study are to:

1. Derive a 1-km comparison water mask for Landsat, MODIS, and CYGNSS data for 2019 over the contiguous United States between latitudes of 24°N-37°N.
2. Compare the regional performance of CYGNSS, MODIS, and Landsat water masks at a watershed level via quantifiable statistics derived from confusion matrices.
3. Assess the 1-km comparison water mask performance using high-resolution optical commercial satellite imagery collected in 2019 for diverse locations within the study area.

Results from this study will serve as a foundational reference for future studies by improving understanding of the relative utility and robustness of CYGNSS, MODIS, and Landsat-based inland water classifications. This contributes valuable insight into the spatial and regional strengths and limitations of each observation system which is important to understand prior to applying these data to real-world hydrological applications.

## 2.3 Data and Methods

Three satellite-based Earth observation systems were used to derive a single comparison water mask: 1) CYGNSS, 2) MODIS, and 3) Landsat. Each product was pre-processed, as described in the corresponding sections 2.3.1 – 2.3.3, to derive a bivariate water mask where each pixel was either classified as inland water or non-inland water. The bivariate water mask was re-gridded to a common spatial resolution and projection of the 1-km National Snow and Ice Data Center (NSIDC) Equal-Area Scalable Earth (EASE) Grid 2.0 using nearest neighbor interpolation which was selected because it maintains the original data values (0 and 1) and performs well for categorical data (Brodzik et al., 2012). Due to uncertainty in inland water classification of coastal areas, data collected within 25-km of coastlines from all three observation systems were excluded for the analyses.  A comparison of the three bivariate water masks was then performed to generate a single comparison water mask where each pixel is 1) classified as inland water or non-water, and 2) indicates which of the three observation systems classified it as such (i.e., Landsat, MODIS, or CYGNSS; see section 2.4 for further details). Examples of high-resolution satellite imagery were overlayed on the comparison water mask to investigate performance. A flow chart of this methodology is provided in Appendix 2.1.

The study area was defined as the contiguous United States between approximate latitudes of 24°N to 37°N and was determined by the spatial coverage of CYGNSS (Fig. 2.1A). A singular annual timestep of 2019 CYGNSS data was used to match the annual temporal resolution of the MODIS and Landsat water mask products. This data was made available in the pre-released

CYGNSS v3.2 ocean/land merged L1 data which are publicly available upon request to the CYGNSS Science Team.

### 2.3.1 Cyclone Global Navigation Satellite System (CYGNSS) Data

CYGNSS, an eight-microsatellite constellation, uses a passive bistatic radar to observe reflected GPS signals within L-band frequencies to obtain a reduced revisit time of 2.8 (median) and 7.2 (mean) hours per day between observations with a spatial coverage of ±38° (Ruf et al., 2018). For this study, the area of interest was covered by 348 days (95% of the year) of usable CYGNSS data in 2019 which were obtained from 8 microsatellites, each equipped with 4 delay doppler maps.

A sensitivity analysis was conducted to determine that the 50th percentile of CYGNSS observations was optimal by maximizing the F1-score relative to a reference dataset (see Supplemental Information for further details). Additionally, sub-basins of the study area were individually considered to determine the optimal surface reflectivity signal-to-noise ratio (SNR) threshold within a given sub-basin which maximized F1-score, a balance between precision and recall, relative to the reference dataset. This is useful when there is an imbalance of classes within the dataset, such as many land pixels and few water pixels across the total study area, because it takes both false positive and false negative errors into account. Small changes in the threshold window change both precision and recall, resulting in either an increased or decreased F1-score. A higher F1-score indicates a better balance between precision and recall, meaning the predicted water mask makes fewer false positive and false negative classifications. However, a high F1-score may also indicate low confidence in the reference dataset as there is high disagreement between the products. For further details on the sensitivity analysis and a table summarizing SNR thresholds used for each sub-basin, please see the Supplemental Information.

To derive the CYGNSS 1-km water mask, the 50th percentile CYGNSS SNR data were resampled to a 1-km NSIDC EASE Grid 2.0 and then classified as either inland water or non-inland water using the SNR thresholds (Appendix 2.7). SNR values within the threshold were classified as inland water whereas SNR values greater than or less than the threshold values were classified as non-inland water.

Additional information and data from CYGNSS can be accessed here in 2024: https://podaac.jpl.nasa.gov/CYGNSS.

## 2.3.2 Moderate Resolution Imaging Spectroradiometer (MODIS) Data

MODIS is a sensor onboard NASA’s Terra and Aqua satellites in sun-synchronous polar orbit which captures 36 spectral bands ranging from the visible (0.4 μm) to thermal infrared (14.4 μm) regions of the electromagnetic spectrum, enabling them to image the Earth’s surface every 1 to 2 days (Sulla-Menashe et al., 2019). In this study, the 250 m Land Water Mask (MCD12Q1) for 2019 was used. This product defines inland water as follows using the International Geosphere-Biosphere Program (IGBP) classification scheme: 1) permanent wetlands (30-60% water cover and greater than 10% vegetation cover), 2) permanent snow and ice (at least 60% of the area covered by snow and ice for at least 10 months of the year), and 3) waterbodies (at least 60% of the area covered by permanent water (Friedl et al., 2010). To derive the MODIS 1-km water mask, the Land Water Mask was resampled to a 1-km EASE Grid 2.0. All pixels classified as inland water using the IGBP classification scheme were classified as inland water in the MODIS 1-km water mask. Otherwise, the pixels were classified as non-inland water.

Additional information and data from MODIS can be accessed here in 2024: https://lpdaac.usgs.gov/products/mcd12q1v006/.

### 2.3.3 Landsat (Pekel) Data

The Landsat Global Surface Water product (commonly referred to as the Pekel water mask) shows surface water occurrence since 1984 at a spatial resolution of 30 m using three million archival image scenes from the Landsat 5 Thematic Mapper (TM), Landsat 7 Enhanced Thematic Mapper-plus (ETM+), and Landsat 8 Operational Land Imager (OLI) which have an over 10-day temporal resolution (Pekel et al., 2016). In this study, the Pekel Seasonality Map was used which classifies both permanent water (areas inundated for 12 months) and seasonal water (areas inundated for less than 12 months), so long as the inland water is open to the sky, larger than 30 m, and unobstructed by vegetation (Sulla-Menashe et al., 2019). To derive the Landsat 1-km water mask, the Pekel Seasonality Map was resampled to a 1-km EASE Grid 2.0 and pixels which were classified as inland water by the Pekel Seasonality Map were also classified as inland water in the Landsat 1-km water mask. Otherwise, the pixels were classified as non-inland water.

Additional information and data from the Landsat Global Surface Water product can be accessed here in 2024: https://global-surface-water.appspot.com/#data.

### 2.3.4 Confusion Matrices and Related Statistics

To quantifiably compare the three bivariate water masks, confusion matrices and related statistics were used by defining the CYGNSS water mask as the *predicted* water mask and the other products (either Landsat, MODIS, or a combination of Landsat and MODIS) as the *reference* water mask. Additionally, Landsat and MODIS were directly compared by assuming each as the *reference* and *predicted* water masks. For each comparison, confusion matrix values were calculated for the number of true positives (TP), true negatives (TN), false positives (FP), and false negatives (FN). The following statistics were then calculated for each sub-basin and results were visualized as heatmaps: precision (P, Eq. 1), recall (R, Eq. 2), specificity (SP, Eq. 3), miss rate (M, Eq. 4), false detection rate (FDR, Eq. 5), F1-score (F1, Eq. 6), and accuracy (A, Eq. 7).

$$P = \frac{TP}{TP + FP} \qquad Eq. 1$$

$$R = \frac{TP}{TP + FN} \qquad Eq. 2$$

$$SP = \frac{TN}{TN + FP} \qquad Eq. 3$$

$$M = \frac{FN}{FN + TN} \qquad Eq. 4$$

$$FDR = \frac{FP}{FP + TP} \qquad Eq. 5$$

$$F1 = 2\left(\frac{\frac{TP}{TP + FP} * \frac{TP}{TP + FN}}{\frac{TP}{TP + FP} + \frac{TP}{TP + FN}}\right) = 2\left(\frac{P * R}{P + R}\right) \qquad Eq. 6$$

$$A = \frac{TP + TN}{TP + TN + FP + FN} \qquad Eq. 7$$

### 2.3.5 High-Resolution Optical Commercial Satellite Data

Commercial imagery obtained from Planet Labs, Inc. and DigitalGlobe (a subsidiary of Maxar Technologies) were used for visual assessment of the comparison water mask for select locations. Multispectral observations collected by Planet Labs were obtained from the Dove R and Dove Classic satellite constellations (spatial resolution of approximately 3 m and temporal revisit period of 1-day). Multispectral observations collected by DigitalGlobe were obtained from

GeoEye-1 (spatial resolution of approximately 1.65 m and temporal revisit period of 1-3 days) and WorldView-3 (spatial resolution of 0.31-30 m and temporal revisit period of 1-4.5 days).

Additional information of the commercial satellite imagery can be accessed here in 2024: https://www.planet.com/ and https://www.maxar.com/.

## 2.4 Results and Discussion

### 2.4.1 CYGNSS Observations and Bivariate Water Masks

In Fig. 1A., the 50th percentile CYGNSS surface reflectivity SNR values for 2019 were spatially plotted and varied between 138-223 dB with a mean of 150 dB, a median of 149 dB, and a standard deviation of 6.65 dB. A CYGNSS bivariate water mask (Fig. 1B) was derived using the sub-basin SNR thresholds defined in section 2.2.1. The bivariate water masks for MODIS and Landsat are respectively shown in Fig. 2.1C and 2.1D. Overall, MODIS classified the smallest percentage of the study area as inland water at just 1.1%. CYGNSS classified 1.3% of the study area as inland water. Lastly, Landsat classified the greatest percentage of the study area as inland water at 1.4%. To improve understanding of these differences in inland water area estimates, an evaluation indicator of the ratio of inland water to catchment area is provided for sub-basins within the study area. This reveals the spatial variabilities of the CYGNSS, MODIS, and Landsat water masks which had the highest disagreement in regions of wetlands and branching inland waterways (see section 2.3.3 for further details). Additionally, the number of daily 1-km pixel observations by CYGNSS, MODIS, and Landsat were calculated for 2019 within the study area (Appendix 2.8). Fewer MODIS and Landsat observations occurred from May to October, likely due to seasonal precipitation and cloud cover. CYGNSS daily observation counts were relatively consistent throughout the year due to its usage of GNSS-R.

**CYGNSS observations and bivariate water mask products for the contiguous United States between latitudes of approximately 24-37º N for 2019**

**(A) CYGNSS 1-km 50th percentile surface reflectivity signal-to-noise ratio (SNR) data**

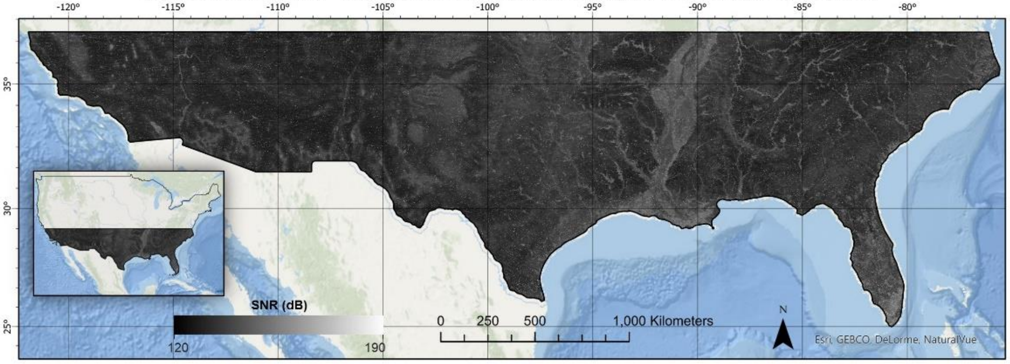

Esri, GEBCO, DeLorme, NaturalVue

**(B) CYGNSS bivariate water mask**

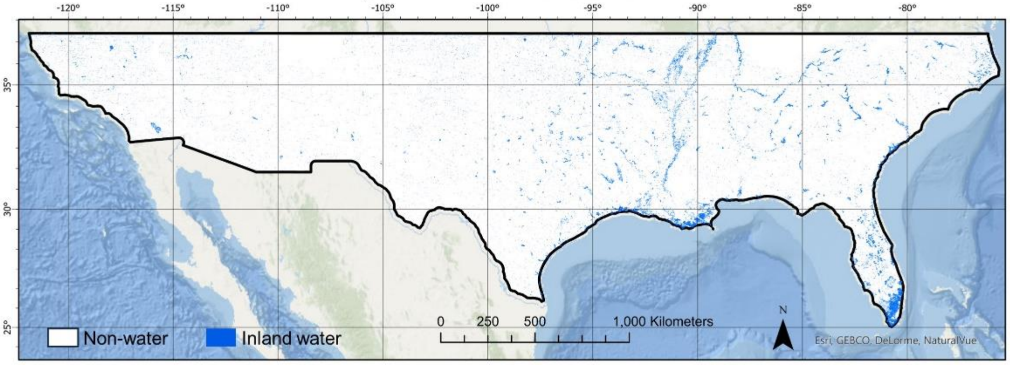

Esri, GEBCO, DeLorme, NaturalVue

**(C) MODIS bivariate water mask**

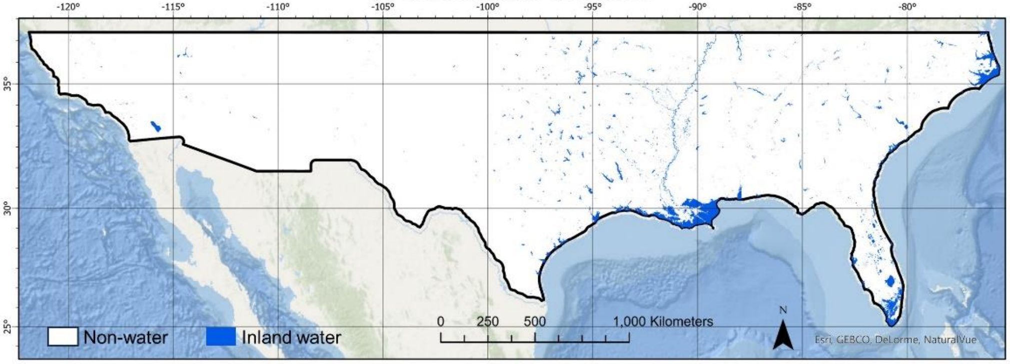

Esri, GEBCO, DeLorme, NaturalVue

**(D) Landsat bivariate water mask**

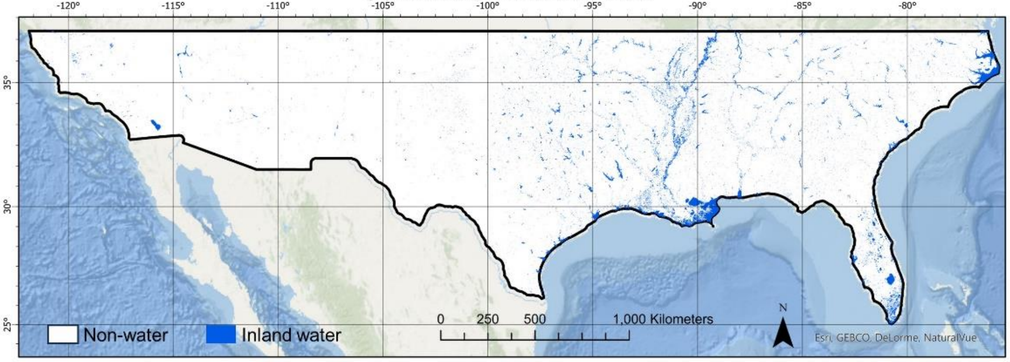

Esri, GEBCO, DeLorme, NaturalVue

***Fig. 2.1:*** *CYGNSS observations and bivariate water mask products for the contiguous United States between latitudes of approximately 24-37°N for 2019.* ***(A)*** *Spatial plot of CYGNSS 1-km 50th percentile surface reflectivity signal-to-noise-ratio (SNR) data.* ***(B)*** *CYGNSS bivariate water mask at 1-km spatial resolution derived from basin-specific binary thresholding of SNR values.* ***(C)*** *MODIS bivariate water mask at 1-km spatial resolution derived from the Land Water Mask (MCD12Q1) for 2019.* ***(D)*** *Landsat bivariate water mask at 1-km spatial resolution derived from the Landsat Global Surface Water product (commonly referred to as the Pekel water mask) for 2019.*

### 2.4.2 Comparison Water Mask

The three bivariate water masks from CYGNSS, MODIS, and Landsat were compared at a pixel-by-pixel level to generate a 1-km comparison water mask. A given pixel was classified as non-inland water in the comparison water mask only if all three bivariate water masks concurred that the pixel was land. If one or more of the bivariate water masks classified a given pixel as water, the comparison water mask designated the pixel as inland water and the observation system(s) that classified it as such were indicated: Landsat only, MODIS only, CYGNSS only, MODIS and Landsat, CYGNSS and MODIS, CYGNSS and Landsat, or all three systems (CYGNSS, MODIS, and Landsat). Because the purpose of the comparison water mask is to spatially investigate the extent by which the three water mask products agree or disagree on the classification of inland water, it is important to note that the comparison water mask is not intended to serve as a stand-alone water mask itself.

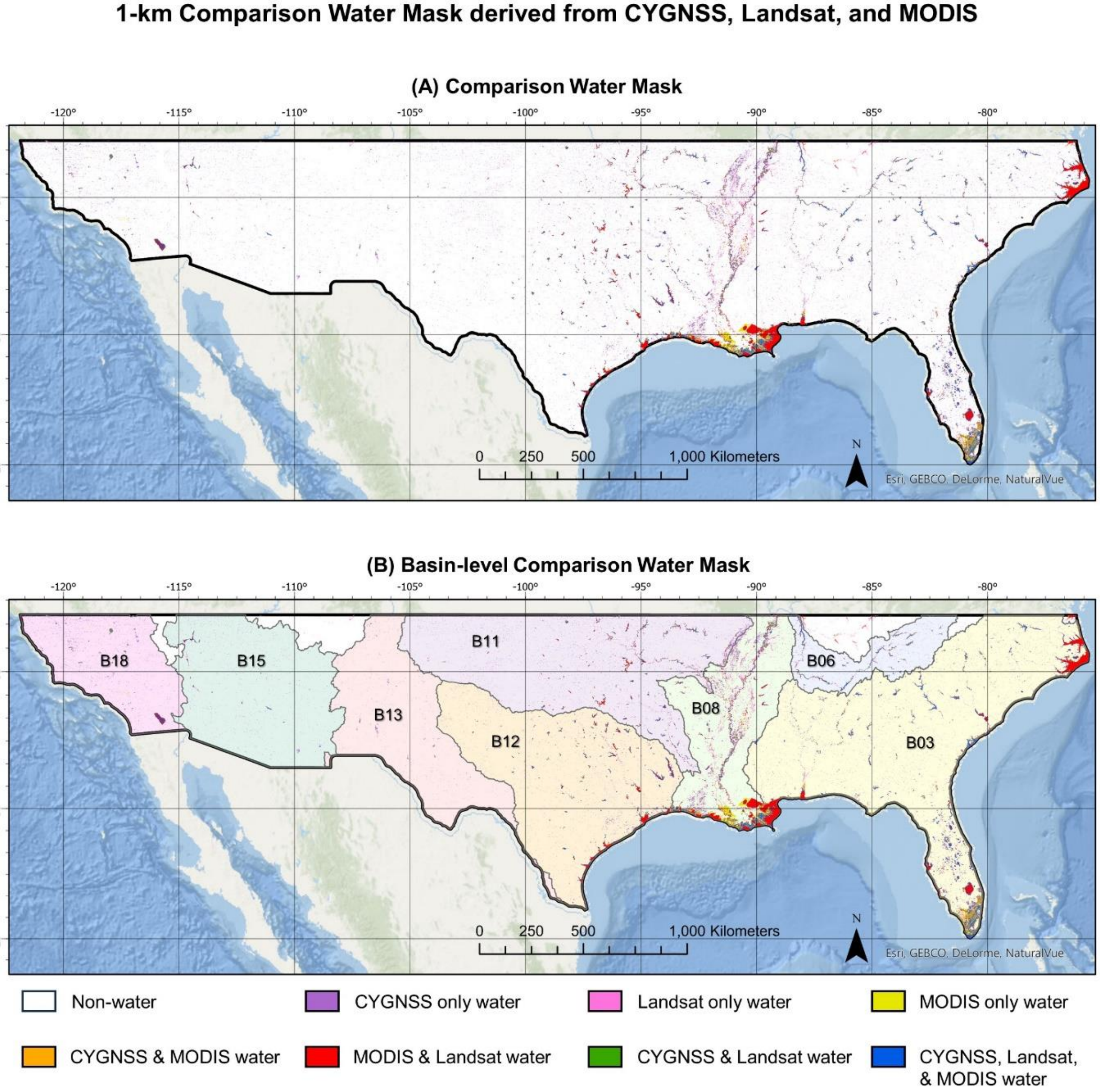

***Fig. 2.2:*** *Comparison Water Mask derived from CYGNSS, Landsat, and MODIS for the contiguous United States between latitudes of approximately 24-37°N for 2019.* ***(A)*** *1-km Comparison Water Mask across the study area for 2019 derived from the CYGNSS, Landsat, and MODIS bivariate water masks.* ***(B)*** *The 1-km Comparison Water Mask subdivided into USGS Hydrological Unit Code-02 Watersheds. The watersheds are referred to as the South Atlantic Gulf basin (B03), the Tennessee basin (B06), the Lower Mississippi basin (B08), the Arkansas-White River basin (B11), the Texas-Gulf basin (B12), the Rio Grande basin (B13), the Lower Colorado (B15), and the California basin (B18).*

As shown in the comparison water mask (Fig. 2.2A), the observation systems collectively classified 2.3% of the study area as inland water. Of the pixels classified as inland water, 14.2% were classified by all three observation systems. 30.6% were classified by at least two observation systems: 18.2% by Landsat and MODIS, 6.5% by Landsat and CYGNSS, and 5.9% by CYGNSS and MODIS. The remaining 55% of inland water pixels were classified by only one system: 29% by CYGNSS, 19.4% by Landsat, and 6.8% by MODIS. While this indicates a relatively high level of false positives and thus disagreement between the three inland water masks, it is important to note that the disagreements vary spatially across the study area. This is further discussed in section 3.3.

In the comparison water mask, red pixels indicate locations where CYGNSS did not classify inland water which both Landsat and MODIS agreed were water (18.2%). High concentrations of red pixels are observed along outlets of waterways to the Gulf of Mexico and Atlantic Ocean and may be explained by the lower dielectric constant of brackish water than freshwater due to its salat content (Lang et al., 2016). Additionally, red pixels are in the middle of expansive lakes, such as Lake Okeechobee in Florida, even though CYGNSS tends to correctly classify the boundary between the lake and land (i.e., the perimeter of the lake). Green pixels indicate locations where CYGNSS and Landsat classified inland water while MODIS did not (6.5%). These instances are primarily concentrated within the Mississippi River basin. Orange pixels indicate locations where CYGNSS and MODIS classified inland water while Landsat did not (5.9%). The highest concentration of orange pixels can be found in wetland regions of southern Louisiana and Florida.

Pixels classified as inland water by only CYGNSS are represented as dark purple (29.0%) and are scattered across the study region but are particularly prevalent in the Mississippi River basin and the Western USA. The abundance of false positive classifications in dry and densely vegetated areas may be due to the high SNR of CYGNSS in these regions. Dry soil or sand could have erroneously high SNR because the individual grains reflect a significant amount of GPS signals due to their rough, irregular surfaces. Additionally, the spaces between the grains allow for L-band signals to penetrate and reflect off the underlying surface, which further contributes to the coherent scatterings. In densely vegetated areas, water on the canopy can reflect signals and increase the SNR, which may not be suitable for detecting waterbodies using the CYGNSS SNR threshold set in the present study. As a result, it may be necessary to consider alternative approaches to detect waterbodies in these areas in future studies. To address this issue, other proxies such as soil moisture or vegetation indices from other microwave satellite systems may be used to more accurately classify these pixels as waterbodies assuming that independence from Landsat and MODIS land cover products is not required. By incorporating thresholds for these values with CYGNSS SNR, dry and densely vegetated areas can be effectively masked out in the future.

Instances of inland water classification solely by MODIS are represented in yellow (6.8%) and are primarily concentrated in the wetlands of Louisiana and southern Florida. Lastly, occurrence of Landsat only inland water classifications are depicted in pink (19.4%) and tend to be located within networks of branching waterways. In these instances, CYGNSS frequently captured portions of the waterways but was discontinuous, which lead to classifications made only by Landsat.

### 2.4.3 Confusion Matrix Statistics of Bivariate Water Masks

To further investigate region-specific variability in the comparison water mask performance, the study area was sub-divided into 8 smaller regions via the United States Geological Survey (USGS) Hydrologic Unit Code-02 (HUC-02) watershed boundaries (Fig. 2.2B). For each region, the results of the confusion matrix statistics (Eq. 1-7) were visualized as heatmaps which are shown in Fig. 2.3. F1-score was determined to the be most applicable to this study (Fig. 2.3G). A high F1-score indicates a high level of agreement between the *predicted* and *reference* water mask. A low F1-score may indicate low confidence in the reference dataset as there is a high disagreement between the products. The remaining confusion matrix statistics (R, P, SP, M, FDR, and A) are discussed in detail in the Supplemental Materials.

A higher F1-score was generally obtained when the SNR threshold was tailored for each basin as opposed to using a singular threshold for the entire study area. This indicates high variability in inland water surface reflectivity due to geographical differences such as vegetation and topography, meaning that a single threshold to define inland water over a large study area introduces bias. The lowest F1-scores were observed in the Rio Grande Basin (B13), the Lower Colorado basin (B15), and the California basin (B18), indicating a high level of disagreement between all three datasets. CYGNSS obtained the highest F1-scores in B03, B06, and B08 which had up to a 34% increase in F1-score compared to the total study area (Fig. 2.3G). In most scenarios, the F1-score was improved when CYGNSS was combined with either Landsat or MODIS.

Lastly, a ratio of the inland water area to catchment area was calculated for each sub-basin Appendix 2.10). These results demonstrated that the ratio of inland water to sub-basin area varies across the study area with the highest ratio in the Mississippi River Basin (B08) and the lowest ratio in the Rio Grande Basin (B13). MODIS tended to estimate the lowest ratio, however, all three datasets had comparable ratios within 2.3% of each other regardless of the sub-basin observed.

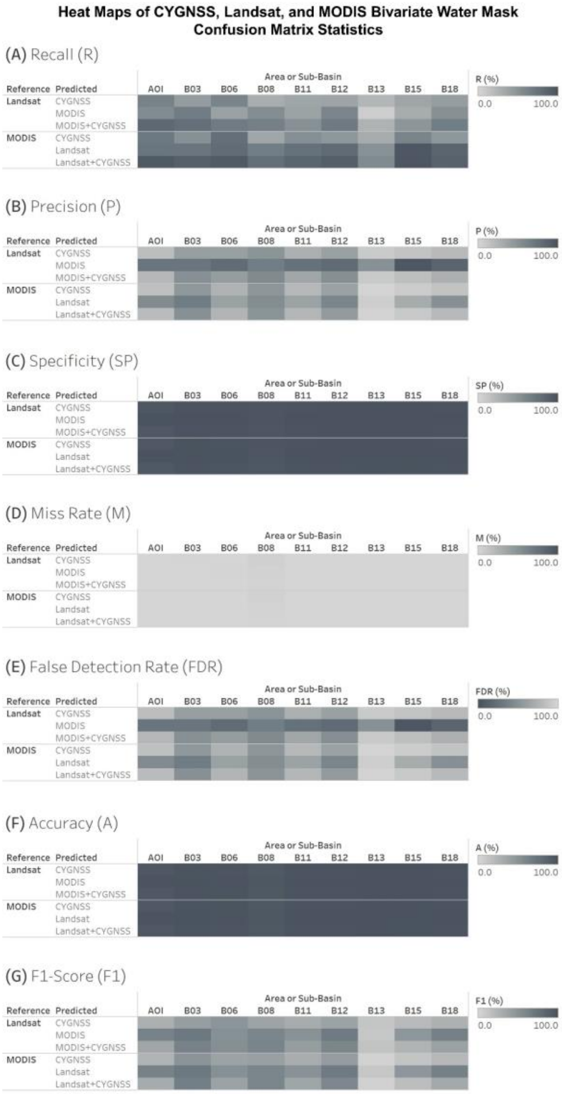

***Fig. 2.3:*** *CYGNSS, Landsat, and MODIS bivariate water mask confusion matrix statistics visualized as heat maps for* ***(A)*** *Recall (R),* ***(B)*** *Precision (P),* ***(C)*** *Specificity (SP),* ***(D)*** *Miss Rate (M),* ***(E)*** *False Detection Rate (FDR),* ***(F)*** *Accuracy, and* ***(G)*** *F1-score (F1). For each, the total study area (AOI) or sub-basin of interest (USGS HUC-02) is indicated. The assumed reference water mask is indicated as either Landsat or MODIS. The predicted water mask is indicated as either CYGNSS, MODIS, Landsat, a combination of MODIS and CYGNSS, or a combination of Landsat and CYGNSS.*

### 2.4.4 Comparison Water Mask with High-Resolution Commercial Satellite Imagery

To assess our confidence in the water mask product, the comparison water mask was overlayed with high-resolution commercial satellite imagery for select locations including manmade reservoirs, natural lakes, wetlands, and rivers. A qualitative assessment of the Comparison Water Mask compared to the commercial satellite imagery is shown in Fig. 2.4. A quantitative assessment of the percentage of commercial image scene classified by each observation system is provided in Appendix.12.

The highest disagreement between classification systems was often observed along the shorelines, particularly since CYGNSS tended to estimate a wider lake extent which encompassed surrounding vegetated areas. Additionally, CYGNSS did not continuously classify large lakes, which may be explained by salinity (such as for the Salton Sea (Fig. 2.4A) and Lakes Maurepas and Pontchartrain (Fig. 2.4B)) and/or the expansive nature (such as for the freshwater Lake Kissimmee (Fig. 2.4E), which concurs with the results of Al-Khaldi et al., 2021).

In Fig. 2.4A and 2.4B, MODIS and CYGNSS concurred on classifications of wetlands, exposed salt deposits, and sediment along lakebeds, whereas Landsat did not. This is likely due to violation of the conditions required to classify inland water by the Landsat product, such as the area must be open to the sky, larger than 30 m, and unobstructed by vegetation. Lake Hartwell (Fig. 2.4C) and the Tennessee River (Fig. 2.4D) demonstrate two examples where there were no instances of only MODIS and Landsat classification of a pixel as water (indicated by red pixels). For these locations, a noticeable enhancement in the waterbody continuity was observed when CYGNSS is combined with both Landsat and MODIS.

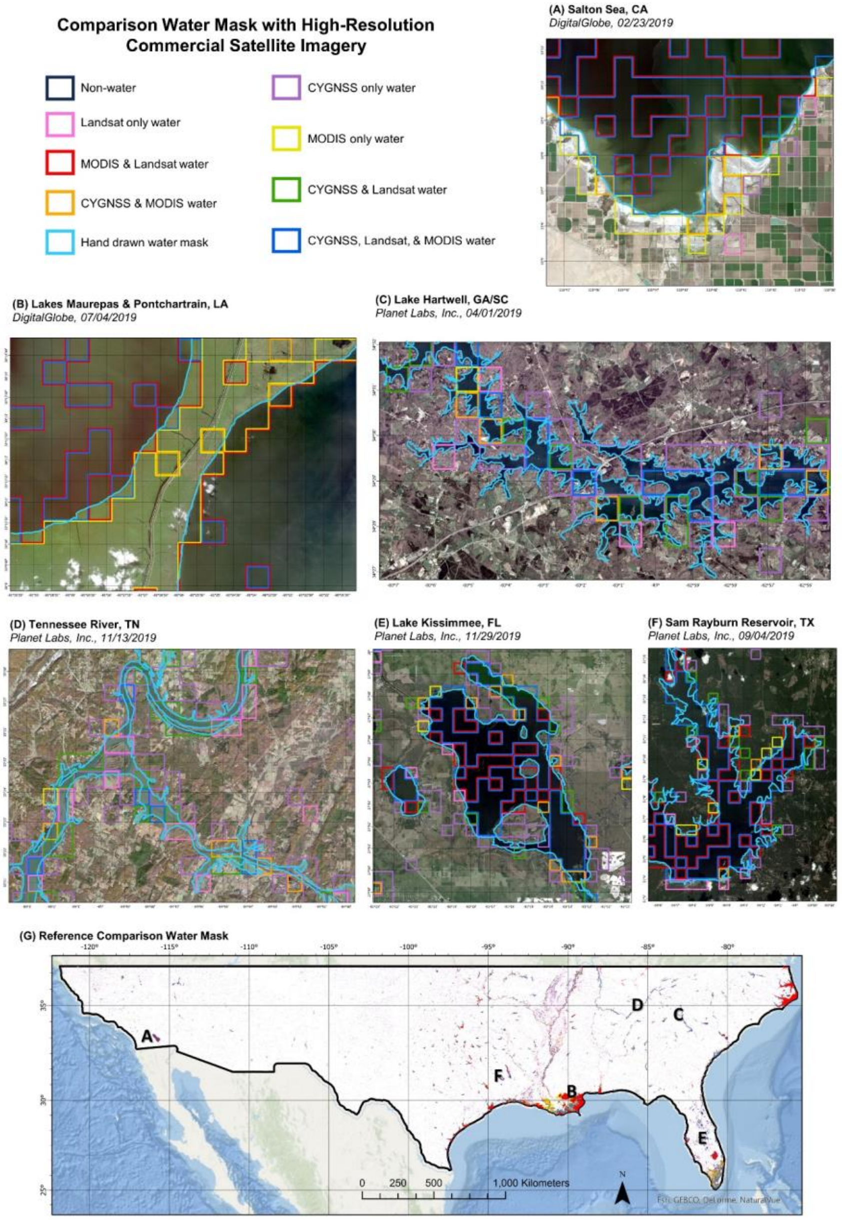

***Fig. 2.4:*** *Comparison water mask overlayed onto high-resolution commercial satellite imagery from Planet Labs, Inc. and DigitalGlobe for select locations:* ***(A)*** *Salton Sea, CA,* ***(B)*** *Lake Maurepas and Pontchartrain, LA,* ***(C)*** *Lake Hartwell, GA/SC,* ***(D)*** *Tennessee River, TN,* ***(E)*** *Lake Kissimmee, FL,* ***(F)*** *Sam Rayburn Reservoir, TX.* ***(G)*** *Reference locations for the commercial images are provided on the comparison water mask. Hand drawn water masks are displayed in light blue for visual purposes. For additional information on the high-resolution imagery, including date of acquisition and image identification number(s), see Appendix 2.11.*

## 2.5 Future Research and Limitations

As the utility of CYGNSS data for land-based applications is increasingly realized, it is important to understand its relative strengths and limitations compared to existing Earth observation systems. The comparison water mask reveals various levels of agreement/disagreement across the study area between the observation products of CYGNSS, Landsat, and MODIS. Caution should be exercised when applying these data across varying geographic regions for inland waterbody identification. Additionally, the optical high-resolution commercial satellite imagery revealed numerous instances of FP occurrence over waterbodies. Thus, FP indicated disagreements between the systems should not be dismissed as land but rather as indications of disagreement. Further, the CYGNSS water mask resulted in discontinuous waterways when portions of the waterbody had SNR values outside of the basin's defined threshold. Gap-filling, random walkers, or other algorithms may be appropriate methods to improve continuity. For example, data collected within 25-km of coastlines were excluded from this study due to the uncertainty of classifying this interface using the MODIS, Landsat, and CYGNSS products. In combination with other data products, fuzzy logic could be used to decrease the uncertainty of CYGNSS-based inland water classification of coastal regions (Demir et al., 2016). Lastly, the study was limited by the temporal confinement of a single annual timestep (2019). Future research should explore the capability of CYGNSS to reliably observe sub-annual inland waterbody dynamics, which is challenging to observe using MODIS and Landsat due to their reliance on cloud-free observations.

In addition to inland waterbody delineation (Al-Khaldi et al., 2021; Gerlein-Safdi & Ruf, 2019; Ghasemigoudarzi et al., 2020; Loria et al., 2020; Ruf et al., 2021), CYGNSS has proven to be a useful observation system for other land-based applications including but not limited to soil moisture retrievals (Kim & Lakshmi, 2018), enhancement of soil moisture estimates from land surface models through data assimilation (Kim et al., 2021), flooding (Chew et al., 2018; Ghasemigoudarzi et al., 2020; Rajabi et al., 2020; Wan et al., 2019), lake height estimates (Li et al., 2018), and wetland dynamics (Downs et al., 2021; Morris et al., 2019). Temporally and spatially accurate inland waterbody mapping using CYGNSS will support future research in these CYGNSS land-based application areas as well.

## 2.6 Conclusions

A 1-km CYGNSS-based bivariate water mask was compared with two widely accepted Earth observation water masks derived from MODIS and Landsat for 2019 over the contiguous United States between latitudes of approximately 24-38°N. A mosaic of binary thresholds using sub-basins defined by the USGS HUC-02 codes was used to classify inland water with CYGNSS SNR values. This approach accounted for the varying thresholds required in different regions, such as the dry areas of the Midwest USA versus the wet Southeast USA, and performed better than a singular binary threshold for the entire study area. This approach of using a mosaic of binary thresholds increased F1-score up to 34% for sub-basins within the study area. Confusion matrices and related statistics revealed that the performance of the comparison water mask varied regionally, with particularly high disagreements along the Lower Mississippi basin (B08), brackish or saltwater regions, extensive lakes, and wetlands. Additionally, the performance metric of ratio of inland water to catchment area revealed that CYGNSS, MODIS, and Landsat were within 2.3% of each other regardless of the sub-basin observed.

To assess performance of the comparison water mask, high-resolution optical satellite imagery from commercial companies (Planet and DigitalGlobe) were used. This improved understanding of each water mask product's performance over natural lakes, manmade reservoirs, wetlands, and rivers. In multiple instances, CYGNSS successfully identified inland water which both MODIS and Landsat failed to classify.

Overall, this study contributes a valuable foundational comparison of CYGNSS versus optical-sensor-based inland water masks. It provides a straightforward method for spatially comparing water masks derived from Earth observations, particularly in conjunction with optical high-resolution commercial satellite imagery. This work can guide future exploration of algorithms and data processing techniques to continually improve the performance of inland waterbody delineation using CYGNSS to support water resources management and a variety of hydrological applications.

## 2.7 Acknowledgements

We sincerely thank the CYGNSS Science Team for their support by providing the pre-released v3.2 CYGNSS ocean/land merged L1 data for 2019 with us. Daily commercial imagery from Planet Labs, Inc., were accessed via the NASA Commercial Satellite Data Acquisition program (https://www.earthdata.nasa.gov/esds/csda). DigitalGlobe imagery was accessed through a Cooperative Research and Development Agreement (CRADA) between the National Geospatial-Intelligence Agency (NGA) and the University of Virginia via the NextView License. This paper is based on work supported by the National Science Foundation Graduate Research Fellowship Program (NSF GRFP) under Grant No. 182490 and the National Science Foundation Research Traineeship (NSF NRT) program under Grant No. 1829004. Any opinions, findings, conclusions, or recommendations expressed in this work are those of the author(s) and do not necessarily reflect the view of the University of Virginia or the National Science Foundation.

# **Chapter 3:** Observing the Recent Floods and Drought in the Lake Victoria Basin Using Earth Observations and Hydrological Anomalies[2]

## 3.1 Abstract

The Lake Victoria Basin, home of Africa’s largest freshwater lake, experienced extensive floods in 2019–2020 and anomalous drought conditions in early 2022. Both antithetical hydrological events raised concerns for an estimated 35 million people within the basin who are vulnerable to these continually recurrent hydrometeorological extremes. While there is a need for high resolution spatial and temporal hydrological monitoring, in-situ observations are limited and insufficient within the basin. This study assesses the capability of publicly available Earth observations and models to capture the occurrence of recent hydrological extremes within the Lake Victoria Basin. Spatial and temporal comparisons of the following hydrological variables are conducted within the Lake Victoria Basin from June 2002 – June 2022: precipitation,

---

[2] The work presented in this chapter resulted in the following journal article:

Pavur, G., Lakshmi, V. Observing the recent floods and drought in the Lake Victoria Basin using Earth observations and hydrological anomalies. *J. of Hydrology: Regional Studies,* 46 (2023). https://doi.org/10.1016/j.ejrh.2023.101347

evapotranspiration, runoff, soil moisture, lake height, and total water storage anomaly (TWSA). Results from the time series and spatial analyses confirm that the anomalous wet and dry events respectively occurred from October 2019 – March 2020 and November 2021 – March 2021. The observations also indicated a quick recovery from the drought event by June 2022. Additionally, a comparison of 9-km soil moisture and 1-km downscaled near-surface soil moisture products improves understanding of wetness spatial variability within the basin. These results were validated using in-situ soil moisture data available through the International Soil Moisture Network, making this the first study to validate the downscaled 1-km soil moil moisture product within the African continent. Methods from this study demonstrate the utility of a diverse array of publicly available Earth observation and model data to improve understanding of recent hydrological anomalies and extreme events within the Lake Victoria Basin. This can be applied to water resources management, particularly in regions lacking sufficient in-situ hydrological data.

## 3.2 Introduction

Africa's largest lake, Lake Victoria, provides valuable ecosystem services to five East African countries within its basin: Burundi, Kenya, Rwanda, Tanzania, and Uganda. Freshwater from Lake Victoria supports domestic use, diverse aquatic and terrestrial ecosystems, and economic industries including agriculture, livestock, fisheries, and hydropower production (Awange, 2006, 2020). Tourism, recreation, and transportation of goods via inland waterways are further supported by the lake (Awange, 2020; Reynolds, 2005). As the source of the White Nile River and a subbasin of the greater Nile watershed, the Lake Victoria Basin plays a critical role in supplying freshwater locally to an estimated 35 million people and indirectly to 340 million people in downstream countries (Mugo et al., 2020; Ramillien et al., 2014).

Over the previous decades, hydrometeorological extremes such as floods and droughts have proven to be continual and recurrent in the Lake Victoria Basin (Nyeko-Ogiramoi et al., 2013). Historically, devastating floods in this region occur practically every year during the October-December rainy season and cause substantial loss of life and property (Nyeko-Ogiramoi et al., 2013). Periods of extreme drought are equally concerning because decreased or delayed rainfall can lead to crop failure, widespread famine, and food insecurity (Agutu et al., 2021; Coughlan de Perez et al., 2019; FEWS NET, 2021). As the frequency and severity of hydrological extremes is predicted to increase due to climate change, accurate and continual monitoring of hydrological conditions at the basin level is vital for sustainable water resources management (Alsdorf et al., 2016; Paris et al., 2022; Wainwright et al., 2021). This is particularly true for the Lake Victoria Basin, particularly given that previous research has identified it as a significant hotspot for population-climate burdens which are exacerbated by recurrent droughts and flooding due to variable rainfall (López-Carr et al., 2014). Since the populations of Burundi, Kenya, Rwanda, Tanzania, and Uganda are respectively forecasted to increase by 114%, 68%, 77%, 117%, and 114% between mid-2020 and mid-2050, there is further motivation to improve water resources management to support such population growth and demands (Table 3.1) (Kaneda et al., 2020).

***Table 3.1:*** *Population forecasts for Burundi, Kenya, Rwanda, Tanzania, and Uganda for mid-2020 to mid-2050 (Kaneda et al., 2020).*

| **Country** | **Mid-2020 population (millions)** | **Mid-2035 population (millions)** | **Mid-2050 population (millions)** | **Percent population change from 2020 – 2050 (%)** |
|---|---|---|---|---|
| **Burundi** | 11.9 | 18.3 | 25.5 | + 114% |
| **Kenya** | 53.5 | 71.9 | 89.7 | + 68% |
| **Rwanda** | 13.0 | 17.9 | 23.0 | + 77% |
| **Tanzania** | 59.7 | 90.4 | 129.4 | + 117% |
| **Uganda** | 45.7 | 69.5 | 97.7 | + 114% |

As with many regions in Africa, the Lake Victoria Basin lacks sufficient in-situ, public, and ground-based hydrological observations to meet these needs (Hu et al., 2021; Khan et al., 2011; Ndehedehe et al., 2016). While discharge data from Uganda's hydropower dam located at Lake Victoria's outlet is collected, this data is not publicly available. This is likely due to political concerns regarding the Agreed Curve, which is an international treaty between Uganda and Egypt through which Uganda agrees to operate its hydropower dams in a way that reflect the natural outflows of Lake Victoria (Getirana et al., 2020; Kull, 2006; Shamsudduha et al., 2017; Swenson & Wahr, 2009; Vanderkelen et al., 2018). Similarly, the few ground-based rainfall stations within the Lake Victoria Basin are unreliably operated and sparsely distributed, making it an insufficient data source for basin-wide hydrological analyses (Awange et al., 2019). Therefore, there is a need for publicly available and remotely observed hydrological data at sufficient spatial and temporal resolutions in the Lake Victoria Basin to monitor the recent hydrological extreme events.

Satellite remote sensing has proven to be a useful tool to obtain hydrological observations in regions limited by sparse temporal and spatial coverage of ground-based in-situ data. This is particularly true for comparisons of satellite sensor precipitation with gauge observations (Hashemi et al., 2018; H. Le et al., 2018; Mondal et al., 2018). Numerous studies have relied on remote sensing and land surface models to reliably estimate components of the hydrological cycle within the Lake Victoria Basin and other African basins (Awange et al., 2019; Grippa et al., 2011; Kansara et al., 2021; Khan et al., 2011; Lakshmi et al., 2018; Ndehedehe et al., 2016; Shamsudduha et al., 2017; Vanderkelen et al., 2018). Other studies in the Lower Mekong River Basin have also demonstrated the synergistic utility of satellite remote sensing observations within hydrological models (Le et al., 2020, 2022; Mohammed et al., 2018a, 2018b, 2018c). These techniques, particularly the utilization of a wide array of publicly available hydrological Earth observations, can be applied to the Lake Victoria Basin to update previous studies and to compare the recent hydrological extreme events. Additionally, this is a valuable method for collecting hydrological data across country borders since Lake Victoria is geopolitically divided between Kenya (6%), Uganda (43%), and Tanzania (51%) (Awange, 2020). Thus, Earth observations are a promising method for obtaining uniform and publicly available hydrological observations at sufficient spatial and temporal resolutions across the international boundaries of this basin.

In this paper, we examine components of the hydrological water balance (precipitation, evapotranspiration, runoff, and change in total water storage) and additional hydrological variables (soil moisture, lake level height, and lake extent) for the Lake Victoria Basin from June 2002 – June 2022 with particular focus on the 2019–2020 flood events and the 2021–2022 drought period. This is accomplished by leveraging publicly available data from seven satellite-based Earth observations and one land surface model, which is necessary given the limited in-situ data available in this region. Since previous studies identified the Lake Victoria Basin as an area where populations are particularly vulnerable to seasonal hydrological variabilities, we conducted a hydrological anomaly analysis at monthly timescales to identify periods of anomalous positive and negative hydrological conditions. Our analysis includes monthly basin-wide averaged time series of precipitation, evapotranspiration, runoff, total water storage anomaly, soil moisture, and lake level height from June 2002 – June 2022. Spatial anomaly plots at spatial resolution up to 0.1◦ are provided for precipitation, evapotranspiration, runoff, total water storage anomaly, and soil moisture for two months of interest: the local maxima and minima monthly anomalies between January 2019 – June 2022. These represent a wet and dry month which respectively occurred during the identified flood and drought events. To our knowledge, this is the first study to conduct a hydrological spatial anomaly comparison for the 2019–2020 flood and 2021–2022 drought events in the Lake Victoria Basin.

Additionally, to improve understanding of wetness spatial variability during the flood and drought periods, a spatial comparison of 9-km near-surface soil moisture and 1-km downscaled near-surface soil moisture products is included for the basin. These spatial plots are displayed for the wet and dry months identified in the root zone soil moisture anomaly time series as local maxima and minima between January 2019 – June 2022. The 1-km downscaled near-surface soil moisture data was validated using 28 ground soil moisture stations available via the International Soil Moisture Network. This is the first study to validate the 1-km downscaled near-surface soil moisture product within the African continent. Because the Lake Victoria Basin and other areas in the Greater Horn of Africa lack sufficient in-situ soil moisture observations for widespread analysis, validation and assessment of remotely sensed and modeled soil moisture data are vital for determining the utility of these data for future studies and operational usage (Agutu et al., 2021). This is especially necessary for soil moisture due to the region's dependence on rain-fed subsistence agriculture (Agutu et al., 2021).

Methods from this study for observing hydrological anomalies as time series and spatial plots demonstrate a simple tool for monitoring hydrological variables using publicly available datasets in a region that is traditionally limited by insufficient ground observations. These methods could be applied to inform water management and agricultural planning within the Lake Victoria Basin, as well as other regions lacking sufficient ground-based hydrological observations. Further research could be conducted to assess applications of this work for water management. Here, we show that Earth observations can monitor hydrological variables during extreme and anomalous events, such as the 2019–2020 flood and 2021–2022 drought. This work aims to support ongoing efforts to decrease the community's vulnerability to anomalous hydrological conditions, such as extreme floods and droughts, by improving monitoring of components of the hydrological cycle (precipitation, evapotranspiration, runoff, and change in total water storage) and other hydrological variables (soil moisture, lake level height, and lake extent) within the Lake Victoria Basin.

## 3.3 Study Area

Lake Victoria, locally called Lake Nulabale, is the largest tropical lake and the second largest freshwater lake in the world with an approximate surface area of 65,295 km$^2$ (Awange, 2020). Despite its large spatial extent, Lake Victoria is relatively shallow with a maximum depth of 80 m and an average depth of 40 m (Nyeko-Ogiramoi et al., 2013). The basin has a catchment surface area of approximately 229,815 km$^2$ and encompasses portions of Uganda, Kenya, Tanzania, Rwanda, and Burundi (Hamilton, 2016). A singular outlet of Lake Victoria is found at Ripon Falls near Jinja, Uganda. Here, the Lake Victoria Basin directly contributes to the White Nile River. Thus, as shown in Fig. 3.1A, the Lake Victoria Basin is a subbasin of the Nile Watershed.

A digital elevation model (DEM) of the Lake Victoria Basin derived from the Shuttle Radar Topography Mission (SRTM) is shown in Fig. 3.1B (USGS, 2018). Tectonic and volcanic activity within the Great Rift Valley contribute to the basin's varying topography which ranges in altitude from approximately 1109 – 4309 m above mean sea level (MSL). The highest elevations are found in the northeastern mountainous regions in Kenya and along the southwestern edge of the basin in Burundi and Rwanda. The lowest elevations are found directly along the perimeter of Lake Victoria.

Approximately 25 major rivers within the basin contribute directly to Lake Victoria (Vanderkelen et al., 2018). However, precipitation accounts for approximately 86% of the input into Lake Victoria (Nyeko-Ogiramoi et al., 2013). The humid, tropical climate in combination with Lake Victoria's large extent contributes to a distinct diurnal meteorological pattern within the basin. During afternoons, intense convective thunderstorms typically form over the land due to a nocturnal lake-land breeze system (Shamsudduha et al., 2017; Thiery et al., 2016). On seasonal timescales, the long rains and short rains respectively occur from May – March and September – November. Hydrological patterns within the basin are further influenced on seasonal and interannual scales by the Intertropical Convergence Zone (ITCZ), the Indian Ocean Dipole (IOD), and the El-Nino Southern Oscillation (ENSO) (Becker et al., 2010; FEWS NET, 2020, 2021; Wainwright et al., 2021).

### 3.3.1 Land cover of the Lake Victoria Basin

Land cover classifications derived from MODIS Terra and Aqua reflectance data at a spatial resolution of 500 m are shown for the Lake Victoria Basin in Fig. 3.2. For purposes of this study, land cover is assumed to be constant between June 2019 to June 2022 since analysis of land cover change were outside the scope of this study.

Inland waterbodies, including Lake Victoria, make up 25% of the basin's total area. Grasslands are 35% of the basin area and are predominately located in Tanzania. Croplands (including natural vegetation mosaics) are collectively 21% of the basin extent and include portions of all five countries. The main crops produced within the basin are maize, beans, sorghum, millet, paddy rice, sugarcane, tea, coffee, cotton, and meats (Mugo et al., 2020; Reynolds, 2005). Only 0.2% of the basin area is classified as urban and built-up lands even though an estimated 35 million people live within a 100 km buffer zone of Lake Victoria (Mugo et al., 2020). A study conducted by Mugo et al. (2020) used optical imagery from Landsat and field data to assess land

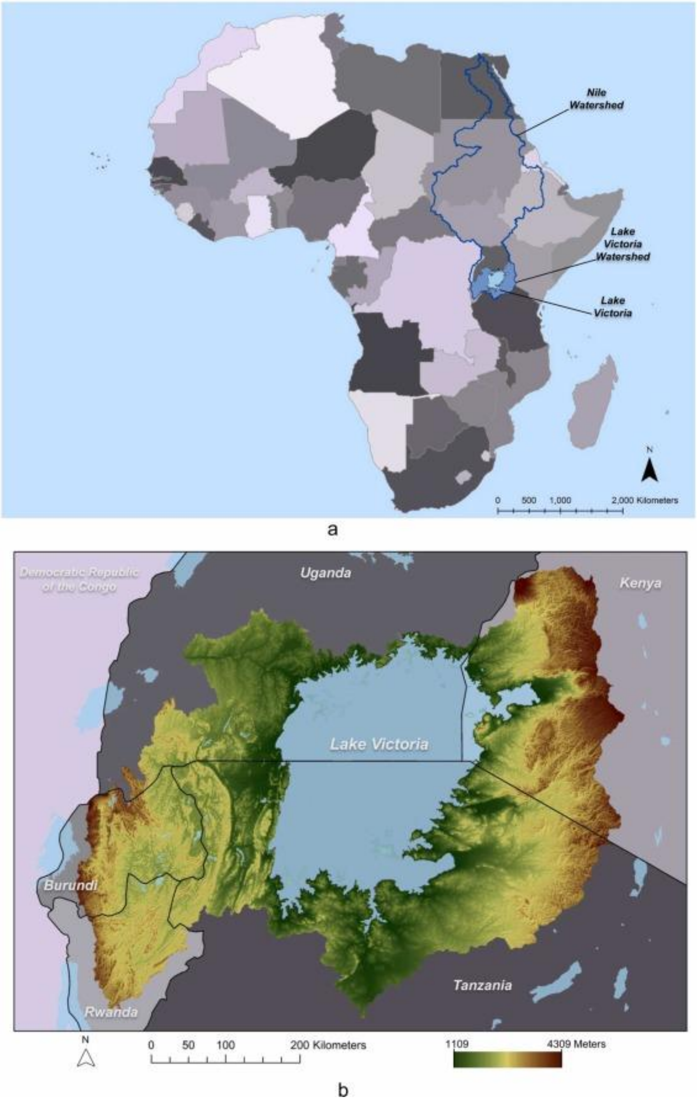

***Fig. 3.1: (A)*** *Map of watershed delineations for the Nile and Lake Victoria watersheds. Lake Victoria is the source of the White Nile River and thus plays a critical role in the hydrology of downstream countries within the Nile watershed. Country boundaries are provided to give context to the watershed at the continental scale* (ESRI, 2021; World Bank, 2019; WWF, 2019). ***(B)*** *Digital elevation model (DEM) for the Lake Victoria Basin, derived from the Shuttle Radar Topography Mission (SRTM). Delineation of the basin includes portions of Uganda, Kenya, Tanzania, Rwanda, and Burundi. Major lakes are displayed in light blue. The highest topography is found in the northwestern portion of the basin in Kenya and along the southwestern rim in Burundi and Rwanda. The lowest topography is found along the perimeter of Lake Victoria* (ESRI, 2021; USGS, 2018; World Bank, 2019; WWF, 2019).

use changes between 1985 and 2014 in the Lake Victoria Basin and found an 800% increase in urbanized areas between 1985 and 2020 (Mugo et al., 2020). Human-centric activities were found to be the primary motivation for land use land cover changes during this period, particularly through the conversion of forests, woodlands, grasslands, and wetlands to farmlands and settlements (Mugo et al., 2020).

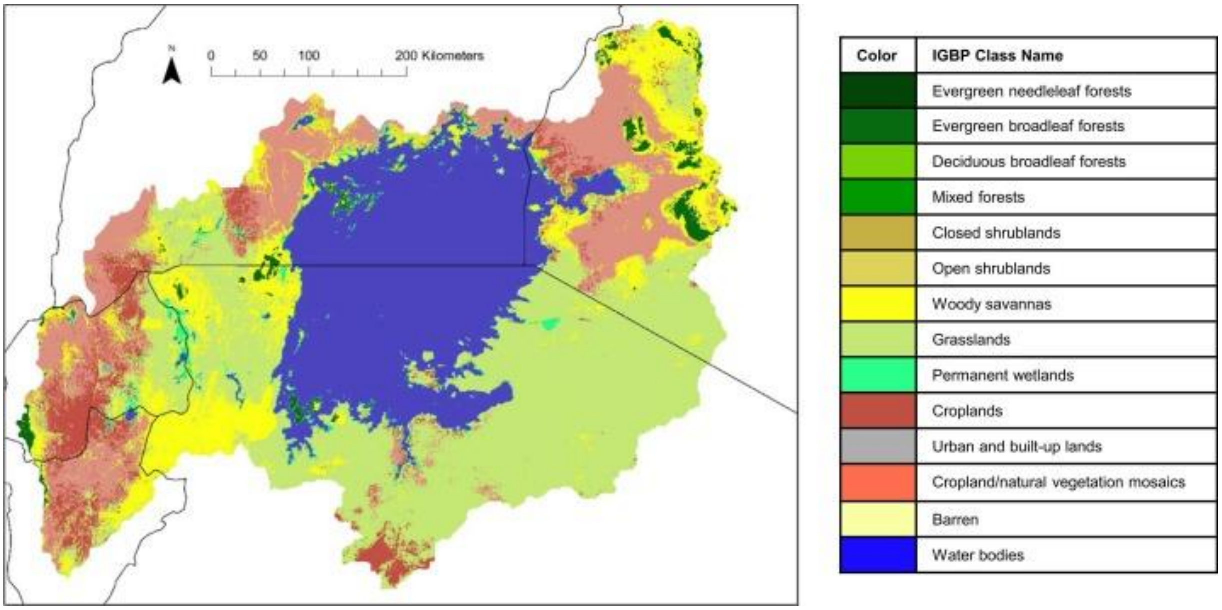

***Fig. 3.2:*** *Land cover classifications for the Lake Victoria Basin in 2019 derived from MODIS/Terra + Aqua Yearly L3 Global 500 m SIN GRID (MCD12Q1 V006). The classifications are based on the Annual International Geosphere-Biosphere Program (IGBP) classification scheme.*

## 3.4 Data

A summary table of the satellite-based Earth observations and model outputs used in this study for precipitation, evapotranspiration, runoff, soil moisture (root zone and near-surface), lake height, and total water storage anomaly (TWSA) are summarized in Table 3.2. Each variable was averaged at a monthly timescale in the native resolution of the source data. Monthly spatial averages were calculated across the basin extent to construct time series for each variable. For spatial mapping purposes, precipitation, evapotranspiration, runoff, and root zone soil moisture were re-gridded to a common spatial resolution. The near-surface soil moisture observations were not gridded to allow for spatial comparison of the 9-km and 1-km products. Similarly, TWSA was not re-gridded to avoid misleading visual representation of these data given the coarse spatial resolution of GRACE. Lake height is assumed to be constant across the extent of Lake Victoria and thus is not spatially mapped. Further details concerning each data product can be found in Sections 3.4.1–3.4.6.

### 3.4.1 Precipitation data from the Integrated Multisatellite Retrievals for Global Precipitation Measurement (GPM IMERG)

The Integrated Multisatellite Retrievals for Global Precipitation Measurement (GPM IMERG) is a joint mission between the National Aeronautics Space Administration (NASA) and the Japan Aerospace and Exploration Agency (JAXA) which uses a constellation of satellites with passive microwave and infrared sensors to provide high spatial and temporal resolution precipitation measurements (Huffman et al., 2015a, 2015b). For regions lacking ground-based in-situ precipitation measurements, remotely sensed precipitation observations are commonly used from GPM IMERG, the Tropical Rainfall Measurement Mission (TRMM), and the Climate Hazards Group InfraRed Precipitation with Station data (CHIRPS) (Dezfuli et al., 2017; Hou et al., 2014; Huffman et al., 2015b). For purposes of this study, GPM IMERG Final Precipitation L3 V06 and GPM IMERG Late Precipitation L3 V06 were used to obtain monthly precipitation data at 0.1◦ spatial resolution from June 2002 – June 2022. This was used to construct time series and spatial plots of monthly precipitation anomalies. More information about the GPM IMERG data set can be found at https://gpm.nasa.gov/documents/IMERGV06-Technical-Documentation.

***Table 3.2:*** *Summary of hydrological data used in this study.*

| Hydrological Variable | Sensor/Model | Spatial Resolution | Temporal Resolution | Study period | Sources |
|---|---|---|---|---|---|
| Precipitation | GPM IMERG Final Precipitation L3 V06 | 0.1° | 1 month | Jun. 2002 – Oct. 2021 | Huffman et. al. (2019) |
| | GPM IMERG Late Precipitation L3 V06 | 0.1° | 1 day | Nov. 2021 – Jun. 2022 | Huffman et al. (2019) |
| Evapotranspiration | MODIS MOD16A2.006 | 0.05° | 8 days | Jun. 2002 – Jan. 2022 | Running et al. (2017) |
| Land Cover | MODIS MDC12Q1.006 | 0.05° | 1 year | 2019 | Friedl et al. (2019) |
| Runoff | GLDAS Noah Land Surface Model L4 V2.1 | 0.25° | 1 month | Jun. 2002 – Apr. 2022 | Rodell et al. (2004) |
| | GLDAS Noah Land Surface Model L4 Early Product V2.1 | 0.25° | 1 month | May. 2022 – Jun. 2022 | Rodell et al. (2004) |
| Root Zone Soil Moisture<br>(0 – 2 m depth) | GLDAS Noah Land Surface Model L4 V2.1 | 0.25° | 1 month | Jun. 2002 – Apr. 2022 | Rodell et al. (2004) |
| | GLDAS Noah Land Surface Model L4 Early Product V2.1 | 0.25° | 1 month | May. 2022 – Jun. 2022 | Rodell et al. (2004) |
| Near-surface Soil Moisture<br>(0 – 5 cm depth) | SMAP | 0.09° | 1 day | Jan. 2015 – Jan. 2022 | Entekhabi et al. (2010) |
| | SMAP | 0.01° | 1 day | Jan. 2015 – Jan. 2022 | Fang et al. (2022) |
| Lake Height | Jason-1/USDA G-REALM | >100 km$^2$ | 10 days | Jun. 2002 – 2008 | USDA G-REALM (2022) |
| | Jason-2/USDA G-REALM | >100 km$^2$ | 10 days | 2008 – 2016 | USDA G-REALM (2022) |
| | Jason-3/USDA G-REALM | >100 km$^2$ | 10 days | 2016 – Jun. 2022 | USDA G-REALM (2022) |
| Total Water Storage Anomaly | GRACE/GRACE-FO Tellus L3 V02 | 0.5° | 1 month | Jun. 2002 – May. 2022 | Landerer & Swenson (2012) |

### 3.4.2 Evapotranspiration and land cover data from the Moderate Resolution Imaging Spectroradiometer (MODIS)

The Moderate Resolution Imaging Spectroradiometer (MODIS) is a sensor onboard the sun-synchronous polar orbiting satellites, Terra and Aqua. In this study, MODIS was used to obtain monthly evapotranspiration data from June 2002 to June 2022 and one year of land cover data (2019). The global MODIS evapotranspiration product is based on the Penman-Monteith equation (Mu et al., 2007, 2011). This product has a temporal repeat of 8 days and a spatial resolution of 0.05◦ (Running et al., 2017). For this study, the MODIS MOD16A2.006 evapotranspiration data were averaged at monthly timescales to construct a time series and spatial plots of monthly evapotranspiration anomalies. It is important to note that the MODIS MOD16A2.006 evapotranspiration product masks inland water. Thus, a limitation of this observation data source is that no evapotranspiration data is available directly over Lake Victoria. The MODIS MCD12Q1.006 product was used to construct a map of land cover type for the Lake Victoria Basin in 2019 using the annual International Geosphere-Biosphere Program (IGBP) classification scheme (Friedl et al., 2019). Additional information about MODIS evapotranspiration and land cover products can be found at https://modis.gsfc.nasa.gov.

### 3.4.3 Runoff and root zone soil moisture data from the Global Land Data Assimilation System (GLDAS)

The Global Land Data Assimilation System (GLDAS) is a global, high resolution (0.25◦), publicly available hydrological model that assimilates ground and satellite-based observations in offline land surface models to output land surface states and fluxes (Rodell et al., 2004). For hydrological basins lacking continual and extensive in-situ observations, GLDAS model outputs have performed well when estimating hydrological variables for water balance studies (Hu et al., 2021; Kansara et al., 2021; Lakshmi & Fang, 2023; Ndehedehe et al., 2016; Shamsudduha et al., 2017). For purposes of this study, the GLDAS Noah land surface model was used to obtain monthly runoff and root zone soil moisture (0 – 2 m depth) data. These data were used to construct time series and spatial plots of monthly runoff and root zone soil moisture anomalies. The GLDAS Noah Land Surface Model L4 V2.1 was used from June 2002 – April 2022 and the GLDAS Noah Land Surface Model L4 Early Product V2.1 was used from May 2022 – June 2022. Further details about GLDAS and the Noah land surface model can be found at https://ldas.gsfc.nasa.gov/gldas.

### 3.4.4 Soil moisture data from the Soil Moisture Active Passive (SMAP) mission

The Soil Moisture Active Passive (SMAP) mission launched in 2015 to estimate near-surface soil moisture (0–5 cm depth) using a 1.41 GHz L-band radiometer (Chan et al., 2016; Entekhabi et al., 2010). SMAP overpasses occur at 6:00AM and 6:00PM local time every 2–3 days with a spatial resolution on 0.09°. For this study, monthly 9-km SMAP soil moisture data from the 6:00PM overpasses were used from January 2015 – January 2022. A 1-km soil moisture product, which was downscaled from the 9-km SMAP data using correlations between surface temperature differences and vegetation, were averaged to a monthly timescale (Fang et al., 2022). Validation of the 1-km soil moisture product were performed using data available from 28 ground stations via the International Soil Moisture Network (https://ismn.geo.tuwien.ac.at). Additional information about SMAP and the 1-km downscaled soil moisture product can be found at https://smap.jpl.nasa.gov and Fang et al. (2022). Due to the limited observation record of SMAP of 8 years, this study uses observed monthly values of 9-km and 1-km near-surface soil moisture data as opposed to monthly anomalies. These data were used to construct time series and spatial plots of monthly near-surface soil moisture at 9-km and 1-km resolutions.

### 3.4.5 Lake level height data from satellite radar altimetry (Jason-1, Jason-2, Jason-3)

Satellite radar altimetry has proven to be a reliable method for monitoring inland waterbody elevation over large lakes, rivers, and wetlands, particularly in regions lacking adequate stream gage data (Becker et al., 2010; Birkett & Beckley, 2010; Ndehedehe et al., 2016; Ramillien et al., 2014). To calculate lake surface height, a nadir-pointing antenna onboard the satellite emits microwave pulses and measures the elapsed time between emission and receiving of the reflected pulse. Altitude, elapse time, and geophysical corrections are used to estimate lake surface height. The microwave spectra enable measurements regardless of day/night or cloudy conditions.

Since stream gage data at Lake Victoria's outlet is not publicly available, satellite radar altimetry data obtained from the United States Department of Agriculture (USDA) Foreign Agricultural Service Global Reservoir and Lake Monitor (G-REALM) were used to estimate lake level height in millimeters relative to MSL (USDA, 2022). Previous studies have also utilized G-REALM altimetry data for analysis within the Lake Victoria Basin (Becker et al., 2010; Reynolds, 2005; Swenson & Wahr, 2009). A validation study was conducted by Reynolds in 2005 that compared Lake Victoria gage data from 2000 to 2004 to G-REALM and found very similar agreement (better than 10 cm RSM) (Reynolds, 2005). In our study, the following satellites and sensors with an approximate repeat period of 10 days were used from the G-REALM Lake Victoria height product to construct a time series of monthly lake height anomalies: Jason-1 GDR 20 Hz from 2002 to 2008, Jason-2/OSTM GDR from 2008 to 2016, and Jason-3 Interim GDR 20 Hz from 2016 to 2022. Further details about G-REALM can be found at https://ipad.fas.usda.gov/cropexplorer/global_reservoir/.

### 3.4.6 Total water storage anomaly data from the Gravity Recovery and Climate Experiment (GRACE/GRACE-FO)

Satellite gravimetry via the Gravity Recovery and Climate Experiment (GRACE) and Follow-On (GRACE-FO) missions has proven to be a reliable method for observing changes in total water storage with a geoid height accuracy of one centimeter (Ramillien et al., 2014). Changes in catchment storage from aquifers, soil moisture, groundwater, surface water, etc. are observable as GRACE-derived total water storage anomaly (TWSA). Previous studies have utilized GRACE TWSA for hydrological balance analysis in the Lake Victoria Basin and surrounding African basins (Agutu et al., 2021; Awange et al., 2008; Grippa et al., 2011; Kansara et al., 2021; Khaki & Awange, 2021; Lakshmi et al., 2018; Ndehedehe et al., 2016). In this study, the GRC Tellus JPL Monthly Mass Grid Global Mascons (JPL RL06 V02) data with 0.5◦ spatial resolution were used (please see the GRACE-FO L3 Handbook: https://podaac-tools.jpl.nasa.gov/drive/files/allData/gracefo/docs/GRACE-FO_L3_Handbook_JPL.pdf). While the GRC Tellus JPL Monthly Mass Grid Global Mascon data is provided at this spatial resolution of 0.5◦, it is important to note that the size of a single mascon is 3◦ and neighboring 0.5◦ grid cells may not be independent of each other. However, it is common to use the GRC Tellus JPL Monthly Mass Grid Global Mascon dataset at 0.5◦ resolution (Bonsor et al., 2018; Kansara et al., 2021; Shamsudduha et al., 2017). Thus, a scale factor derived from land surface models was applied to the GRACE land water equivalent (LWE) thickness data by multiplying the raw GRACE LWE thickness by the scale factor. This is necessary to obtain a spatial resolution of 0.5◦ and it is not pre-applied to the GRC Tellus JPL Monthly Mass Grid Global Mascon data. Additionally, a gap in GRACE/GRACE-FO observations occurred in 2017–2018 due to mission lifespan and battery complications (Landerer et al., 2020). For purposes of this study, linear interpolation is used to fill the missing monthly TWSA data. These data were used to construct time series and spatial plots of monthly TWSA. Further information about the GRACE mission and the GRC Tellus JPL Monthly Mass Grid Global Mascon dataset can be found at https://gracefo.jpl.nasa. gov and https://podaac-tools.jpl.nasa.gov/drive/files/allData/gracefo/docs/GRACE-FO_L3_Handbook_JPL.pdf.

## 3.5 Methodology

### 3.5.1 Hydrological components of the water balance equation

The water balance equation is as follows:

$$P - ET - R = \Delta S \tag{1}$$

where $P$ is precipitation, $ET$ is evapotranspiration, $R$ is runoff, and $\Delta S$ is change in total water storage. For purposes of this study, $P$ and $ET$ are derived from Earth observations (GPM IMERG and MODIS, respectively) while $R$ is a model output (GLDAS). GRACE/GRACE-FO was used to estimate $\Delta S$. Assessment of water balance closure in the Lake Victoria Basin using these datasets are limited by the MODIS ET observations because this dataset masks out lakes. Given the large spatial extent of Lake Victoria which makes up approximately 25% of the basin, it is unreasonable to assess water balance closure of the basin without evapotranspiration data over the lake itself. Thus, in this study we have chosen to examine individual hydrological components of the water balance equation (specifically precipitation, evapotranspiration over land, runoff, and change in water storage). Additional hydrological variables examined in this study include soil moisture, lake level height, and lake extent.

### 3.5.2 Hydrological anomalies

Monthly climate anomalies for precipitation, runoff, evapotranspiration, and root zone soil moisture were calculated using the difference between the monthly value and the monthly climatology. Monthly climate anomaly (henceforth referred to as 'anomaly') represents the difference between the actual monthly value and the monthly climatology. For example, a positive anomaly represents more rainfall than the climatological average. Likewise, a negative anomaly represents less rainfall than the climatological average. It is important to note that by international standards, climatology calculations should use a record of at least 30 years (WMO, 2017). However, this was not feasible for our study due to the availability and mission durations of Earth observations used for the analysis. Thus, a limitation of our study is that only a record of 20 years (June 2002 – June 2022) was used to calculate monthly climatology. Ideally, an equal time span of observations should be used for each month when calculating monthly climatology, but since the number of years of available observations is below the 30-year threshold, all available data is used for the analysis. Thus, 20 years of observations were used for all months except June, which had 21 years of observations.

Time series and spatial plots of monthly climate anomalies were constructed for each hydrological variable. For visual purposes, linear interpolation was used to re-grid precipitation, evapotranspiration, runoff, and root zone soil moisture to the same spatial scales for the spatial anomaly plots. TWSA was not re-gridded as this would be an overextension of the coarse native spatial resolution.

## 3.6 Results and Discussion

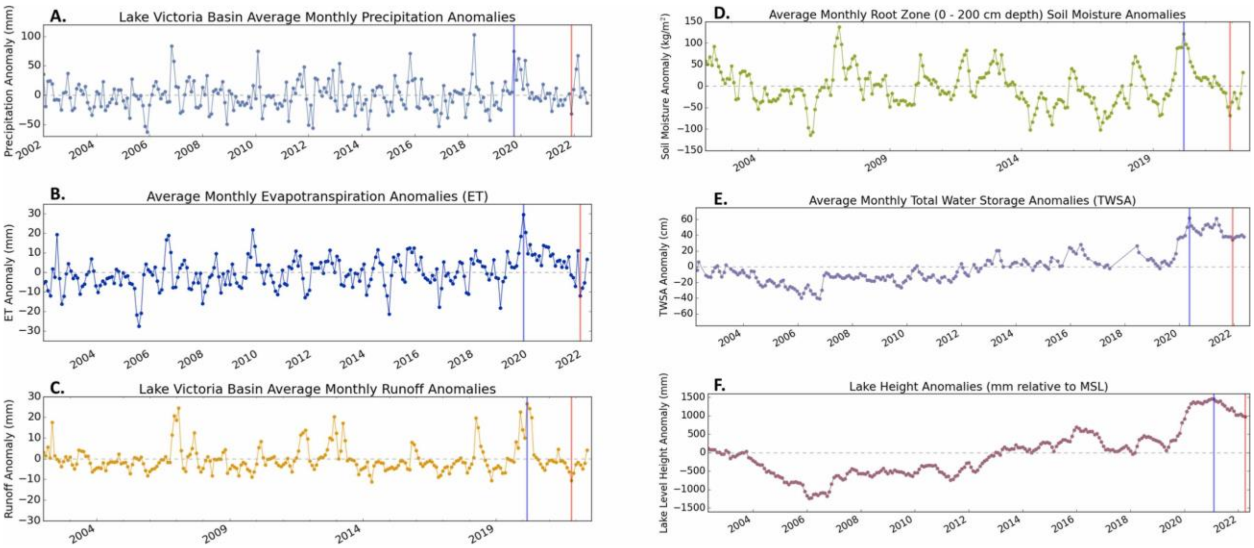

***Fig. 3.3:*** *Time series of average monthly anomalies for hydrological variables (precipitation, evapotranspiration, runoff, root zone soil moisture, total water storage anomaly (TWSA), and lake height) in the Lake Victoria Basin. The local maxima positive anomaly during the 2019 – 2020 flood period is indicated by a blue vertical line (representing the wet month). The local minima negative anomaly during the 2021 – 2022 drought period is indicated by a red vertical line (representing the dry month). Geospatial anomaly plots of the indicated wet and dry months for each hydrological variable are shown:* ***(A)*** *Time series of average monthly precipitation anomalies from Jan. 2002 – Jun. 2022 derived from GPM IMERG.* ***(B)*** *Time series of average monthly evapotranspiration anomalies from Jun. 2002 – Jun. 2022 derived from MODIS abord the Terra mission.* ***(C)*** *Time series of average monthly runoff anomalies from Jun. 2002 – Jun. 2022 derived from GLDAS.* ***(D)*** *Time series of average monthly root zone soil moisture (0 – 2 m depth) anomalies from Jun. 2002 – Jun. 2022 derived from GLDAS.* ***(E)*** *Time series of total water storage anomaly (TWSA) from Jun. 2002 – May 2022 derived from GRACE.* ***(F)*** *Time series of average monthly lake height anomalies relative to mean sea level (MSL) derived from Jason-1, Jason-2, and Jason-3.*

### 3.6.1 Time series of hydrological anomalies

Time series of hydrological anomalies for precipitation, evapotranspiration, runoff, root zone soil moisture, TWSA, and lake height from June 2002 – June 2022 are shown in Fig. 3.3A–E. A key objective of this study is to examine the recent flood and drought periods in the Lake Victoria Basin, so our results and discussion are focused on hydrological anomalies between September 2019 – June 2022. However, the extended period of record provides valuable context for the magnitude and duration of the recent flood and drought events. The highest positive anomalies within this time period of June 2002 – June 2022 were observed during the 2020–2021 flood event for evapotranspiration, runoff, TWSA, and lake height. Negative anomalies during the 2021–2022 drought event, however, were not the most extreme negative anomalies that the Lake Victoria Basin has experienced in the past 20 years. In Fig. 3.3, the local maxima and minima hydrological anomalies are respectively indicated by vertical blue and red lines which show months where the Lake Victoria Basin experienced anomalous wet and dry conditions. Table 3.3 summarizes months within the period of interest that were identified as positive anomalies (wet month) and the negative anomalies (dry month), as well as their respective anomaly values where applicable. Spatial plots corresponding to these identified wet and dry months for precipitation, evapotranspiration, root zone soil moisture, and TWSA are discussed in Section 3.6.2.

In the precipitation anomalies time series shown in Fig. 3.3A, October 2019 was identified as the anomalous wet month with a value of + 73 mm. November 2021 was identified as the anomalous dry month with a value of − 32 mm. While the positive precipitation anomaly during October 2019 was not the most extreme observed within the basin between 2002 and 2022, it was followed by 8 months of persistently positive precipitation anomalies from September 2019 – April

***Table 3.3:*** *Summary of wet/dry months and positive/negative anomaly values for hydrological variables during the recent flood and drought events. These were determined from the time series of monthly basin-averaged anomalies constructed from 20 years of Earth observations or model data (see Fig. 3).*

| Hydrological Variable | Positive Anomaly (Wet Month) | Negative Anomaly (Dry Month) | Spatial Plot |
|---|---|---|---|
| **Precipitation** | Oct. 2019<br>+ 73 mm | Nov. 2021<br>-32 mm | Yes |
| **Evapotranspiration** | Feb. 2020<br>+ 29 mm | Mar. 2022<br>-12 mm | Yes |
| **Runoff** | Mar. 2020<br>+ 27 mm | Nov. 2021<br>-10 mm | Yes |
| **Root Zone Soil Moisture** | Mar. 2020<br>+ 120 kg/m$^2$ | Nov. 2021<br>-71 kg/m$^2$ | Yes |
| **Near-surface Soil Moisture: 9-km*** | Mar. 2020<br>n/a | Nov. 2021<br>n/a | Yes |
| **Near-surface Soil Moisture: 1-km*** | Mar. 2020<br>n/a | Nov. 2021<br>n/a | Yes |
| **Lake Height** | May 2020<br>+ 1481 mm | Feb. 2022<br>+ 972 mm | No |
| **Total Water Storage Anomaly (TWSA)** | May 2020<br>+ 62 cm | Dec. 2021<br>+ 36 cm | Yes |

**: The wet and dry months for near-surface soil moisture were assumed to be the same as those identified by the root zone soil moisture anomaly time series, since there is not a sufficient observation record of near-surface soil moisture data to independently calculate climatology.*

2020, which is one of the longest periods of positive precipitation anomalies experienced in the basin.

The increase in TWSA during the same period (shown in Fig. 3.3E) concurs with the precipitation anomaly time series. TWSA reached its local maximum positive anomaly of + 62 cm in May 2020, which is one month later than the precipitation anomaly peak. This was the highest

TWSA value observed within the Lake Victoria Basin since 2002. During the 2021–2022 drought event, TWSA remains positive. In the past however, the Lake Victoria Basin has experienced dry periods with strong negative anomalies which indicates the relative magnitude of the early 2022 drought in comparison to previous droughts.

Lake height anomalies (shown in Fig. 3.3F) also increased substantially during the flood event. In September 2019, the lake height anomaly was + 340 mm. By May 2020, the lake height anomaly increased to + 1380 mm. At the time, lake level heights in May 2020 were record-breaking (BBC News, 2020). However, the lake height proceeded to reach a higher positive anomaly in February 2021 with a value of + 1470 mm. During the 2021–2022 drought period, lake height anomalies remained positive while decreasing to + 972 mm. The TWSA in late 2021 and early 2022 remained relatively constant, despite the steady decrease in lake height anomalies at this time.

Root zone soil moisture anomalies (shown in Fig. 3.3D) fluctuate from positive to negative between the 2019–2020 flood and 2021–2022 drought events. A maximum root zone soil moisture anomaly of + 120 kg/m$^2$ was observed in March 2020. A minimum root zone soil moisture anomaly of − 71 kg/m$^2$ was observed in November 2021, which was then followed by five months of persistently negative root zone soil moisture anomalies. By June 2022, however, the root zone soil moisture anomalies recovered and were positive. This captures the quick recovery of the recent drought event.

Similar to the root zone soil moisture anomalies, runoff anomalies (shown in Fig. 3.3C) fluctuate from positive values in March 2020 of + 27 mm to negative values in November 2021 of − 10 mm. The runoff anomalies are persistently negative from June 2021-May 2022, before recovering to a positive anomaly in June 2022. In conjunction with the root zone soil moisture anomalies during June 2022, the runoff anomalies in June 2022 also capture the basin’s quick recovery from the recent drought event.

### 3.6.2 Spatial variability of hydrological anomalies

Spatial anomaly plots of precipitation, evapotranspiration, runoff, root zone soil moisture, and TWSA are shown in Fig. 3.4A-E. For each hydrological variable, the previously identified wet and dry months from the hydrological anomalies time series are spatially plotted. Scalebar ranges were manually selected to ensure average variabilities over the basin are visually apparent by displaying outliers as the maximum and minimum colors.

Precipitation anomalies during October 2019 (wet month) and November 2021 (dry month) are shown in Fig. 3.4A1-2. During the wet month, positive precipitation anomalies were dominant across the basin with most regions experiencing anomalies of + 100 mm or greater. This concurs with media and journal articles which reported heavy and atypical rainfall in the Eastern Horn of Africa due to one of the strongest Indian Ocean Dipole (IOD) events on record (FEWS NET, 2020; Wainwright et al., 2021). The greatest precipitation anomaly of + 472 mm was observed directly over Lake Victoria. In the dry month, precipitation anomalies were as severe as approximately − 160 mm over the northeastern and southwestern shores of Lake Victoria. A few patches of positive anomalies were observed throughout the basin such as directly over Lake Victoria. This is likely explained by local meteorology in the nocturnal lake-land breeze system of Lake Victoria which makes precipitation directly over the lake 25 – 30% greater than precipitation over the surrounding land (Shamsudduha et al., 2017; Thiery et al., 2016).

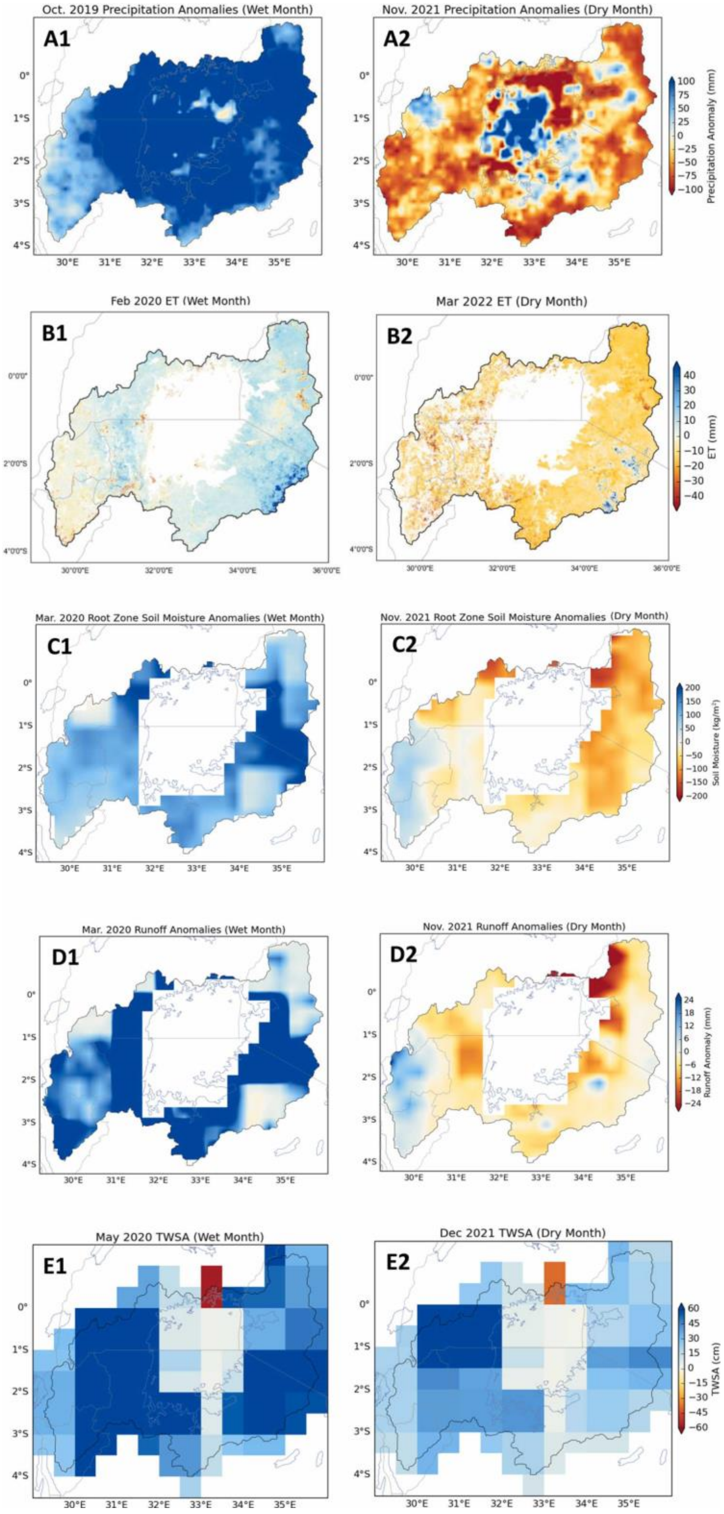

***Fig. 3.4:*** *Average monthly geospatial anomalies of hydrological parameters during the anomalously high (wet) and low (dry) months between Sept. 2019 – Jan. 2022. These months are the local maxima and minima in the basin-averaged monthly time series of hydrological anomalies shown in Figure 3 as the vertical blue and red lines to indicate wet and dry anomalies. For visual*

*purposes, the scalebar was manually selected to represent variability within the basin by displaying outliers as the maximum/minimum colors.* ***(A1)*** *Monthly precipitation anomalies in Oct. 2019 (wet month).* ***(A2)*** *Monthly precipitation anomalies in Nov. 2021 (dry month).* ***(B1)*** *Monthly evapotranspiration anomalies in Mar. 2020 (wet month).* ***(B2)*** *Monthly evapotranspiration anomalies in Jan. 2022 (dry month).* ***(C1)*** *Monthly runoff anomalies in Mar. 2020 (wet month).* ***(C2)*** *Monthly runoff anomalies in Nov. 2021 (dry month).* ***(D1)*** *Monthly root zone soil moisture anomalies in Mar. 2020 (wet month).* ***(D2)*** *Monthly root zone soil moisture anomalies in Dec. 2021 (dry month).* ***(E1)*** *Monthly total water storage anomaly (TWSA) in May 2020 (wet month).* ***(E2)*** *Monthly total water storage anomaly (TWSA) in Dec. 2021 (dry month)*

Evapotranspiration spatial anomaly plots for February 2020 (wet month) and March 2022 (dry month) are shown in Fig. 3.4B1–2. As previously discussed, an unfortunate limitation of this MODIS evapotranspiration product is that lakes and permanent waterbodies are masked out. However, one would expect that a significant portions of the basin’s overall evapotranspiration occurs directly over Lake Victoria due to the lake’s large surface area, shallow depth, and the region’s tropical climate. Previous studies have found that evaporation accounts for 80% of the water leaving Lake Victoria while precipitation accounts for approximately 86% of the total water input into Lake Victoria (Nyeko-Ogiramoi et al., 2013). However, it is not possible to assess these results with the public Earth observations utilized in this study. In Fig. 3.4B1–2, less extreme anomalies (± 10 mm) were observed in the western portion of the basin compared to the eastern regions ( ± 40 mm). When compared alongside land cover type (Fig. 3.2), permanent wetlands are highlighted as positive anomalies during the wet month and the Kenyan forested areas are highlighted as negative anomalies during the dry month. Similar spatial anomaly patterns were observed for runoff (Fig. 3.4C1–2) and root zone soil moisture (Fig. 3.4D1–2). During the wet month (March 2020), the most extreme runoff and root zone soil moisture anomalies were observed in the lower elevations (up to +120 mm for runoff and +254 kg/m2 for root zone soil moisture anomalies). In the dry month (November 2021), root zone soil moisture anomalies ≤ − 100 kg/m2 were observed across most of the eastern portion of the basin. Additionally, there is a clear division between positive/negative runoff and root zone soil moisture anomalies in Burundi and Rwanda. This pattern follows the boundary of cropland versus grassland/savanna land cover types shown in Fig. 3.2.

TWSA spatial plots for May 2020 (wet month) and December 2021 (dry month) are shown in Fig. 3.4E1–2. For both periods, an overall positive TWSA was observed within the basin with regions experiencing peak TWSA greater than or equal to + 60 cm. However, December 2021 has lower positive anomalies than May 2020 in the eastern and southwestern portions of the basin. Observed changes in TWSA are more extreme over land as opposed to the lake itself between the wet and dry months. Additionally, highly negative TWSA are observed in Uganda near Lake Victoria's outlet which is a highly populated urban area. Because the native resolution of GRACE is coarse, it is possible that these observed patterns are indicative of limitations of the enhanced spatial resolution of the GRC Tellus Global Mascon Monthly Mass Grid data. Further research should be conducted to assess the accuracy and limitations of this data product with regard to extreme hydrological events in the Lake Victoria Basin.

Overall, the spatial plots of hydrological anomalies capture significant variability within the Lake Victoria Basin and between periods of flood and drought. This provides valuable spatial hydrological information which complements the previously discussed temporal anomaly analysis. This level of spatial hydrological analysis would not otherwise be obtainable given the region's limited in-situ hydrological observations.

### 3.6.3 Comparison of 9-km and 1-km soil moisture products

Spatial plots of monthly soil moisture observations (0–5 m depth) are shown in Fig. 3.5. Due to the limited mission duration of SMAP (launched in 2015), a sufficient period of record was not available to conduct an anomaly analysis. Additionally, no soil moisture data is collected over Lake Victoria or other waterbodies within the basin.

Consistent with the root zone soil moisture anomaly analysis, March 2020 and November 2021 were selected as wet and dry months of interest. The 9-km SMAP soil moisture observations for the wet month show higher soil moisture values, ranging from approximately 0.34 to 0.44 kg/m$^2$ in the northeastern, southern, and southwestern regions of the basin (Fig. 3.5A1). During the dry month, the 9-km SMAP soil moisture observations showed that the lower elevations in the northeast maintained higher soil moisture values than the higher elevations in Kenya. The southeastern regions of the basin in Rwanda and Burundi also maintained higher soil moisture than the surrounding regions. Based on the land cover classifications, this spatial pattern may be explained by human intervention to maintain soil moisture conditions suitable for agriculture.

The 1-km downscaled soil moisture observations are shown in Fig. 3.5B1–2 for March 2020 and November 2021 as well. Overall, the 1-km soil moisture product demonstrated higher soil moisture values in the southern region compared to the 9-km SMAP product (Fig. 3.5B1). Similarly, in the dry month, the 1-km soil moisture product demonstrated lower soil moisture values (0.05 kg/m$^2$) than the 9-km SMAP product (0.13 kg/m$^2$) in the eastern edge of the basin in Kenya and Tanzania (Fig. 3.5B2). Qualitatively, the 1-km soil moisture product seems to capture more extreme soil moisture values than the 9-km SMAP product.

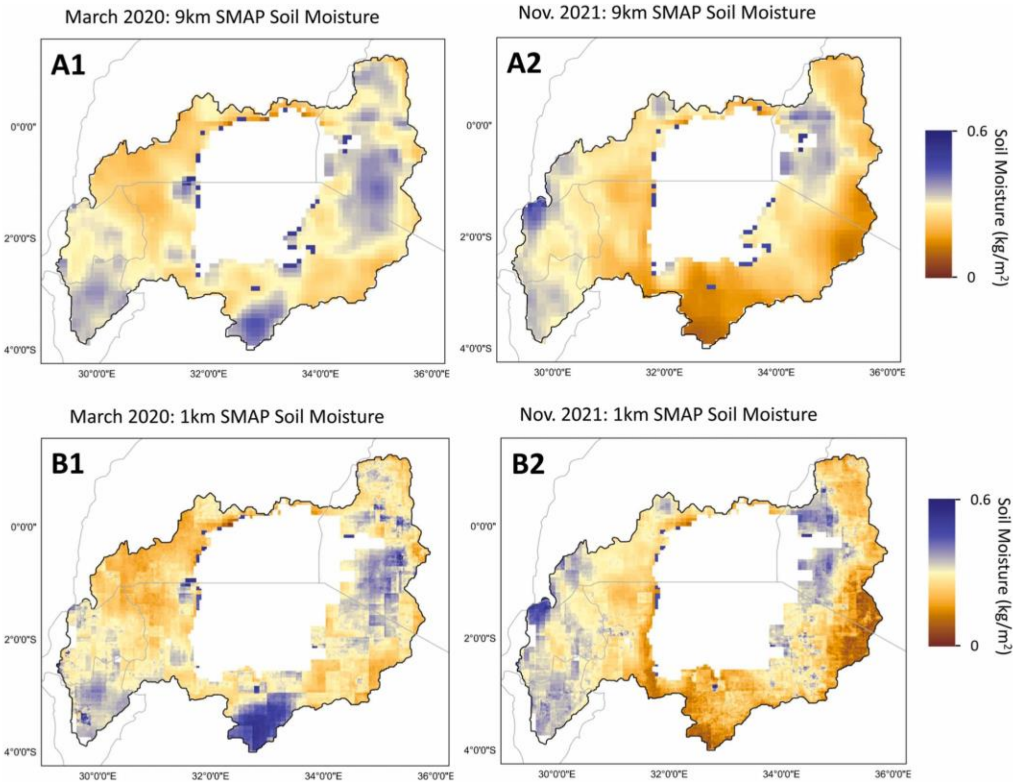

***Fig. 3.5:*** *Spatial plots of monthly soil moisture (0–5 cm depth) observations derived from SMAP. March 2020 and November 2021 were respectively selected as the wet and dry months, based on the time series of monthly root zone soil moisture anomalies (Fig. 4 C1 and C2). The spatial plots are shown at both 9-km and 1-km resolutions. (A1) 9-km monthly soil observations in Mar. 2020 (wet month); (A2) 9-km monthly soil moisture observations in Nov. 2021 (dry month); (B1) 1-km monthly soil moisture observations in Mar. 2020 (wet month); (B2) 1-km monthly soil moisture observations in Nov. 2021 (dry month).*

A quantitative validation analysis was performed with 28 ground-based soil moisture stations through the Trans-African HydroMeteorological Observatory (TAHMO) and the International Soil Moisture Network (ISMN) which is accessible at https://ismn.geo.tuwien.ac.at/en/. Validation statistics, plots, and time series are shown in Figs. 3.6 and 3.7 and the Appendix (3.1− 3.22). It is important to note that this validation is limited by the short period of in-situ observations primarily from mid-2018 to present. Additionally, no ISMN in-situ observations were available in Tanzania.

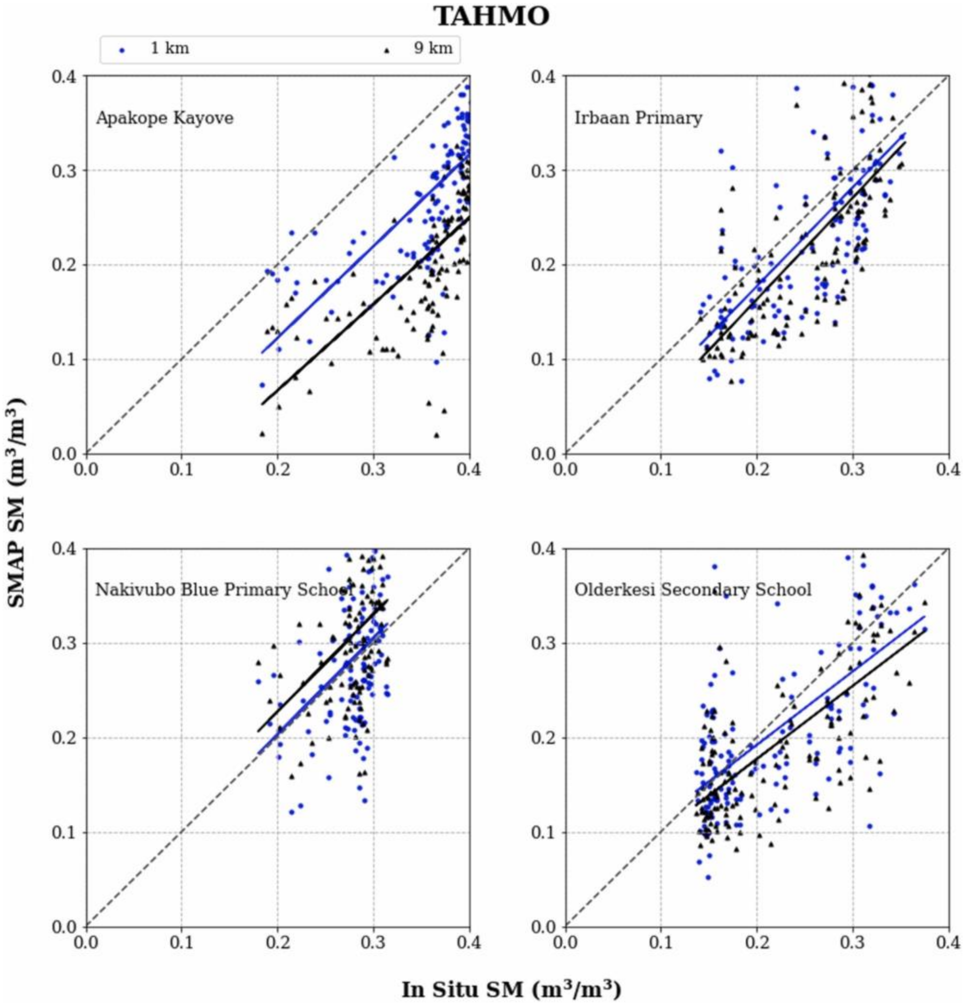

***Fig. 3.6:*** *Results of validation of in-situ near-surface soil moisture observations from the International Soil Moisture Network with the 1-km and 9-km Soil Moisture Active Passive (SMAP) observations at 6:00AM overpasses.*

In Fig. 3.6, data collected at four ISMN soil moisture observation sites were validated with the 1-km and 9-km SMAP observations. The 1-km downscaled soil moisture observations performed better than the 9-km soil moisture product for each site. Fig. 3.7 shows time series of the same four ISMN soil moisture observation sites in comparison with the 1-km and 9-km soil moisture SMAP observations from 2015 to 2021. Here, it is possible to see how the performance of both the 1-km and 9-km soil moisture products vary over time in comparison with the in-situ soil moisture observations. In general, the 1-km data performed comparably or better than the 9-km SMAP observations with lower unbiased RMSE. Both the 1-km and 9-km data had low p-values and were statistically significant. From this validation (Figs. 6 and 7) and the Appendix, it is clear that the downscaled 1-km soil moisture compares better to the available in-situ observations than the original 9-km soil moisture data. Along with the 1-km global validation conducted by Fang et al. (2022), this validation forms a good basis for acceptance of use of the SMAP downscaled 1-km soil moisture data set for analyses in this basin. Future research should be conducted to continue validation efforts across the African continent.

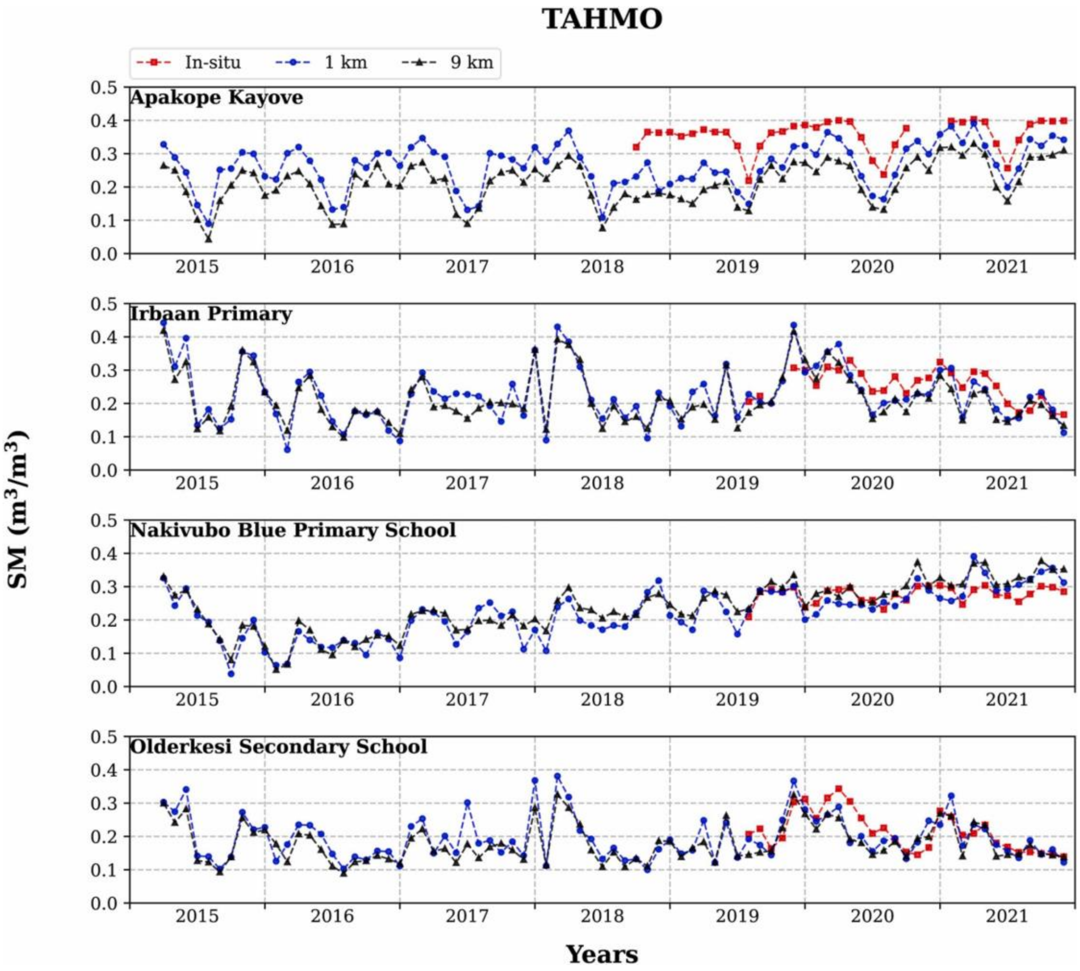

***Fig. 3.7:*** *Time series of in-situ near-surface soil moisture observations from four TAHMO stations compared with 1-km and 9-km SMAP soil moisture observations from 2015 to 2021.*

## 3.6.4 Change in lake volume

To further quantify the relative hydrological variations in this region between hydrological extremes, change in the volume of Lake Victoria were calculated from the identified wet month (May 2021) and dry month (Feb. 2022) in lake level height using the following equation:

$$\Delta V = \Delta A * \Delta H \tag{2}$$

where $\Delta V$ is change in volume, $\Delta A$ is change in surface area, and $\Delta H$ is change in lake level height. The change in surface area between May 2021 and Feb. 2022 were calculated by identifying the total area of inundated pixels over Lake Victoria in Sentinel-1 synthetic aperture radar (SAR) imagery during the two months. Changes in lake level height were derived from the G-REALM altimetry data. Between May 2021 and Feb. 2022, the lake level decreased by 1.19 m and the surface area decreased by approximately 9,270 km$^2$. Thus, the overall change in lake level volume was -11.03 km$^3$. This large decrease in lake volume concurs with the results derived from the other hydrological variables which also experienced large decreases (represented as negative anomalies) during this time period.

## 4.6.6 Relationship between TWSA, precipitation, and lake height

A time series of monthly climatology for precipitation, lake height, and TWSA are shown in Fig. 3.8 (see Section 3.2, equation 2 for more details on the calculation of monthly climatology). This depicts the seasonality of precipitation, lake height, and TWSA based on the period of available data (June 2002 – June 2022 for precipitation and lake height; June 2002 – May 2022 for TWSA). The precipitation monthly climatology captures the distinct short rainy season and long rainy season which respectively occur between March – May and September – November. April has the highest average rainfall of 118 mm/month. July has the lowest average rainfall of 56 mm/month. Lake height follows similar seasonality as precipitation with a slight lag (approximately 1–2 months). May has the highest average lake height with an elevation of 1136 m above MSL. October has the lowest average lake height with an elevation of 1134 m above MSL. As previously discussed, Lake Victoria is sensitive to human management of hydropower dam operations at its outlet so these seasonal changes may be a result of both anthropogenic and natural factors. TWSA depicts similar seasonality as precipitation with a lag of 1–2 months. May has the highest average monthly TWSA value of + 7 cm/month. September has the lowest average monthly TWSA value of − 8 cm/month.

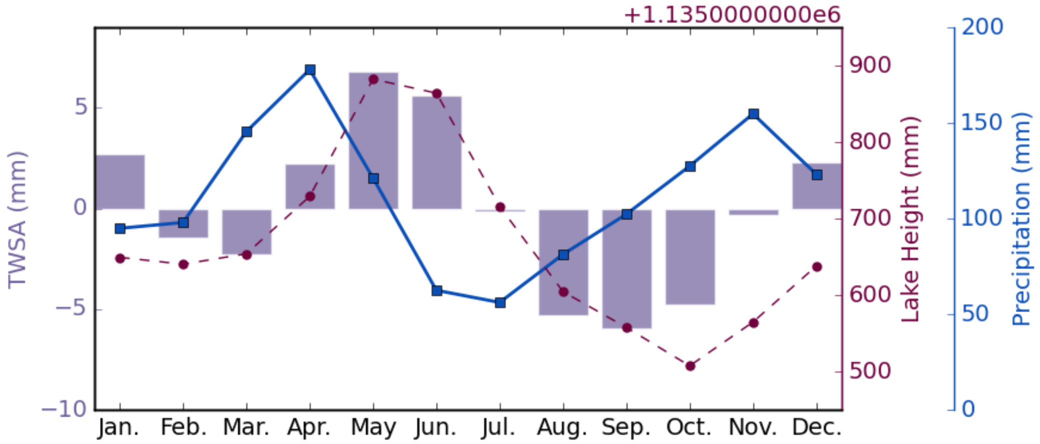

***Fig. 3.8:*** *Variability of monthly climatological values of precipitation, lake height, and total water storage anomaly (TWSA) which were calculated from the duration of the study period from June 2002 – January 2022 using equation 2. This graph shows the seasonality of precipitation, lake height, and TWSA within the basin. It is important to note that lake height is managed by hydropower dams at Lake Victoria's outlet near Jinja, Uganda.*

Fig. 3.9 shows a longer time series comparison from January 2019 – January 2022 for monthly TWSA (purple bars), observed basin averaged monthly precipitation (blue solid line), and monthly climatology of precipitation (dashed gray line). From October 2019 to May 2020, the average observed monthly precipitation exceeded the monthly precipitation climatology by 13–75 mm. This means the basin experienced a positive precipitation anomaly and was wetter than the climatological average. From media articles, it is documented that extensive flooding occurred during this period in the Lake Victoria Basin and East Africa (BBC News, 2020; FEWS NET, 2020; Khaki & Awange, 2021; Kisumu, 2020; Wainwright et al., 2021).

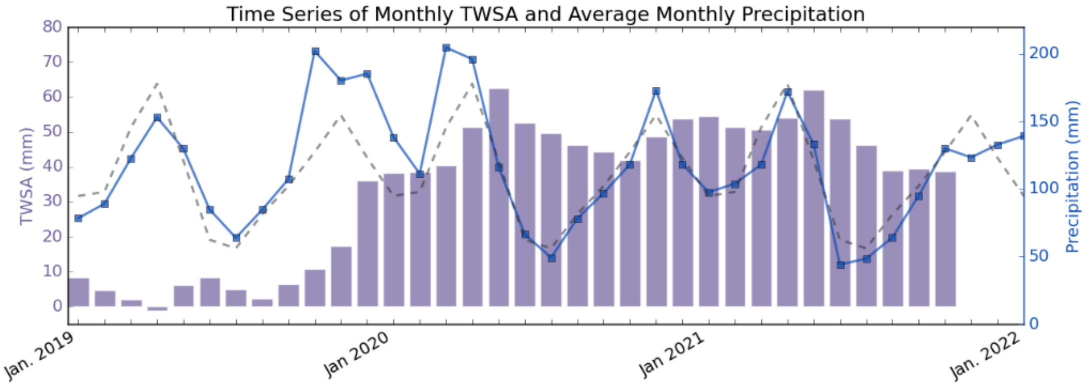

***Fig. 3.9:*** *Time series of monthly total water storage anomaly (TWSA, shown as purple bars), observed basin-averaged monthly precipitation (shown as solid blue line), and climatological monthly precipitation (black dashed line) from Jan. 2019 – Jan. 2022. If the monthly precipitation is greater than the climatological precipitation, the basin experienced a positive anomaly meaning it was wetter than the climatological average. Likewise, if the monthly precipitation is less than the climatological precipitation, the basin experienced a negative anomaly meaning it was drier than the climatological average. Note, TWSA data was not yet published for Nov. 2021-Jan. 2022 when this analysis was conducted.*

Similarly, March 2021 – December 2021 had average observed monthly precipitation below the monthly climatology by − 6 mm to − 31 mm. This indicates a negative precipitation anomalies and drier conditions than the climatological average. These observations concur with a report from the Famine Early Warning Systems Network which documented this period as having a failed rainy season and high risk for crop failure and food insecurity in East Africa (FEWS NET, 2021).

## 3.7 Conclusions

Over the previous decades, hydrometeorological extremes like floods and droughts have been continual and recurrent in the Lake Victoria Basin. Recently, the Lake Victoria Basin experienced extreme floods in 2019–2020 and drought conditions in early 2022. High-resolution spatial and temporal monitoring of hydrological variables are vital for improving understanding of hydrology within the Lake Victoria Basin, particularly given the region's dense population and vulnerability to sub-seasonal hydrological anomalies which can lead to the loss of life and property, crop failure, food insecurity, and increased poverty. However, there are insufficient in-situ hydrological observations in the Lake Victoria Basin to fill this need. Thus, in this study, we leverage publicly available Earth observations and model data to capture occurrence of the recent flood and drought events in the Lake Victoria Basin. We examined and discussed components of the hydrological water balance (precipitation, evapotranspiration, runoff, and change in total water storage) and additional hydrological variables (soil moisture, lake height, and lake extent) with specific regard to the recent hydrological extreme events. This was accomplished through construction of time series and spatial plots of monthly anomalies for each variable. Our results improve understanding and documentation of the severity and duration of the recent flood and drought events.

The innovation of this work is that it offers a simple method of using publicly available Earth observations and model data to improve spatial and temporal analyses of hydrological anomalies at sub-seasonal time scales within a region lacking in-situ data. To our knowledge, this is the first study to conduct a hydrological spatial anomaly comparison for the 2019–2020 flood and 2021–2022 drought events in the Lake Victoria Basin. Thus, this is a novel contribution to the existing record of hydrological research in this region because it updates previous studies and is among the first to integrate such a diverse array of publicly available datasets for the Lake Victoria Basin. Further work could assess this method for informing water resources management in this region, particularly for informing scheduling, planting, irrigation, and harvesting of crops. This would be valuable given the Lake Victoria Basin's growing population and economic reliance on rain-fed subsistence agriculture.

Additionally, a comparison of 9-km and 1-km near-surface soil moisture products derived and downscaled from SMAP was conducted to improve spatial resolution of soil moisture observations in the Lake Victoria Basin. The 1-km near-surface soil moisture product was validated with ground station near-surface soil moisture data available through the International Soil Moisture Network and performed either better or comparably to the 9-km SMAP observations. This was the first validation of the 1-km near-surface soil moisture product in the continent of Africa. Further research should continue validation efforts of soil moisture data derived from Earth observations in the Lake Victoria Basin and Africa in the limited regions where ground-based observations are available.

Methods and findings from this study can be used to advance understanding and monitoring methods of sub-seasonal hydrological anomalies within the Lake Victoria Basin, particularly through publicly available Earth observations. By demonstrating a simple method for improved monitoring of hydrological variables including precipitation, evapotranspiration, runoff, soil moisture, lake height, and TWSA, this study supports the continual effort to decrease the Lake Victoria Basin community's vulnerability to hydrological anomalies during extreme floods and droughts.

## 3.8 Acknowledgements

We thank Nathaniel Doty and Dr. Bin Fang for their contributions to this manuscript. This paper is based upon work supported by the National Science Foundation (NSF) Research Traineeship (NRT) program under Grant No. 1829004 and the NSF Graduate Research Fellowship Program (GRFP) under Grant No. 182490. Any opinions, findings, conclusions, or recommendations expressed in this work are those of the author(s) and do not necessarily reflect the views of the University of Virginia or the National Science Foundation.

# **Chapter 4:** Risk Comparison of Hurricane Scenarios as Disruptions of Hydrologic Basin Order with Criteria of Social Vulnerability[3]

## 4.1 Abstract

Economic damages of hurricanes and tropical cyclones are increasing faster than populations and wealth of many coastal areas. There is urgency to update priorities of agencies engaged with risk assessment, risk mitigation, and risk communication across hundreds or thousands of water basins. This paper evaluates hydrology and social vulnerability factors to develop a risk register at a sub-basin scale for which the priorities of agencies vary by storm scenario using publicly available satellite-based Earth observations. The novelty and innovation of this approach is the quantification and mapping of risk as a disruption of system order, while using social vulnerability indices and sensor data from disparate sources. The results assist with allocating resources across basins under several scenarios of hydrology and social vulnerability.

---

[3] The work presented in this chapter resulted in the following journal article accepted for publication in *ASCE-ASME Journal of Risk and Uncertainty in Engineering Systems, Part A: Civil Engineering:*

Pavur, G. Lambert, H., Lakshmi, V. "Risk Comparison of Hurricane Scenarios as Disruptions of Hydrologic Basin Order with Criteria of Social Vulnerability."

The approach is in several parts as follows: First, a baseline order of basins is defined using the CDC/ATSDR Social Vulnerability Index (SVI). Next, a set of storm scenarios is defined using Earth Observations and modeled data. Next, a swing-weight technique is used to update factor weights under each scenario. Lastly, the importance order of basins relative to the baseline order is used to compare risk of scenarios across the study area. The risk is thus quantified (by least squares difference of order) as a disruption to the ordering of basins by social and hydrologic factors (i.e., SVI, precipitation, wind speed, and soil moisture), with attention to the most disruptive scenarios. An application is described with extensive mapping of hydrologic basins for Hurricane Ian to demonstrate a versatile method to address uncertainty of scenarios of storm nature and extent across coastal mega-regions.

## 4.2 Introduction

Tropical cyclones historically result in social, economic, and environmental losses in coastal mega-regions such as the southeastern United States. Compared to other disasters in the USA, tropical cyclones result in the most damages and fatalities, averaging approximately $30.9 billion in damages and 157 fatalities per year since 1980 (NOAA, 2023). The southeastern USA is a hotspot for disproportionately high losses from climate-sensitive hazards because of elevated exposure and concentrations of socially vulnerable populations (Cutter et al., 2003; Emrich & Cutter, 2011). With predictions that climate change will increase the frequency and intensity of future tropical cyclones, there is a need to reduce tropical cyclone risk and improve system resilience (Lavell et al., 2012; UNDRR, 2015). Evidence-based decision making has been identified as an essential tool to support sustainable, resilient, and risk-informed societies across organizational boundaries during disasters (Kavvada et al., 2022; Shittu et al., 2018). To support this, there is a need to quantity risk using social and environmental data.

*Social vulnerability* of an individual or community refers to their “capacity to anticipate, confront, repair, or recover from the effects of a disaster” (Flanagan et al., 2018). Previous studies have shown that communities of high social vulnerability face significant short and long-term challenges following disasters which limits their ability to recover ( Flanagan et al., 2011, 2018; Fothergill & Peek, 2004; Yarveysi et al., 2023). Disparities of social vulnerability are observable within neighboring blocks, meaning communities with varying social vulnerability will likely suffer different impacts if exposed to the same tropical cyclone conditions (Bakkensen et al., 2017; Yarveysi et al., 2023). For example, the overall economic cost of repairs may be larger within an affluent community, but the losses are disproportionately higher for the socially vulnerable community (Flanagan et al., 2011). Examples of tropical cyclone disaster challenges associated with social vulnerability during each phase of the disaster cycle (mitigation, preparedness, response, and recovery) are provided in Appendix 4.1.

Previous research quantified the relative social vulnerability of the United States at various spatial resolutions including the county level, Census-tract level, and block level (Cutter et al., 2003; Flanagan et al., 2011; Yarveysi et al., 2023). These datasets have been applied to natural and anthropogenic hazards to show the spatial and temporal variability of social vulnerability across the United States. Three social vulnerability indices are described below:

1. **County-level Social Vulnerability Index (SoVI):** Cutter et al., 2003 developed the county-level SoVI by using principal components analysis with socioeconomic and demographic data that were identified as influential to natural hazards vulnerability (Cutter et al., 2003; Emrich & Cutter, 2011). Findings included observable variations in SoVI across widespread regions, such as neighboring states, and the need for higher spatial resolution data to resolve hazard vulnerabilities at the sub-county level (Cutter et al., 2003;

Emrich & Cutter, 2011). Due to the coarse county-level resolution, SoVI was not used in this study.

2. **Block-level Socio-Economic-Infrastructure Vulnerability Index (SEIV):** Yarveysi et al., 2023 developed the SEIV by leveraging machine learning algorithms to provide high-resolution vulnerability data at the block-level (Yarveysi et al., 2023). This allows for analyses at finer spatial resolutions compared to SoVI and SVI. It showed significant inequities among neighboring blocks (Yarveysi et al., 2023). However, SEIV is not currently recommended to be applied to disasters with high levels of damage (> $250 million) since losses at the fine resolution of SEIV are unreasonable to distinguish (Yarveysi et al., 2023). Since this study provides a demonstration of the methodology for a hurricane with damages of over $114 billion, SEIV was not used.
3. **Census-tract level Social Vulnerability Index (SVI):** The Centers for Disease Control (CDC) and Prevention Agency for Toxic Substances and Disease Register (ASTDR) constructed a Census-tract level SVI designed to support disaster management (Flanagan et al., 2011). The index is available for multiple years (2000, 2010, 2014, 2016, 2018, and 2020) using sixteen (16) variables to calculate SVI at national and state levels (see Appendix 4.2; Flanagan et al., 2011). SVI has been validated and applied to natural and anthropogenic disasters including tropical cyclones, wildfires, sea level rise, rural/urban studies, migrant and refugee population studies, etc. (Flanagan et al., 2018). For this study, we have chosen to use SVI as it is the finest resolution social vulnerability data appropriate for disasters with extensive damage greater than $250 million.

A factor of tropical cyclone damage is exposure to intense hydrometeorological conditions. Generally, adequate spatial and temporal ground-based *in-situ* observations are not possible to collect during tropical cyclones due to widespread instrument failures (Bucci et al., 2022). Satellite-based Earth observations can fill this data gap by collecting high-resolution spatial and temporal data during the disaster which may have otherwise been unobservable. For this study, precipitation, wind speed, and soil moisture estimates were obtained from Earth observations and models. Since hurricane damages can occur from exposure to a single extreme environmental variable as well as a combined exposure to multiple environmental variables, this study considers both individual and multiple variables (Clark et al., 2022).

With the above motivation, this paper will address a need for regularly updated disaster risk maps, as outlined in the United Nations Sendai Framework for Disaster Risk Reduction, by providing a methodology to combine disparate sources of information in a risk register at a sub-basin scale (Bonato et al., 2022; Hamilton et al., 2015; Karvetski et al., 2009; UNDRR, 2015; You et al., 2014). Within this *risk register* of basins, hydrological and social vulnerability factors (specifically SVI, cumulative precipitation, maximum hourly precipitation, maximum hourly wind speed, and five-day antecedent soil moisture) are combined in several storm scenarios that disrupt the system order relative to a baseline scenario of SVI. A swing-weight technique is used to calculate new ordering functions for each basin under a given scenario (Karvetski et al., 2009). The swing-weight technique allows for tradeoffs of higher consideration of one or more variables in exchange for lower consideration of other variables (Karvetski et al., 2009). This is advantageous for risk analysis of hydrological disasters because the relative importance of one variable (social or hydrological) over another is uncertain. Thus, comparison of storm scenarios derived from a swing-weight technique reveals the sensitivity of the system to both single and multiple variables input into the model.

The disruption of tropical cyclone disaster scenarios compared to the baseline order are mapped to identify basins of top priority and basins of greatest change in priority. The sum of squares of differences in order of basins relative to the baseline order is used to identify scenarios that are most and least disruptive. A regional demonstration of this approach with features of Hurricane Ian is provided. The approach is an example of multidisciplinary innovation toward providing high-resolution risk communication to disaster managers and policymakers for systems analysis and resource allocation. The maps and other results can inform priorities and strategies aimed to decrease or transfer tropical cyclone risk and improve system resilience within basins of high tropical cyclone exposure and high social vulnerability.

### 4.2.1 Hurricane Ian Damages

In September 2022, Hurricane Ian became the 3rd costliest hurricane in USA history with over \$114 billion in estimated damage (Smith, 2023; Smith & Katz, 2013). Hurricane Ian caused 156 direct and indirect fatalities, 150 of which occurred in Florida, making this the deadliest storm in Florida since 1935 (Bucci et al., 2022; Karimiziarani & Moradkhani, 2023).

Conditions for Hurricane Ian were described by the National Oceanic and Atmospheric Administration (NOAA) National Hurricane Center and the media as *catastrophic, life-threatening,* and *deadly* (Bucci et al., 2022). Damages included, but were not limited to, storm surge up to 15 ft above ground level, extensive flooding, destruction and damage to infrastructure, multiple tornadoes, and tropical-storm force winds (Bucci et al., 2022). Hundreds of water rescues were necessary and an estimated 9.62 million people were without power (Bucci et al., 2022). In the aftermath of Ian, receding stormwater transported pollutants and debris to the Gulf of Mexico which caused harmful algal blooms off the Florida coast (Bucci et al., 2022).

### 4.2.2 Hurricane Ian Meteorology

Ian originated off the west coast of Africa, rapidly intensified in warm Atlantic Ocean water, and made its first landfall in western Cuba as a Category III hurricane on the Saffir-Simpson Hurricane Wind Scale on September 27 (Bucci et al., 2022). The system continued into the Gulf of Mexico where it strengthened to a brief peak intensity of a Category V hurricane (Bucci et al., 2022). Ian weakened slightly to a Category IV hurricane before making landfall near Punta Gorda, Florida on September 28 (Bucci et al., 2022). As Ian slowly traversed Florida, it weakened to tropical storm status before re-entering the Atlantic Ocean near Cape Canaveral, Florida on September 29 (Bucci et al., 2022). Once in the Atlantic Ocean, Ian intensified to a Category I hurricane and made its final landfall near Georgetown, South Carolina. Ian gradually weakened in the Carolinas and dissipated on October 1 (Bucci et al., 2022).

### 4.2.3 Hurricane Ian Data Collection

Numerous data collection methods were employed before, during, and after Hurricane Ian to support forecasting, response, and recovery efforts. For example, data were collected using ground-based weather radars, networks of buoys, dropwindsonde observations, satellite observations, Hurricane Hunter flights, and meteorological/environmental models (Bucci et al., 2022). It is important to note that during Hurricane Ian's landfall in the USA, many *in-situ* observation stations suffered instrument failures due to their exposure to the hurricane and were unable to capture the peak meteorological conditions (Bucci et al., 2022). Thus, satellite-based Earth observations provide a valuable contribution to hurricane data collection by providing high-resolution spatial and temporal data during the disaster that could have been unobservable otherwise.

### 4.2.4 Hurricane Ian Social Vulnerability Challenges

Forecast and warnings for Hurricane Ian were issued 39-48 hours in advance of its landfall in both Florida and South Carolina (Bucci et al., 2022). Even with relatively good forecasting and early issues of warnings, as was the case with Hurricane Ian, previous studies have shown that social vulnerability factors decrease the ability of individuals to safely evacuate (Anand et al., 2023; Flanagan et al., 2011, 2018; Meyer et al., 2018). Social vulnerability may explain the high number of fatalities during Hurricane Ian, particularly considering that reports of indirect causes of death included lack of access to timely medical care, accidents (such as falling during power outages), cardiac events, etc. (Bucci et al., 2022). Additionally, the elderly composed the highest proportion of fatalities during Hurricane Ian, which is generally observed during disasters (Bucci et al., 2022; Flanagan et al., 2011).

## 4.3 Geographic Area of the Demonstration

The NOAA National Weather Service estimates of Hurricane Ian's path and wind swath over the contiguous United States were used to define a study area of 922 sub-basins within and traversing portions of the following five southeastern states: Alabama, Florida, Georgia, North Carolina, and South Carolina (Fig. 4.1). The sub-basins were defined using the Level 08 HydroBASINS product (Lehner & Grill, 2013a). The study area encompassed approximately 700,000 km$^2$.

A digital elevation model (DEM) for the study area is shown in Fig. 1A and was derived from the National Aeronautics and Space Administration (NASA) Shuttle Radar Topography Mission (SRTM). Due to the variability of low-lying terrain and the Appalachian Mountains, elevation within the study area ranged from approximately -29 m to +1977 m relative to mean sea level (MSL). The mean elevation was +145 m MSL.

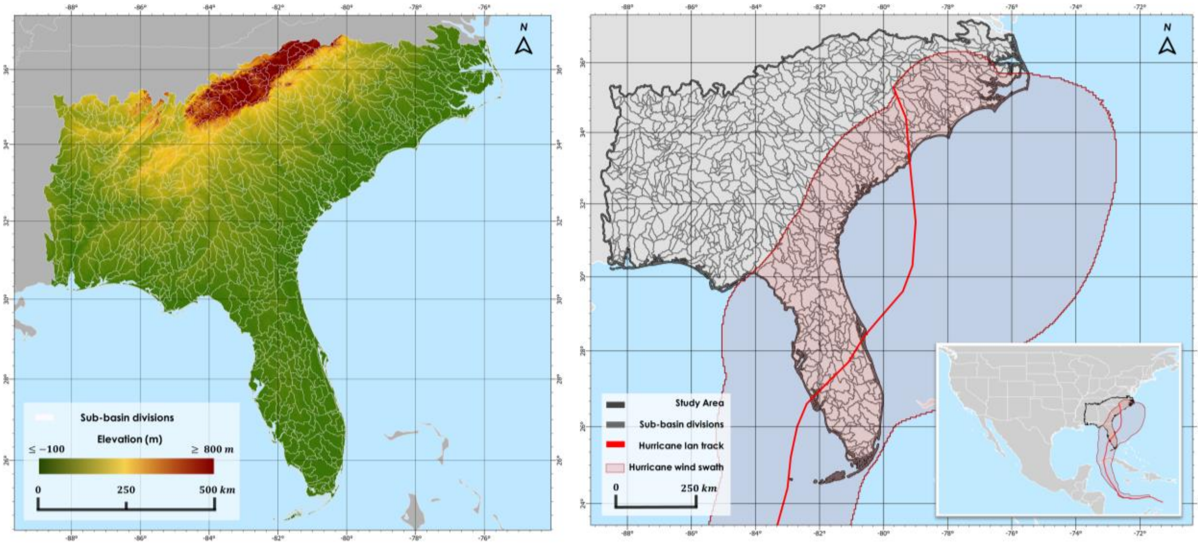

**A:** DEM and HydroBASINS Level 08 sub-basins

**B:** Hurricane Ian track and wind swath (NOAA NWS, 2022)

***Fig. 4.1:*** *Area of demonstration within the southeastern United States.* ***(A)*** *Digital elevation model (DEM) and HydroBASINS Level 08 sub-basins.* ***(B)*** *Hurricane Ian track and wind swath estimates from NOAA National Weather Service and HydroBASINS Level 08 sub-basins.*

## 4.4 Sources of Data for the Demonstration

Descriptions of data used in this study for social factors (i.e., SVI) and hydrology factors (i.e., precipitation, wind speed, and soil moisture) are provided in the following sub-sections. Table 4.1 summarizes the temporal resolution, native spatial resolution, resampled resolution, resampling method, study period, and source for each dataset.

***Table 4.1:*** *Summary of hydrology and social vulnerability data used in this study, including the variable, sensor/model, native spatial resolution, resampled resolution, resampling method, temporal resolution, study period, and sources.*

| Variable | Sensor/ Model | Native Spatial Resolution | Resampled Resolution | Resampling Method | Temporal Resolution | Study Period | Sources |
|---|---|---|---|---|---|---|---|
| Social Vulnerability Index (SVI) | CDC/ATSDR Social Vulnerability Index 2020 Database, USA | Census Tracks | Level 08 Hydro-BASINS | Spatial average | 1 year | 2020 | CDC/ATSDR, 2023 |
| Precipitation | GPM IMERG Late Precipitation L3 Half Hour Precipitation V06 | 0.1° | Level 08 Hydro-BASINS | Spatial sum & spatial maximum | 1 hour | 09/27 – 10/01/2022 | Huffman et al., 2020 |
| Soil Moisture (Near-Surface, 0 – 5 cm) | UVA 1-km Downscaled Soil Moisture Product | 1-km | Level 08 Hydo-BASINS | Spatial average | 12 hours | 09/23 – 09/27/2022 | Lakshmi & Fang, 2023 |
| Wind speed | ECMWF ERA5 | 0.25° | Level 08 Hydro-BASINS | Spatial maximum | 1 hour | 09/27 – 10/02/2022 | Hersbach et al., 2020 |
| Sub-basins | HydroBASINS | Level 08 | N/A | N/A | N/A | N/A | Lehner & Grill, 2023 |

## 4.4.1 Sub-basin delineations from HydroBASINS

HydroBASINS, a secondary dataset of the World Wildlife Fund's HydroSHEDS product, provides hierarchical sub-basin boundaries at a global scale (Lehner & Grill, 2013a). For this demonstration, the Level 08 HydroBASINS product is used because it is the finest sub-basin resolution which guarantees at least one unique Earth observation pixel per sub-basin. In total, the study area has 922 sub-basins with a mean area of 748 $km^2$ and a median area of 533 $km^2$. Additional details of HydroBASINS are available in Appendix 4.3 and in 2023 at: https://www.hydrosheds.org/products/hydrobasins..

### 4.4.2 CDC/ASTDR Social Vulnerability Index (SVI)

Social vulnerability data are obtained from the Center for Disease Control and Prevention Agency for Toxic Substances and Disease Registry Social Vulnerability Index (CDC/ASTDR SVI, henceforth referred to as SVI). This dataset provides vulnerability estimates at the United States Census Tract level for select years between 2000 – 2020 (CDC/ATSDR, 2023). The US wide SVI product for 2020 is used to allow for multi-state analyses and since it was the most up-to-date version available at the time of this study.

A summary of sixteen (16) variables contributing to overall SVI calculations is provided in Appendix 4.I. SVI indices range from 0 – 1, with 1 indicating the most vulnerable and 0 indicating the least vulnerable regions. The SVI data and additional details are available at https://www.atsdr.cdc.gov/placeandhealth/svi/index.html as accessed in 2023 and in Appendix 4.2.

### 4.4.3 Precipitation Data from GPM IMERG

Precipitation data are derived from the Integrated Multi-satellitE Retrievals for Global Precipitation Measurement (GPM IMERG) missions which provides up to half-hourly precipitation observations at a spatial resolution of 0.1° (Huffman et al., 2020).

For this study, the GPM IMERG Late Precipitation V06 Half Hour Precipitation dataset from September 27 – October 2, 2022, is used to calculate maximum hourly precipitation (i.e. precipitation intensity) and cumulative precipitation (i.e. precipitation duration). Additional information and the technical documentation for GPM IMERG is available in Appendix 4.3 and in 2023 at: https://gpm.nasa.gov/documents/IMERG-V06-Technical-Documentation.

## 4.4.4 Wind speed data from ECMWF ERA5

Wind speed data were obtained from the Copernicus Climate Change Service (C3S) European Centre for Medium-Range Weather Forecast (ECMWF) Reanalysis Version 5 (ERA5). For this study hourly wind speed data from September 27 – October 2, 2022 are calculated using Eq. 1 where $u$ is the u-component of wind in the longitudinal direction 10 m above the surface of the Earth and $v$ is the v-component of wind in the latitudinal direction 10 m above the surface of the Earth. Both $u$ and $v$ are utilized at hourly temporal resolutions.

$$Wind\ speed = \sqrt{u^2 + v^2} \qquad (1)$$

Additional information and the technical documentation of ERA5 are available in Appendix 4.3 and in 2023 at: https://confluence.ecmwf.int/display/CKB/ERA5%3A+data+documentation.

## 4.4.5 SMAP-Derived 1-km Downscaled Surface Soil Moisture Product

The Soil Moisture Active Passive (SMAP) Derived 1-km Downscaled Surface Soil Moisture Product is used to calculate the 5-day antecedent near-surface soil moisture (0 – 5 cm depth below the surface of the Earth) (Lakshmi & Fang, 2023). For this study, antecedent soil moisture is examined because of fallen tree damage reports during Hurricane Ian attributed to saturated soil, high winds, and widespread flooding (Bucci et al., 2022). The study period of September 23 – 27, 2022 provided five-day antecedent soil moisture data prior to landfall of Hurricane Ian in Florida. This was the shortest antecedent period with sufficient observational coverage since the dataset is limited by cloud cover. The data and additional details on the SMAP-Derived 1-km Downscaled Surface Soil Moisture Product are available in Appendix 4.3 and in 2023 at: https://doi.org/10.5067/U8QZ2AX5V7B.

## 4.5 Methods

This section describes the methodology in several parts as follows: First, all variables are resampled to a sub-basin scale as defined by the Level 08 HydroBASINS dataset. Second, the sub-basins are characterized from highest to lowest order for each variable. Third, the basin order using SVI is defined as the baseline scenario, which represents initial conditions of the study area prior to the hurricane disturbance. Fourth, storm scenarios are defined based on the hydrology and SVI variables. Fifth, a swing-weight technique is used to update factor weights for each scenario. Sixth, risk is calculated for each scenario as the difference in basin order of the baseline scenario versus a given scenario. Seventh, a score of disruptiveness is calculated for each scenario using the normalized sum of squares of differences in order. Further details of each step are provided in the subsequent paragraphs.

Hydrology and social vulnerability variables are first resampled to each sub-basin (defined by the Level 08 HydroBASINS dataset) to allow for comparisons regardless of the native resolution of each dataset. For SVI and five-day antecedent soil moisture (SM), a spatial average is used. For cumulative precipitation (P1), a spatial sum is used. For maximum hourly precipitation (P2) and maximum hourly wind speed (W), a spatial average of maximum observed values is used. Fig. 2 provides spatial plots of the original resampled variables.

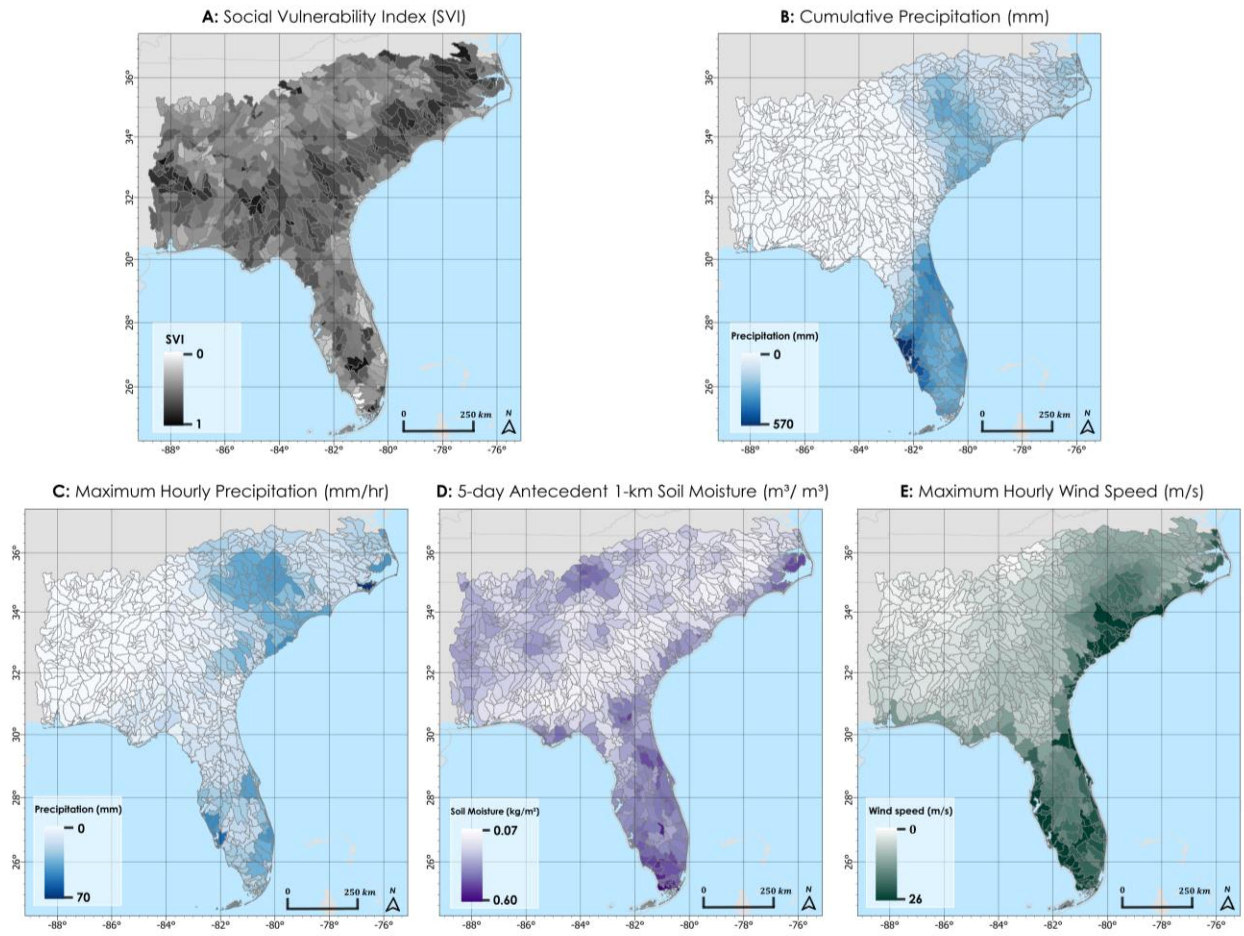

***Fig. 4.2:*** *Spatial maps of the observed social vulnerability and hydrology variables resampled per sub-basin for* ***(A)*** *Social Vulnerability Index,* ***(B)*** *cumulative precipitation,* ***(C)*** *maximum hourly precipitation,* ***(D)*** *five-day antecedent soil moisture, and* ***(E)*** *maximum hourly wind speed.*

The sub-basins are then characterized by ordering from highest to lowest value and assigning an integer value from 1 to the total number of basins using Eq. 2:

$$S_n(b_i) = 100 * \sum_{j=1}^{k} w_j v_{ij} \qquad (2)$$

$$where \left\{w_j \middle| \sum_{j=1}^{k} w_j = 1, 0 \leq w_j \leq 1, j = 1, \ldots, k\right.$$

Here, the basin order for the $i^{th}$ basin ($b_i$) under the $n^{th}$ scenario ($S_n$) is defined as the summation of $j$ to $k$ variables for the $i^{th}$ basin ($v_i$) multiplied by the $j^{th}$ defined weight ($w_j$). For example, the basin with the most observed cumulative precipitation during Hurricane Ian has an order value of 1 whereas the basin with the least observed cumulative precipitation will have an order of 922 (the maximum value of $i$).

Then, the swing-weight technique is used to update factor weights for each of the twenty (20) scenarios for the study. As previously mentioned, the swing-weight technique allows for tradeoffs of higher consideration of one or more variables in exchange for lower consideration of other variables within a scenario. Table 2 summarizes the scenarios and weights for each hydrology and social vulnerability variable. Scenarios using a single variable are S1-S5. Scenarios using a combination of variables (up to five in total) are S6-S20. The *uncertainty* is addressed by the identification of the several scenarios, without assessing probabilities. Subsequently the *risk* is quantified as of the degree of disruption of system order by each of the scenarios (Hassler et al., 2020). Since the motivation of this study is to understand the extent by which hydrological extremes disrupt social vulnerability, S1 is defined as the baseline order as it exclusively uses SVI and is assumed to represent conditions prior to the hurricane disturbance. For S6-S20, a constant SVI weight of 0.5 was used. This ensures a balance between SVI and the hydrological contributions within each new order calculation, as well as equal contributions of SVI across the remaining scenarios.

***Table 4.2:*** *A swing-weight technique is used to update factor weights for each of the twenty (20) scenarios of the contributing hydrology and social vulnerability variables. These include Social Vulnerability Index*

*(SVI), cumulative precipitation (P1), maximum hourly precipitation (P2), maximum hourly wind speed (W), and five-day antecedent soil moisture (SM).*

| **Scenario ($S_n$)** | **Swing Weights ($w_j$) of contributing variables ($v_j$)** | | | | |
|---|---|---|---|---|---|
| | **$v_1$: SVI** | **$v_2$: P1** | **$v_3$: P2** | **$v_4$: W** | **$v_5$: SM** |
| $S_1$: SVI (baseline order) | 1 | 0 | 0 | 0 | 0 |
| $S_2$: Hurricane Ian cumulative precipitation | 0 | 1 | 0 | 0 | 0 |
| $S_3$: Hurricane Ian maximum hourly precipitation | 0 | 0 | 1 | 0 | 0 |
| $S_4$: Hurricane Ian maximum hourly wind speed | 0 | 0 | 0 | 1 | 0 |
| $S_5$: Hurricane Ian 5-day antecedent soil moisture | 0 | 0 | 0 | 0 | 1 |
| $S_6$: SVI and Hurricane Ian cumulative precipitation | 0.5 | 0.5 | 0 | 0 | 0 |
| $S_7$: SVI and Hurricane Ian maximum hourly precipitation | 0.5 | 0 | 0.5 | 0 | 0 |
| $S_8$: SVI and Hurricane Ian maximum hourly wind speed | 0.5 | 0 | 0 | 0.5 | 0 |
| $S_9$: SVI and Hurricane Ian 5-day antecedent soil moisture | 0.5 | 0 | 0 | 0 | 0.5 |
| $S_{10}$: SVI, Hurricane Ian cumulative precipitation and maximum hourly precipitation | 0.5 | 0.25 | 0.25 | 0 | 0 |
| $S_{11}$: SVI, Hurricane Ian cumulative precipitation and maximum hourly windspeed | 0.5 | 0.25 | 0 | 0.25 | 0 |
| $S_{12}$: SVI, Hurricane Ian cumulative precipitation and 5-day antecedent soil moisture | 0.5 | 0.25 | 0 | 0 | 0.25 |
| $S_{13}$: SVI, Hurricane Ian maximum hourly precipitation and maximum hourly wind speed | 0.5 | 0 | 0.25 | 0.25 | 0 |
| $S_{14}$: SVI, Hurricane Ian maximum hourly precipitation and 5-day antecedent soil moisture | 0.5 | 0 | 0.25 | 0 | 0.25 |
| $S_{15}$: SVI, Hurricane Ian maximum hourly wind speed and 5-day antecedent soil moisture | 0.5 | 0 | 0 | 0.25 | 0.25 |
| $S_{16}$: SVI, Hurricane Ian cumulative precipitation, maximum hourly precipitation, and maximum hourly wind speed | 0.5 | 0.167 | 0.167 | 0.167 | 0 |
| $S_{17}$: SVI, Hurricane Ian cumulative precipitation, maximum hourly precipitation, and 5-day antecedent soil moisture | 0.5 | 0.167 | 0.167 | 0 | 0.167 |
| $S_{18}$: SVI, Hurricane Ian cumulative precipitation, maximum hourly wind speed, and 5-day antecedent soil moisture | 0.5 | 0.167 | 0 | 0.167 | 0.167 |
| $S_{19}$: SVI, Hurricane Ian maximum hourly precipitation, maximum hourly wind speed, and 5-day antecedent soil moisture | 0.5 | 0 | 0.167 | 0.167 | 0.167 |
| $S_{20}$: SVI, Hurricane Ian cumulative precipitation, maximum hourly precipitation, maximum hourly wind speed, and 5-day antecedent soil moisture | 0.5 | 0.125 | 0.125 | 0.125 | 0.125 |

For each scenario, we define risk $(R)$ as the difference between the baseline order and scenario order for a given basin using Eq. 3:

$$R_n(b_i) = B(b_i) - S_n(b_i) \qquad (3)$$

In Eq. 3, risk of a given scenario and basin $R_n(b_i)$ equals the difference between the baseline order of the basin $B(b_i)$ and the scenario order of the basin $S_n(b_i)$. A positive value for $R$ indicates the basin increased in order due to the disruption. A negative $R$ indicates the basin decreased in order following the disruption. For the demonstration of Hurricane Ian, a positive value for $R$ would occur for a basin with low SVI and high hydrological exposure. A negative value for $R$ would occur for a basin with high SVI and low hydrological exposure. A near-zero $R$ would occur for a basin either with high SVI and high hydrological exposure or a basin with low SVI and low hydrological exposure. Spatial plots of scenario basin orderings $S_n(b_i)$ and risk $R_n(b_i)$ are used to examine spatial patterns of social vulnerability and hydrology across the study area.

Lastly, the most and least disruptive scenarios were determined using the normalized sum of squares of differences in order, as in Eq. 4 and Eq. 5:

$$x(S_n) = \sum_{i}^{N} \big(B(b_i) - D(b_i)\big)^2 = \sum_{i}^{N} R(b_i)^2 \qquad (4)$$

$$X(S_n) = \frac{x(S_n) - x(S)_{min.}}{x(S)_{max.} - x(S)_{min.}} \qquad (5)$$

In Eq. 4, $x(S_n)$ represents the score of disruptiveness for a given scenario $(S_n)$ as the sum over the basins of the squared differences of the baseline order and disrupted order. This calculation quantifies risk as an influence of each scenario to the system order (Bonato et al., 2022; Karvetski et al., 2009; You et al., 2014a). The normalized score of disruptiveness ($X(S_n)$) is calculated (Eq. 5) as the score of disruptiveness for a given scenario $x(S_n)$ minus the minimum score of disruptiveness ($x(S)_{min.}$) divided by the maximum score of disruptiveness ($x(S)_{max.}$) minus the minimum score of disruptiveness ($x(S)_{min.}$). The least disruptive scenario had the lowest normalized score of disruptiveness. The most disruptive scenario had the highest normalized score of disruptiveness.

## 4.6 Sample of Results

The results and discussion are organized into the following sub-sections: 1) single variable basin order results, 2) scenario results, 3) basin ordering for select scenarios, and 4) basin risk for select scenarios. For each of the variables and scenarios, lower order/percentiles indicate greater concern and thus might be prioritized for near-term disaster recovery, response, and future mitigation efforts.

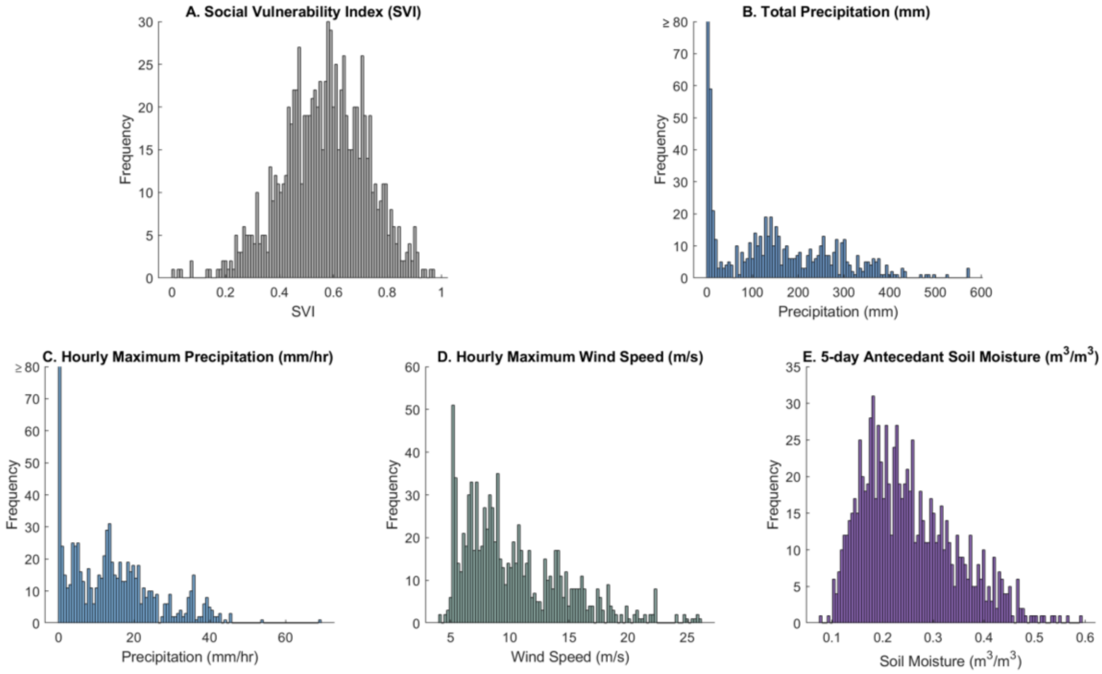

***Fig. 4.3:*** *Histograms of the observed social vulnerability and hydrology variables resampled per sub-basin in the area of demonstration for* ***(A)*** *Social Vulnerability Index (SVI),* ***(B)*** *total precipitation,* ***(C)*** *hourly maximum precipitation,* ***(D)*** *hourly maximum wind speed, and* ***(E)*** *five-day antecedent soil moisture.*

## 4.6.1 Single variable basin order results

### 4.6.1.1 Social Vulnerability Index (SVI) order

As previously discussed, the SVI order shown in Fig. 4.4A was defined as the baseline order for this study. Even though SVI is based on a national scale, a wide distribution of SVI was observed in the study area with a minimum of 0.005, maximum of 0.974, mean of 0.548, and median of 0.576 (Fig. 4.3A). The spatial plot of SVI order in Fig. 4.3A shows that the lowest order SVI basins are concentrated in the southeastern portions of Alabama, Georgia, South Carolina, and North Carolina.

Coastal basins tended to have higher order compared to adjacent inland basins. This indicates inland basins have populations with more social vulnerability than coastal basins. This is particularly apparent in Florida and may be explained by recent trends of increased demand for 'coastal lifestyle housing' observed by Florida real estate agents (Palm & Bolsen, 2023).

### 4.6.1.2 Precipitation (P1 and P2) orders

Precipitation is separately analyzed as cumulative precipitation (*mm*, P1) and maximum hourly precipitation rate (*mm/hr*, P2) to account for both precipitation intensity and duration.

Fig. 4.3B shows a histogram of total precipitation within the study area. Fig. 4.3B shows the spatial distribution of basin ordering based on cumulative precipitation. While little to no precipitation is observed in the western portion of the study area, basins located within the path of Hurricane Ian were exposed to extreme precipitation amounts of up to 500 *mm* within the six-day period. The mean and median cumulative precipitation are respectively 31 *mm* and 104 *mm*. The highest prioritization of basins follows the path of Hurricane Ian over Central Florida and South Carolina.  Cumulative precipitation order is higher in Florida than in the Carolinas. This is likely due to the duration of the hurricane's presence over Florida because the system was relatively slow-moving and took approximately 16 hours for the eyewall to pass from Florida's Gulf Coast to Atlantic Coast (Bucci et al., 2022). In the Carolinas, it took approximately 6 hours for the system to transition to an extratropical cyclone after making landfall (Bucci et al., 2022).

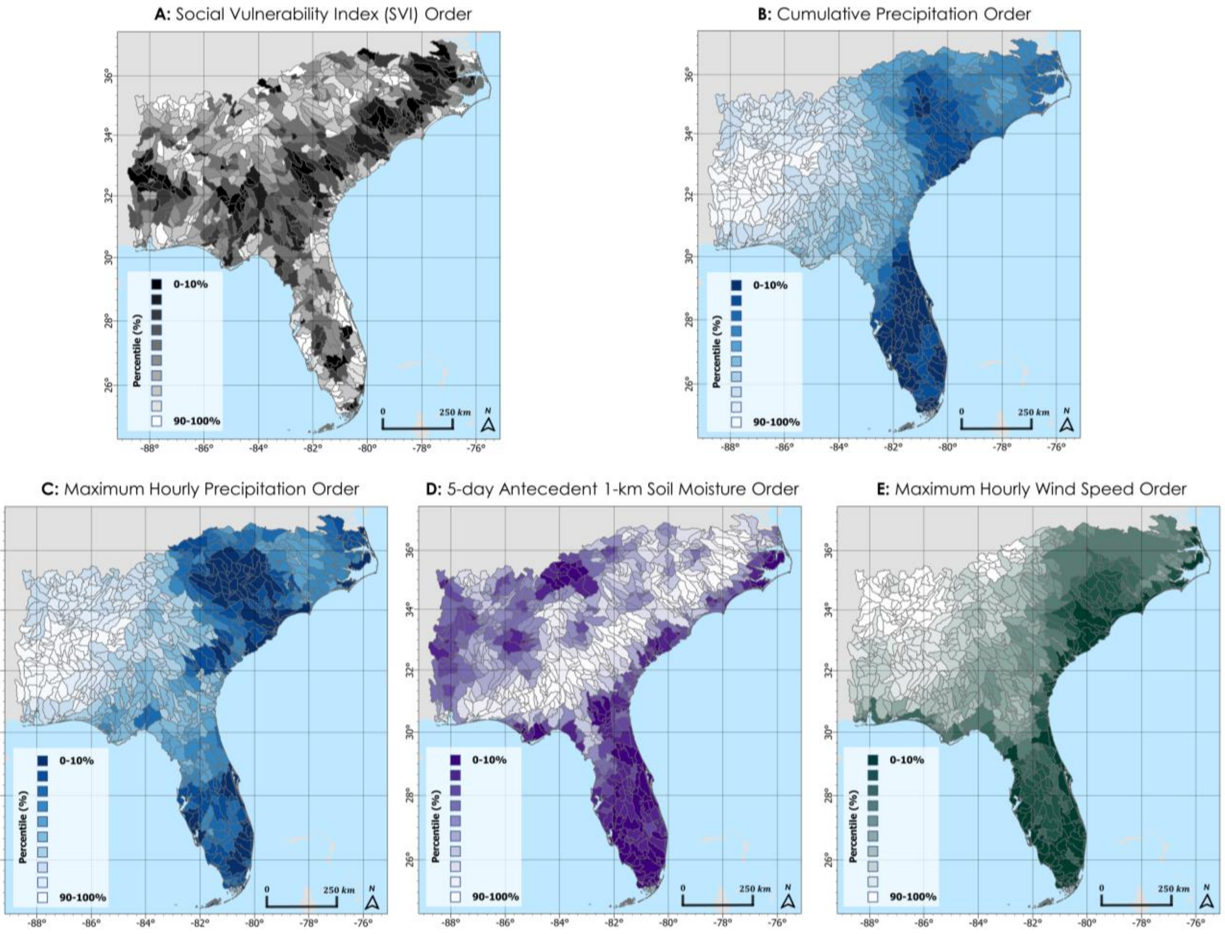

***Fig. 4.4:*** *Maps of the ordered percentiles within the area of demonstration at the sub-basin level for the following social vulnerability and hydrology variables:* ***(A)*** *Social Vulnerability Index (SVI),* ***(B)*** *cumulative precipitation,* ***(C)*** *maximum hourly precipitation,* ***(D)*** *five-day antecedent 1-km soil moisture, and* ***(E)*** *maximum hourly wind speed.*

Hourly maximum precipitation (P2) exhibited a similar distribution as the cumulative precipitation, particularly with western basins of the study period observing little to no precipitation rates (Fig. 4.3C). A wide distribution of precipitation rates was observed with a maximum of 69 *mm/hr*, mean of 12 *mm/hr*, and median of 10.6 *mm/hr* (Fig. 4.3C). The spatial order plot of maximum hourly precipitation showed the highest prioritization of basins in the Carolinas, followed by Florida (Fig. 4.4C). This indicates that the Carolinas were exposed to more intense rainfall than Florida, despite the greater cumulative precipitation observed in Florida.

#### 4.6.1.3 Wind speed (W) order

The distribution of maximum hourly wind speed in Fig. 4.3D shows the study area was exposed to varying wind speeds from a minimum of 4.2 *m/s* to a maximum of 26.1 *m/s*. The median and mean wind speeds are respectively 9.0 *m/s* and 10.3 *m/s*. In the spatial order plot of maximum hourly wind speed shown in Fig. 4.4E, coastal basins tend to be higher priority than inland basins. This is expected because of coastal convection processes. However, the inland basins of Florida and the Carolinas tended to exhibit higher prioritization over other basins outside of the path of Hurricane Ian.

#### 4.6.1.4 Soil Moisture (SM) order

Fig. 4.3E shows the distribution of 5-day antecedent soil moisture which had a minimum of 0.8 $m^3/m^3$, a maximum of 0.59 $m^3/m^3$, a mean of 0.25 $m^3/m^3$, and a median of 0.24 $m^3/m^3$. In this study, higher soil moisture is prioritized because soil with a high degree of water saturation has less pore space readily available to store additional water. When exposed to extreme precipitation events, the decreased pore capacity to store water can result in flooding because the volumetric water content of the soil increases to its porosity, rendering it saturated.

The spatial plot of ordered 5-day antecedent soil moisture shown in Fig. 4.4D reveals that the highest priority soil moisture values are observed in Florida and coastal basins. Notably, the lowest soil moisture values are opposite to the spatial distribution of SVI order; basins of high SVI tend to be co-located with basins of low soil moisture in the non-coastal basins of southern Alabama, Georgia, South Carolina, and North Carolina. Future research should be dedicated to comparing the spatial and temporal distributions of SVI and soil moisture using a longer study period and national scale. This would improve understanding of if the inverse relationship of SVI and soil moisture observed in this study are correlated or coincidental.

### 4.6.2 Scenario results

To further investigate basin sensitivity to each scenario, the average order of the top 10% of basins (92) from $S_{20}$ are plotted across all scenarios ($S_1$ - $S_{20}$) in Fig. 5. When only one variable was used to define a scenario ($S_1$ – $S_5$), a wide distribution of average orders was observed. As more variables contributed to a given scenario (three variables for $S_{10}$ – $S_{15}$, four variables for $S_{16}$ – $S_{19}$, and five variables for $S_{20}$), the overall average basin orders stabilized and exhibited less variability of order compared to scenarios with one to two variables.

Notable peaks in order occurred during $S_5$ and $S_9$, both of which relied on the five-day antecedent soil moisture data for ordering. This indicates the soil moisture data contributes different ordering priorities compared to the other variables, likely because it was the only hydrology variable observed prior to the hurricane event. However, when two or more variables contribute to a scenario in combination with the five-day antecedent soil moisture data, the peaks are not pronounced. Thus, incorporating multiple hydrology variables into a given scenario is important to reduce basin sensitivity to an individual variable and to improve representation of exposure to the extreme hydrological event.

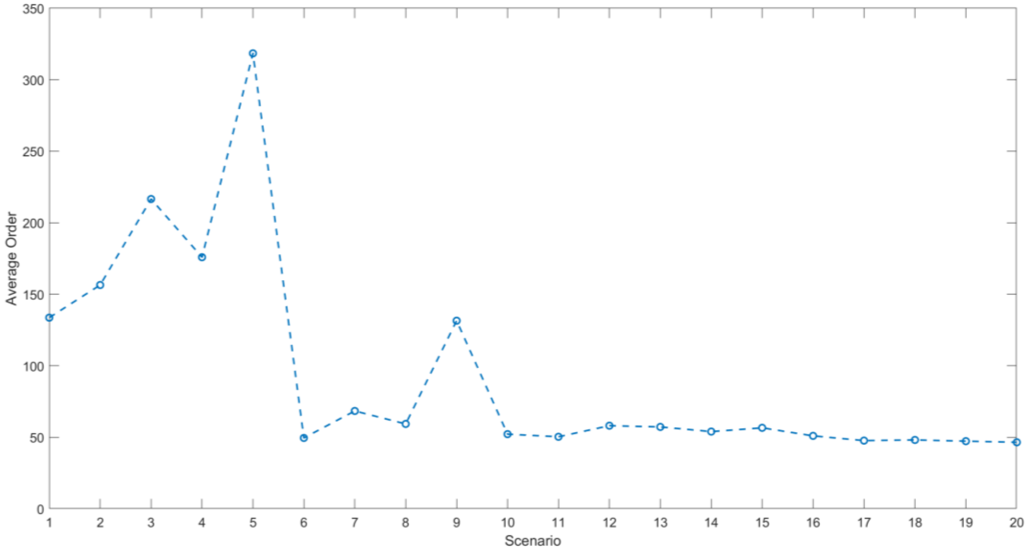

***Fig. 4.5:*** *Average order of the top 10% of basins from Scenario $S_{20}$ across all scenarios ($S_1$ – $S_{20}$). The overall ordering stabilizes as more hydrology and social vulnerability variables contribute to a given scenario.*

Fig. 4.6 shows a bar graph of the normalized score of disruptiveness for each scenario which was calculated using Eq. 4 – 5. The most disruptive scenarios were $S_5$ (Hurricane Ian five-day antecedent soil moisture), $S_3$ (Hurricane Ian maximum hourly precipitation), and $S_2$ (Hurricane Ian cumulative precipitation) because they exhibited the highest normalized scores of disruptiveness. Each of these scenarios had only one contributing variable with different spatial orderings compared to the baseline order, resulting in the highest disruption. The least disruptive scenarios, exhibiting the lowest normalized scores of disruptiveness, were $S_{19}$ (SVI, Hurricane Ian maximum hourly precipitation, maximum hourly wind speed, and five-day antecedent soil moisture) and $S_{14}$ (SVI, Hurricane Ian maximum hourly precipitation and five-day antecedent soil moisture). These scenarios accounted for three and four hydrology and social vulnerability factors, resulting in basin ordering that were least different from the baseline order compared to the other scenarios.

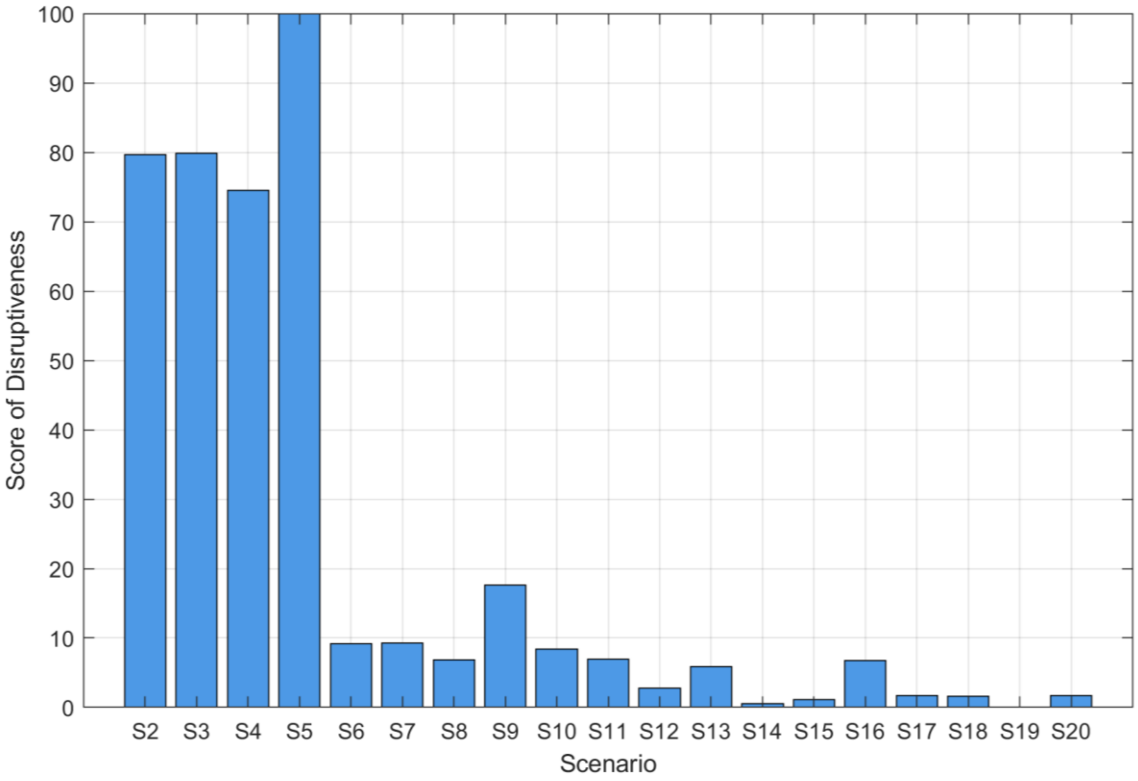

***Fig. 4.6:*** *Normalized score of disruptiveness for scenarios ($S_2 – S_{20}$) to determine the most and least disruptive scenarios compared to the baseline SVI order ($S_1$).*

Table 4.3 describes the disruption of order of basins across scenarios compared to the baseline order, using 10% increments of disruption. Similar to Fig. 4.5 and Fig. 4.6, the most disruptive scenarios are $S_2$, $S_3$, $S_4$, and $S_5$ since each hydrology variable individually orders the basins dissimilarly to SVI. Scenario $S_5$ has the fewest number of basins in the 0 – 10% disruption category indicating that antecedent soil moisture ordering differed the greatest from the SVI order. As previously noted, this disruption may indicate that low soil moisture corresponds to regions of high social vulnerability but would require additional research to confirm whether this is correlated or coincidental.

***Table 4.3:*** *Summary of the number of basins within 10% increments of disruption across scenarios* $S_2$ *–* $S_{20}$ *compared to the baseline order (*$S_1$*).*

| **Scenario ($S_n$)** | **Number of basins within a percentage of disruption (%) compared to $S_1$** | | | | | | | | | |
|---|---|---|---|---|---|---|---|---|---|---|
| | **0 – 10%** | **10 – 20%** | **20 – 30%** | **30 – 40%** | **40 – 50%** | **50 – 60%** | **60 – 70%** | **70 – 80%** | **80 – 90%** | **90 – 100%** |
| $S_2$ | 196 | 176 | 127 | 101 | 107 | 70 | 53 | 39 | 33 | 20 |
| $S_3$ | 196 | 169 | 128 | 111 | 97 | 80 | 49 | 39 | 34 | 19 |
| $S_4$ | 210 | 178 | 122 | 109 | 109 | 63 | 52 | 31 | 29 | 19 |
| $S_5$ | 166 | 130 | 115 | 118 | 113 | 92 | 75 | 53 | 42 | 18 |
| $S_6$ | 308 | 269 | 167 | 94 | 84 | 0 | 0 | 0 | 0 | 0 |
| $S_7$ | 300 | 274 | 165 | 110 | 70 | 3 | 0 | 0 | 0 | 0 |
| $S_8$ | 322 | 262 | 173 | 104 | 59 | 2 | 0 | 0 | 0 | 0 |
| $S_9$ | 263 | 217 | 182 | 144 | 104 | 12 | 0 | 0 | 0 | 0 |
| $S_{10}$ | 289 | 297 | 154 | 117 | 65 | 0 | 0 | 0 | 0 | 0 |
| $S_{11}$ | 326 | 249 | 166 | 126 | 55 | 0 | 0 | 0 | 0 | 0 |
| $S_{12}$ | 368 | 269 | 164 | 69 | 51 | 1 | 0 | 0 | 0 | 0 |
| $S_{13}$ | 327 | 254 | 181 | 117 | 43 | 0 | 0 | 0 | 0 | 0 |
| $S_{14}$ | 371 | 271 | 180 | 71 | 29 | 0 | 0 | 0 | 0 | 0 |
| $S_{15}$ | 387 | 259 | 168 | 69 | 38 | 1 | 0 | 0 | 0 | 0 |
| $S_{16}$ | 312 | 271 | 174 | 108 | 57 | 0 | 0 | 0 | 0 | 0 |
| $S_{17}$ | 320 | 308 | 186 | 80 | 28 | 0 | 0 | 0 | 0 | 0 |
| $S_{18}$ | 348 | 294 | 176 | 66 | 38 | 0 | 0 | 0 | 0 | 0 |
| $S_{19}$ | 343 | 310 | 179 | 61 | 29 | 0 | 0 | 0 | 0 | 0 |
| $S_{20}$ | 335 | 274 | 203 | 80 | 30 | 0 | 0 | 0 | 0 | 0 |

Across all scenarios, disruptions of basin order are at least 50% (Table 4.3). Scenarios $S_{19}$ and $S_{14}$ were previously identified as the least disruptive scenarios (Fig. 4.6) with no basin disruptions greater than 50% (Table 4.3). For $S_{19}$, 37% of the study area (343 basins) had 0 – 10% disruption, 33% (310 basins) had 10 – 20% disruption, 19% (179 basins) had 20 – 30% disruption, 6% (61 basins) had 30 – 40% disruption, and 3% (29 basins) had 40 – 50% disruption. For $S_{14}$, 40% of the study area (371 basins) had 0 – 10% disruption, 29% (271 basins) had 10 – 20% disruption, 20% (180 basins) had 20 – 30% disruption, 8% (71 basins) had 30 – 40% disruption, and 3% (29 basins) had 40 – 50% disruption.

## 4.6.3 Basin ordering for select scenarios

Spatial plots of the basin ordering are provided in Fig. 4.7 to investigate spatial patterns of the following three selected scenarios: 1) the most disruptive scenario which includes both social vulnerability and hydrology ($S_9$), 2) the most disruptive scenario which includes social vulnerability and three or more hydrology variables ($S_{16}$), and 3) the least disruptive scenario ($S_{19}$). Even though each scenario has a unique basin ordering spatial map, these three selected scenarios ($S_9$, $S_{16}$, $S_{19}$) adequately represent the range of basin orders and risk across the scenarios and thus are provided in this manuscript.

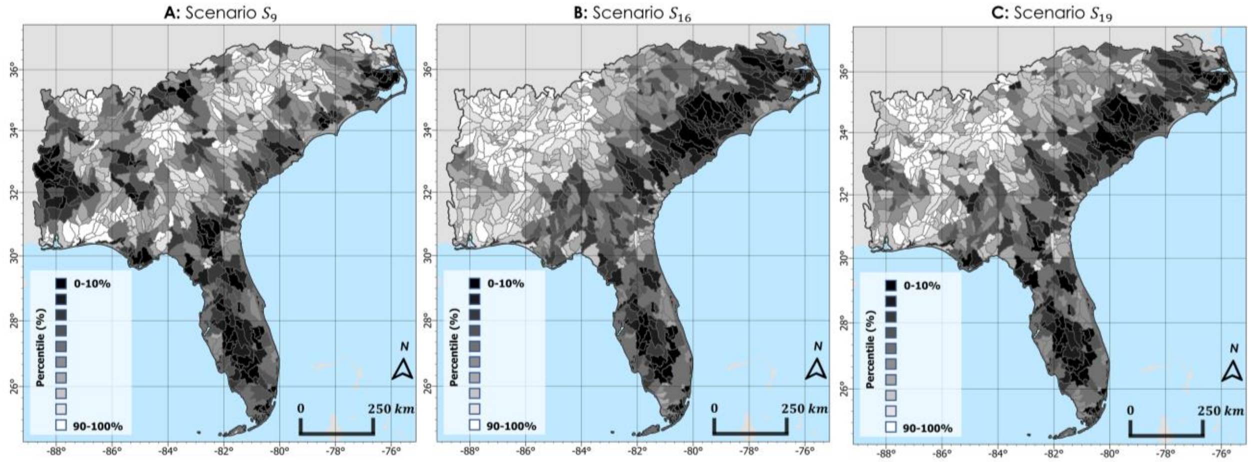

***Fig. 4.7:*** *Spatial plot of the basin ordering for the following scenarios:* ***(A)*** *$S_9$ – SVI and Hurricane Ian 5-day antecedent soil moisture,* ***(B)*** *$S_{16}$ – SVI, Hurricane Ian maximum cumulative precipitation, maximum hourly precipitation, and maximum hourly wind speed, and* ***(C)*** *$S_{19}$ – SVI, Hurricane Ian maximum hourly precipitation, maximum hourly wind speed, and 5-day antecedent soil moisture.*

Fig. 4.7A shows the basin ordering of the most disruptive scenario, $S_9$, which was defined as equal contributions of SVI and 5-day antecedent soil moisture. Basins of the lowest order are found in western Alabama and inland Florida because they had both high soil moisture and social vulnerability.

For scenarios $S_{16}$ (Fig. 4.7B) and $S_{19}$ Fig. 4.7C), the lowest order basins were found in Central Florida and the southeastern portions of the Carolinas. This is consistent with the first landfall of Hurricane Ian in Florida and its second landfall in South Carolina. Conversely, the highest order basins occurred safely beyond the path of Hurricane Ian in Alabama, northern Georgia, and the northwestern portions of the Carolinas.

Surprisingly, coastal basins within the path of Hurricane Ian exhibited higher order than their adjacent inland basins, even though the single variable basin ordering (Fig. 4.4) reveals that coastal basins tend to exhibit the lowest order. Thus, this pattern is due to SVI which is the only variable to prioritize inland basins more than coastal basins.

Table 4.4 shows the top-20 basins (2%) of prioritization based on the basin ordering of scenario $S_{16}$. A reference map of the basin locations is shown in Fig. 4.9A. This serves as a conservative estimate of which basins should be prioritized because it had the lowest score of disruptiveness. Basins in Florida, South Carolina, and North Carolina are all represented in the top 2% of prioritization. Moreover 20% (4) were coastal basins and 80% (16) were inland. The baseline orders of these basins are within the top 16% of the overall SVI order of the study area. Since these basins ordered in the top 2% of the $S_{16}$ order, it indicates they were also exposed to extreme hydrological conditions due to Hurricane Ian.

***Table 4.4:*** *Summary of top-20 basins (2% of the study area) which prioritized highest in the disrupted order (D) for scenario $S_{16}$. The HydroBASINS Level-08 basin name, state, basin type (coastal or inland), and baseline order ($S_1$) are provided. A reference map of the basin locations is available in Fig. 9A.*

| **$S_{16}$ Order** | **Basin Name ($b_i$)** | **State** | **Basin Type** | **Baseline Order ($S_1$)** |
|---|---|---|---|---|
| 1 | 7080044390 | FL | Coastal | 10 |
| 2 | 7080044450 | FL | Coastal | 1 |
| 3 | 7080789240 | FL | Inland | 4 |
| 4 | 7080696960 | SC | Inland | 45 |
| 5 | 7080791760 | FL | Inland | 2 |
| 6 | 7080791840 | FL | Inland | 20 |
| 7 | 7080684980 | SC | Inland | 35 |
| 8 | 7080791630 | FL | Inland | 11 |
| 9 | 7080684850 | SC | Inland | 73 |
| 10 | 7080691080 | SC | Inland | 25 |
| 11 | 7080791790 | FL | Inland | 6 |
| 12 | 7080676370 | SC/NC | Inland | 36 |
| 13 | 7080667100 | SC/NC | Inland | 97 |
| 14 | 7080677550 | SC/NC | Inland | 69 |
| 15 | 7080043160 | SC | Coastal | 135 |
| 16 | 7080675620 | SC | Inland | 98 |
| 17 | 7080684690 | SC | Inland | 96 |
| 18 | 7080690650 | SC | Inland | 39 |
| 19 | 7080043100 | SC | Coastal | 147 |
| 20 | 7080675700 | SC | Inland | 142 |

## 4.6.4 Risk as the Disruption of Basin Order

Figure 4.8 provides a map of the risk basin order results (calculated using Eq. 3) for the three scenarios previously examined in section 5.3: $S_9$, $S_{16}$, and $S_{19}$. It is important to note that if a basin experienced high order in both the baseline map and the disrupted order map, it is reflected as low risk in Fig. 4.8; the order did not significantly change. The greatest increases in order are found in basins with low social vulnerability but high hydrological exposure. Conversely, the greatest decreases in order are found in basins with high social vulnerability but low hydrological exposure. Thus, this tool is intended to be used in conjunction with the disrupted basin order map

(Fig. 4.7) to identify basins which were disrupted due to exposure to the extreme hydrological conditions.

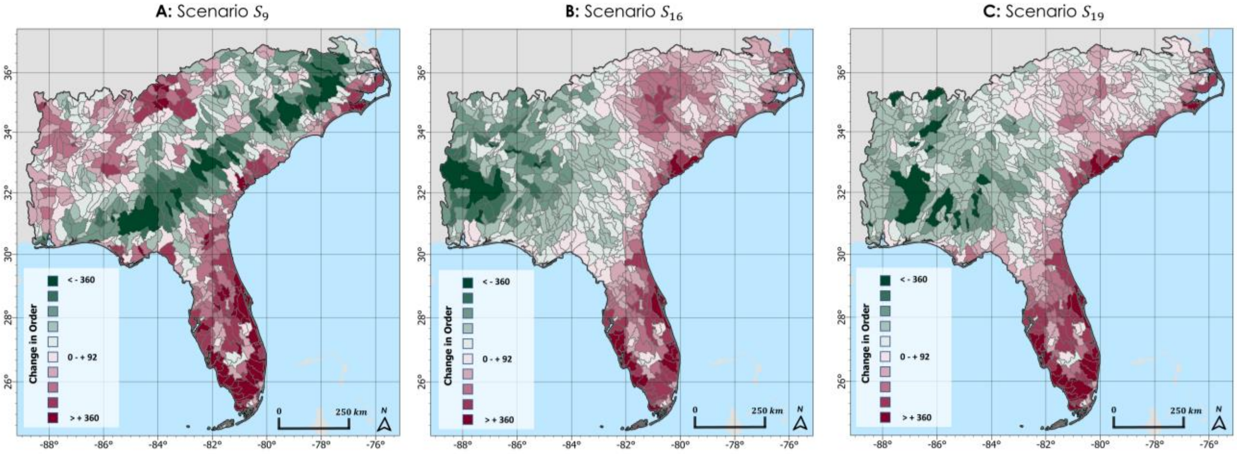

***Fig. 4.8:*** *Spatial plot of the basin risk for the following scenarios:* ***(A)*** $S_9$ *– SVI and Hurricane Ian 5-day antecedent soil moisture,* ***(B)*** $S_{16}$ *– SVI, Hurricane Ian maximum cumulative precipitation, maximum hourly precipitation, and maximum hourly wind speed, and* ***(C)*** $S_{19}$ *– SVI, Hurricane Ian maximum hourly precipitation, maximum hourly wind speed, and 5-day antecedent soil moisture. Basins which increased in order are depicted in red. Basins which decreased in order are depicted in green.*

In Fig. 4.8A, the risk map of scenario $S_9$ had approximately 466 basins (51%) experience an increase in order and thus positive risk (depicted in red). Conversely, 454 basins (49%) decrease in order (depicted in green). Only 2 basins (less than 1%) have no change in order. This indicates that few basins have both low social vulnerability and low soil moisture conditions.

Similar to the disrupted basin order maps shown in Fig. 4.7, the risk basin maps are consistent with the path of Hurricane Ian in Fig. 4.8B and Fig. 4.8C. The highest risk basins are found in the Carolinas while the lowest risk basins are found in Alabama and Georgia. For scenario $S_{16}$ (Fig. 4.7B), 458 basins (~50%) increase in order while 462 (~50%) decrease in order. Few basins had no change in order (2 basins, less than 1%). 312 basins (33%) have less than a 10% increase or decrease in order. In scenario $S_{19}$ (Fig. 8C), approximately 422 basins (45%) increase in priority and 496 basins (54%) decrease in priority. Only 4 basins (less than 1%) have no change in order. However, 343 basins (37%) experience less than 10% increase or decrease in order.

The largest increase in prioritization for the top 10 basins (1%) occurs under scenarios of only one hydrological variable ($S_2$, $S_3$, $S_4$, $S_5$), with the majority occurring during $S_5$ (Table 4.5A). The minimum order under these scenarios are all within the top 2%, indicating these basins had high hydrological exposure. However, the social vulnerability of these basins are within the bottom 95-100% of the baseline order (i.e., low social vulnerability). The reference map in Fig. 4.9B shows that these basins correspond to areas of protected national parks, national and state preserves, and wildlife management areas and have low populations. Thus, these basins experience large increases in prioritization since their baseline order was low (SVI) but their exposure to hydrological conditions during Hurricane Ian was high.

Similarly, the largest decrease in prioritization for the top 10 basins (1%) occurs under scenarios of only one hydrological variable ($S_2$, $S_4$, and $S_5$), with the majority occurring during $S_2$ (Table 4.5B). The baseline order of all 10 basins are within the top 9% of the baseline order. This indicates these basins are among the most socially vulnerable in the study area. However, the scenario results indicate how these regions had low exposure to hydrological extremes. The reference map shown in Fig. 4.9C shows the basins were located outside of the hurricane path. For the two basins located within the path of Hurricane Ian in the Carolinas, the $S_5$ scenario was responsible for the highest order, indicating that these basins had very low antecedent soil moisture conditions.

***Table 4.5:*** *Summary of top 10 basins (1%) with* ***(A)*** *largest increase and* ***(B)*** *largest decrease in priority across scenarios compared to the baseline order ($S_1$). The rank of largest increase/decrease in priority, HydroBASINS Level-08 basin name, increase/decrease in prioritization percentage, baseline order ($S_1$), scenario of minimum order, and minimum order are provided for each basin. Reference maps for Table 5A and 5B are respectively shown in Fig. 9B and 9C.*

***(5A)*** *Top 10 basins (1%) with largest increase in priority across scenarios compared to the baseline order ($S_1$). See Fig. 9B for a reference map of basins.*

| **Rank of largest increase in priority** | **Basin Name ($b_i$)** | **Increase in prioritization (%)** | **Baseline Order ($S_1$)** | **Scenario of Minimum Order ($S_n$)** | **Minimum Order** |
|---|---|---|---|---|---|
| 1 | 7080044540 | 99.35 | 921 | 5 | 5 |
| 2 | 7080044200 | 98.16 | 912 | 3 | 7 |
| 3 | 7080044210 | 98.05 | 913 | 2 | 9 |
| 4 | 7080044520 | 97.94 | 922 | 5 | 19 |
| 5 | 7080044600 | 97.94 | 920 | 5 | 17 |
| 6 | 7080044460 | 97.61 | 901 | 5 | 1 |
| 7 | 7080044610 | 97.51 | 906 | 4 | 7 |
| 8 | 7080044910 | 96.96 | 896 | 2 | 2 |
| 9 | 7080796400 | 95.88 | 893 | 5 | 9 |
| 10 | 7080042770 | 95.01 | 877 | 3 | 1 |

***(5B)*** *Top 10 basins (1%) with largest decrease in priority across scenarios compared to the baseline order ($S_1$). See Fig. 9C for a reference map of basins.*

| **Rank of largest decrease in priority** | **Basin Name ($b_i$)** | **Decrease in prioritization (%)** | **Baseline Order ($S_1$)** | **Scenario of Maximum Order ($S_n$)** | **Maximum Order** |
|---|---|---|---|---|---|
| 1 | 7080649710 | -97.40 | 23 | 4 | 921 |
| 2 | 7080719300 | -95.23 | 18 | 2 | 896 |
| 3 | 7080719830 | -94.47 | 26 | 2 | 897 |
| 4 | 7080659420 | -93.49 | 33 | 5 | 895 |
| 5 | 7080676370 | -93.49 | 36 | 5 | 898 |
| 6 | 7080719170 | -93.28 | 34 | 2 | 894 |
| 7 | 7080715300 | -93.17 | 14 | 5 | 873 |
| 8 | 7080705670 | -91.97 | 17 | 2 | 865 |
| 9 | 7080703900 | -91.87 | 8 | 2 | 855 |
| 10 | 7080743880 | -90.67 | 85 | 5 | 921 |

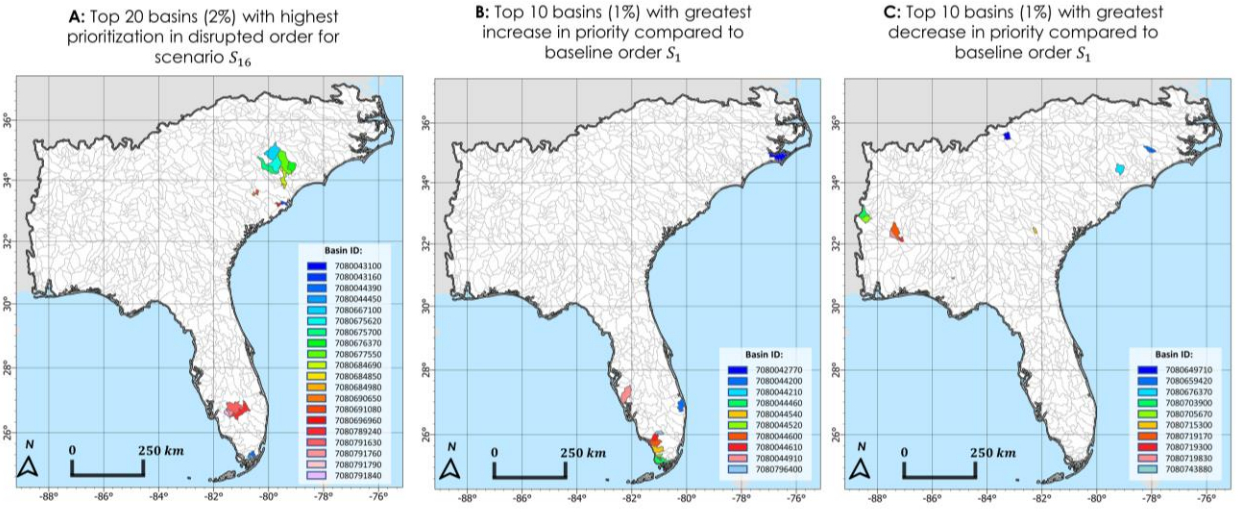

***Fig. 4.9:*** *Reference maps for the following:* ***(A)*** *Top 20 basins (2%) with highest prioritization in the disrupted order for scenario $S_{16}$. A table summary of these basins can be found in Table 4.* ***(B)*** *Top 10 basins (1%) with greatest increase in priority across any scenario compared to the baseline order $S_1$. A table summary of these basins can be found in Table 5A.* ***(C)*** *Top 10 basins (1%) with greatest decrease in priority across any scenario compared to the baseline order $S_1$. A table summary of these basins can be found in Table 5B.*

## 4.7 Discussion

### 4.7.1 Machine Learning for Basin-Level Risk Assessment

One might consider machine learning, a subset of artificial intelligence, in the theory part of this paper. Machine learning has emerged as a technology to support disaster management given its ability to efficiently process large volumes of data (Reda Taha et al., 2021; Sreelakshmi & Vinod Chandra, 2022). This is valuable for supporting disaster predictions, early warnings, response, and recovery efforts (Sreelakshmi & Vinod Chandra, 2022).

Theoretically, basin-level risk management could work in partnership with machine learning by using the methodology of this study as a foundational framework. One opportunity for future work is using machine learning to increase the number of factors and complexities of scenarios. However, it is important to ensure any additional data input into the model are derived from reliable, accurate, and spatially complete data (Sreelakshmi & Vinod Chandra, 2022). Human supervision may be necessary to avoid unintended algorithm bias, discrimination, and unfairness (Köchling & Wehner, 2020).

### 4.7.2 Validation

*Validation* of the new approach of this paper has the following considerations. The quantification of risk as a disruption of system order (following Hassler et al., 2020) is an artifact of an importance model that is grounded in part in the social sciences (social vulnerability) and in part in the physical sciences; the disruption of basin order is not a quantity that is observable either in a storm instance or as a frequency over time. It is useful rather for an integrated comparison of hurricane scenarios and for the allocation of resources to basins in anticipation of hurricane scenarios.

## 4.8 Conclusions

This study developed a methodology to quantify risk as the disruption of basin order by combining social and hydrology factors derived from disparate sources. A swing-weight technique was used to update factor weights of scenarios. This is advantageous for risk analysis using multidisciplinary factors because the relative importance of one variable over another is uncertain. Spatial plots at a sub-basin scale of the most and least disruptive scenarios (defined by sum of squares of differences in order) and risk (calculated as the difference in baseline and scenario order) showed geographic distribution of basin priority. Stakeholders may use the results as a tool for allocating resources at a basin level to decrease risk and increase resilience.

An application to Hurricane Ian was demonstrated using publicly available data derived from census, models, and Earth observations. A qualitative summary of key findings is provided in Table 4.6. Scenarios of only hydrology factors identified coastal basins as high-risk areas. However, scenarios of both social vulnerability and hydrology factors identified inland basins as higher risk than coastal basins. Basins of except to these patterns included protected wildlife management areas within the hurricane path (basins of greatest increase in priority) and basins of high social vulnerability outside the hurricane path (basins of greatest decrease in priority).

***Table 4.6:*** *Summary of qualitative results of this study including descriptions and figures/tables to references within the manuscript.*

| **Types of Results** | **Specific Results** | **Comments** | **Sources** |
|---|---|---|---|
| Most disruptive scenarios | $S_5$ – *Hurricane Ian 5-day antecedent soil moisture,*<br>$S_3$ – *Hurricane Ian maximum hourly precipitation,*<br>$S_2$ – *Hurricane Ian cumulative precipitation* | Scenarios of only one contributing variable exhibited the disruptive spatial patterns, relative to the baseline order ($S_1$). | Fig. 4.6<br>Table 4.3 |
| Least disruptive scenarios | $S_{19}$ – *SVI, Hurricane Ian maximum hourly precipitation, maximum hourly wind speed, and 5-day antecedent soil moisture*<br>$S_{18}$ – *SVI, Hurricane Ian cumulative precipitation, maximum hourly wind speed, and 5-day antecedent soil moisture* | Scenarios of four hydrology and social variables resulted in spatial patterns that were least disruptive to the baseline order ($S_1$). | Fig. 4.6<br>Table 4.3 |
| Highest priority basins in disrupted orders | Inland basins of Florida and South Carolina followed by coastal basins of Florida, South Carolina, and North Carolina | Basins of high social vulnerability located within the hurricane path were exposed to the most extreme hydrological conditions and may be | Figure 4.7<br>Table 4.4<br>Figure 4.9A |

| | | | |
|---|---|---|---|
| | | prioritized for near-term recovery, response, and future mitigation efforts. | |
| Lowest priority basins in disrupted orders | Alabama and North Georgia basins | Basins of low social vulnerability located outside the hurricane path had low priority. | Figure 4.7<br>Figure 4.8 |
| Greatest increase in basin priority | Coastal basins of Florida | These basins had very high exposure to hydrological conditions during Hurricane Ian but low social vulnerability in the baseline order. They are protected wetlands, nature preserves, parks, and affluent communities with low social vulnerability. | Figure 4.8<br>Table 4.5A<br>Figure 4.9B |
| Greatest decrease in basin priority | Inland basins of Alabama, South Carolina, and North Carolina | These basins had the highest social vulnerability in the baseline order but were located outside the hurricane path meaning they had low hydrological exposure | Figure 4.8<br>Table 4.5B<br>Figure 4.9C |

It is important to note how the model results can be sensitive to the baseline scenario. For example, medical first responders tasked with selecting locations for temporary medical tents could define the baseline scenario as the SVI sub-variable “Aged 65 and Older” (see Appendix 4.1). The differences of system order from the baseline to each of the other scenarios are the focus of interest, and modelers should thus remind the source(s) of the baseline scenario in interpreting the results to stakeholders (see, e.g., Hassler et al., 2020).

Future work includes using this study as a framework to explore the capacity of machine learning to increase the number of factors considered and the complexities of scenarios. For the application to major tropical cyclones, future work should explore the relationship of multiple hydrological disasters and social vulnerability over an extended period of time. This would improve understanding of the spatial and temporal patterns of hurricane exposure and social vulnerability in climate-sensitive-hazard regions.

Given the disproportionate impacts of major tropical cyclones and hydrological disasters on socially vulnerable communities, this study provides a tool for risk assessment at the basin level to order basins considering multidisciplinary factors. As demonstrated by the application to Hurricane Ian, results of this work can be used by policymakers and disaster managers to inform future investments designed to decrease the impacts of future major tropical cyclones for vulnerable populations.

## 4.9 Acknowledgements

This paper is based on work supported by the National Science Foundation (NSF) Graduate Research Fellowship Program (GRFP) under Grant No. 182490. Any opinions, findings, conclusions, or recommendations expressed in this work are those of the author(s) and do not necessarily reflect the views of the University of Virginia or the National Science Foundation. The authors are in addition grateful for the support of the Commonwealth Center for Advanced Logistics Systems, as well as for engagement and feedback from some of the following entities: the United States Army Corps of Engineers (USACE), the United States Agency for International Development (USAID), the Iraq Ministry of Water Resources, attendees of the 2023 European Geophysical Union (EGU) General Assembly, and other local and international collaborators.

# **Chapter 5:** Modeling Resilience of System Order for Investments in Environmental Justice and Social Vulnerability[4]

## 5.1 Abstract

Resilience of vulnerable populations to environmental extremes is a concern for policymaking across environmental justice, economic development, technology innovation, etc. This study models the resilience of system order for a portfolio of investments, focusing on the spatial distributions of risk exposure, social vulnerability, and environmental stressors. The approach quantifies risk as a disruption of baseline order under each of several scenarios that combine social and environmental factors, with attention to vulnerable populations. Scenarios of the greatest and least disruption of system order are identified using the normalized sum of differences in a priority order of investments. The spatial distributions of scenario impacts to order

---

[4] The work presented in this chapter resulted in a journal article in preparation:

Pavur, G., Trump, B.D., Linkov, I., Polmateer, T.L., Lambert, J.H., Lakshmi, V. "Modeling Resilience of System Order for Investments in Environmental Justice and Social Vulnerability."

are highlighted in maps of the relevant water basins. A realistic example is described with features of a southeastern region of the USA. The results of this study are a rationale and evidence for the allocations of investments for economic development and system resilience, balancing among several criteria of social vulnerability and environmental justice.

## 5.2 Introduction

*Environmental justice* has a multidisciplinary perspective that can improve understanding of the extent that environmental conditions disproportionately impact vulnerable populations, such as the socially vulnerable (Brinkley & Wagner, 2024; Mohai et al., 2009). As climate change is predicted to increase the frequency and intensity of hydrological and environmental extremes, criteria of environmental conditions are expected to further exacerbate environmental justice concerns in the future (Brinkley & Wagner, 2024; Lavell et al., 2012). To support priorities aimed to address environmental justice, there is a need to improve understanding of system risk when multidisciplinary criteria of society and the environment are jointly considered.

This study develops and demonstrates a methodology to quantify system risk as the disruption of basin order across scenarios of social and environmental stressors. The methodology is as follows: First, criteria of society and the environment are individually sorted from highest to lowest in importance. Second, a baseline scenario of only societal criteria is defined to represent system order prior to consideration of environmental criteria. Third, scenarios are defined by considering both social and environmental criteria. Fourth, a swing-weight technique is used to update factor weights of criteria (Karvetski et al., 2009). Fifth, risk is quantified as the disruption of order between the baseline and each other scenario (Bonato et al., 2022; M. C. Hamilton et al., 2015; Hassler et al., 2019a; You et al., 2014b). Sixth, the normalized sum of difference in order is used to calculate scores of disruption to identify the scenarios that are most and least disruptive to system order (Bonato et al., 2022; Eddy et al., 2022; M. C. Hamilton et al., 2015; Hassler et al., 2019a; Loose et al., 2022a, 2022b, 2023; Pennetti et al., 2021; Sambo, Bonato, et al., 2023; Sambo, Sano, et al., 2023; Thekdi & Lambert, 2015; Thorisson & Lambert, 2017; You et al., 2014b). Seventh, spatial plots of scenario order and scenario risk at a basin-level telemetry are used to improve understanding of the spatial distribution of disruption to system order.

A demonstration is provided for a region of the southeastern USA, which previous studies have identified as a hotspot for concerns of vulnerable populations with high exposure to extreme environmental conditions (Flanagan et al., 2011; Tate et al., 2021). The social criteria data (i.e., social vulnerability, socioeconomic status, household composition and disability, minority status and language, housing type and transportation) is derived the Social Vulnerability Index (SVI) which is based on societal data collected via the United States Census Bureau (Flanagan et al., 2011, 2018). The environmental criteria data (i.e., precipitation, soil moisture, temperature, and elevation) is derived from satellite-based Earth Observations and global models (Farr et al., 2007; Huffman et al., 2015a; Rodell, Houser, Jambor, Gottschalck, Mitchell, Meng, Arsenault, Cosgrove, Radakovich, Bosilovich, Entin, Walker, Lohmann, et al., 2004).

For the systems engineering community, a principal innovation of the methodology of this paper is its use of data from disparate sources in a *risk register* of water basins, featuring an analysis of the spatial distribution of the disruption of system order. Results, rationale, and methodologies of this study can inform decision makers in the allocation of resources for system *resilience.* A particular concern is to understand the potential for disruption of system order of basins with attention to both environmental justice and social vulnerability.

## 5.3 Data

This section describes the criteria datasets (i.e., social or environmental) and pre-processing steps used for the demonstration. Each criterion is spatially resampled to the Level 08 HydroBASINS product to allow for basin-level analysis regardless of the native resolutions of the datasets (Lehner & Grill, 2013b). The HydroBASINS data is available in 2024 at: https://www.hydrosheds.org/products/hydrobasins.

Social vulnerability data were derived for the census-track level CDC/ATSDR SVI for 2020 [25]. In addition to a spatially averaged SVI for each sub-basin, the following four sub-components of SVI were considered: 1) socioeconomic status, 2) household composition and disability index, 3) minority status and language index, and 4) housing type and transportation index. The data is available in 2024 at: https://www.atsdr.cdc.gov/placeandhealth/svi/data_documentation_download.html.

The annual average precipitation (considering 2001 – 2022) was derived from the Global Precipitation Measurement (GPM) Integrated Multi-satellitE Retrievals for GPM (IMERG) Final Precipitation L3 V07 product (Huffman et al., 2015a). The data is available in 2024 at: https://gpm.nasa.gov/data/imerg.

Annual average surface temperature and root zone soil moisture (depth of 0 – 2 m below the surface) for 2001 – 2022 were derived from the Global Land Data Assimilation System (GLDAS) Noah Land Surface Model L4 V2.1 (Rodell et al., 2004). The data is available in 2024 at: https://ldas.gsfc.nasa.gov/gldas.

Average elevation for the sub-basins was derived from the NASA Shuttle Radar Topography Mission (SRTM) (Farr et al., 2007). The data is available in 2024 at: https://www.earthdata.nasa.gov/sensors/srtm.

## 5.4 Methodology

This section describes the framework methodology in several parts as follows. Elements of the methodology include the following:

1) $S_c = \{c_1, \ldots, c_j\}$: the set of *j* performance criteria,
2) $S_n = \{S_o, \ldots, S_n\}$: the set of *n* scenarios containing one or more performance criteria, with $S_0$ representing the baseline order,
3) $b_i = \{b_1, \ldots, b_i\}$: the set of *i* basins in the area of demonstration,
4) $w_j$: the weight assigned to criterion $c_j$ in scenario $s_n$.

***Table 5.1:*** *Sample of importance criteria and sorting methods in modeling disruption of system order.*

| Index | Criterion / Sorting Method |
|---|---|
| $c_1$ | Social Vulnerability Index (SVI) / descending |
| $c_2$ | Socioeconomic status index / descending |
| $c_3$ | Household composition and disability index / descending |
| $c_4$ | Minority status and language index / descending |
| $c_5$ | Housing type and transportation index / descending |
| $c_6$ | Annual average precipitation / descending |
| $c_7$ | Annual average precipitation / ascending |
| $c_8$ | Elevation / descending |
| $c_9$ | Elevation / ascending |
| $c_{10}$ | Annual average root zone soil moisture / descending |
| $c_{11}$ | Annual average root zone soil moisture / ascending |
| $c_{12}$ | Annual average temperature / descending |
| $c_{13}$ | Annual average temperature / ascending |

Table 5.1 summarizes criteria used for the demonstration. Social criteria are represented by $c_1 - c_5$. Environmental criteria are represented by $c_6 - c_{13}$.

First, the criteria are each characterized from highest to lowest order using Eq. 1. This prioritization for is henceforth referred to as the 'basin order.' The baseline order is defined using scenario *s.00*, which is the SVI basin order. This represents the system prior to consideration of environmental criteria. A variety of scenarios are defined which consider both social criteria and environmental criteria.

$$S_n(b_i) = 100 * \sum_{j=1}^{k} w_j c_{ij} \tag{1}$$

$$where\ 0 \leq w_j \leq 1\ \forall j \in J\ and \sum_{j \in J} w_j = 1$$

Second, a baseline order is defined using scenario *s.00,* SVI, to represent the system order prior to consideration of environmental criteria. For example, the basin with the highest SVI is assigned the highest order (a value of one). Conversely, the basin with the lowest SVI is assigned the lowest order (a value of *i*).

Third, a variety of scenarios are defined through consideration of both social and environmental criteria. Table 5.2 summarizes the scenarios and the contributing criteria. As previously mentioned, scenario *s.00* represents the baseline order. Scenarios *s.01 – s.08* represent SVI and one other criteria. Scenarios *s.09 – s.12* represent one social criteria and four environmental criteria prioritized as 'wet' conditions. Scenarios *s.13 – s.16* represent one social criteria and four environmental criteria prioritized as 'dry' conditions.

***Table 5.2:*** *Sample of scenarios and criteria in modeling of disruption of system order.*

| **Scenario** | **Criteria** |
|---|---|
| *s.00: baseline, SVI* | $c_1$ |
| *s.01: SVI + precipitation (max.)* | $c_1, c_6$ |
| *s.02: SVI + elevation (max.)* | $c_1, c_8$ |
| *s.03: SVI + root zone soil moisture (max.)* | $c_1, c_{10}$ |
| *s.04: SVI + temperature (max.)* | $c_1, c_{13}$ |
| *s.05: SVI + precipitation (min.)* | $c_1, c_7$ |
| *s.06: SVI + elevation (min.)* | $c_1, c_9$ |
| *s.07: SVI + root zone soil moisture (min.)* | $c_1, c_{11}$ |
| *s.08: SVI + temperature (min.)* | $c_1, c_{12}$ |
| *s.09: socioeconomic status + wet environmental conditions* | $c_2, c_6, c_8, c_{10}, c_{13}$ |
| *s.10: Household composition and disability + wet environmental conditions* | $c_3, c_6, c_8, c_{10}, c_{13}$ |
| *s.11: Minority status and language + wet environmental conditions* | $c_4, c_6, c_8, c_{10}, c_{13}$ |
| *s.12: Housing type and transportation + wet environmental conditions* | $c_5, c_6, c_8, c_{10}, c_{13}$ |
| *s.13: socioeconomic status + dry environmental conditions* | $c_2, c_7, c_9, c_{11}, c_{12}$ |
| *s.14: Household composition and disability + dry environmental conditions* | $c_3, c_7, c_9, c_{11}, c_{12}$ |
| *s.15: Minority status and language + dry environmental conditions* | $c_4, c_7, c_9, c_{11}, c_{12}$ |
| *s.16: Housing type and transportation + dry environmental conditions* | $c_5, c_7, c_9, c_{11}, c_{12}$ |

Fourth, the swing-weight technique is used to update the factor weights for each scenario. This allows for tradeoffs of the relative considerations of each criteria within a given scenario, which is advantageous considering that the importance of social versus environmental criteria is unknown. However, for all scenarios, the combined criteria weights of all social and environmental criteria is maintained as 0.5. This ensures equal contributions from both social and environmental criteria within a given scenario.

Fifth, scenario risk ($R_n$) at the basin-level ($b_i$) is defined as the difference in basin order between the baseline order and the scenario order using Eq. 2:

$$R_n(b_i) = S_0(b_i) - S_n(b_i) \tag{2}$$

In Eq. 2, a positive R indicates an increase in basin order compared to the baseline scenario. A negative R indicates a decrease in basin order compared to the baseline scenario.

Sixth, the most and least disruptive scenarios are determined by calculating the normalized sum of squares of differences in order using Eq. 3 and 4. $X(S_n)$ is henceforth referred to as the normalized score of disruption for scenario *n*. These calculations defines the influence of each scenario to the system order as a quantification of risk (Alsultan et al., 2020; Bonato et al., 2022; Eddy et al., 2022; Hassler et al., 2019b; Karvetski et al., 2009; Loose et al., 2022a, 2023; Pennetti et al., 2021; Sambo, Bonato, et al., 2023; Thekdi & Lambert, 2015; Thorisson & Lambert, 2017; Xu & Lambert, 2013; You et al., 2014a).

$$x(S_n) = \sum_i^N \left(S_0(b_i) - S_n(b_i)\right)^2 \tag{3}$$

$$X(S_n) = \frac{x(S_n) - x(S)_{min.}}{x(S)_{max.} - x(S)_{min.}} \tag{4}$$

Seventh, spatial plots of scenario basin order and risk are examined. This is used to improve understanding of the spatial distributions of priority and risk within the area of demonstration.

## 5.5 Sample of Results of Demonstration

For the demonstration, the study area is defined as the Level 08 HyroBASINS product in Alabama, Florida, Georgia, North Carolina, and South Carolina. Fig. 5.1 shows the spatial plot of basin order for the baseline scenario, *s.00* (SVI). Basins of the highest priority (i.e., an order value equal to or near one) are depicted in black and are generally located in inland Florida and southeastern Georgia, South Carolina, and North Carolina. Conversely, basins of lowest priority (i.e., an order value equal to or near 920) are depicted in white and are generally located in coastal Florida and northwestern Georgia, South Carolina, and North Carolina.

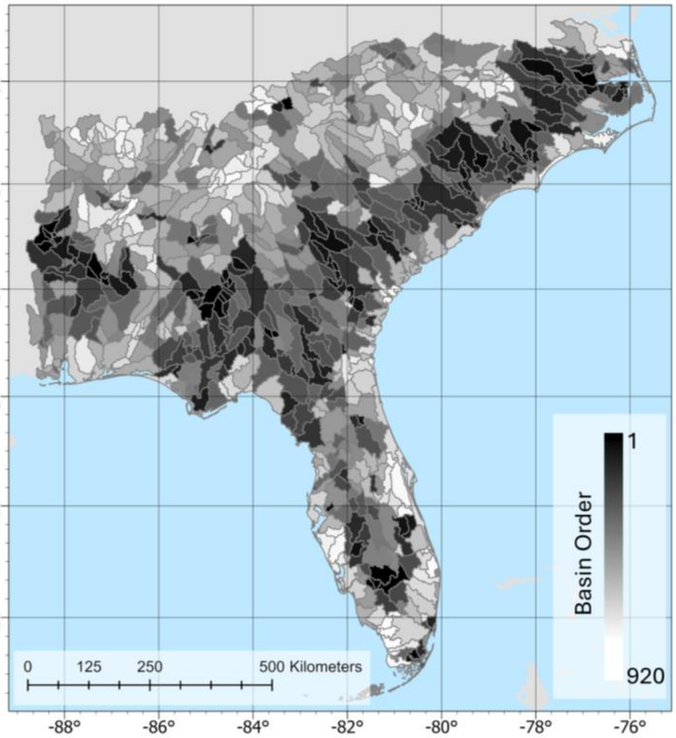

***Fig. 5.1:*** *The basin order for scenario s.00: Social Vulnerability Index. This is described as the baseline order in the demonstration.*

Fig. 5.2 shows the normalized score of disruption for the scenarios. When only SVI and one environmental criterion are considered (*s.01 – s.08*), the most disruptive scenario is *s.02: SVI*

+ *elevation (max.)* and the least disruptive scenario is *s.06: SVI + elevation (min.)*. This indicates that generally, populations of high social vulnerability are co-located in basins of low elevation.

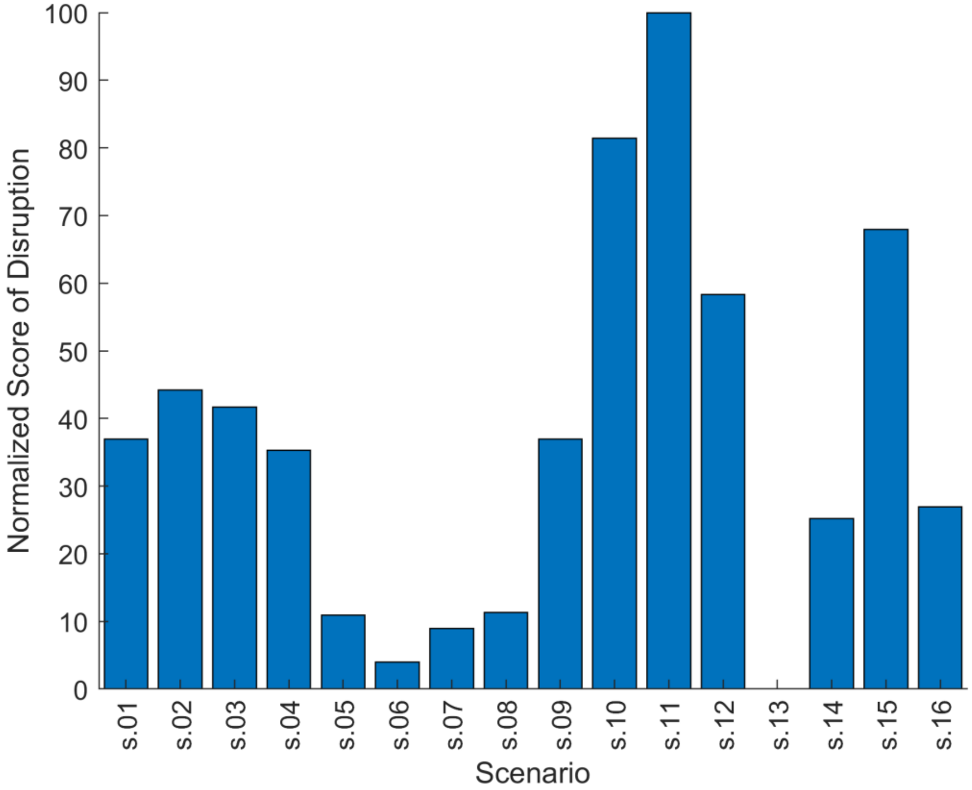

***Fig. 5.2:*** *Summary of normalized score of disruption for each of the scenarios, s.01 – s.16, in the demonstration.*

Across scenarios, disruption was generally greater when considering social criteria in combination with wet environmental variables than dry environmental variables (Fig. 5.2). This suggests populations of high SVI are generally found in basins of drier environmental conditions. The overall most disruptive scenario is *s.11: minority status and language + wet environmental conditions* (Fig. 5.2). The overall least disruptive scenario is *s.13: socioeconomic status and dry environmental conditions* (Fig. 5.2). To further examine these scenarios of interest, spatial plots of scenario basin order and risk are provided in Fig. 5.3.

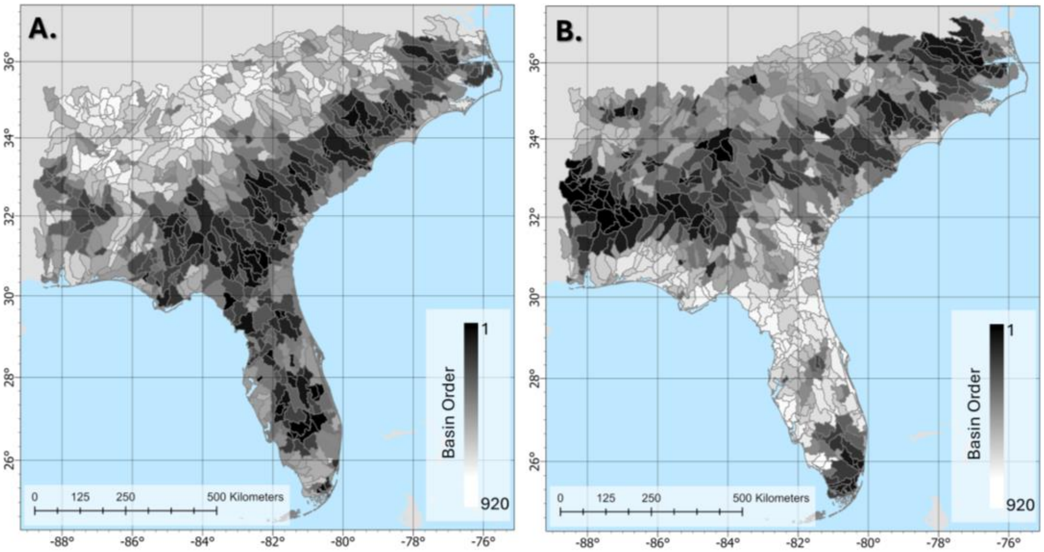

***Fig. 5.3:*** *The maps describe the disruptions to system order across water basins for the following scenarios:* ***(A)*** *the most disruptive scenario, s.11, and* ***(B)*** *the least disruptive scenario, s.13.*

In Fig. 5.3A, the basin order spatial plot of the most disruptive scenario, *s.11*, is shown. Basins of very high priority are primarily located in inland Florida, southeastern Georgia, South Carolina, and North Carolina. These basins have highest order due to the combined high priority of criteria $c_4$ (minority status and language) and wet environmental conditions ($c_6$, $c_8$, $c_{10}$, $c_{13}$).

In Fig. 5.3B, the basin order spatial plot of the least disruptive scenario, *s.13*, is shown. Basins of highest priority are found in central Alabama, Georgia, South Carolina, and North Carolina. These basins have highest order due to the combined high priority of criteria $c_2$ (socioeconomic status) and dry environmental conditions ($c_7$, $c_9$, $c_{11}$, $c_{12}$). Low priority is found in most basins of Florida.

To improve understanding of the spatial changes in order between the baseline scenario, *s.00*, and the scenarios of interest (*s.11* and *s.13*), spatial plots of risk are provided (Fig. 5.4). Fig. 5.4A shows the spatial plot of risk of the most disruptive scenario, *s.11*. Fig. 5.4B shows the spatial plot of risk for the least disruptive scenario, *s.13*. Generally, greater changes in basin order (and thus risk) are observed in the most disruptive scenario, *s.11*.

In Fig. 5.4B, basins of the northwestern portion of the study area have increased order and are depicted in red to represent increased risk. Basins in Florida and southeastern Georgia, South Carolina, and North Carolina have decreased order and are depicted in green to represent decreased risk. This indicates that the social and environmental criteria of scenario *s.11* leads to an increase in priority for northwestern basins and a decrease in priority for southern/southeastern basins compared to the baseline scenario, *s.00*.

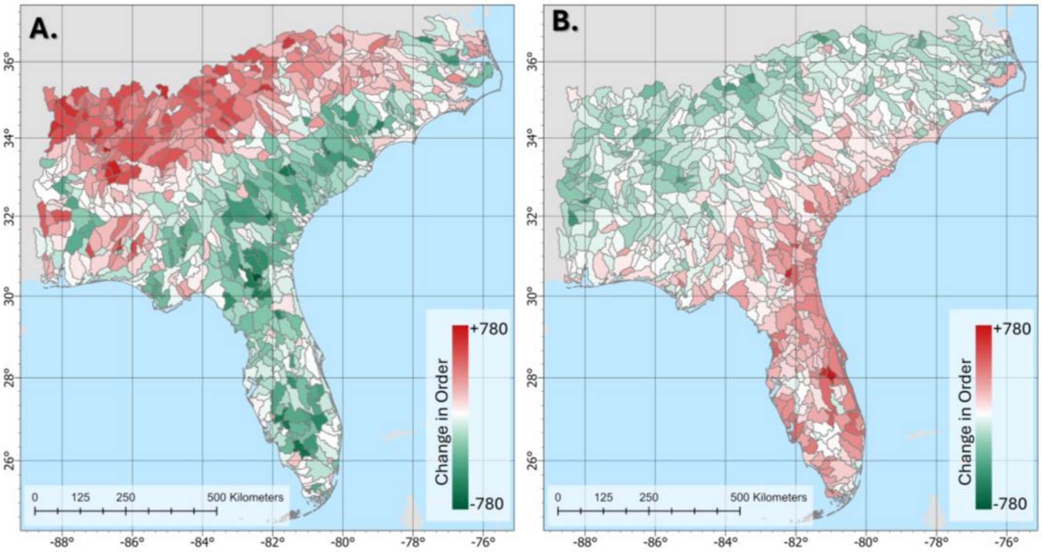

***Fig. 5.4:** The maps describe the disruption to system order across basins for the following scenarios: **(A)** the most disruptive scenario, s.11, and **(B)** the least disruptive scenario, s.13.*

## 5.6 Discussion and Conclusions

In this study, a methodology is demonstrated to quantify risk as the disruption of system order at a basin-level telemetry given consideration of multi-disciplinary criteria (i.e., social and environmental) derived from disparate sources. Scenarios of the most disruption and least disruption are identified and spatially plotted as basin order and risk.

A demonstration for the southeastern USA is provided. The most and least disrupted scenarios when SVI is considered in combination with one environmental criterion both included elevation ($c_8$ and $c_9$). This indicates populations of high SVI are generally co-located in basins of low elevation. Across scenarios, disruption was generally greater when considering social criteria in combination with wet environmental variables than dry environmental variables. This suggests populations of high SVI are generally found in basins of drier environmental conditions. The overall most and least disruptive scenarios were identified as *s.11* (most disruptive) and *s.13* (least disruptive). This revealed that criteria of wet environmental conditions in combination with social criteria of minority status and language greatly disrupt system order compared to the baseline order. Conversely, criteria of dry environmental conditions in combination with socioeconomic status depict the least disruption compared to the baseline order. This suggests that populations of concerning socioeconomic status are located in basins of the driest environmental conditions within the study area.

Methodology and results of this study demonstrate the ability to combine multi-disciplinary criteria in a *risk register* of basins to improve understanding of system order and risk. The scenario-based risk analysis and spatial plots of order and risk provide insights into the system resilience to societal and environmental conditions. Findings of this study can be used to support allocation of resources at a basin-level for environmental justice priorities.

## 5.7 Acknowledgements

This work was supported by the National Science Foundation Graduate Research Fellowship Program (NSF GRFP) under Grant No. 182490. The authors are grateful to the Commonwealth Center for Advanced Logistics Systems, the US Army Corps of Engineers, and the US Agency for International Development for insights from related sponsored efforts at the University of Virginia.

# **Chapter 6:** Uncertainty and Sensitivity of Development Goals to Water Scarcity of Iraq and Transboundary Regions[5]

## 6.1 Abstract

Iraq and its transboundary regions have significant challenges from water scarcity in combination with other social and environmental factors. There are short- and long-term implications for vulnerable demographics, such as youth. With Iraq's dependence on upstream water management, there is a need to address several critical factors of transboundary watersheds such as the Haditha, Mosul, Dokan, and Euphrates-Tigris basin. This paper develops the use of particular social, hydrological, and other environmental factors in a *risk register of basins* and vulnerable populations, where societal priorities vary across scenarios of hydrology and water. Social data (i.e., gridded youth population data) and hydrological observations (i.e., precipitation,

---

[5] The work presented in this chapter resulted in a journal article in preparation:

Pavur, G., Marcellin, M., Loose, D.C., Cardenas, J.J., Trump, B.D., Linkov, I., Waheed, S.Q., Almashhadani, M., Polmateer, T.L., Lambert, J.H., Lakshmi, V. "Uncertainty and Sensitivity of Development Goals to Water Scarcity of Iraq and Transboundary Regions."

temperature, root zone soil moisture, and Normalized Difference Vegetation Index (NDVI)) are obtained from publicly available satellite-based Earth observations and global models. The methods are as follows. First, a baseline order of basins is defined using demographic population data in 2020. Second, a variety of water scarcity scenarios are analyzed using the swing-weight method to update factor weights. Third, risk is quantified as the disruption of basin order. Fourth, the disruption of scenarios to the baseline order is compared using sum of least square difference to identify basins of highest water scarcity risk given societal priorities and other factors. Fifth, spatial maps of basin order and disruption are provided to improve understanding of the spatial distribution of water scarcity challenges in the region with regard to vulnerable populations. The results feature identification of the most and least disruptive scenarios including: 1) population density is lowest in basins exposed to the highest air temperatures, 2) an urban-to-rural migration pattern (such as prompted by a public health crisis) would significantly disrupt basin order, and 3) populations with greatest exposure to extreme hydrological conditions of water scarcity are found in the southern basins of Iraq in or near the Al-Muthanna governorate. The impacts of this work are to steer future investments that mitigate risk of disrupted system orders and to increase system resilience of vulnerable populations to water scarcity.

## 6.2 Introduction

The Middle East is one of the most water scarce regions of the world (UNICEF, 2021). Globally, Iraq is ranked as the fifth most vulnerable country to water and food shortages and extreme temperatures (UNICEF, 2023). The combination of decreased water availability in the region and high dependence on surface water of the Tigris and Euphrates Rivers makes Iraq increasingly vulnerable to water scarcity (Jaff, 2023; UNICEF, 2021). There is a need to improve system resilience in the region to disruptions in water supply (Linkov et al., 2022; Linkov & Trump, 2019).

Challenges of water scarcity and society are closely intertwined and multidisciplinary (Van Loon et al., 2016). In the Middle East, factors compounding the severity of drought on society include, but are not limited to, development of upstream countries, population growth, food insecurity, economic insecurity, decreased power availability, insufficient health and sanitation systems, slow-onset disaster events (i.e., prolonged drought), and rapid-onset disaster events (i.e., floods and earthquakes) (Chumky et al., 2022; Jaime et al., 2022; McAuliffe & Triandayfllidou, 2022; Peters, 2021; UNICEF, 2021).

An example of the complex relationship between water scarcity and societal priorities was evident in Basra, Iraq in 2018 when the combination of severe drought and decreased streamflow of the Euphrates-Tigris Rivers led to prolonged saltwater intrusion (UNICEF, 2018, 2021). The lack of water availability, adverse health impacts, and public dissatisfaction in the region led to unrest and violent protests (UNICEF, 2018, 2021). Similarly, high concentrations of saltwater have been found moving further upstream in the Shatt Al-Arab River as the amount of freshwater flow declines (Al-Asadi et al., 2023). This is concerning for sustainable development, as this is an important water source for domestic and industrial usage in southern Iraq (Al-Asadi et al., 2023).

Climate change, however, is predicted to continue exacerbating water scarcity challenges in Iraq and surrounding Middle Eastern countries through decreased precipitation, increased temperatures, increased desertification, and more frequent and intense hydrological extremes (Lavell et al., 2012; UNDRR, 2015). An adaptation method to climate change is climate migration, or the physical movement of populations due to the environment resulting in Internally Displaced Peoples (IDPs) or international migrants (McAuliffe & Triandayfllidou, 2022; Šedová et al., 2021).

In 2018, an estimated 630 families were displaced in southern Iraq due to water scarcity (UNICEF, 2021). Similarly, approximately, 20,000 Iraqis were displaced in 2021 due to water scarcity when only 10 governorates were analyzed (IOM, 2020; IOM Iraq, 2022).

Previous studies have reported that severe climate change prevents IDPs from returning to their homes in Iraq and the number of climate migrants is likely underestimated in the region due to identification and reporting challenges (Chumky et al., 2022; Jaff, 2023). Given future climate change projections, the number of climate refugees, migrants, and IDPs are expected to increase within the region (Mazhin et al., 2020). For example, four million Iraqis are predicted to be internally displaced due to water scarcity in the next eight years (UNICEF, 2021). Furthermore, the most vulnerable populations living in high-risk areas will likely lack the physical or financial means to migrate without external assistance and aide (McAuliffe & Triandayfllidou, 2022).

With limited water availability in Iraq, cooperative international water management in the transboundary basins of the region is vital for sustainable development (UNICEF, 2021, 2023). However, political disagreements prevent the ubiquitous sharing of in-situ hydrology data between countries in the region (Albarakat et al., 2018, 2022; Albarakat & Lakshmi, 2019). One method to mitigate this data gap is through the use of satellite-based Earth Observations collected at high spatial and temporal resolutions to observe hydrological factors of water scarcity such as precipitation, air surface temperature, root zone soil moisture (depth of 0 – 2 m below the surface), and Normalized Difference Vegetation Index (NDVI) (Albarakat et al., 2018, 2022; Albarakat & Lakshmi, 2019; Besnier et al., 2024; Marcellin et al., 2023; Pavur & Lakshmi, 2023; Waheed et al., 2020, 2022, 2023).

In this study, we combine a variety of interdisciplinary factors of water scarcity (i.e., social, hydrological, and environmental) in a risk register to examine the basin-level risk of population and water scarcity in transboundary basins of Iraq. Hydrological observations are obtained from approximately 19 years of free and publicly available satellite-based Earth Observations. By defining a baseline scenario of youth population density in 2020, particular attention is given to youth populations (defined as persons less than twenty years of age for purposes of this study) who are a vulnerable demographic to water scarcity on both short and long-term timescales (UNICEF, 2021, 2023). Then, a variety of scenarios which disrupt the system order are considered including 1) economic insecurity, 2) food insecurity, 3) current population density, 4) future population growth, 5) health crisis (such as the COVID-19 pandemic), and 6) distance from disaster (such as the 2023 Türkiye/Syria earthquake). To update the new ordering functions for each basin in the scenarios, the swing-weight technique is used to change the factor weights across scenarios (Karvetski et al., 2009). This allows for tradeoffs of greater weighting of one or more variables in exchange for less consideration of other variables, which is advantageous for this study since the relative importance of one variable (social, hydrological, or environmental) over another is uncertain (Bonato et al., 2022; M. C. Hamilton et al., 2015; Karvetski et al., 2009; You et al., 2014a). Risk at the sub-basin scale is quantified as the disruption of the scenarios to the baseline order using the least square difference of order (Hassler et al., 2019b). Spatial maps of the most and least disruptive scenarios are provided to improve understanding of the spatial distribution of societal priorities and water scarcity. Results from this study can be used to inform priorities and future investments aimed to decrease risk and increase resilience to water scarcity in transboundary basins of Iraq, particularly with regard to societal priorities.

### 6.2.1 Geographic Area of Demonstration

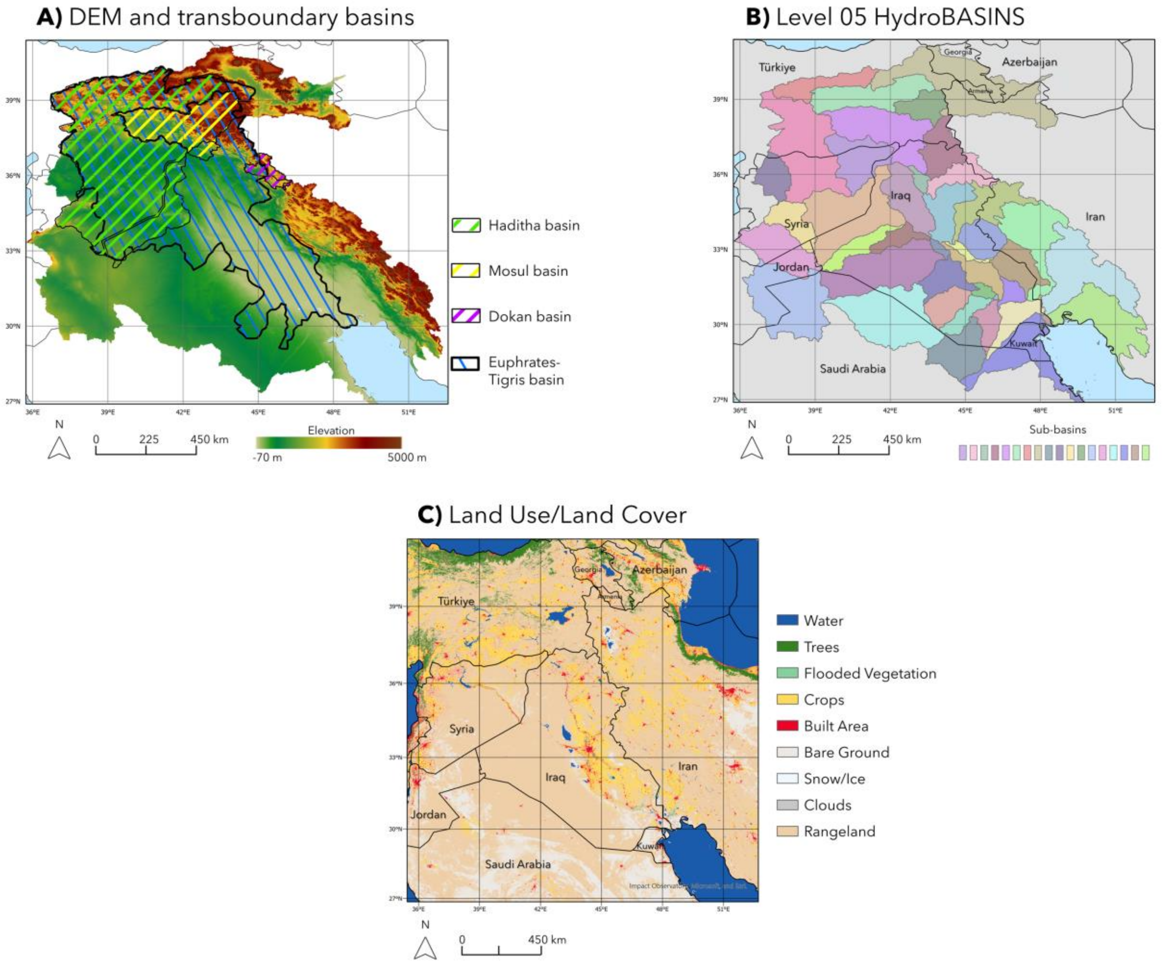

***Fig. 6.1:*** ***(A)*** *Digital elevation model (DEM) derived from NASA Shuttle Radar Topography Mission (SRTM) for the geographic area of demonstration with basin delineations shown for the Haditha, Mosul, Dokan, and Euphrates-Tigris River basins.* ***(B)*** *Sub-basin delineations for the geographic area of demonstration, as defined by the Level 05 HydroBASINS dataset.* ***(C)*** *Land use/land cover map of Iraq and surrounding countries derived from Sentinel-2 data.*

The study area is defined using the Level 05 HydroBASINS dataset within the following major river basins which are transboundary with Iraq: the Euphrates-Tigris River basin, the Mosul basin, the Dokan basin, and the Haditha basin (Albarakat et al., 2022). Fig. 6.1A shows a digital elevation model (DEM) with basin delineations for the Haditha, Mosul, Dokan, and Euphrates-Tigris River basins. The Haditha, Mosul, and Dokan basins were delineated using dam locations, as described in Albarakat et al., 2022. Fig. 6.1B shows the 43 sub-basins delineated by the Level

05 HydroBASINS dataset. Nineteen of the sub-basins of Iraq are transboundary, crossing borders into other countries, while an additional four sub-basins are transboundary across borders of other countries. Fig. 6.1C shows a land use/land cover map derived from Sentinel-2 for the study area for 2022. Built area in Iraq is predominately located between and northeast of the Euphrates and Tigris Rivers (Fig. 6.1C).

## 6.3 Sources of Data for the Demonstration

This section describes the open data (i.e., free and publicly available data) used for social factors (i.e., youth population density and population growth rate), hydrology observations (i.e., precipitation, air temperature, root zone soil moisture, and NDVI), and other environmental factors (i.e., land use/land cover and distance from earthquake epicenters). To allow for dataset comparisons regardless of the native resolutions, all datasets are resampled to a sub-basin scale defined by the World Wildlife Fund's Level 05 HydroBASINS dataset (Lehner & Grill, 2013a). Table 6.1 summarizes each dataset used in this study by temporal resolution, native spatial resolution, resampled resolution, resampling method, study period, and sources. Appendix 6.2 shows annual time series from 2003 – 2022 for all social and hydrology factors with data available over this period. Brief dataset descriptions and pre-processing steps are provided in the remainder of this section.

***Table 6.1:*** *Summary of open data used in this study including variable, sensor/model, native spatial resolution, resampled resolution, resampling method, temporal resolution, study period, and sources.*

| Variable | Sensor/Model | Native Spatial Resolution | Resampled Resolution | Resampling Method | Temporal Resolution | Study Period | Sources |
|---|---|---|---|---|---|---|---|
| Sub-basins | HydroBASINS | Level 05 | N/A | N/A | N/A | N/A | Lehner & Grill, 2013 |
| Youth Population Density | WorldPop, Age and sex structures, constrained individual countries 2020 UN adjusted | 100 m | Level 05 HydroBASINS | Spatial average | Yearly | 2020 | Bondarenko et al., 2020 |
| Population Growth Rate | LandScan Global | 1 km | Level 05 HydroBASINS | Spatial average | Yearly | 2003 – 2022 | Sims et al., 2023 |
| Land Use Land Cover | Sentinel-2 10 m Land Use Land Cover | 10 m | Level 05 HydroBASINS | Spatial sum | Yearly | 2022 | Karra & et al., 2021 |
| Precipitation | GPM IMERG Final Precipitation L3 V06<br>GPM IMERG Late Precipitation L3 V06 | 0.1°<br>0.1° | Level 05 HydroBASINS | Spatial average | Yearly | 2003 – 2022 | Huffman et al., 2020 |
| Surface Air Temperature | GLDAS Noah Land Surface Model L4 V2.1<br>GLDAS Noah Land Surface Model L4 Early Product V2.1 | 0.25°<br>0.25° | Level 05 HydroBASINS | Spatial average | Yearly | 2003 – 2022 | Rodell et al., 2004 |
| Root Zone Soil Moisture (0 – 2 m depth) | GLDAS Noah Land Surface Model L4 V2.1 | 0.25° | Level 05 HydroBASINS | Spatial average | Yearly | 2003 – 2022 | Rodell et al., 2004 |

| | | | | | | | |
|---|---|---|---|---|---|---|---|
| | GLDAS Noah Land Surface Model L4 Early Product V2.1 | 0.25° | | | | | |
| Normalized Difference Vegetation Index (NDVI) | MODIS/Terra Surface Reflectance Daily L2G 500 m Global V006 | 500 m | Level 05 HydroBASINS | Spatial average | Yearly | 2003 – 2022 | Vermote & Wolfe, 2015 |
| Distance from Earthquake Epicenter to Basin Centroid | The Global Centroid-Moment-Tensor (CMT) Project | N/A | Level 05 HydroBASINS | Spatial distance | N/A | 2023 | Dziewonski et al., 1981;<br>Ekström et al., 2012 |

## 6.3.1 Social Factors Data

Two social factors considered in this study are (1) youth population density and (2) population growth rate. Youth population density is calculated at the basin-level using Eq. 1 and the WorldPop “age and sex structures constrained individual countries 2020, UN Adjusted” dataset for the following countries: Armenia, Azerbaijan, Georgia, Iran, Iraq, Jordan, Kuwait, Saudi Arabia, Syria, and Türkiye (Bondarenko et al., 2020). In Eq. 1, youth population density for a given basin ($YPD(b_i)$) equals the total youth population within the basin ($YP(b_i)$) divided by basin area ($A(b_i)$). For purposes of this study and due to the availability of WorldPop data, *youth* is defined as persons less than twenty years of age. The WorldPop data is available in 2024 at: https://hub.worldpop.org/doi/10.5258/SOTON/WP00698.

$$YPD(b_i) = \frac{YP(b_i)}{A(b_i)} \tag{1}$$

Population growth rate from 2003 – 2022 is calculated at the basin-level using Eq. 2 and the Oak Ridge National Laboratory “LandScan Global” product (Sims et al., 2023). In Eq. 2, the population growth rate of a basin ($PGR(b_i)$) equals the ratio of the difference in basin population density in 2022 ($PD_{t_2}(b_i)$) and 2003 ($PD_{t_1}(b_i)$) and the change in time ($t_2 - t_1$). The LandScan Global product is available in 2024 at: https://landscan.ornl.gov/.

$$PGR = \frac{PD_{t_2}(b_i) - PD_{t_1}(b_i)}{t_2 - t_1} * 100\% \tag{2}$$

### 6.3.2 Hydrology Factors Data

Four hydrology factors considered in this study are (1) precipitation, (2) air surface temperature, (3) root zone soil moisture, and (4) NDVI. All hydrological observations are derived from publicly available Earth observations and modeled data. The factors are resampled as basin-level annual spatial averages using monthly observations from 2003 – 2022. Precipitation data is available in 2024 at: https://gpm.nasa.gov/data/imerg. Air surface temperature and root zone soil moisture data are available in 2024 at: https://ldas.gsfc.nasa.gov/gldas. NDVI data is available in 2024 at: https://lpdaac.usgs.gov/products/mod09gav006/.

### 6.3.3 Other Environmental Factors Data

Two additional environmental factors considered in this study are (1) land use/land cover and (2) distance from the 2023 Türkiye/Syria earthquake epicenters. The land use/land cover data for 2022 was obtained using the Sentinel-2 10 m Land Use Land Cover product (Karra & et al., 2021). From this dataset, the percentage of urbanized basin area (URB) and percentage of agriculture basin area (AGR) are calculated using Eq. 3 and Eq. 4, respectively, where $A(b_i)$ is the basin area.

Sentinel-2 10 m Land Use Land Cover data is available in 2024 at: https://www.arcgis.com/home/item.html?id=cfcb7609de5f478eb7666240902d4d3d.

$$URB = \frac{A_{urban}(b_i)}{A(b_i)} * 100\% \tag{3}$$

$$AGR = \frac{A_{agriculture}(b_i)}{A(b_i)} * 100\% \tag{4}$$

Distance from the 2023 Türkiye/Syria earthquake epicenters was calculated as the Euclidean distance from the epicenter to each basin centroid. The latitude/longitude coordinates of the two earthquake epicenters were obtained from the Global Centroid-Moment-Tensor (CMT) Project and is available in 2024 at: https://www.globalcmt.org/.

## 6.4 Methods

This section describes the methodology in several parts as follows: (1) the sub-basins of the study area are characterized for each social, hydrology, and environmental factor from highest to lowest order based on priorities of stakeholders; (2) a baseline scenario is defined using the basin ordered youth population density data to represent initial conditions of the study area prior to disturbances; (3) a variety of scenarios are defined using the social, hydrology, and environmental factors and stakeholder feedback; (4) the swing-weight technique is used to update factor weights for each scenario; (5) risk is calculated as the difference in basin order of a given scenario compared to the baseline scenario; (6) a normalized score of disruptiveness is calculated using the sum of squares of differences in order to identify the most and least disruptive scenarios; (7) results are mapped for select scenarios to improve understanding of the spatial distribution of basin-level priority and risk. Additional details of each step are provided in the remainder of this section.

In the first step, sub-basins of the study area are ordered from 1 to *i* according to their level of concern to stakeholders, with sub-basins of greatest concern being the highest order. This is calculated using Eq. 5 where the basin order for a given scenario is $S_n(b_i)$ is the summation of $j$ to $k$ factors ($f_{ij}$) multiplied by the $j^{th}$ defined weight ($w_j$). For each factor, basins are ordered as either ascending or descending values depending on the priorities of stakeholders. A summary of ordering methods for each factor is provided in Appendix 6.1.

$$S_n(b_i) = 100 * \sum_{j=1}^{k} w_j f_{ij} \tag{5}$$

$$where\ 0 \leq w_j \leq 1\ \forall j \in J\ and \sum_{j \in J} w_j = 1$$

Second, the baseline scenario is defined using the basin ordered youth population density data. This represents the initial conditions of the study area prior to consideration of water scarcity and other disturbances. Third, a variety of scenarios are defined using the social, hydrological, and environmental factors. While an infinite number of scenarios are theoretically possible, this study considers fifteen main scenarios aimed to improve understanding of youth vulnerability to water scarcity under conditions of current youth population density, projected future youth population density, economic security, food security, public health security, and natural disaster. Fourth, the swing-weight technique is used to update factor weights for each scenario. As previously described, the swing-weight technique allows for tradeoffs of higher consideration of one or more variables in exchange for lower consideration of other variables in the scenario (Karvetski et al., 2009). When a scenario considers multiple factors, the combined weighting of hydrology factors and non-hydrology factors is defined as 0.5 for each. Table 6.2 summarizes the fifteen scenarios and respective factor weights. Results of the basin order for select scenarios are spatially plotted to map the distribution of basin order. Additionally, basins of the greatest increase and decrease in priority for scenarios considering water scarcity ($S_{10} - S_{15}$) are identified and spatially plotted.

***Table 6.2:*** *Scenario descriptions and swing weights for each of the fifteen scenarios using social, hydrological, and other environmental factors. These include youth population density (YPD), population growth rate (PGR), percentage of urbanized basin area in 2022 (URB), percentage of agricultural basin area in 2022 (AGR), distance from earthquake epicenters to basin centroids (D), annual average precipitation (P), annual average air surface temperature (T), annual average root zone soil moisture (RZSM), and annual average normalized difference vegetation index (NDVI).*

| Scenario ($\boldsymbol{S_n}$) | Swing weights ($\boldsymbol{w_j}$) of contributing factors ($\boldsymbol{f_j}$) | | | | | | | | |
|---|---|---|---|---|---|---|---|---|---|
| | $\boldsymbol{f_1}$: YPD | $\boldsymbol{f_2}$: PGR | $\boldsymbol{f_3}$: URB | $\boldsymbol{f_4}$: AGR | $\boldsymbol{f_5}$: D | $\boldsymbol{f_6}$: P | $\boldsymbol{f_7}$: T | $\boldsymbol{f_8}$: RZSM | $\boldsymbol{f_9}$: NDVI |
| $\boldsymbol{S_1}$: Youth population density in 2020 (baseline order) | 1 | 0 | 0 | 0 | 0 | 0 | 0 | 0 | 0 |
| $\boldsymbol{S_2}$: Population growth rate from 2003 – 2022 | 0 | 1 | 0 | 0 | 0 | 0 | 0 | 0 | 0 |
| $\boldsymbol{S_3}$: Percentage of urbanized basin area in 2022 | 0 | 0 | 1 | 0 | 0 | 0 | 0 | 0 | 0 |
| $\boldsymbol{S_4}$: Percentage of agriculture basin area in 2022 | 0 | 0 | 0 | 1 | 0 | 0 | 0 | 0 | 0 |
| $\boldsymbol{S_5}$: Distance from disaster to basin centroid | 0 | 0 | 0 | 0 | 1 | 0 | 0 | 0 | 0 |
| $\boldsymbol{S_6}$: Annual average precipitation | 0 | 0 | 0 | 0 | 0 | 1 | 0 | 0 | 0 |
| $\boldsymbol{S_7}$: Annual average air surface temperature | 0 | 0 | 0 | 0 | 0 | 0 | 1 | 0 | 0 |
| $\boldsymbol{S_8}$: Annual average root zone soil moisture | 0 | 0 | 0 | 0 | 0 | 0 | 0 | 1 | 0 |
| $\boldsymbol{S_9}$: Annual average NDVI | 0 | 0 | 0 | 0 | 0 | 0 | 0 | 0 | 1 |
| $\boldsymbol{S_{10}}$: Current youth population vulnerability to hydrological | 0.5 | 0 | 0 | 0 | 0 | 0.125 | 0.125 | 0.125 | 0.125 |

| | | | | | | | | | |
|---|---|---|---|---|---|---|---|---|---|
| conditions of water scarcity | | | | | | | | | |
| $S_{11}$: Future youth population vulnerability to hydrological conditions of water scarcity | 0.25 | 0.25 | 0 | 0 | 0 | 0.125 | 0.125 | 0.125 | 0.125 |
| $S_{12}$: Youth population vulnerability to hydrological conditions of water scarcity when migrating to urbanized areas for economic security | 0.25 | 0 | 0.25 | 0 | 0 | 0.125 | 0.125 | 0.125 | 0.125 |
| $S_{13}$: Youth population vulnerability to hydrological conditions of water scarcity and agricultural stress for food security and economic security | 0.25 | 0 | 0 | 0.25 | 0 | 0.125 | 0.125 | 0.125 | 0.125 |
| $S_{14}$: Youth population vulnerability to hydrological conditions of water scarcity when migrating away from urbanized areas for public health security (such as pandemic) | 0.25 | 0 | 0.25* | 0 | 0 | 0.125 | 0.125 | 0.125 | 0.125 |
| $S_{15}$: Youth vulnerability to hydrological conditions of water scarcity when nearby natural disaster (such as 2023 Türkiye/Syria earthquakes) | 0.25 | 0 | 0 | 0 | 0.25 | 0.125 | 0.125 | 0.125 | 0.125 |

*: sorted in opposite order (ascending) to prioritize basins with least urbanized areas

Fifth, risk is quantified for each scenario as the degree of disruption of system order (Hassler et al., 2019). This is calculated as the difference in basin order of a given scenario compared to the baseline scenario ($S_1$) using Eq. 6 where $R_n(b_i)$ is the basin risk in scenario *n*, $S_1(b_i)$ is the basin order in the baseline scenario, and $S_n(b_i)$ is the basin order in scenario *n.* The results are spatially plotted to map the basin-level risk for select scenarios.

$$R_n(b_i) = S_1(b_i) - S_n(b_i) \tag{6}$$

Sixth, a score of disruption is calculated for each scenario using the normalized sum of squares of differences in order (Eq. 7 and 8). This metric quantifies the influence of each scenario to the system order (Bonato et al., 2022; Hassler et al., 2019b; Karvetski et al., 2009; You et al., 2014a). Thus, the least disruptive scenario has the lowest normalized score of disruption and the most disruptive scenario has the highest normalized score of disruption.

$$x(S_n) = \sum_{i}^{N} \left(S_1(b_i) - S_n(b_i)\right)^2 \tag{7}$$

$$X(S_n) = \frac{x(S_n) - x(S)_{min.}}{x(S)_{max.} - x(S)_{min.}} \tag{8}$$

In Eq. 7 and 8 above, $x(S_n)$ is the sum of squares of differences in order for scenario $n$. $X(S_n)$ is the normalized sum of squares of differences in order, which is also referred to as the score of disruption.

## 6.5 Results and Discussion

This section is organized as follows: section 6.5.1 describes results of the basin ordered spatial plots for scenarios; section 6.5.2 describes results of risk as the disruption of basin order; section 6.5.3 describes results of the most and least disruptive scenarios.

### 6.5.1 Basin Ordered Spatial Plots for Scenarios

The basin order for each scenario is represented in Fig. 6.2 with values of 1 indicating the highest priority and values of 43 indicating the lowest priority. The baseline scenario ($S_1$) shows that youth population density tends to be highest outside of Iraq, particularly in the northern sub-basins of Türkiye and Syria ($S_1$, Fig. 6.2A). An exception to this is a high youth population basin located in the Kurdistan Region of Iraq ($S_1$, Fig. 6.2A), which concurs with the spatial variation of population in the region published by Jaafar Alnajm (2023). Population growth rate from 2003 –

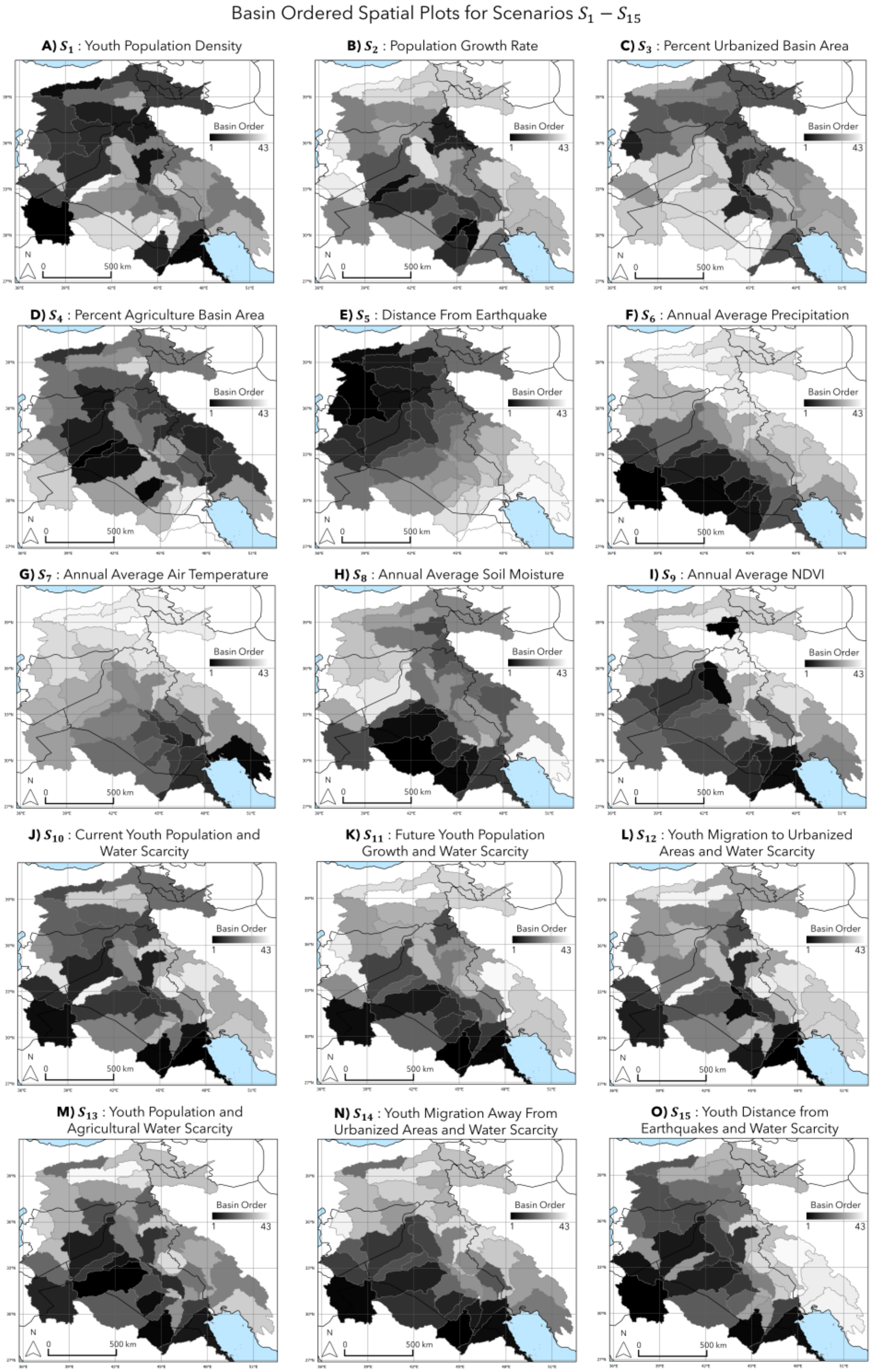

Basin Ordered Spatial Plots for Scenarios $S_1 - S_{15}$

**A)** $S_1$ : Youth Population Density

**B)** $S_2$ : Population Growth Rate

**C)** $S_3$ : Percent Urbanized Basin Area

**D)** $S_4$ : Percent Agriculture Basin Area

**E)** $S_5$ : Distance From Earthquake

**F)** $S_6$ : Annual Average Precipitation

**G)** $S_7$ : Annual Average Air Temperature

**H)** $S_8$ : Annual Average Soil Moisture

**I)** $S_9$ : Annual Average NDVI

**J)** $S_{10}$ : Current Youth Population and Water Scarcity

**K)** $S_{11}$ : Future Youth Population Growth and Water Scarcity

**L)** $S_{12}$ : Youth Migration to Urbanized Areas and Water Scarcity

**M)** $S_{13}$ : Youth Population and Agricultural Water Scarcity

**N)** $S_{14}$ : Youth Migration Away From Urbanized Areas and Water Scarcity

**O)** $S_{15}$ : Youth Distance from Earthquakes and Water Scarcity

***Fig. 6.2:*** *Basin ordered spatial plots for single variable scenarios ($S_1 - S_9$) and multiple variable scenarios ($S_{10} - S_{15}$). Basins in black are low order values (near or equal to 1) representing high priority/high concern. Basins in white are high order values (near or equal to the maximum number of basins) representing low priority/little concern.*

2022 shows that basins of Iraq tend to be higher priority (i.e., greater population growth rates) than elsewhere in the study area ($S_2$, Fig. 6.2B).

Basins of the greatest percentage of urbanized area tend to be in the northern half of the study area ($S_3$, Fig. 6.2C), whereas basins of the greatest percentage of agricultural area tend to be in southwestern Iraq and to the northeast of Iraq ($S_4$, Fig. 6.2D). These results concur with the land use/land cover changes from 2000 – 2022 documented by Al-Taei et al. (2023).

Fig. 6.2E ($S_5$) shows distance from the Türkiye/Syria earthquake epicenters to the basin centroid. Basins near the epicenters have highest priority and basins furthest from the epicenters have lowest priority ($S_5$, Fig. 6.2E). The basins of highest priority concur with regions of extensive damage to infrastructure and loss of life due to the earthquakes reported by the media (Robles et al., 2023).

Annual average precipitation is highest priority (i.e., lowest precipitation) in the southern portions of Iraq ($S_6$, Fig. 6.2F). Annual average air surface temperature is highest priority at the outlet of the study area, near the Gulf ($S_7$, Fig. 6.2G). Annual average soil moisture is highest priority in southern Iraq ($S_8$, Fig. 6.2H), which corresponds to the regions of least precipitation ($S_6$, Fig. 6.2F). Similarly, annual average NDVI is highest priority (i.e., lowest observed values) in the southern portions of Iraq with low soil moisture and low precipitation ($S_9$, Fig. 6.2I). These results concur with previous studies that examine the spatial distribution of precipitation, temperature, soil moisture, and NDVI in Iraq and the Middle East (Al-Taei et al., 2023; Al-Timimi & Al-Khudhairy, 2018; Karakani et al., 2021; Yehia et al., 2023).

Scenarios $S_{10} - S_{15}$ consider social/other environmental factors in combination with water scarcity. In all six scenarios, basins of lower order (i.e., higher priority/concern) are generally found in Iraq. The spatial distribution of priority is similar for current youth population with exposure to water scarcity ($S_{10}$, Fig. 6.2J) and youth population and agricultural water scarcity ($S_{13}$, Fig. 6.2M). The southern basins of Iraq generally have the lowest order (i.e., higher priority/concern) when considering future youth population growth and water scarcity ($S_{11}$, Fig. 2K) and youth migration away from urbanized areas and water scarcity ($S_{14}$, Fig. 6.2N). Conversely, basins of southern Iraq have higher order when youth migration to urbanized areas and water scarcity is considered ($S_{12}$, Fig. 6.2L). Lastly, basins of western Iraq generally have lower order when youth distance from the 2023 Türkiye/Syria earthquakes are considered, as these basins were closest to the disaster and have high water scarcity concerns ($S_{15}$, Fig. 6.2O).

## 6.5.2 Risk as the Disruption of Basin Order

Fig. 6.3 shows spatial maps of basin-level risk for scenarios $S_{10} - S_{15}$ (i.e., scenarios of three or more factors) to improve understanding of where sub-basins increased or decreased in priority compared with the baseline scenario (defined by $S_1$). The greatest increase in basin order was approximately +36 while the greatest decrease in basin order was approximately -36. Generally, the greatest increase in order was observed in Iraq sub-basins south of the Euphrates-Tigris Rivers, regardless of the scenario, indicating the basins have the greatest youth population density exposed to extreme conditions of water scarcity. However, the relative increase/decrease in orders varies between the scenarios, with $S_{11}$ (Fig. 6.3B) depicting the greatest range in change in order and $S_{10}$ (Fig. 6.3A) depicting the smallest range in change in order.

Appendix 6.3 summarizes the top five basins with the largest increase and decrease in priority across the scenarios, with a reference map shown in Appendix 6.4. Sub-basins south of the Euphrates and Tigris Rivers in Iraq were generally identified as the highest priority basins when at least two factors were considered, indicating the basins have high youth population densities with exposure to extreme conditions of water scarcity. Southern basins of Iraq, in or near the Al-Muthanna governorate, were identified as basins of the greatest increase in priority when both water scarcity and youth population density are considered. Coincidentally, previous studies have identified this region as the highest rate of poverty in Iraq (Vishwanath & Krishnan, 2015).

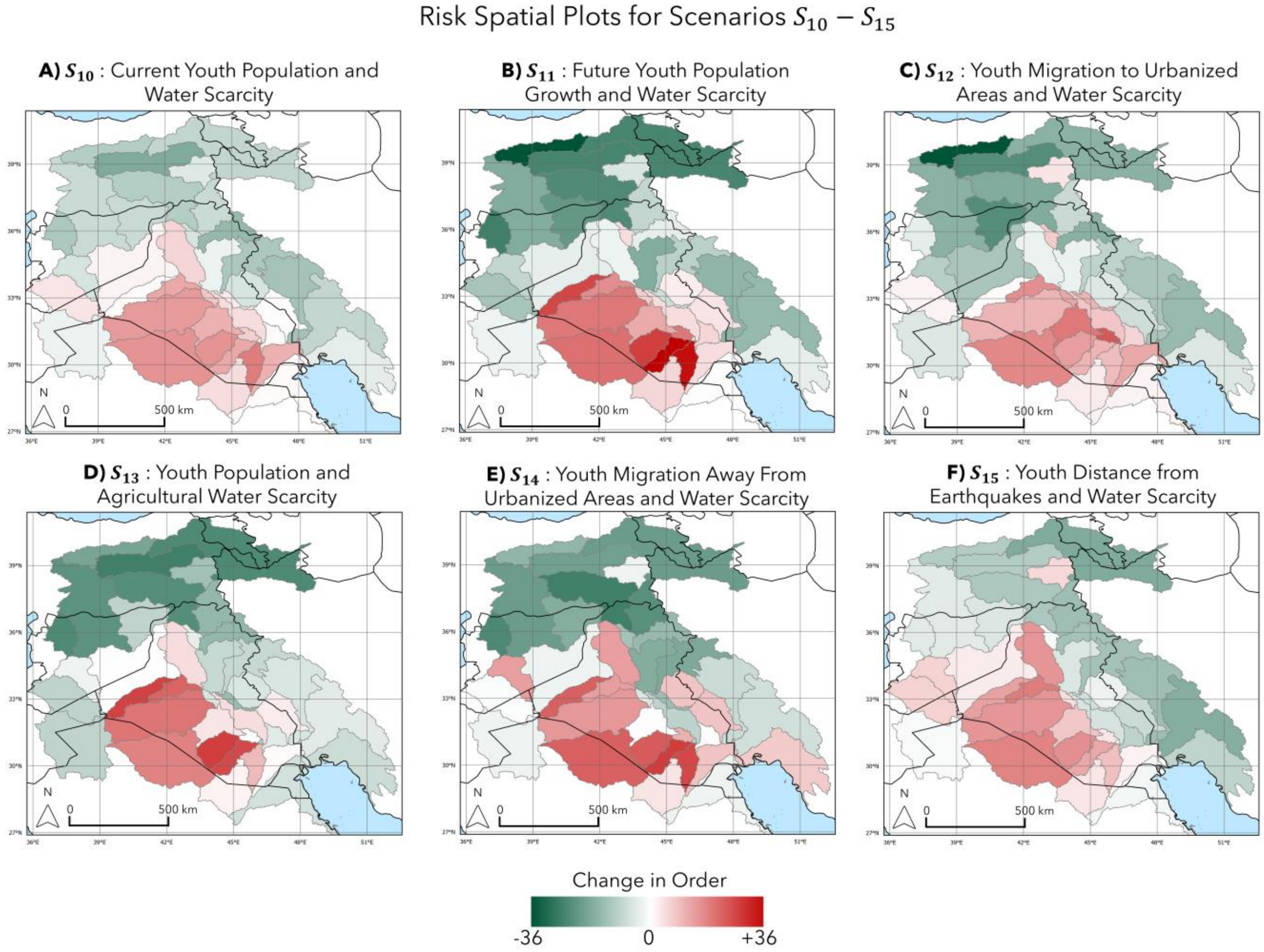

***Fig. 6.3:*** *Spatial maps of basin-level risk for scenarios of three or more factors (i.e., $S_{10} - S_{15}$). Basins in red indicate increased risk (i.e., a positive change in basin order). Basins in green indicate decreased risk (i.e., a negative change in basin order).*

### 6.5.3 Most and Least Disruptive Scenarios

Fig. 6.4A shows a bar graph of the sum of least square difference calculated for scenarios $S_2 - S_{15}$ using Eq. 7. Fig. 6.4B shows a bar graph of the normalized score of disruption calculated for scenarios $S_2 - S_{15}$ using Eq. 8.

Generally, scenarios of two or more factors ($S_{10} - S_{15}$) exhibited less disruption compared to scenarios of one factor ($S_2 - S_9$). Scenario $S_{10}$ (current youth population and water scarcity) had the least disruption across all scenarios, indicating youth population density generally tends to be highest in basins of greatest water availability. When considering only one factor, Scenario $S_5$ (distance from earthquake) had the least disruption. This indicates that basins of high youth population density were located close to the disaster. Thus, the priorities (i.e., basin order) showed little change.

Scenario $S_{14}$ (youth migration away from urbanized areas and water scarcity) had the most disruption when two or more factors were considered. This suggests that even though youth population density is low in basins of high agricultural area, an urban-to-rural migration pattern (such as caused by a public health crisis like the COVID-19 pandemic) would significantly disrupt basin priorities.

When only one factor was considered, Scenario $S_7$ (annual average air temperature) had the most disruption. This may reflect that populations have been detracted from development in these basins due to the high temperatures.

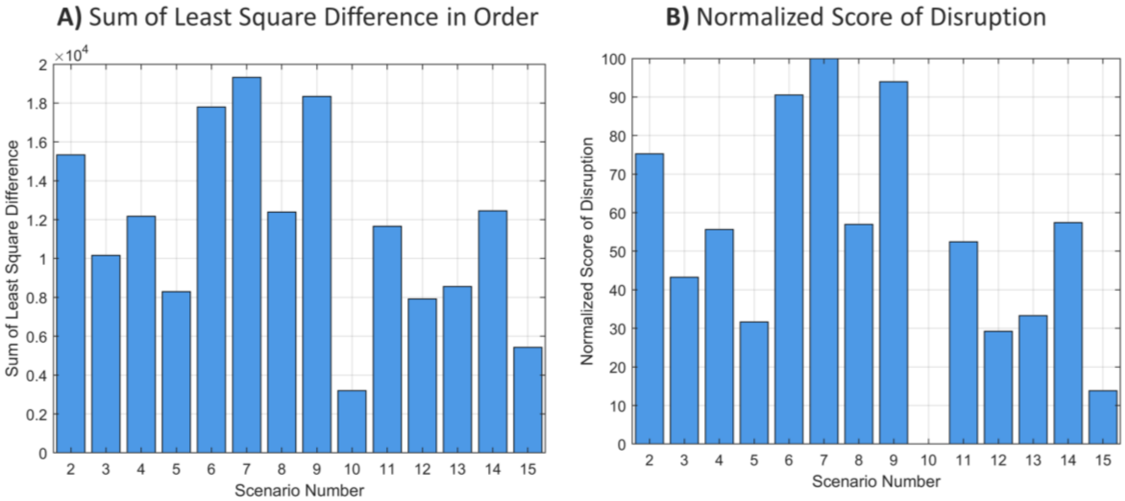

***Fig. 6.4:*** ***(A)*** *Sum of least square difference in order for scenarios* $S_2 - S_{15}$ *and* ***(B)*** *normalized score of disruption in order for scenarios* $S_2 - S_{15}$*. Both metrics are used to determine the most and least disruptive scenarios compared to the baseline order (*$S_1$*).*

## 6.6 Conclusions

In this study, we examine the spatial distribution of priority and risk at a sub-basin level with attention to water scarcity for transboundary basins of Iraq and the Middle East. Given that the region faces complex challenges of international water management and lacks extensive in-situ hydrological observations, this study leverages publicly available satellite-based Earth Observations to obtain hydrology data with sufficient spatial coverage of the transboundary basins, regardless of political borders. A qualitative summary of key findings is provided in Table 3 and described below.

Scenario order and risk spatial plots may be used by stakeholders to climate-conscious decisions when allocating resources to basins for sustainable development. For example, stakeholders may choose to invest in basins of the greatest overall risk (i.e., decrease risk) and greatest overall basin order (i.e., increase resilience). Conversely, stakeholders may decide to allocate resources aimed to incentivize climate migration away from basins of the greatest risk/priority during scenarios of water scarcity and towards basins of low risk (i.e., the most water resources). Preparation sudden-onset disasters in combination with water scarcity priorities, such as the 2023 Türkiye/Syria earthquake, may be challenging as the location of the future disaster is unknown. However, the spatial maps of basin order and risk could be used to support informed decisions on refugee relocation to the nearest basins with maximum water availability, as opposed to closest basins to the disaster (which may or may not have severe water scarcity challenges).

As previously noted, water scarcity and population are intertwined and multidisciplinary. While the scenarios demonstrated in this study make meaningful progress towards analyzing the combination of priorities using social, hydrological, and environmental factors, a limitation of this study is that it does not account for all potential factors influencing the system. For example, we did not consider factors of policy, religion, or conflict. Future work may build upon this research to continue identifying and incorporating factors which disrupt basin order considering both social priorities and water scarcity in the region.

Overall, the results of this paper improve understanding of the spatial distribution of basin-level priorities and risk considering social priorities, particularly for youth populations, and water scarcity in transboundary basins of Iraq and the Middle East. Findings from this study can support decision makers tasked with allocating resources aimed to decrease water scarcity risk and increase resilience in the region, particularly for vulnerable populations.

***Table 6.3:*** *Qualitative summary of results from this study including descriptions of figures/tables to reference within the manuscript and appendix.*

| Types of Results | Specific Results | Comments | Sources |
|---|---|---|---|
| Most disruptive scenarios | $S_{14}$ – *youth migration away from urbanized areas and water scarcity*<br>$S_7$ – *annual average air temperature* | Youth population density is relatively low in agricultural areas. A public health crisis, like COVID-19, which causes urban-to-rural migration would significantly disrupt priorities.<br>Youth population density is relatively low in the basins of highest air temperature, which may indicate that temperature extremes detract from development in these basins. | Fig. 6.2<br>Fig. 6.4 |
| Least disruptive scenarios | $S_{10}$ – *current youth population and water scarcity*<br>$S_5$ - *distance from earthquake* | Youth population density generally tends to be highest in basins with the most water availability in the region.<br>Basins of high youth population density were located closely to the 2023 Türkiye/Syria earthquake epicenters. | Fig. 6.2<br>Fig. 6.4 |
| Highest priority basins in disrupted orders of at least two factors | Iraq sub-basins south of the Tigris and Euphrates rivers | Basins of youth population with relatively high exposure to extreme hydrological conditions of water scarcity. | Fig. 6.2<br>Fig. 6.3 |

| | | | |
|---|---|---|---|
| Lowest priority basins in disrupted orders of at least two factors | Sub-basins north of Iraq | Basins of youth population with relatively low exposure to extreme hydrological conditions of water scarcity. | Fig. 6.2<br>Fig. 6.3 |
| Greatest increase in basin priority | Southern basins of Iraq in or near the Al-Muthanna governorate | Basins of youth population with the greatest exposure to extreme hydrological conditions of water scarcity. | Appendix 6.3A<br>Appendix 6.4 |
| Greatest decrease in basin priority | Northwestern basins, generally outside of Iraq | Basins of youth population with the least exposure to extreme hydrological conditions of water scarcity. | Appendix 6.3B<br>Appendix 6.4 |

## 6.7 Acknowledgements

The authors are grateful for the support and engagement of the Commonwealth Center for Advanced Logistics Systems, the United States Army Corps of Engineers (USACE), the United States Agency for International Development (USAID), and Ministries of Iraq including the Ministry of Water Resources, Ministry of Agriculture, and Ministry of Environment. The authors are additionally grateful to Tara Clark, USACE Transatlantic Division. This paper is based on work supported by the National Science Foundation (NSF) Graduate Research Fellowship Program (GRFP) under Grant No. 182490. Any opinions, findings, conclusions, or recommendations expressed in this work are those of the author(s) and do not necessarily reflect the views of the University of Virginia or the National Science Foundation.

# **Chapter 7:** Conclusions

## 7.1 Overview

This section is organized as follows. Section 7.2 provides a summary of the dissertation research. Section 7.3 provides a summary of key research contributions. Section 7.4 describes future work in natural disasters hydrology and risk. Section 7.5 provides final remarks.

## 7.2 Research Summary

This dissertation describes five interdisciplinary studies of monitoring hydrological natural disasters and risk associated with these extreme events. Throughout each, space-based Earth Observations were leveraged to obtain high-resolution spatial and temporal hydrological data. This was advantageous in regions traditionally limited by insufficient in-situ hydrological observations such as the Lake Victoria Basin of Africa, Iraq and transboundary regions of the Middle East, and hurricane regions of the Southeastern United States.

Two studies demonstrated methodology for hydrological monitoring using space-based Earth Observations (Chapters 2 and 3). This supports efforts to improve the accuracy and reliability of foundational hydrological data, such as the extent and location of inland waterbodies (Chapter

2) and the spatial and temporal variability of components of the water balance equation (Chapter 3).

Three studies demonstrated methodology for hydrological risk analysis using space-based Earth Observations and societal data (Chapters 4, 5, and 6). In each, we define *risk* as the disruption of system order. A *risk register of basins* was used to consider scenarios with criteria of hydrology and society, such as population and social vulnerability. Results of these chapters support efforts to improve understanding of basin-level risk given scenarios of hurricanes and social vulnerability (Chapter 4), multidecadal hydrological conditions and social vulnerability (Chapter 5), and water scarcity and population dynamics (Chapter 6).

Results and findings of this dissertation support the advancement of applications of remote sensing for hydrological monitoring, particularly in data-sparse regions of the world, and risk assessment of hydrological natural disasters where complex systems of society and the environment challenge the resilience of populations. This supports ongoing global efforts to decrease risk and increase resilience to hydrological disasters including floods, droughts, hurricanes, and water scarcity.

## 7.3 Summary of Key Contributions

Key contributions of this dissertation include the following:

**Chapter 2:** This study provided a foundational comparison of CYGNSS versus optical-sensor-based inland water masks. We found that a mosaic of binary thresholds using sub-basins and SNR improved performance compared to a singular binary threshold for the study area. A performance metric of ratio of inland water to catchment area revealed that CYGNSS, MODIS, and Landsat were within 2.3% of each other regardless of the sub-basin observed.

**Chapter 3:** This study was the first to validate the 1-km downscaled SMAP soil moisture dataset within the continent of Africa for describing hydrological extremes of floods and droughts. To our knowledge, this was the first study to conduct a hydrological spatial anomaly comparison for the 2019 – 2020 flood and the 2021 – 2022 drought events in the Lake Victoria Basin.

**Chapter 4:** This study was among the first to demonstrate a hydrological risk assessment for Hurricane Ian. The results indicated that while coastal basins had the most extreme hydrological exposure, inland basins tended to have higher priority due to social vulnerability.

**Chapter 5:** This study modeled resilience to multidecadal hydrological conditions. The results indicated patterns of populations of high socioeconomic concern co-located in basins of driest hydrological conditions. Similarly, populations of high SVI were found to be generally co-located in basins of low elevation.

**Chapter 6:** This study is among the first to examine the spatial distribution of basin-level priorities and risk of water scarcity and youth populations in Iraq and transboundary regions. The results indicated that population density is lowest in basins exposed to the highest temperatures. Additionally, populations with greatest exposure to extreme hydrological conditions of water scarcity are found in the southern basin of Iraq in or near the Al-Muthanna governate, which coincidentally has the highest poverty rate in Iraq.

## 7.4 Future Work in Natural Disasters Hydrology and Risk

Opportunities for future work in the field of natural disasters hydrology and risk are numerous, particularly considering the pattern of substantial economic and societal loss observed from hydrological disasters each year across the globe.

Two opportunities for future work related to hydrological monitoring include:

1) Further validation of hydrological Earth Observations in data-sparse regions of the world, especially Africa.
2) Further development of accurate and timely foundational hydrological data for applications of future disasters management.

Three opportunities for future work related to hydrological risk analysis include:

1) Increasing the complexity of scenarios by incorporating criteria of additional disciplines disrupted by hydrological disasters, such as public health and economy.
2) Developing scenarios to account for disruption of society due to cascading/compound hydrological disasters (For example, a wildfire can destroy vegetation cover, making the region at risk for flooding and landslides. Similarly, prolonged drought conditions can lead to crop failure, making the region susceptible to dust storms and increased air quality health concerns.).
3) Feasibility assessment of leveraging machine learning to forecast future scenarios and assess risk of hydrological disasters and social data with particular attention to ethics and algorithm bias.

## 7.5 Final Remarks

Satellite-based Earth Observations continually collect useful environmental information about our planet. As demonstrated in this dissertation, these high-resolution data at regular temporal scales can inform and improve hydrological monitoring and risk assessment. Because hydrological natural disasters transcend manmade and political boundaries, this perspective from space allows research to also cross borders and ensure that vulnerable communities lacking extensive ground monitoring are not neglected.

Bridging the gap between hydrology and society is necessary to address the complex environmental and societal challenges of hydrological natural disasters. Interdisciplinary research can catalyze innovative solutions. Increasing decision maker accessibility to timely and accurate data obtained through Earth Observations for hydrological monitoring and disaster risk reduction is paramount. When applied properly, these data can save lives.

This dissertation serves as a framework for further development of applications of Earth Observations data for hydrological natural disasters and risk. It supports the global efforts to advance the frontier of scientific knowledge to address the environmental and social challenges that natural disasters unleash across our planet.

# Appendices

## Appendix 2.1

Methodology Flow Chart:

The methodology includes the following three steps: 1) derive bivariate water masks from Earth Observations (CYGNSS, MODIS, Landsat), 2) compare bivariate water masks in a comparison water mask, and 3) overlay comparison water mask with commercial satellite imagery for select examples.

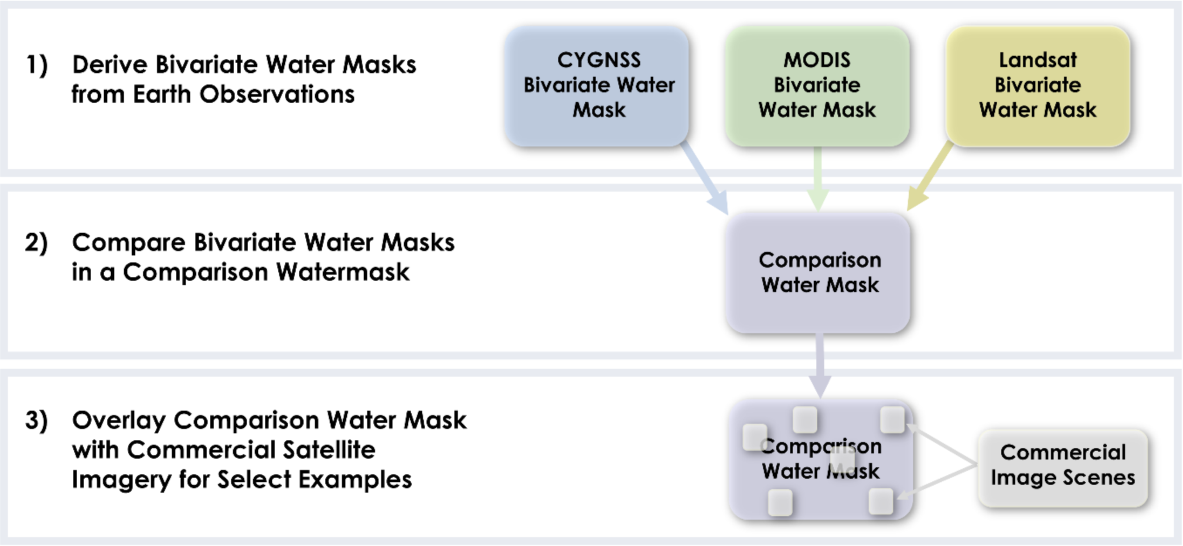

## Appendix 2.2

### HydroLAKES data:

HydroLAKES is a global database of over 1.43 million surface water polygons representing lakes and human-made reservoirs with surface areas of at least 10 ha (Messager et al., 2016). The HydroLAKES polygons were derived using a geo-statistical model based on land surface topography and includes estimates of lake volume and hydraulic residence time (Messager et al., 2016). This dataset was published in 2016 and is co-registered in the HydroSHEDS database. For this study, HydroLAKES was used to inform the SNR threshold to classify CYGNSS data as inland water (see Appendix 2.3 for further details).

## Appendix 2.3

USGS Watershed Boundary data:

For this project, the United States Geological Survey Hydrological Unit Code-02 (USGS HUC-02) watershed boundaries dataset was used. The USGS HUC-02 basin boundaries are obtained from the Watershed Boundary Dataset (WBD) which is a national hierarchical dataset of hydrological units at 2- to 16-digit codes. For more information about the USGS WBD, please visit https://user.gov/national-hydrography/watershed-boundary-dataset.

## Appendix 2.4

Summary Table of CYGNSS:

This table provides a concise overview of key specifications and characteristics of the CYGNSS mission. It includes information about the launch, manufacturer, spacecraft design, observation technology, and more (Al-Khaldi et al., 2021; C. S. Ruf et al., 2018).

| **CYGNSS Information** | |
|---|---|
| **Full mission name:** | Cyclone Global Navigation Satellite System (CYGNSS) |
| **Launch date:** | December 15, 2016 |
| **Manufacturer:** | University of Michigan and Southwest Research Institute |
| **Funding agency:** | National Aeronautics and Space Administration (NASA) |
| **Launch provider:** | Orbital ATK |
| **Number of microsatellites in constellation:** | 8 microsatellites |
| **Mass of one microsatellite:** | 24.7 kg |
| **Outer dimensions of one microsatellite:** | 51 x 24 x 159 cm |
| **Channels of receiver of one microsatellite:** | 4-channels |
| **Number of simultaneous measurements of constellation (maximum):** | 32 simultaneous measurements (4-channels on 8 microsatellites) |
| **Orbit altitude:** | Low Earth Orbit (~510 km) |
| **Observation technology:** | Global Navigation Satellite System Reflectometry (GNSS-R) |
| **Band wavelength of reflected signals:** | L-band frequency (1.575 GHz) |
| **Mean revisit between microsatellites:** | ~ 7 hours |
| **Median revisit between microsatellites:** | ~ 3 hours |
| **Designed spatial coverage to achieve 70% coverage within a 24-hour period:** | 35°S - 35°N |
| **Maximum spatial coverage:** | 38°S - 38°N |
| **Incoherent (diffuse) bistatic scattering spatial resolution:** | ~ 10 km (determined by delay and doppler filters) |
| **Coherent (specular) bistatic scattering spatial resolution:** | ~ 500 m (determined by First Fresnel Zone) |
| **Total mission cost:** | $150 million |

## Appendix 2.5

### Sensitivity Analysis:

In order to select threshold values of CYGNSS SNR to differentiate between inland water and land, a sensitivity analysis was conducted for both the percentile of SNR observations and the threshold window sizes for each sub-basin. HydroLAKES data were assumed to be ground-truth lake extent and location information for purposes of this study.

The sensitivity analyses aimed to maximize F1-score (a balance of P and R) between HydroLAKES (the *reference* water mask) and CYGNSS (the *predicted* water mask). A 50th percentile of CYGNSS observations obtained the maximum F1-score when the entire study area was compared to the reference water mask, and thus was used when testing for the threshold windows of each sub-basin. The Table below (Appendix 2.7) summarizes the SNR thresholds calculated for each USGS HUC-02 basin. Appendix 2.6 shows a graph of how F1-scores of CYGNSS surface reflectivity SNR values vary depending on the thresholding interval for each basin.

## Appendix 2.6

F1-scores versus SNR values:

F1-scores versus various CYGNSS surface reflectivity signal-to-noise ratio (SNR) values to define inland water for each USGS HUC-02 basin.

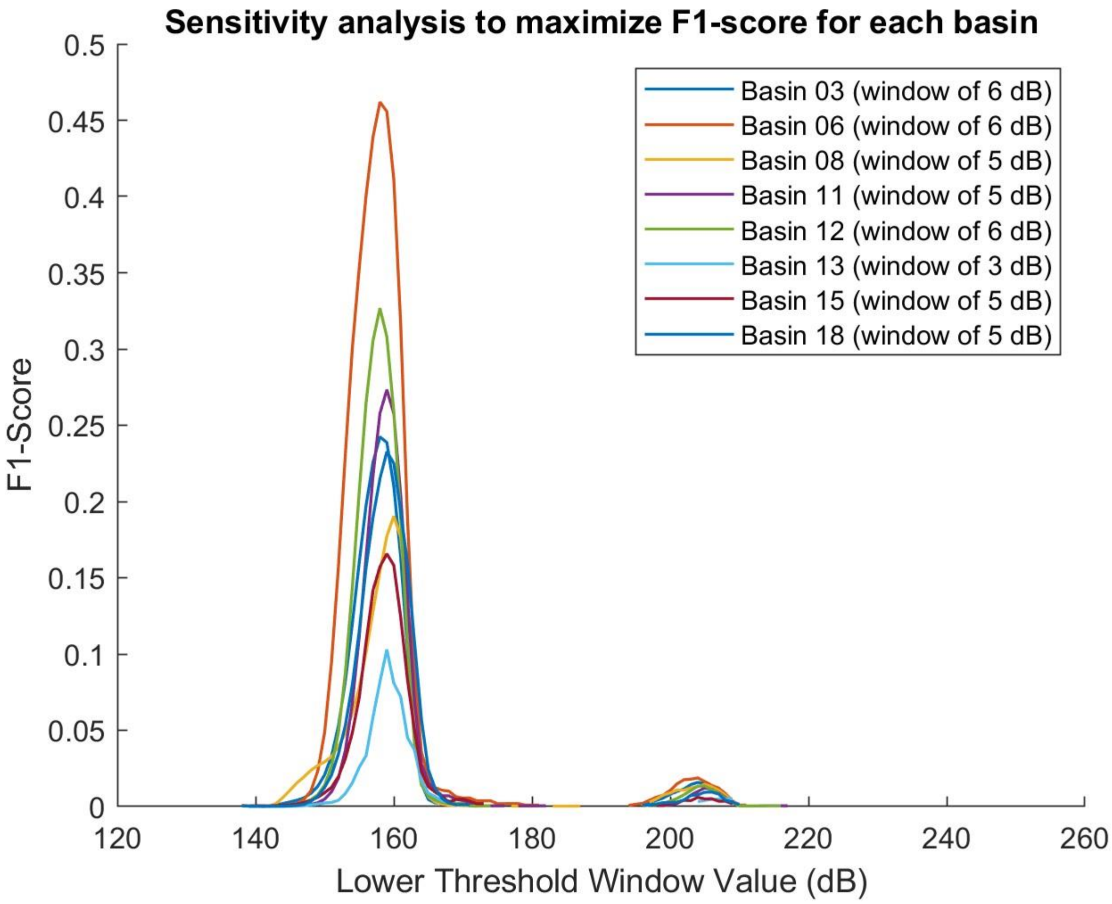

## Appendix 2.7

Table of SNR Threshold Windows:

Inland water surface reflectivity signal-to-noise-ratio (SNR) values for various basins determined from a sensitivity analysis which maximized F1-score compared to a reference dataset (HydroLAKES)

| Study Area | SNR Threshold Window |
|---|---|
| Total Study Area | 158 – 164 dB |
| USGS HUC – 02 Basin 03<br>South Atlantic Gulf basin (B03) | 158 – 164 dB |
| USGS HUC – 02 Basin 06<br>Tennessee basin (B06) | 158 – 165 dB |
| USGS HUC – 02 Basin 08<br>Lower Mississippi basin (B08) | 160 – 165 dB |
| USGS HUC – 02 Basin 11<br>Arkansas-White River basin (B11) | 159 – 164 dB |
| USGS HUC – 02 Basin 12<br>Texas-Gulf basin (B12) | 158 – 164 dB |
| USGS HUC – 02 Basin 13<br>Rio Grande basin (B13) | 159 – 162 dB |
| USGS HUC – 02 Basin 15<br>Lower Colorado basin (B15) | 159 – 164 dB |
| USGS HUC – 02 Basin 18<br>California basin (B18) | 159 – 164 dB |

## Appendix 2.8

Daily Water Pixel Occurrences in 2019 for CYGNSS, MODIS, and Landsat:

The number of daily 1-km water pixel observations within the study area for 2019 by CYNGSS, MODIS, and Landsat are shown below. Fewer MODIS and Landsat observations occur from May to October. This is likely due to seasonal precipitation and cloud cover. Conversely, CYNGSS observations are relatively consistent throughout the year due to usage of radar reflectometry (i.e., GNSS-R).

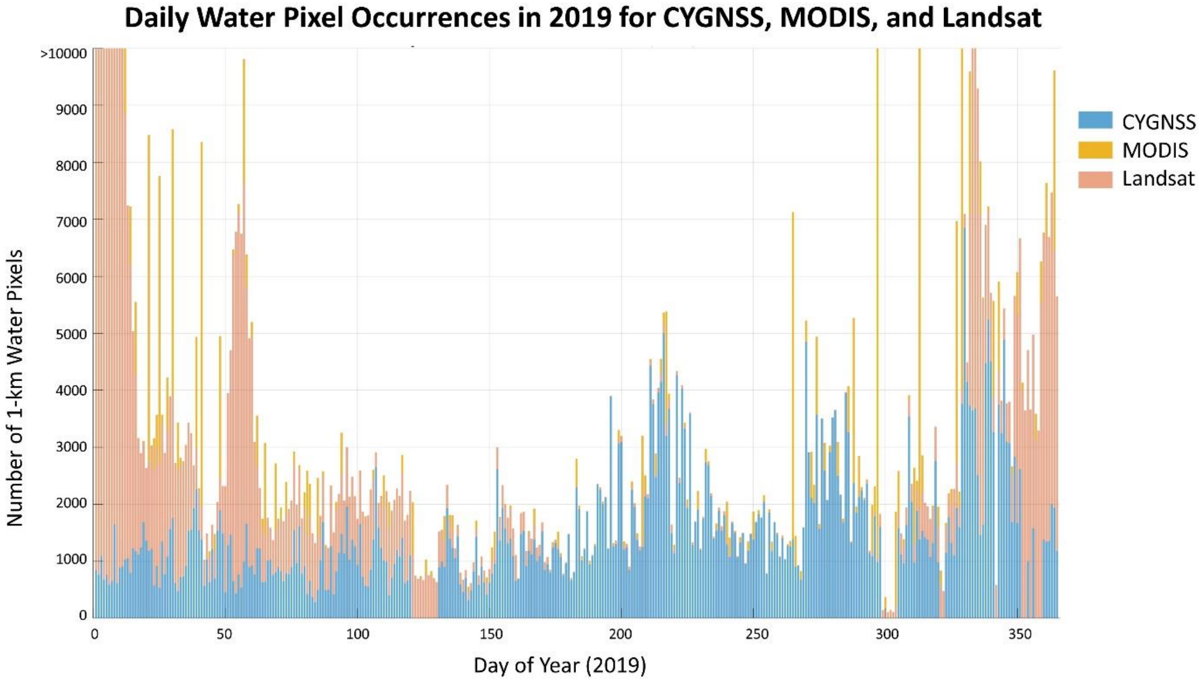

## Appendix 2.9

Basin-level confusion matrix statistics:

Results and discussions for the following confusion matrix statistics are provided in appendices 2.9.1-2.9.6: Recall (R), Precision (P), Specificity (SP), Miss Rate (M), False Detection Rate (FDR), and Accuracy (A). Please refer to the heatmaps in Fig. 3 of the main manuscript.

### Appendix 2.9.1: Recall (R)

A higher R indicates fewer TP classified than FP, meaning that the *predicted* water mask is more likely to capture positive instances. Thus, R should be maximized. However, this can often be at the expense of an increased FDR which may be undesirable for specific applications. The heatmap for R is shown in Fig. 2A. The lowest R tended to be observed in the Rio Grande basin (B13), regardless of the *predicted* water mask. This indicates either a low number of TP, a high number of FN, or a combination of both. For all basins, the R values tended to improve when CYGNSS was combined with either MODIS or Landsat for the *predicted* water mask.

### Appendix 2.9.2: Precision (P)

P indicates the level of confidence in positive predictions. Thus, a higher precision is desirable, and a lower precision is indicative of many FP. P is often used in combination with R to balance the trade-off between FP and FN. As shown in the P heatmap in Fig. 2B, P is generally lower across the entire study area and indicates a high percentage of FP predictions and thus disagreement between the water masks. The western basins (B13, B15, and B18) have the lowest P and the highest disagreement between the CYGNSS, Landsat, and MDOIS water masks.

### Appendix 2.9.3: Specificity (SP)

SP represents the percentage of land pixels classified by the *reference* water mask that were also classified as land by the *predicted* water mask. A higher SP indicates that fewer negative instances were classified as positive, which is desirable for many applications. Like R, a higher SP value alone is not always ideal and it is necessary to determine a balance with SN. The heat map for SP is shown in Fig. 2C. Here, the Lower Mississippi basin (B08) and the total study area (AOI) had the lowest SP and thus the most disagreement of land classifications. The Rio Grande Basin (B13) has the highest SP, yet as previously discussed, had one of the lowest R.

### Appendix 2.9.4: Miss Rate (M)

M indicates the percentage of water pixels in the *reference* water mask which were classified as land by the *predicted* water mask. Thus, a low M is desirable. Fig. 2D shows the M heatmaps for each basin. Generally, M is low across the study area and each basin, indicating that relatively few water pixels identified by the *reference* water mask were classified as land by the *predicted* water mask. However, the Lower Mississippi basin (B08) had the highest M regardless of the *reference/predicted* water mask compared.

### Appendix 2.9.5: False Detection Rate (FDR)

FDR in this study quantifies the percentage of land pixels in the *reference* water mask classified as water pixels in the *predicted* water mask. A higher FDR indicates strong disagreement between the water masks. Hence, FDR should be minimized for this application. The FDR heatmap is shown in Fig. 2E. Generally, FDR is lower in the eastern portion of the study area compared to the western portion. This can likely be explained by a high number of FP water pixels classified by the *predicted* water mask in the western portions of the study area. Additionally, the lowest FDR was obtained in the Lower Mississippi basin (B08).

### Appendix 2.9.6: Accuracy (A)

Accuracy (A) in a confusion matrix indicates that the *predicted* water mask has few errors in its prediction when compared to the *reference* water mask. Fig. 2F shows the heatmaps for accuracy at the basin-level and total study area, which is relatively low regardless of the observation region. The lowest accuracy for all predicted water masks was observed in the Lower Mississippi basin (B08) which is likely due to disagreements in water classifications along the Mississippi River watershed. It is important to note however that accuracy alone may not be a sufficient measure of the predicted water mask's performance, especially when the class distribution is imbalanced. For example, a high number of FN would still result in high accuracy even if the *predicted* water mask never predicts TP. In these instances, precision, recall, and F1-score (a balance between precision and recall) should also be considered to gain a more comprehensive understanding of the predicted water mask's performance.

# Appendix 2.10

Table of ratio of inland water area to catchment area for sub-basins:

A summary of the performance metric of the ratio of inland water area to catchment area for sub-basins is provided in the table below.

| **Basin** | **Ratio of inland water area to sub-basin catchment area (%)** | | | | |
|---|---|---|---|---|---|
| | Landsat | CYGNSS | MODIS | MODIS + CYGNSS | Landsat + CYGNSS |
| B03 | 1.38 | 1.44 | 1.27 | 2.05 | 2.24 |
| B06 | 1.30 | 1.96 | 0.62 | 2.10 | 2.48 |
| B08 | 5.63 | 3.37 | 4.62 | 6.42 | 7.37 |
| B11 | 0.93 | 1.16 | 0.46 | 1.38 | 1.77 |
| B12 | 0.98 | 0.90 | 0.73 | 1.29 | 1.53 |
| B13 | 0.05 | 0.13 | 0.01 | 0.13 | 0.16 |
| B15 | 0.25 | 0.68 | 0.08 | 0.72 | 0.85 |
| B18 | 0.61 | 1.29 | 0.37 | 1.48 | 1.65 |

## Appendix 2.11

Summary Table of Commercial High-Resolution Satellite Imagery

Information for the commercial satellite data used in this study is provided in the table below. This includes the name of the location, the commercial company provider, the date of acquisition of the image scenes, and the image identification number(s). For additional details of the commercial data, please consult the meta-data associated with the image identification number(s) via the respective commercial data provider.

| **Location** | **Commercial Company** | **Date of Acquisition** | **Image Identification Number(s)** |
|---|---|---|---|
| Salton Sea, California | DigitalGlobe | 02/23/2019 | 10400100499A8000<br>1040010048634500 |
| Lake Maurepas and Lake Pontchartrain, Louisiana | DigitalGlobe | 07/04/2019 | 104001004F688700 |
| Lake Hartwell, Georgia and South Carolina | Planet Labs, Inc. | 04/01/2019 | 20190401_154607_0e0f<br>20190401_154606_0e0f |
| Tennessee River, Tennessee | Planet Labs, Inc. | 11/13/2019 | 20191113_162215_98_1057<br>20191113_162213_96_1057<br>20191113_162211_93_1057<br>20191113_162209_93_1057<br>20191113_162207_87_1057 |
| Lake Kissimmee, Florida | Planet Labs, Inc. | 11/29/2019 | 20191129_154208_1025<br>20191129_154207_1025<br>20191129_154206_1025<br>20191129_154205_1025 |
| Sam Rayburn Reservoir, Texas | Planet Labs, Inc. | 09/04/2019 | 20190904_163504_1013<br>20190904_163503_1013<br>20190904_163502_1013<br>20190904_163501_1013<br>20190904_163500_1013 |

## Appendix 2.12

Summary table of percent of commercial satellite image scene classified as inland water by CYGNSS, Landsat, MODIS, and hand drawn water masks:

The percentage of commercial satellite image scenes classified as inland water by CYGNSS, Landsat, MODIS, and hand drawn water masks is summarized in the table below. The commercial image scenes are visually displayed in Fig. 2.4 of the main manuscript. Regional, topographic, and vegetative differences of the image scenes may explain the percentage of image scene pixel classified by each observation system for the select examples (see section 2.3.4 of the main manuscript for further discussion of the commercial satellite imagery and Comparison Water Mask).

| **Classification of pixels** | **Commercial image scene (shown in Fig. 4)** | | | | | |
|---|---|---|---|---|---|---|
| | A | B | C | D | E | F |
| Hand drawn water mask | 44% | 60% | 18% | 13% | 23% | 24% |
| Non-water (based on hand drawn water mask) | 56% | 40% | 82% | 87% | 77% | 76% |
| MODIS only water | 7% | 26% | 0% | 0% | 1% | 2% |
| Landsat only water | 1% | 0% | 2% | 1% | 0% | 2% |
| CYGNSS only water | 0% | 13% | 13% | 12% | 9% | 5% |
| MODIS & Landsat water | 19% | 48% | 0% | 7% | 0% | 12% |
| CYGNSS & MODIS water | 3% | 2% | 2% | 2% | 3% | 1% |
| MODIS & Landsat water | 27% | 11% | 0% | 16% | 16% | 18% |
| CYGNSS & Landsat water | 1% | 5% | 5% | 7% | 0% | 3% |
| CYGNSS, Landsat, and MODIS water | 27% | 11% | 0% | 16% | 16% | 18% |

## Appendix 3.1

Summary of four soil moisture stations used for validation from the Trans-African Hydro-Meteorological Observatory (TAHMO) network. Data was accessed through the International Soil Moisture Network (ISMN).

| ISMN Station Name | Country | Observation Depth (m) | Start Date | End Date |
|---|---|---|---|---|
| Apakope Kayove | Rwanda | 0.20 | 10/23/2018 | 12/31/2021 |
| Irbaan Primary | Kenya | 0.20 | 8/2/2019 | 12/31/2021 |
| Nakivubo Blue Primary School | Uganda | 0.20 | 8/22/2019 | 12/31/2021 |
| Olderkesi Secondary School | Kenya | 0.2 | 8/6/2019 | 12/31/2021 |

## Appendix 3.2

Metrics and statistics from validation of in-situ near-surface soil moisture observations from the International Soil Moisture Network (ISMN) with the 1-km and 9-km Soil Moisture Active Passive (SMAP) observations at 6:00AM overpasses. Number of observations, $R^2$, unbiased root mean square error (ubRMSE), bias, and p-value are provided for 1-km (table A) and 9-km (table B) SMAP validation at each site.

### A: Validation Statistics of 1-km SMAP Observations

| **ISMN Station Name** | **Number of Observations** | **$R^2$** | **ubRMSE** | **Bias** | **p-value** |
|---|---|---|---|---|---|
| Apakope Kayove | 126 | 0.494085 | 0.082586 | 0.082567 | 4.54E-20 |
| Irbaan Primary | 130 | 0.505022 | 0.020658 | 0.020462 | 2.79E-21 |
| Nakivubo Blue Primary School | 111 | 0.153645 | 0.004623 | -0.00459 | 2.1E-05 |
| Olderkesi Secondary School | 141 | 0.427319 | 0.019615 | 0.011919 | 1.53E-18 |

### B: Validation Statistics of 9-km SMAP Observations

| **ISMN Station Name** | **Number of Observations** | **$R^2$** | **ubRMSE** | **Bias** | **p-value** |
|---|---|---|---|---|---|
| Apakope Kayove | 126 | 0.457544 | 0.146901 | 0.146819 | 3.55E-18 |
| Irbaan Primary | 130 | 0.548914 | 0.033146 | 0.032838 | 7.04E-24 |
| Nakivubo Blue Primary School | 111 | 0.159815 | 0.029315 | -0.0293 | 1.38E-05 |
| Olderkesi Secondary School | 141 | 0.477956 | 0.031178 | 0.026849 | 2.33E-21 |

# Appendix 3.3

Results of validation of in-situ near-surface soil moisture observations from the International Soil Moisture Network with the 1-km and 9-km Soil Moisture Active Passive (SMAP) observations at 6:00AM overpasses.

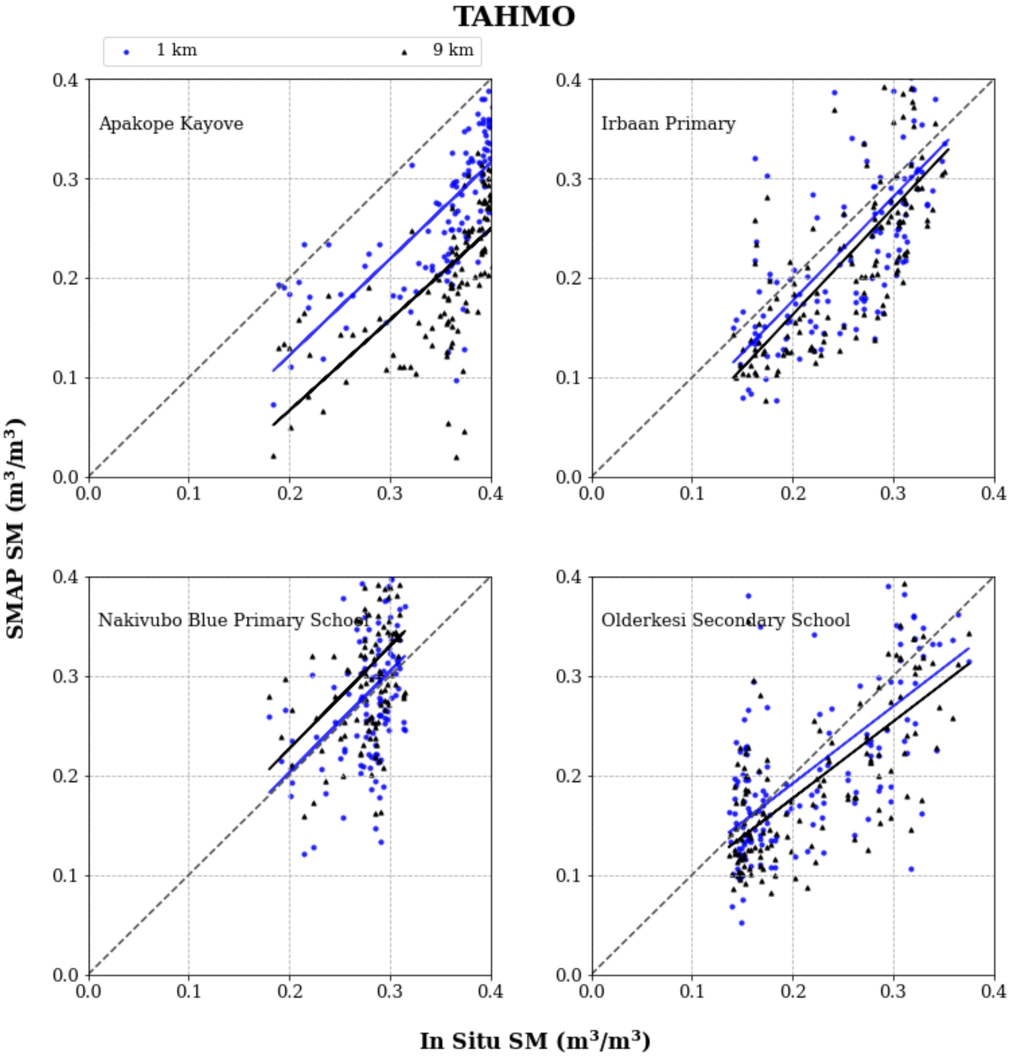

# Appendix 3.4

Time series of in-situ near-surface soil moisture observations from four TAHMO stations compared with 1-km and 9-km SMAP soil moisture observations from 2015 – 2021.

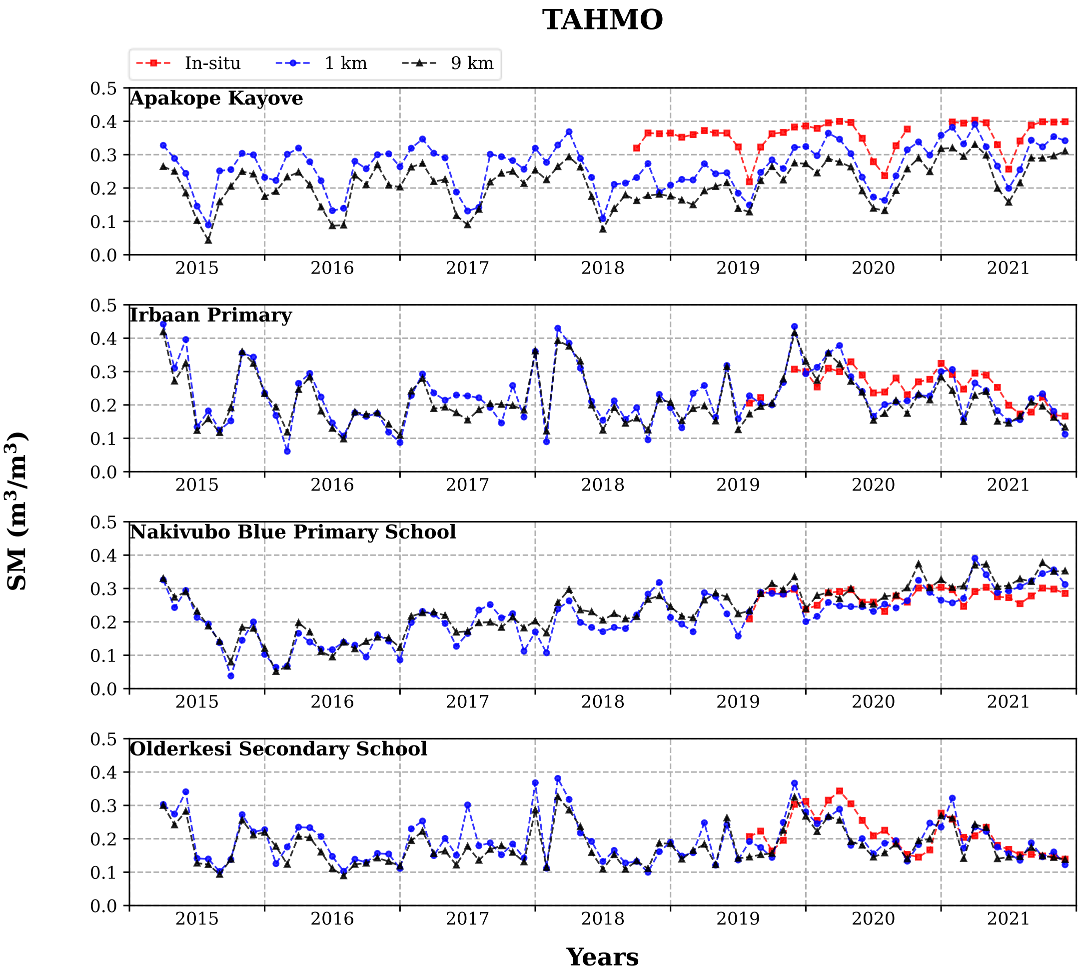

## Appendix 4.1

Examples of tropical cyclone disaster challenges associated with social vulnerability during each phase of the disaster cycle:

- **Mitigation:** Socially vulnerable individuals are less likely to have the financial means to purchase insurance or to live outside of hazard-prone areas (Cutter et al., 2003; Flanagan et al., 2011, 2018; Fothergill & Peek, 2004; Yarveysi et al., 2023). Housing structures, such as mobile homes, are typically ill-equipped to withstand exposure to tropical cyclone conditions (Flanagan et al., 2011; Fothergill & Peek, 2004; Yarveysi et al., 2023).
- **Preparedness:** The socially vulnerable are less likely to have the physical or financial means to evacuate prior to a tropical cyclone (Anand et al., 2023; Flanagan et al., 2011; Meyer et al., 2018). This may stem from a lack of transportation access (i.e., no vehicle, no affordable public transportation alternatives, etc.), an inability to afford evacuation costs (i.e., hotels/temporary lodging, food, fuel, etc.), or a need for increased evacuation assistance (i.e., for the elderly, disabled, and children) (Cutter et al., 2003; Emrich & Cutter, 2011; Flanagan et al., 2011).
- **Response:** Emergency notifications and messaging may not be readily available in languages other than English, making it difficult for racial and ethnic minorities to receive timely emergency information if they are not proficient in English (Cutter et al., 2003; Flanagan et al., 2011). If English is not the first language, cultural and language barriers can increase the difficulty of navigating access to post-disaster funding and aid for the socially vulnerable (Cutter et al., 2003).

- **Recovery:** Communities of high social vulnerability tend to be the slowest to recover following major disasters (Flanagan et al., 2018). Their livelihoods are disproportionately affected by post-disaster damages such as water contamination, loss of sewer systems, power outages, etc. (Cutter et al., 2003).

## Appendix 4.2

Summary of themes and variables contributing to Census-tract level Social Vulnerability Index (SVI) calculation (CDC/ATSDR, 2023).

| **Overall Vulnerability** | |
|---|---|
| **Themes** | **Variables** |
| Socioeconomic Status | I. Below 150% Poverty<br>II. Unemployed<br>III. Housing Cost Burden<br>IV. No High School Diploma<br>V. No Health Insurance |
| Household Characteristics | I. Aged 65 and Older<br>II. Aged 17 and Younger<br>III. Civilian with a Disability<br>IV. Single-Parent Households<br>V. English Language Proficiency |
| Racial and Ethnic Minority Status | I. Hispanic or Latino (of any race)<br>II. Black and African American, Not Hispanic or Latino<br>III. American Indian and Alaska Native, Not Hispanic or Latino<br>IV. Asian, Not Hispanic or Latino<br>V. Native Hawaiian or Other Pacific Islander, Not Hispanic or Latino<br>VI. Other Races, Not Hispanic or Latino |
| Housing Type and Transportation | I. Multi-Unit Structures<br>II. Mobile Homes<br>III. Crowding<br>IV. No Vehicle<br>V. Group Quarters |

## Appendix 4.3

Additional details on datasets used for demonstration of the methodology for Hurricane Ian:

### HydroBASINS

HydroBASINS is a global dataset of hierarchical sub-basin boundaries at up to 12 scales (Lehner & Grill, 2013). This dataset is derived from NASA SRTM DEMs at a spatial resolution of approximately 3 arc seconds. The nested sub-basins are determined by continually delineating two sub-basins where two rivers converge, so long as each sub-basin maintains a minimum upstream area of at least 100 $km^2$ (Lehner & Grill, 2013). Additional details of HydroBASINS are available in 2023 at https://www.hydrosheds.org/products/hydrobasins.

### GPM IMERG

Precipitation data are derived from the Integrated Multi-satellitE Retrievals for Global Precipitation Measurement (GPM IMERG) missions. This satellite constellation of infrared and passive microwave sensors is a joint mission between NASA and the Japan Aerospace and Exploration Agency (JAXA) which provides up to half-hourly precipitation observations at a spatial resolution of 0.1° (Huffman et al., 2020). Previous studies have demonstrated that GPM IMERG adequately detects the spatial variability of major hurricanes, albeit tendencies to underrepresent precipitation in coastal areas and near the core of hurricanes (Omranian et al., 2018; Pradhan et al., 2022). However, GPM IMERG remains a useful observation for spatial and temporal precipitation estimates during extreme meteorological events because *in-situ* observation systems may suffer instrument failures during hurricanes, as occurred during Hurricane Ian (Bucci et al., 2022). The technical documentation for GPM IMERG is available in 2023 at: https://gpm.nasa.gov/documents/IMERG-V06-Technical-Documentation.

### ECMWF ERA5

Wind speed data were obtained from the Copernicus Climate Change Service (C3S) European Centre for Medium-Range Weather Forecast (ECMWF) Reanalysis Version 5 (ERA5). This global reanalysis product, ERA5, is derived from physics-based modeling using both observations and model data as inputs to achieve an atmospheric spatial resolution of approximately 0.25° (Hersbach et al., 2020). Recently, ERA5 has demonstrated an improved representation of tropical cyclones compared to previous ERA versions (Hersbach et al., 2020; Slocum et al., 2022; Zarzycki et al., 2021). The technical documentation of ERA5 is available in 2023 at: https://confluence.ecmwf.int/display/CKB/ERA5%3A+data+documentation.

### SMAP-Derived 1-km Downscaled Surface Soil Moisture Product

The Soil Moisture Active Passive (SMAP) Derived 1-km Downscaled Surface Soil Moisture Product is used to calculate the 5-day antecedent near-surface soil moisture (0 – 5 cm depth below the surface of the Earth) (Lakshmi & Fang, 2023). This global dataset is derived from the SMAP L-band radiometer and utilizes the Moderate Resolution Imaging Spectroradiometer (MODIS) land surface temperature data to downscale soil moisture to a high spatial resolution of 1-km (Fang et al., 2022). This dataset has been validated across various biomes and topographies, including within the continental United States, by using networks of *in-situ* soil moisture instruments (Fang et al., 2020, 2022; Pavur & Lakshmi, 2023). The data and additional details on the SMAP-Derived 1-km Downscaled Surface Soil Moisture Product are available in 2023 at: https://doi.org/10.5067/U8QZ2AX5V7B.

## Appendix 4.4

List of acronyms used in manuscript:

DEM: Digital Elevation Model

ERA5: Reanalysis Version 5, produced by the Copernicus Climate Change Service (C3S) European Centre for Medium-Range Weather Forecast (ECMWF)

GPM IMERG: Integrated Multi-satellitE Retrievals for Global Precipitation Measurement mission

JAXA: Japan Aerospace and Exploration Agency (JAXA)

MSL: Mean Sea Level

MODIS: Moderate Resolution Imaging Spectroradiometer

NASA: National Aeronautics and Space Administration

NOAA: National Oceanic and Atmospheric Administration

SEIV: Block-level Socio-Economic-Infrastructure Vulnerability Index developed by Yarveysi et al., 2023

SMAP: Soil Moisture Active Passive

SoVI: County-level Social Vulnerability Index developed by Cutter et al., 2003

SVI: Census-tract level Social Vulnerability Index developed by the Centers for Disease Control (CDC) and Prevention Agency for Toxic Substances and Disease Register (ASTDR)

USA: United States of America

## Appendix 4.5

List of variables used in manuscript:

$P1$: cumulative precipitation

$P2$: maximum hourly precipitation

$R$: risk; the difference between the baseline order and scenario order of a given basin

$SM$: five-day antecedent soil moisture

$SVI$: basin order using Social Vulnerability Index data; the baseline order

$u$ : u-component of wind in the longitudinal direction 10 m above the surface of the Earth

$w$: maximum hourly wind speed

$x(S_n)$: score of disruptiveness for a given scenario $(S_n)$; the sum over the basins of the squared differences of the baseline order and disrupted order

$X(S_n)$: normalized score of disruptiveness for a given scenario $(S_n)$; the score of disruptiveness for a given scenario $x(S_n)$ minus the minimum score of disruptiveness $(x(S)_{min.})$ divided by the maximum score of disruptiveness $(x(S)_{max.})$ minus the minimum score of disruptiveness $(x(S)_{min.})$

## Appendix 6.1

Summary of basin ordering methods for each social, hydrological, and environmental factor, depending on the priorities of stakeholders. The maximum and minimum order basins are indicated as either the basin of lowest order (equal to or near a value of 1, i.e., the greatest water needs) or basin of highest order (equal to or near a value of 43, i.e., the least water needs).

| Factor | Basin ordering method | Basin of lowest order (~1) (i.e., greatest water needs) | Basin of highest order (~43) (i.e., least water needs) |
|---|---|---|---|
| Youth population density (YPD) | Descending | Maximum | Minimum |
| Population growth rate (PGR) | Descending | Maximum | Minimum |
| Percentage of urbanized basin area (URB) | Descending | Maximum | Minimum |
| Percentage of agriculture basin area (AGR) | Descending | Maximum | Minimum |
| Precipitation (P) | Ascending | Minimum | Maximum |
| Air surface temperature (T) | Descending | Maximum | Minimum |
| Root zone soil moisture (RZSM) | Ascending | Minimum | Maximum |
| NDVI | Ascending | Minimum | Maximum |
| Distance from earthquake epicenter to basin centroid (D) | Ascending | Minimum | Maximum |

## Appendix 6.2

Annual time series of select social and hydrological factors in the geographic area of demonstration from 2003 – 2022 including **(a)** total population, **(b)** precipitation, **(c)** surface temperature, **(d)** normalized difference vegetation index (NDVI), and **(e)** root zone soil moisture.

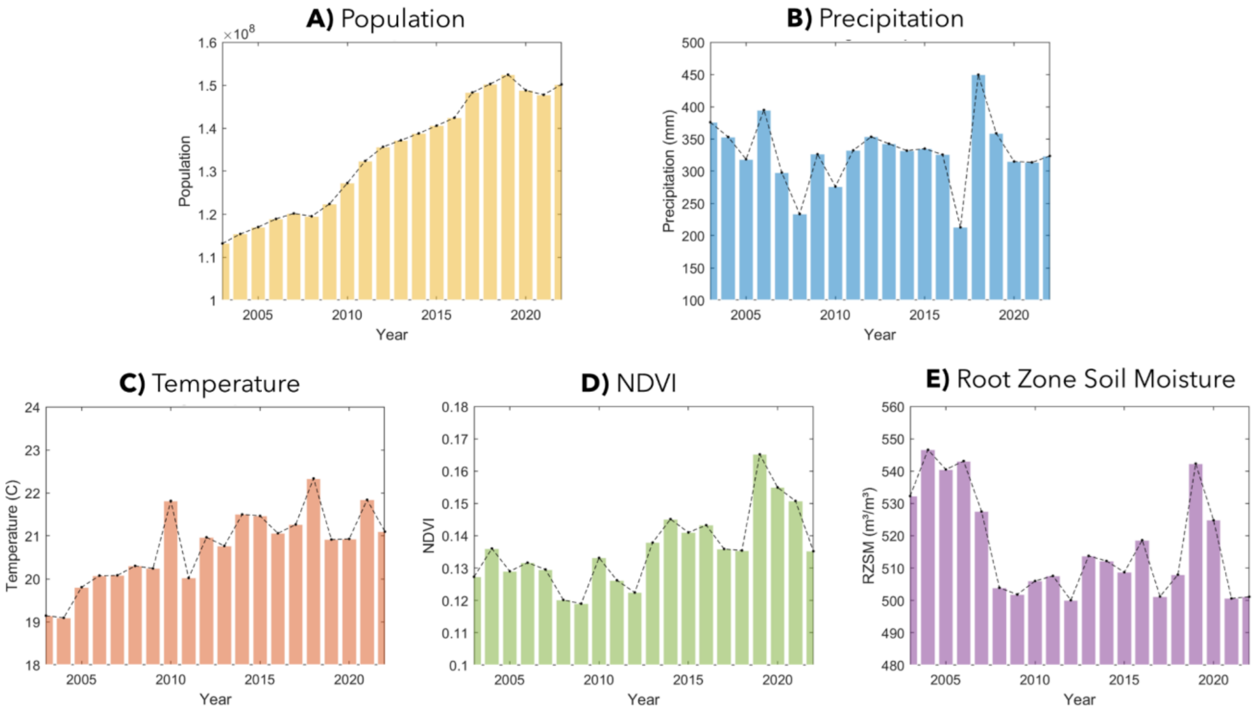

# Appendix 6.3

Summary of the basins of **(a)** greatest increase in priority and **(b)** decrease in priority compared to the baseline scenario, $S_1$. For basins of the largest increase in priority, the regions had high baseline order (i.e., relatively low youth population density) but low scenario order due to relatively high concerns for water scarcity (Appendix 6.3A). Conversely, basins of the largest decrease in priority had low baseline order (i.e., relatively high youth population density) but high scenario order due to greater water availability (Appendix 6.3B). A reference map of basin locations is provided in Appendix 6.4.

***(A)*** *Top five basins (~1%) with largest increase in priority across scenarios compared to the baseline order ($S_1$). See Appendix 6.4 for a reference map of the basins.*

| Rank of largest increase in priority | Basin Name ($b_i$) | Increase in Order | Baseline Order ($S_1$) | Scenario of Minimum Order ($S_n$) | Minimum Order |
|---|---|---|---|---|---|
| 1 | 2050815450 | +36 | 43 | $S_{11}$ | 7 |
| 2 | 2050815450 | +35 | 43 | $S_{14}$ | 8 |
| 3 | 2050816590 | +34 | 38 | $S_{11}$ | 4 |
| 4 | 2050816590 | +33 | 38 | $S_{14}$ | 5 |
| 5 | 2050810230 | +33 | 36 | $S_{13}$ | 3 |

***(B)*** *Top five basins (~1%) with largest decrease in priority across scenarios compared to the baseline order ($S_1$). See Appendix 6.4 for a reference map of the basins.*

| Rank of largest decrease in priority | Basin Name ($b_i$) | Decrease in Order | Baseline Order ($S_1$) | Scenario of Maximum Order ($S_n$) | Maximum Order |
|---|---|---|---|---|---|
| 1 | 2050668190 | -35 | 3 | $S_{11}$ | 38 |
| 2 | 2050668190 | -34 | 3 | $S_{12}$ | 38 |

| | | | | | |
|---|---|---|---|---|---|
| 3 | 2050723850 | -29 | 6 | $S_{14}$ | 35 |
| 4 | 2050086110 | -27 | 14 | $S_{14}$ | 41 |
| 5 | 2050086110 | -26 | 14 | $S_{11}$ | 40 |

## Appendix 6.4

Reference map of basins of greatest increase and decrease in basin order, as summarized in Appendix 6.3. Basins of greatest decrease in order are circled in green. Basins of greatest increase in order are circled in red.

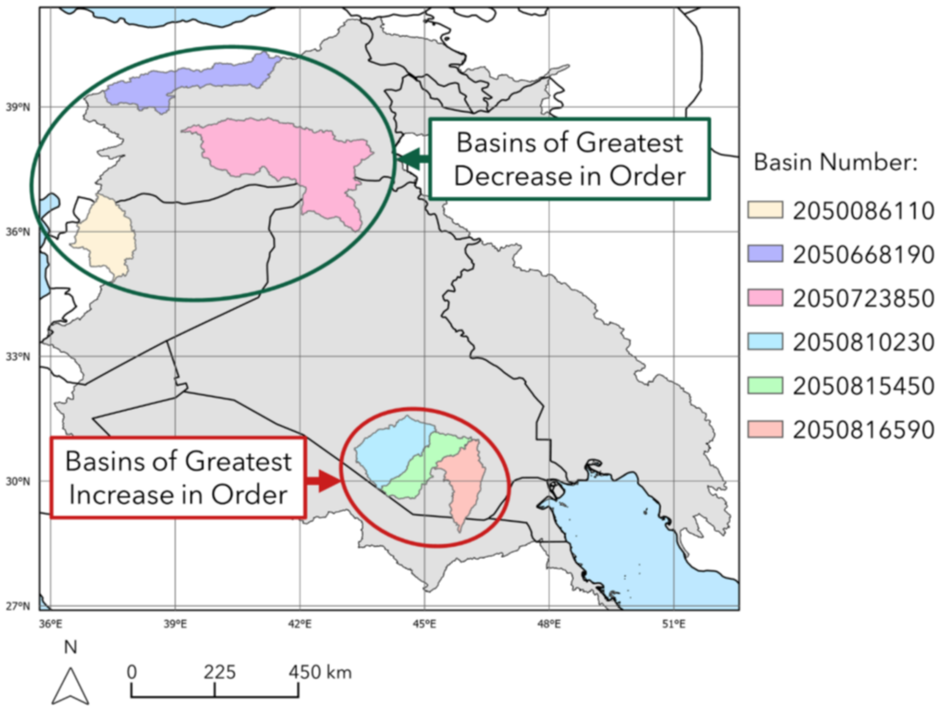

# References

Agutu, N. O., Ndehedehe, C. E., Awange, J. L., Kirimi, F., & Mwaniki, M. (2021). Understanding uncertainty of model-reanalysis soil moisture within Greater Horn of Africa (1982–2014). *Journal of Hydrology*, *603*. https://doi.org/10.1016/j.jhydrol.2021.127169

Al-Asadi, S. A. R., Alhello, A. A., Ghalib, H. B., Muttashar, W. R., & Al-Eydawi, H. T. (2023). Seawater intrusion into Shatt Al-Arab River, Northwest Arabian/Persian Gulf. *Journal of Applied Water Engineering and Research*, *11*(2), 289–302. https://doi.org/10.1080/23249676.2022.2113460

Albarakat, R., & Lakshmi, V. (2019). Monitoring dust storms in Iraq using satellite data. *Sensors (Switzerland)*, *19*(17). https://doi.org/10.3390/s19173687

Albarakat, R., Lakshmi, V., & Tucker, C. J. (2018). Using satellite remote sensing to study the impact of climate and anthropogenic changes in the Mesopotamian Marshlands, Iraq. *Remote Sensing*, *10*(10). https://doi.org/10.3390/rs10101524

Albarakat, R., Le, M. H., & Lakshmi, V. (2022). Assessment of drought conditions over Iraqi transboundary rivers using FLDAS and satellite datasets. *Journal of Hydrology: Regional Studies*, *41*. https://doi.org/10.1016/j.ejrh.2022.101075

Al-Khaldi, M. M., Johnson, J. T., Gleason, S., Chew, C. C., Gerlein-Safdi, C., Shah, R., & Zuffada, C. (2021). Inland Water Body Mapping Using CYGNSS Coherence Detection. *IEEE Transactions on Geoscience and Remote Sensing*. https://doi.org/10.1109/TGRS.2020.3047075

Alsdorf, D., Beighley, E., Laraque, A., Lee, H., Tshimanga, R., O'Loughlin, F., Mahé, G., Dinga, B., Moukandi, G., & Spencer, R. G. M. (2016). Opportunities for hydrologic research in the

Congo Basin. *Reviews of Geophysics*, *54*(2), 378–409. https://doi.org/10.1002/2016RG000517

Alsultan, M., Jun, J., & Lambert, J. H. (2020). Program evaluation of highway access with innovative risk-cost-benefit analysis. *Reliability Engineering & System Safety*, *193*, 106649. https://doi.org/10.1016/j.ress.2019.106649

Al-Taei, A. I., Alesheikh, A. A., & Darvishi Boloorani, A. (2023). Land Use/Land Cover Change Analysis Using Multi-Temporal Remote Sensing Data: A Case Study of Tigris and Euphrates Rivers Basin. *Land*, *12*(5). https://doi.org/10.3390/land12051101

Al-Timimi, Y. K., & Al-Khudhairy, A. A. (2018). Spatial and Temporal Temperature trends on Iraq during 1980-2015. *Journal of Physics: Conference Series*, *1003*(1). https://doi.org/10.1088/1742-6596/1003/1/012091

Anand, H., Shafiee-Jood, M., & Alemazkoor, N. (2023). Perspicuity of Evacuation Behavior in Communities during Hurricanes using Large-scale Mobility Patterns and Communal Characteristics. *2023 57th Annual Conference on Information Sciences and Systems, CISS 2023*. https://doi.org/10.1109/CISS56502.2023.10089754

Asadzadeh Jarihani, A., Callow, J. N., Johansen, K., & Gouweleeuw, B. (2013). Evaluation of multiple satellite altimetry data for studying inland water bodies and river floods. *Journal of Hydrology*, *505*, 78–90. https://doi.org/10.1016/j.jhydrol.2013.09.010

Awange, J. L. (2006). *Lake Victoria: Ecology, Resources, Environment*. Springer Science & Business Media.

Awange, J. L. (2020). *Lake Victoria Monitored from Space*. Springer Nature.

Awange, J. L., Hu, K. X., & Khaki, M. (2019). The newly merged satellite remotely sensed, gauge and reanalysis-based Multi-Source Weighted-Ensemble Precipitation: Evaluation over Australia and Africa (1981–2016). *Science of The Total Environment*, *670*, 448–465. https://doi.org/10.1016/j.scitotenv.2019.03.148

Awange, J. L., Sharifi, M. A., Ogonda, G., Wickert, J., Grafarend, E. W., & Omulo, M. A. (2008). The falling Lake Victoria water level: GRACE, TRIMM and CHAMP satellite analysis of the lake basin. *Water Resour. Manag.*, *22*(7), 775–796.

Bakkensen, L. A., Fox-Lent, C., Read, L. K., & Linkov, I. (2017). Validating Resilience and Vulnerability Indices in the Context of Natural Disasters. *Risk Analysis*, *37*(5), 982–1004. https://doi.org/10.1111/risa.12677

BBC News. (2020). Ugandan Floating Island Causes National Power Cut. *BBC*.

Becker, M., LLovel, W., Cazenave, A., Güntner, A., & Crétaux, J.-F. (2010). Recent hydrological behavior of the East African great lakes region inferred from GRACE, satellite altimetry and rainfall observations. *Comptes Rendus Geoscience*, *342*(3), 223–233. https://doi.org/10.1016/j.crte.2009.12.010

Besnier, J., Getirana, A., Beaudoing, H., & Lakshmi, V. (2024). Characterizing the 2019-2021 drought in La Plata River Basin with GLDAS and SMAP. *Journal of Hydrology: Regional Studies*, *52*, 101679. https://doi.org/10.1016/j.ejrh.2024.101679

Birkett, C. M., & Beckley, B. (2010). Investigating the Performance of the Jason-2/OSTM Radar Altimeter over Lakes and Reservoirs. *Marine Geodesy*, *33*(sup1), 204–238. https://doi.org/10.1080/01490419.2010.488983

Bonato, M., Sambo, B., Sperotto, A., Lambert, J. H., Linkov, I., Critto, A., Torresan, S., & Marcomini, A. (2022). Prioritization of Resilience Initiatives for Climate-Related Disasters in the Metropolitan City of Venice. *Risk Analysis*, *42*(5), 931–952. https://doi.org/10.1111/risa.13823

Bondarenko, M., Kerr, D., Sorichetta, A., & Tatem, A. J. (2020). Estimates of 2020 total number of people per grid square, adjusted to match the corresponding UNPD 2020 estimates and broken down by gender and age groupings, produced using Built-Settlement Growth Model (BSGM) outputs. *WorldPop, University of Southampton, UK.*

Bonsor, H., Shamsudduha, M., Marchant, B., MacDonald, A., & Taylor, R. (2018). Seasonal and Decadal Groundwater Changes in African Sedimentary Aquifers Estimated Using GRACE Products and LSMs. *Remote Sensing*, *10*(6), 904. https://doi.org/10.3390/rs10060904

Brinkley, C., & Wagner, J. (2024). Who Is Planning for Environmental Justice—and How? *Journal of the American Planning Association*, *90*(1), 63–76. https://doi.org/10.1080/01944363.2022.2118155

Brodzik, M. J., Billingsley, B., Haran, T., Raup, B., & Savoie, M. H. (2012). EASE-Grid 2.0: Incremental but significant improvements for earth-gridded data sets. *ISPRS International Journal of Geo-Information*, *1*(1), 32–45. https://doi.org/10.3390/ijgi1010032

Brönmark, C., & Hansson, L. A. (2002). Environmental issues in lakes and ponds: Current state and perspectives. In *Environmental Conservation* (Vol. 29, Issue 3, pp. 290–307). https://doi.org/10.1017/S0376892902000218

Bucci, L., Alaka, L., Hagen, A., Delgado, S., & Beven, J. (2022). National Hurricane Center Tropical Cyclone Report: Hurricane Ian (AL092022). *National Oceanic and Atmospheric Administration: National Hurricane Center*. https://doi.org/10.1175/WAF-D-20-0234.1

Bullock, A., & Acreman, M. (2003). Andy Bullock and Mike Acreman The role of wetlands in the hydrological cycle. In *Hydrology and Earth System Sciences* (Vol. 7, Issue 3).

CDC/ATSDR. (n.d.). CDC/ATSDR Social Vulnerability Index. *Database*.

Chan, S. K., Bindlish, R., O'Neill, P. E., Njoku, E., Jackson, T., Colliander, A., Chen, F., Burgin, M., Dunbar, S., Piepmeier, J., Yueh, S., Entekhabi, D., Cosh, M. H., Caldwell, T., Walker, J., Wu, X., Berg, A., Rowlandson, T., Pacheco, A., … Kerr, Y. (2016). Assessment of the SMAP Passive Soil Moisture Product. *IEEE Transactions on Geoscience and Remote Sensing*, *54*(8), 4994–5007. https://doi.org/10.1109/TGRS.2016.2561938

Chew, C., Reager, J. T., & Small, E. (2018). CYGNSS data map flood inundation during the 2017 Atlantic hurricane season. *Scientific Reports*, *8*(1). https://doi.org/10.1038/s41598-018-27673-x

Chumky, T., Basu, M., Onitsuka, K., & Hoshino, S. (2022). The current research landscape of disaster-induced migration: A systematic review and bibliometric analysis. In *International Journal of Disaster Risk Reduction* (Vol. 74). Elsevier Ltd. https://doi.org/10.1016/j.ijdrr.2022.102931

Clark, U., Ahn, J. E., & Bauer, S. K. (2022). Investigating the Impacts of Economic Factors on Recovery to Further Develop Hurricane Resilience Model for Residential Homes. *ASCE-ASME Journal of Risk and Uncertainty in Engineering Systems, Part A: Civil Engineering*, *8*(2). https://doi.org/10.1061/ajrua6.0001228

Coughlan de Perez, E., van Aalst, M., Choularton, R., van den Hurk, B., Mason, S., Nissan, H., & Schwager, S. (2019). From rain to famine: assessing the utility of rainfall observations and seasonal forecasts to anticipate food insecurity in East Africa. *Food Security*, *11*(1), 57–68. https://doi.org/10.1007/s12571-018-00885-9

Cutter, S. L., Boruff, B. J., & Shirley, W. L. (2003). Social vulnerability to environmental hazards. *Social Science Quarterly*, *84*(2), 242–261. https://doi.org/10.1111/1540-6237.8402002

Dezfuli, A. K., Ichoku, C. M., Huffman, G. J., Mohr, K. I., Selker, J. S., van de Giesen, N., Hochreutener, R., & Annor, F. O. (2017). Validation of IMERG Precipitation in Africa. *Journal of Hydrometeorology*, *18*(10), 2817–2825. https://doi.org/10.1175/JHM-D-17-0139.1

Downs, B., Chapman, B., Russo, I. M., Lavalle, M., Di Bisceglie, M., Galdi, C., Morris, M., O’Brien, A., & Zuffada, C. (2021). Leveraging Nisar Activities to Support CYGNSS Wetlands Calibration & Validation. *IEEE Specialist Meeting on Reflectometry Using GNSS and Other Signals of Opportunity 2021, GNSS+R 2021 - Proceedings*, 101–104. https://doi.org/10.1109/GNSSR53802.2021.9617692

Dziewonski, A. M., Chou, T. A., & Woodhouse, J. H. (1981). Determination of earthquake source parameters from waveform data for studies of global and regional seismicity. *J. Geophys. Res.*, *86*, 2825–2852.

Eddy, T. L., Loose, D. C., Polmateer, T. L., Manasco, M. C., & Lambert, J. H. (2022). Why System Requirements Must Influence the Selection of Causal Models to Address

Congestion in Freight Logistics. *2022 IEEE International Systems Conference (SysCon)*, 1–7. https://doi.org/10.1109/SysCon53536.2022.9773871

Ekström, G., Nettles, M., & Dziewonski, A. M. (2012). The global CMT project 2004-2010: Centroid-moment tensors for 13,017 earthquakes. *Phys. Earth Planet. Inter.*, *200*, 1–9.

Emrich, C. T., & Cutter, S. L. (2011). Social vulnerability to climate-sensitive hazards in the Southern United States. *Weather, Climate, and Society*, *3*(3), 193–208. https://doi.org/10.1175/2011WCAS1092.1

Entekhabi, D., Njoku, E. G., O'Neill, P. E., Kellogg, K. H., Crow, W. T., Edelstein, W. N., Entin, J. K., Goodman, S. D., Jackson, T. J., Johnson, J., Kimball, J., Piepmeier, J. R., Koster, R. D., Martin, N., McDonald, K. C., Moghaddam, M., Moran, S., Reichle, R., Shi, J. C., … Van Zyl, J. (2010). The Soil Moisture Active Passive (SMAP) Mission. *Proceedings of the IEEE*, *98*(5), 704–716. https://doi.org/10.1109/JPROC.2010.2043918

ESRI. (2021). DeLorme, CIA World Factbook United Nations Development Programme, Flagpedia. African Countries Feature Service. In *ESRI Africa*.

Fang, B., Lakshmi, V., Cosh, M., Liu, P., Bindlish, R., & Jackson, T. J. (2022). A global 1-km downscaled SMAP soil moisture product based on thermal inertia theory. *Vadose Zone Journal*, *21*(2). https://doi.org/10.1002/vzj2.20182

Farr, T. G., Rosen, P. A., Caro, E., Crippen, R., Duren, R., Hensley, S., Kobrick, M., Paller, M., Rodriguez, E., Roth, L., Seal, D., Shaffer, S., Shimada, J., Umland, J., Werner, M., Oskin, M., Burbank, D., & Alsdorf, D. (2007). The Shuttle Radar Topography Mission. *Reviews of Geophysics*, *45*(2). https://doi.org/10.1029/2005RG000183

FEWS NET. (2020). *East African Special Report: 2019 Short Rains in East Africa Among the Wettest on Historical Record*. Famine Early Warning Systems Network (FEWS NET). https://fews.net/sites/default/files/documents/reports/East_Africa_Special_Report_January_2020_Final_3.pdf

FEWS NET. (2021). East African Food Security Alert: Over 20 million people in need of urgent food aid in the Horn of Africa amid severe drought and conflict. *Famine Early Warning Systems Network*. https://reliefweb.int/sites/reliefweb.int/files/resources/east-africa-alert-20211229-final.pdf

Flanagan, B. E., Gregory, E. W., Hallisey, E. J., Heitgerd, J. L., & Lewis, B. (2011). A Social Vulnerability Index for Disaster Management. *Journal of Homeland Security and Emergency Management*, *8*(1). https://doi.org/10.2202/1547-7355.1792

Flanagan, B. E., Hallisey, E. J., Adams, E., & Lavery, A. (2018). *Measuring Community Vulnerability to Natural and Anthropogenic Hazards: The Centers for Disease Control and Prevention's Social Vulnerability Index*.

Fothergill, A., & Peek, L. A. (2004). Poverty and Disasters in the United States: A Review of Recent Sociological Findings. In *Natural Hazards* (Vol. 32).

Friedl, D. S., & Sulla-Menashe, M. D. (2019). *MCD12Q1 MODIS/Terra+Aqua Land Cover Type Yearly L3 Global 500m SIN Grid v006*. NASA EOSDIS Land Processes DAAC.

Friedl, M. A., Sulla-Menashe, D., Tan, B., Schneider, A., Ramankutty, N., Sibley, A., & Huang, X. (2010). MODIS Collection 5 global land cover: Algorithm refinements and characterization of new datasets. *Remote Sensing of Environment*, *114*(1), 168–182. https://doi.org/10.1016/j.rse.2009.08.016

Gerlein-Safdi, C., & Ruf, C. S. (2019). A CYGNSS-Based Algorithm for the Detection of Inland Waterbodies. *Geophysical Research Letters*, *46*(21), 12065–12072. https://doi.org/10.1029/2019GL085134

Getirana, A., Jung, H. C., Van Den Hoek, J., & Ndehedehe, C. E. (2020). Hydropower dam operation strongly controls Lake Victoria's freshwater storage variability. *Science of The Total Environment*, *726*, 138343. https://doi.org/10.1016/j.scitotenv.2020.138343

Ghasemigoudarzi, P., Huang, W., & De Silva, O. (2020). Detecting Floods Caused by Tropical Cyclone Using CYGNSS Data. *IEEE International Conference on Multisensor Fusion and Integration for Intelligent Systems*, *2020-September*, 212–215. https://doi.org/10.1109/MFI49285.2020.9235243

Ghasemigoudarzi, P., Huang, W., De Silva, O., Yan, Q., & Power, D. (2022). A Machine Learning Method for Inland Water Detection Using CYGNSS Data. *IEEE Geoscience and Remote Sensing Letters*, *19*. https://doi.org/10.1109/LGRS.2020.3020223

Grippa, M., Kergoat, L., Frappart, F., Araud, Q., Boone, A., de Rosnay, P., Lemoine, J. -M., Gascoin, S., Balsamo, G., Ottlé, C., Decharme, B., Saux-Picart, S., & Ramillien, G. (2011). Land water storage variability over West Africa estimated by Gravity Recovery and Climate Experiment (GRACE) and land surface models. *Water Resources Research*, *47*(5). https://doi.org/10.1029/2009WR008856

Hamilton, M. C., Lambert, J. H., Keisler, J. M., Holcomb, F. H., & Linkov, I. (2013). Research and Development Priorities for Energy Islanding of Military and Industrial Installations. *Journal of Infrastructure Systems*, *19*(3), 297–305. https://doi.org/10.1061/(asce)is.1943-555x.0000133

Hamilton, M. C., Lambert, J. H., & Valverde, L. J. (2015). Climate and Related Uncertainties Influencing Research and Development Priorities. *ASCE-ASME Journal of Risk and Uncertainty in Engineering Systems, Part A: Civil Engineering*, *1*(2). https://doi.org/10.1061/ajrua6.0000814

Hamilton, S. (2016). *Basin, Lake Victoria Watershed (inside), vector polygon, ~2015*. Harvard Dataverse, V3.

Hashemi, H., Nordin, M., Lakshmi, V., Huffman, G. J., & Knight, R. (2018). Bias correction of long-term satellite monthly precipitation product (TRMM 3B43) over the conterminous United States. *J. Hydrometeorol.*, *18*(9), 2491–2509.

Hassler, M. L., Andrews, D. J., Ezell, B. C., Polmateer, T. L., & Lambert, J. H. (2019a). *Multi-Perspective Scenario-Based Preferences in Enterprise Risk Analysis of Public Safety Wireless Broadband Network*. https://www.sciencedirect.com/science/article/pii/S0951832018304022

Hassler, M. L., Andrews, D. J., Ezell, B. C., Polmateer, T. L., & Lambert, J. H. (2019b). *Multi-Perspective Scenario-Based Preferences in Enterprise Risk Analysis of Public Safety Wireless Broadband Network*. https://www.sciencedirect.com/science/article/pii/S0951832018304022

Highfield, W. E., Peacock, W. G., & Van Zandt, S. (2014). Mitigation Planning: Why Hazard Exposure, Structural Vulnerability, and Social Vulnerability Matter. *Journal of Planning Education and Research*, *34*(3), 287–300. https://doi.org/10.1177/0739456X14531828

Hou, A. Y., Kakar, R. K., Neeck, S., Azarbarzin, A. A., Kummerow, C. D., Kojima, M., Oki, R., Nakamura, K., & Iguchi, T. (2014). The Global Precipitation Measurement Mission.

*Bulletin of the American Meteorological Society*, *95*(5), 701–722. https://doi.org/10.1175/BAMS-D-13-00164.1

Hu, K. X., Awange, J. L., Kuhn, M., & Nanteza, J. (2021). Inference of the spatio-temporal variability and storage potential of groundwater in data-deficient regions through groundwater models and inversion of impact factors on groundwater, as exemplified by the Lake Victoria Basin. *Science of The Total Environment*, *800*, 149355. https://doi.org/10.1016/j.scitotenv.2021.149355

Huffman, G. J., Bolvin, D. T., Braithwaite, D., Hsu, K., Joyce, R., Kidd, C., Nelkin, E. J., Sorooshian, S., Tan, J., & Xie, P. (2020). *NASA Global Precipitation Measurement (GPM) Integrated Multi-satellitE Retrievals for GPM (IMERG) Prepared for: Global Precipitation Measurement (GPM) National Aeronautics and Space Administration (NASA)*. https://pmm.nasa.gov/sites/default/files/imce/times_allsat.jpg

Huffman, G. J., Bolvin, D. T., Braithwaite, D., Hsu, K., Joyce, R., Xie, P., & Yoo, S. H. (2015a). *NASA Global Precipitation Measurement (GPM) Integrated Multi-satellitE Retrievals for GPM (IMERG). Algorithm Theoretical Basis Document (ATBD) Version, 4, p. 26*. NASA.

Huffman, G. J., Bolvin, D. T., Braithwaite, D., Hsu, K., Joyce, R., Xie, P., & Yoo, S.-H. (2015b). NASA Global Precipitation Measurement (GPM) Integrated Multi-Satellite Retrievals for GPM (IMERG). *Algorithm Theoretical Basis Document (ATBD), Version 4*, *26*.

IOM. (2020). Republic of Iraq: Migration Governance Indicators; Profile 2020. *International Organization for Migration (IOM)*.

IOM Iraq. (2022). *POLICY BRIEF: OPPORTUNITIES FOR ACTION CLIMATE CHANGE AND MIGRATION IN IRAQ BACKGROUND*.

Jaafar Alnajm, D. (2023). SPATIAL VARIATION IN THE GROWTH OF THE POPULATION OF THE GOVERNORATES OF IRAQ FOR THE PERIOD 2010-2020 AND ITS EXPECTATIONS FOR THE YEAR 2030 AD. In *RUSSIAN LAW JOURNAL: Vol. XI*.

Jaff, D. (2023). Conflict, environmental destruction and climate change: a tragedy in Iraq that demands action. In *Medicine, Conflict and Survival* (Vol. 39, Issue 2, pp. 162–171). Routledge. https://doi.org/10.1080/13623699.2023.2200346

Jaime, C., Coughlan de Perez, E., van Aalst, M., Raju, E., & Sheaffer, A. (2022). What was known: Weather forecast availability and communication in conflict-affected countries. *International Journal of Disaster Risk Reduction*, *83*. https://doi.org/10.1016/j.ijdrr.2022.103421

Kaneda, T., Greenbaum, C., & Kline, K. (2020). *2020 World Population Data Sheet*. Population Reference Burs.

Kansara, P., Li, W., El-Askary, H., Lakshmi, V., Piechota, T., Struppa, D., & Abdelaty Sayed, M. (2021). An Assessment of the Filling Process of the Grand Ethiopian Renaissance Dam and Its Impact on the Downstream Countries. *Remote Sensing*, *13*(4), 711. https://doi.org/10.3390/rs13040711

Karakani, E. G., Malekian, A., Gholami, S., & Liu, J. (2021). *Spatiotemporal monitoring and change detection of vegetation cover for drought management in the Middle East*. https://doi.org/10.1007/s00704-021-03543-x/Published

Karimiziarani, M., & Moradkhani, H. (2023). Social response and Disaster management: Insights from twitter data Assimilation on Hurricane Ian. *International Journal of Disaster Risk Reduction*, *95*, 103865. https://doi.org/10.1016/j.ijdrr.2023.103865

Karra, K., & et al. (2021). Global land use/land cover with Sentinel-2 and deep learning. *IGARSS 2021-2021 IEEE International Geoscience and Remote Sensing Symposium. IEEE*.

Karvetski, C. W., Lambert, J. H., & Linkov, I. (2009). Emergent conditions and multiple criteria analysis in infrastructure prioritization for developing countries. *Journal of Multi-Criteria Decision Analysis*, *16*(5–6), 125–137. https://doi.org/10.1002/mcda.444

Kavvada, A., Cripe, D., & Friedl, L. (2022). *Earth observation applications and global policy frameworks*.

Khaki, M., & Awange, J. (2021). The 2019–2020 rise in Lake Victoria monitored from space: exploiting the state-of-the-art GRACE-FO and the newly released ERA-5 reanalysis products. *Sensors*, *21*(13), 4304.

Khan, S. I., Hong, Y., Wang, J., Yilmaz, K. K., Gourley, J. J., Adler, R. F., Brakenridge, G. R., Policelli, F., Habib, S., & Irwin, D. (2011). Satellite Remote Sensing and Hydrologic Modeling for Flood Inundation Mapping in Lake Victoria Basin: Implications for Hydrologic Prediction in Ungauged Basins. *IEEE Transactions on Geoscience and Remote Sensing*, *49*(1), 85–95. https://doi.org/10.1109/TGRS.2010.2057513

Kim, H., & Lakshmi, V. (2018). Use of Cyclone Global Navigation Satellite System (CyGNSS) Observations for Estimation of Soil Moisture. *Geophysical Research Letters*, *45*(16), 8272–8282. https://doi.org/10.1029/2018GL078923

Kim, H., Lakshmi, V., Kwon, Y., & Kumar, S. V. (2021). First attempt of global-scale assimilation of subdaily scale soil moisture estimates from CYGNSS and SMAP into a land surface model. *Environmental Research Letters*, *16*(7). https://doi.org/10.1088/1748-9326/ac0ddf

Kisumu, E. R. (2020). *'The Water Will Come Back': Why Kenya's Struggle Against Flooding Is Far from Over*. The Guardian: Global Development. https://www.theguardian.com/global-development/2020/jun/02/the-water-will-come-back-why-kenyas-struggle-against-flooding-is-far-from-over

Köchling, A., & Wehner, M. C. (2020). Discriminated by an algorithm: a systematic review of discrimination and fairness by algorithmic decision-making in the context of HR recruitment and HR development. *Business Research*, *13*(3), 795–848. https://doi.org/10.1007/s40685-020-00134-w

Kull, D. (2006). *Connections Between Recent Water Level Drops in Lake Victoria, Dam Operations and Drought*. https://aquadocs.org/handle/1834/7032

Kunreuther, H., Gupta, S., Bosetti, V., Böttcher Austria, H., Cullen, H., Jasanoff, S., Elgizouli, I., Linnerooth-Bayer, J., Gupta, S., Bosetti, V., Cooke, R., Dutt, V., Ha-Duong, M., Held, H., Llanes-Regueiro, J., Patt, A., Shittu, E., Pichs-Madruga, R., Sokona, Y., … Minx, J. (2014). *Integrated Risk and Uncertainty Assessment of Climate Change Response Policies Coordinating Lead Authors: Lead Authors: Contributing Authors: Review Editors: Chapter Science Assistants: Mitigation of Climate Change. Contribution of Working Group III to the Fifth Assessment Report of the Intergovernmental Panel on Climate Change [Edenhofer Integrated Risk and Uncertainty Assessment of Climate Change Response Policies Contents*.

Lakshmi, V., & Fang, B. (2023). SMAP-Derived 1-km Downscaled Surface Soil Moisture Product, Version 1. *NASA National Snow and Ice Data Center Distributed Active Archive Center.*

Lakshmi, V., Fayne, J., & Bolten, J. (2018). A comparative study of available water in the major river basins of the world. *Journal of Hydrology*, *567*, 510–532. https://doi.org/10.1016/j.jhydrol.2018.10.038

Landerer, F. W., Flechtner, F. M., Save, H., Webb, F. H., Bandikova, T., Bertiger, W. I., Bettadpur, S. V., Byun, S. H., Dahle, C., Dobslaw, H., Fahnestock, E., Harvey, N., Kang, Z., Kruizinga, G. L. H., Loomis, B. D., McCullough, C., Murböck, M., Nagel, P., Paik, M., … Yuan, D. (2020). Extending the Global Mass Change Data Record: GRACE Follow-On Instrument and Science Data Performance. *Geophysical Research Letters*, *47*(12). https://doi.org/10.1029/2020GL088306

Lang, R., Zhou, Y., Utku, C., & Le Vine, D. (2016). Accurate measurements of the dielectric constant of seawater at L band. *Radio Science*, *51*(1), 2–24. https://doi.org/10.1002/2015RS005776

Lavell, A., Rica, C., Oppenheimer, M., Diop, C., Moser, S., & Takeuchi, K. (2012). *Climate Change: New Dimensions in Disaster Risk, Exposure, Vulnerability, and Resilience. In: Managing the Risks of Extreme Events and Disasters to Advance Climate Change Adaptation*.

Le, H., Sutton, J., Bui, D., Bolten, J., & Lakshmi, V. (2018). Comparison and Bias Correction of TMPA Precipitation Products over the Lower Part of Red–Thai Binh River Basin of Vietnam. *Remote Sensing*, *10*(10), 1582. https://doi.org/10.3390/rs10101582

Le, M.-H., Lakshmi, V., Bolten, J., & Bui, D. Du. (2020). Adequacy of Satellite-derived Precipitation Estimate for Hydrological Modeling in Vietnam Basins. *Journal of Hydrology*, *586*, 124820. https://doi.org/10.1016/j.jhydrol.2020.124820

Le, M.-H., Nguyen, B. Q., Pham, H. T., Patil, A., Do, H. X., Ramsankaran, R., Bolten, J. D., & Lakshmi, V. (2022). Assimilation of SMAP Products for Improving Streamflow Simulations over Tropical Climate Region—Is Spatial Information More Important Than Temporal Information? *Remote Sensing*, *14*(7), 1607. https://doi.org/10.3390/rs14071607

Lehner, B., & Grill, G. (2013a). Global river hydrography and network routing: Baseline data and new approaches to study the world’s large river systems. *Hydrological Processes*, *27*(15), 2171–2186. https://doi.org/10.1002/hyp.9740

Lehner, B., & Grill, G. (2013b). Global river hydrography and network routing: baseline data and new approaches to study the world’s large river systems. *Hydrological Processes*, *27*(15), 2171–2186. https://doi.org/10.1002/hyp.9740

Li, W., Cardellach, E., Fabra, F., Ribó, S., & Rius, A. (2018). Lake Level and Surface Topography Measured With Spaceborne GNSS-Reflectometry From CYGNSS Mission: Example for the Lake Qinghai. *Geophysical Research Letters*, *45*(24), 13,332-13,341. https://doi.org/10.1029/2018GL080976

Linkov, I., & Trump, B. D. (2019). *The Science and Practice of Resilience*. https://doi.org/https://doi.org/10.1007/978-3-030-04565-4

Linkov, I., Trump, B. D., Trump, J., Pescaroli, G., Hynes, W., Mavrodieva, A., & Panda, A. (2022). Resilience stress testing for critical infrastructure. In *International Journal of Disaster Risk Reduction* (Vol. 82). Elsevier Ltd. https://doi.org/10.1016/j.ijdrr.2022.103323

Loose, D. C., Eddy, T. L., Polmateer, T. L., Hendrickson, D. C., Moghadasi, N., & Lambert, J. H. (2023). Reinforcement Learning and Automatic Control for Resilience of Maritime

Container Ports. *2023 9th International Conference on Control, Decision and Information Technologies (CoDIT)*, 01–06. https://doi.org/10.1109/CoDIT58514.2023.10284324

Loose, D. C., Eddy, T. L., Polmateer, T. L., Manasco, M. C., Moghadasi, N., & Lambert, J. H. (2022a). Managing Pandemic Resilience with Other Cascading Disruptions of a Socio-Technical System. *2022 IEEE International Systems Conference (SysCon)*, 1–6. https://doi.org/10.1109/SysCon53536.2022.9773915

Loose, D. C., Eddy, T. L., Polmateer, T. L., Manasco, M. C., Moghadasi, N., & Lambert, J. H. (2022b). Managing Pandemic Resilience with Other Cascading Disruptions of a Socio-Technical System. *2022 IEEE International Systems Conference (SysCon)*, 1–6. https://doi.org/10.1109/SysCon53536.2022.9773915

López-Carr, D., Pricope, N. G., Aukema, J. E., Jankowska, M. M., Funk, C., Husak, G., & Michaelsen, J. (2014). A spatial analysis of population dynamics and climate change in Africa: potential vulnerability hot spots emerge where precipitation declines and demographic pressures coincide. *Population and Environment*, *35*(3), 323–339. https://doi.org/10.1007/s11111-014-0209-0

Loria, E., O’Brien, A., Zavorotny, V., Downs, B., & Zuffada, C. (2020). Analysis of scattering characteristics from inland bodies of water observed by CYGNSS. *Remote Sensing of Environment*, *245*, 111825. https://doi.org/10.1016/j.rse.2020.111825

Marcellin, M. C., Pavur, G., Loose, D. C., Cardenas, J. J., Denehy, D., Almashhadani, M., Trump, B. D., Polmateer, T. L., Linkov, I., Lakshmi, V., & Lambert, J. H. (2023). *Risk Model of Climate Change and Water Scarcity for Energy Resources of Iraq*. https://doi.org/10.21203/rs.3.rs-3581219/v1

Mazhin, S., Khankeh, H., Farrokhi, M., Aminizadeh, M., & Poursadeqiyan, M. (2020). Migration health crisis associated with climate change: A systematic review. *Journal of Education and Health Promotion*, *9*(1). https://doi.org/10.4103/jehp.jehp_4_20

McAuliffe, M., & Triandayfllidou, A. (2022). *World Migration Report 2022* (M. McAuliffe & A. (eds. ) Triandayfllidou, Eds.). International Organization for Migration (IOM).

Messager, M. L., Lehner, B., Grill, G., Nedeva, I., & Schmitt, O. (2016). Estimating the volume and age of water stored in global lakes using a geo-statistical approach. *Nature Communications*, *7*. https://doi.org/10.1038/ncomms13603

Meyer, M. A., Mitchell, B., Purdum, J. C., Breen, K., & Iles, R. L. (2018). Previous hurricane evacuation decisions and future evacuation intentions among residents of southeast Louisiana. *International Journal of Disaster Risk Reduction*, *31*, 1231–1244. https://doi.org/10.1016/j.ijdrr.2018.01.003

Mohai, P., Pellow, D., & Roberts, J. T. (2009). Environmental justice. *Annual Review of Environment and Resources*, *34*, 405–430. https://doi.org/10.1146/annurev-environ-082508-094348

Mohammed, I., Bolten, J., Srinivasan, R., & Lakshmi, V. (2018). Improved Hydrological Decision Support System for the Lower Mekong River Basin Using Satellite-Based Earth Observations. *Remote Sensing*, *10*(6), 885. https://doi.org/10.3390/rs10060885

Mohammed, I. N., Bolten, J. D., Srinivasan, R., & Lakshmi, V. (2018). Satellite observations and modeling to understand the Lower Mekong River Basin streamflow variability. *Journal of Hydrology*, *564*, 559–573. https://doi.org/10.1016/j.jhydrol.2018.07.030

Mohammed, I. N., Bolten, J. D., Srinivasan, R., Meechaiya, C., Spruce, J. P., & Lakshmi, V. (2018). Ground and satellite based observation datasets for the Lower Mekong River Basin. *Data in Brief*, *21*, 2020–2027. https://doi.org/10.1016/j.dib.2018.11.038

Mondal, A., Lakshmi, V., & Hashemi, H. (2018). Intercomparison of trend analysis of Multisatellite Monthly Precipitation Products and Gauge Measurements for River Basins of India. *Journal of Hydrology*, *565*, 779–790. https://doi.org/10.1016/j.jhydrol.2018.08.083

Morris, M., Chew, C., Reager, J. T., Shah, R., & Zuffada, C. (2019). A novel approach to monitoring wetland dynamics using CYGNSS: Everglades case study. *Remote Sensing of Environment*, *233*. https://doi.org/10.1016/j.rse.2019.111417

Mu, Q., Heinsch, F. A., Zhao, M., & Running, S. W. (2007). Development of a global evapotranspiration algorithm based on MODIS and global meteorology data. *Remote Sensing of Environment*, *111*(4), 519–536. https://doi.org/10.1016/j.rse.2007.04.015

Mu, Q., Zhao, M., & Running, S. W. (2011). Improvements to a MODIS global terrestrial evapotranspiration algorithm. *Remote Sensing of Environment*, *115*(8), 1781–1800. https://doi.org/10.1016/j.rse.2011.02.019

Mugo, R., Waswa, R., Nyaga, J. W., Ndubi, A., Adams, E. C., & Flores-Anderson, A. I. (2020). Quantifying Land Use Land Cover Changes in the Lake Victoria Basin Using Satellite Remote Sensing: The Trends and Drivers between 1985 and 2014. *Remote Sensing*, *12*(17), 2829. https://doi.org/10.3390/rs12172829

Nations Office for Disaster Risk Reduction, U. (2015). *Sendai Framework for Disaster Risk Reduction 2015 - 2030*.

Ndehedehe, C., Awange, J., Agutu, N., Kuhn, M., & Heck, B. (2016). Understanding changes in terrestrial water storage over West Africa between 2002 and 2014. *Advances in Water Resources*, *88*, 211–230. https://doi.org/10.1016/j.advwatres.2015.12.009

NOAA. (n.d.). *National Centers for Environmental Information (NCEI) U.S. Billion-Dollar Weather and Climate Disasters (2023). https://www.ncei.noaa.gov/access/billions/, DOI: 10.25921/stkw-7w73*.

Nyeko-Ogiramoi, P., Willems, P., & Ngirane-Katashaya, G. (2013). Trend and variability in observed hydrometeorological extremes in the Lake Victoria basin. *Journal of Hydrology*, *489*, 56–73. https://doi.org/10.1016/j.jhydrol.2013.02.039

Palm, R., & Bolsen, T. (2023). Perspectives of Southwest Florida Homeowners and Real Estate Agents before Hurricane Ian. *Professional Geographer*. https://doi.org/10.1080/00330124.2023.2194372

Palmer, S. C. J., Kutser, T., & Hunter, P. D. (2015). Remote sensing of inland waters: Challenges, progress and future directions. In *Remote Sensing of Environment* (Vol. 157, pp. 1–8). Elsevier Inc. https://doi.org/10.1016/j.rse.2014.09.021

Papa, F., Prigent, C., Aires, F., Jimenez, C., Rossow, W. B., & Matthews, E. (2010). Interannual variability of surface water extent at the global scale, 1993-2004. *Journal of Geophysical Research Atmospheres*, *115*(12). https://doi.org/10.1029/2009JD012674

Paris, A., Calmant, S., Gosset, M., Fleischmann, A. S., Conchy, T. S. X., Garambois, P., Bricquet, J., Papa, F., Tshimanga, R. M., Guzanga, G. G., Siqueira, V. A., Tondo, B., Paiva, R., da Silva, J. S., & Laraque, A. (2022). *Monitoring Hydrological Variables from Remote Sensing* *and Modeling in the Congo River Basin* (pp. 339–366). https://doi.org/10.1002/9781119657002.ch18

Pavur, G., & Lakshmi, V. (2023). Observing the recent floods and drought in the Lake Victoria Basin using Earth observations and hydrological anomalies. *Journal of Hydrology: Regional Studies*, *46*. https://doi.org/10.1016/j.ejrh.2023.101347

Pekel, J. F., Cottam, A., Gorelick, N., & Belward, A. S. (2016). High-resolution mapping of global surface water and its long-term changes. *Nature*, *540*(7633), 418–422. https://doi.org/10.1038/nature20584

Pennetti, C. A., Jun, J., Jones, G. S., & Lambert, J. H. (2021). Temporal Disaggregation of Performance Measures to Manage Uncertainty in Transportation Logistics and Scheduling. *ASCE-ASME Journal of Risk and Uncertainty in Engineering Systems, Part A: Civil Engineering*, *7*(1). https://doi.org/10.1061/AJRUA6.0001096

Peters, L. E. R. (2021). Beyond disaster vulnerabilities: An empirical investigation of the causal pathways linking conflict to disaster risks. *International Journal of Disaster Risk Reduction*, *55*. https://doi.org/10.1016/j.ijdrr.2021.102092

Rajabi, M., Nahavandchi, H., & Hoseini, M. (2020). Evaluation of CYGNSS observations for flood detection and mapping during Sistan and Baluchestan Torrential Rain in 2020. *Water (Switzerland)*, *12*(7). https://doi.org/10.3390/w12072047

Ramillien, G., Frappart, F., & Seoane, L. (2014). Application of the Regional Water Mass Variations from GRACE Satellite Gravimetry to Large-Scale Water Management in Africa. *Remote Sensing*, *6*(8), 7379–7405. https://doi.org/10.3390/rs6087379

Reda Taha, M., Ayyub, B. M., Soga, K., Daghash, S., Heras Murcia, D., Moreu, F., & Soliman, E. (2021). Emerging Technologies for Resilient Infrastructure: Conspectus and Roadmap. *ASCE-ASME Journal of Risk and Uncertainty in Engineering Systems, Part A: Civil Engineering*, *7*(2). https://doi.org/10.1061/AJRUA6.0001134

Reynolds, C. (2005). *Low Water Levels Observed on Lake Victoria.* Production Estimates and Crop Assessment Division of USDA Foreign Agricultural Service. https://reliefweb.int/report/kenya/usda-low-water-levels-observed-lake-victoria

Robles, P., Chang, A., Leatherby, L., Reinhard, S., & Wu, A. (2023). Mapping the Damage From the Earthquake in Turkey and Syria. *The New York Times*.

Rodell, M., Houser, P. R., Jambor, U., Gottschalck, J., Mitchell, K., Meng, C.-J., Arsenault, K., Cosgrove, B., Radakovich, J., Bosilovich, M., Entin, J. K., Walker, J. P., Lohmann, D., & Toll, D. (2004). The Global Land Data Assimilation System. *Bulletin of the American Meteorological Society*, *85*(3), 381–394. https://doi.org/10.1175/BAMS-85-3-381

Rodell, M., Houser, P. R., Jambor, U., Gottschalck, K., Mitchell, C. J., Meng, K., Arsenault, B., Cosgrove, J., Radakovich, M., Bosilovich, J. K., Entin, J. K., Walker, J. P., Kohmann, D., & Toll, D. (2004). The Global Land Data Assimilation System. *Bull. Am. Meteorol. Soc.*, *85*(3), 381–294.

Ruf, C., Chew, C., Gerlein-Safdi, C., & Warnock, A. (2021). Resolving Inland Waterways with CYGNSS. *2021 IEEE International Geoscience and Remote Sensing Symposium IGARSS*, 954–957. https://doi.org/10.1109/IGARSS47720.2021.9554192

Ruf, C. S., Chew, C., Lang, T., Morris, M. G., Nave, K., Ridley, A., & Balasubramaniam, R. (2018). A New Paradigm in Earth Environmental Monitoring with the CYGNSS Small Satellite Constellation. *Scientific Reports*, *8*(1). https://doi.org/10.1038/s41598-018-27127-4

Running, S. W., Mu, Q., Zhao, M., & Moreno, A. (2017). *MODIS Global Terrestrial Evapotranspiration (ET) Product (NASA MOD16A2/A3) NASA Earth Observing System MODIS Land Algorithm*. NASA: Washington, DC, USA.

Sambo, B., Bonato, M., Sperotto, A., Torresan, S., Furlan, E., Lambert, J. H., Linkov, I., & Critto, A. (2023). Framework for multirisk climate scenarios across system receptors with application to the Metropolitan City of Venice. *Risk Analysis*, *43*(11), 2241–2261. https://doi.org/10.1111/risa.14097

Sambo, B., Sano, M., Sperotto, A., Zanetti, M., Torresan, S., Lambert, J. H., Linkov, I., & Critto, A. (2023). Sensitivity analysis for a participatory approach to enhance the climate resilience of Venice, Italy. *Risk Analysis*. https://doi.org/10.1111/risa.14258

Šedová, B., Čizmaziová, L., & Cook, A. (2021). *A meta-analysis of climate migration literature (CEPA Discussion Papers ; 29)*. https://doi.org/10.25932/publishup-49982

Shamsudduha, M., Taylor, R. G., Jones, D., Longuevergne, L., Owor, M., & Tindimugaya, C. (2017). Recent changes in terrestrial water storage in the Upper Nile Basin: an evaluation of commonly used gridded GRACE products. *Hydrology and Earth System Sciences*, *21*(9), 4533–4549. https://doi.org/10.5194/hess-21-4533-2017

Shittu, E., Parker, G., & Mock, N. (2018). Improving communication resilience for effective disaster relief operations. *Environment Systems and Decisions*, *38*(3), 379–397. https://doi.org/10.1007/s10669-018-9694-5

Sims, K., Reith, A., Kaufman, J., Pyle, J., Epting, J., Gonzales, J., Adams, D., Powell, E., Urban, M., & Rose, A. (2023). LandScan Global 2022 [Data set]. *Oak Ridge National Laboratory*.

Smith, A. B. (2023). U.S. Billion-dollar Weather and Climate Disasters, 1980-present (NCEI Accession 0209268). *NOAA National Centers for Environmental Information*.

Smith, A. B., & Katz, R. W. (2013). US billion-dollar weather and climate disasters: Data sources, trends, accuracy and biases. *Natural Hazards*, *67*(2), 387–410. https://doi.org/10.1007/s11069-013-0566-5

Soman, M. K., & Indu, J. (2022). Sentinel-1 based Inland water dynamics Mapping System (SIMS). *Environmental Modelling and Software*, *149*. https://doi.org/10.1016/j.envsoft.2022.105305

Sreelakshmi, S., & Vinod Chandra, S. S. (2022). Machine Learning for Disaster Management: Insights from past research and future implications. *2022 International Conference on Computing, Communication, Security and Intelligent Systems (IC3SIS)*, 1–7. https://doi.org/10.1109/IC3SIS54991.2022.9885494

Sulla-Menashe, D., Gray, J. M., Abercrombie, S. P., & Friedl, M. A. (2019). Hierarchical mapping of annual global land cover 2001 to present: The MODIS Collection 6 Land Cover product. *Remote Sensing of Environment*, *222*, 183–194. https://doi.org/10.1016/j.rse.2018.12.013

Swenson, S., & Wahr, J. (2009). Monitoring the water balance of Lake Victoria, East Africa, from space. *Journal of Hydrology*, *370*(1–4), 163–176. https://doi.org/10.1016/j.jhydrol.2009.03.008

Tate, E., Rahman, M. A., Emrich, C. T., & Sampson, C. C. (2021). Flood exposure and social vulnerability in the United States. *Natural Hazards*, *106*(1), 435–457. https://doi.org/10.1007/s11069-020-04470-2

Thekdi, S. A., & Lambert, J. H. (2015). Integrated risk management of safety and development on transportation corridors. *Reliability Engineering & System Safety*, *138*, 1–12. https://doi.org/10.1016/j.ress.2014.11.015

Thiery, W., Davin, E. L., Seneviratne, S. I., Bedka, K., Lhermitte, S., & van Lipzig, N. P. M. (2016). Hazardous thunderstorm intensification over Lake Victoria. *Nature Communications*, *7*(1), 12786. https://doi.org/10.1038/ncomms12786

Thorisson, H., & Lambert, J. H. (2017). Multiscale identification of emergent and future conditions along corridors of transportation networks. *Reliability Engineering & System Safety*, *167*, 255–263. https://doi.org/10.1016/j.ress.2017.06.005

UNICEF. (2018). *Iraq Humanitarian Situation Report, August 2018*. https://www.unicef.org/media/76731/file/Iraq-SitRep-August-2018.pdf

UNICEF. (2021). *The impact of water scarcity on children in the Middle East and North Africa Running*. https://www.unicef.org/mena/reports/running-dry-impact-water-scarcity-children

UNICEF. (2023). *CLIMATE LANDSCAPE ANALYSIS FOR CHILDREN AND YOUNG PEOPLE IN IRAQ UNICEF IN IRAQ EXECUTIVE SUMMARY*. https://www.unicef.org/iraq/media/2896/file/CLAC%20-%20Executive%20summary%20-%20EN.pdf

USDA. (2022). *Global Reservoirs and Lake Monitor (G-REALM). U.S. Department of Agriculture Foreign Agriculture Service*. U.S. Department of Agriculture Foreign Agriculture Service. https://ipad.fas.usda.gov/cropexplorer/global_reservoir/

USGS. (2018). *Digital Elevation-Shuttle Radar Topography Mission (SRTM)*. United States Geological Survey Earth Resources Observation and Science (EROS) Archive.

Van Loon, A. F., Gleeson, T., Clark, J., Van Dijk, A. I. J. M., Stahl, K., Hannaford, J., Di Baldassarre, G., Teuling, A. J., Tallaksen, L. M., Uijlenhoet, R., Hannah, D. M., Sheffield, J., Svoboda, M., Verbeiren, B., Wagener, T., Rangecroft, S., Wanders, N., & Van Lanen, H. A. J. (2016). Drought in the Anthropocene. In *Nature Geoscience* (Vol. 9, Issue 2, pp. 89–91). Nature Publishing Group. https://doi.org/10.1038/ngeo2646

Vanderkelen, I., van Lipzig, N. P. M., & Thiery, W. (2018). Modelling the water balance of Lake Victoria (East Africa) – Part 1: Observational analysis. *Hydrology and Earth System Sciences*, *22*(10), 5509–5525. https://doi.org/10.5194/hess-22-5509-2018

Vermote, E., & Wolfe, R. (2015). MOD09GA MODIS/Terra Surface Reflectance Daily L2G Global 1kmand 500m SIN Grid V006 [Data set]. *NASA EOSDIS Land Processes Distributed Active Archive Center*.

Vishwanath, T., & Krishnan, N. (2015). *Where are Iraq's Poor: Mapping Poverty in Iraq*. https://hdl.handle.net/10986/22351

Vörösmarty, C. J., Green, P., Salisbury, J., & Lammers, R. B. (n.d.). *Global Water Resources: Vulnerability from Climate Change and Population Growth* (Vol. 17). https://www.science.org

Waheed, S. Q., Alobaidy, M. N., & Grigg, N. S. (2022). Forcing Data Organization for the Lesser Zab River Basin in Iraq to Build a Coherent Hydrological Model. *Journal of Hydrologic Engineering*, *27*(12). https://doi.org/10.1061/(asce)he.1943-5584.0002209

Waheed, S. Q., Alobaidy, M. N., & Grigg, N. S. (2023). Resilience Appraisal of Water Resources System under Climate Change Influence Using a Probabilistic-Nonstationary Approach. *Environments - MDPI*, *10*(5). https://doi.org/10.3390/environments10050087

Waheed, S. Q., Grigg, N. S., & Ramirez, J. A. (2020). Variable Infiltration-Capacity Model Sensitivity, Parameter Uncertainty, and Data Augmentation for the Diyala River Basin in Iraq. *Journal of Hydrologic Engineering*, *25*(9). https://doi.org/10.1061/(asce)he.1943-5584.0001975

Wainwright, C. M., Finney, D. L., Kilavi, M., Black, E., & Marsham, J. H. (2021). Extreme rainfall in East Africa, October 2019–January 2020 and context under future climate change. *Weather*, *76*(1), 26–31. https://doi.org/10.1002/wea.3824

Wan, W., Liu, B., Zeng, Z., Chen, X., Wu, G., Xu, L., Chen, X., & Hong, Y. (2019). Using CYGNSS data to monitor China’s flood inundation during typhoon and extreme precipitation events in 2017. *Remote Sensing*, *11*(7). https://doi.org/10.3390/RS11070854

Wang, J., Hu, Y., & Li, Z. (2022). A New Coherence Detection Method for Mapping Inland Water Bodies Using CYGNSS Data. *Remote Sensing*, *14*(13). https://doi.org/10.3390/rs14133195

WMO. (2017). *WMO Guidelines on the Calculation of Climate Normal*. World Meteorological Organization (WMO). https://library.wmo.int/doc_num.php?explnum_id=4166

WorldBank. (2019). *World Bank Data Catalog, 2019. Major River Basins of The World*. The World Bank International Bank for Reconstruction and Development (IBRD) and International Audit Vice Presidency (IAD).

WWF. (2019). *HydroSHEDS, DEG, Water Risk Filter. Hydrology in Africa*. World Wildlife Fund (WWF), Esri Map Service.

Xu, J., & Lambert, J. H. (2013). Distributed travel time savings of a multiscale transportation access management program. *Environment Systems and Decisions*, *33*, 362–375.

Yarveysi, F., Alipour, A., Moftakhari, H., Jafarzadegan, K., & Moradkhani, H. (2023). Block-level vulnerability assessment reveals disproportionate impacts of natural hazards across the conterminous United States. *Nature Communications*, *14*(1), 4222. https://doi.org/10.1038/s41467-023-39853-z

Yehia, M. A., Al-Taai, O. T., & Ibrahim, M. K. (2023). Spatiotemporal Distribution of Mean Temperature and Total Precipitation over Iraq for a Period (1980-2017). *IOP Conference Series: Earth and Environmental Science*, *1158*(3). https://doi.org/10.1088/1755-1315/1158/3/032004

You, H., Lambert, J. H., Clarens, A. F., & McFarlane, B. J. (2014a). Quantifying the influence of climate change to priorities for infrastructure projects. *IEEE Transactions on Systems, Man, and Cybernetics: Systems*, *44*(2), 133–145. https://doi.org/10.1109/TSMC.2013.2248709

You, H., Lambert, J. H., Clarens, A. F., & McFarlane, B. J. (2014b). Quantifying the Influence of Climate Change to Priorities for Infrastructure Projects. *IEEE Transactions on Systems, Man, and Cybernetics: Systems*, *44*(2), 133–145. https://doi.org/10.1109/TSMC.2013.2248709